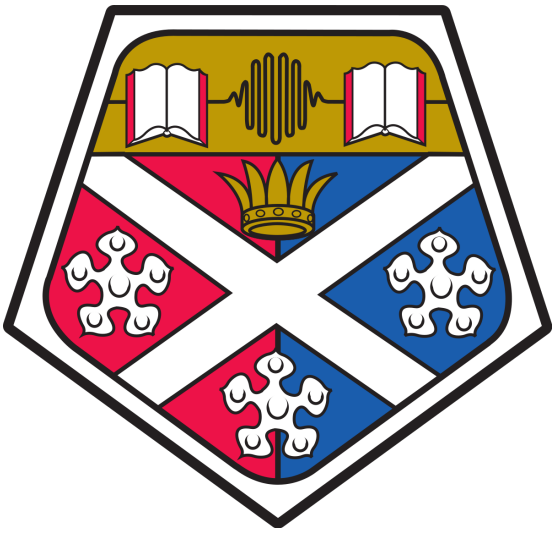

Imaging and quantification of nutrient-transporting channels in *Escherichia coli* biofilms

Beatrice Bottura

Submitted in fulfilment of the requirements for the degree of

Doctor of Philosophy

Department of Physics

Faculty of Science

University of Strathclyde

November 2023

A Davide

Declaration of Authenticity and Author's Rights

This thesis is the result of the author's original research. It has been composed by the author and has not been previously submitted for examination which has led to the award of a degree.

The figures presented in this work are a result of my own work, except those that have been adapted or reproduced from other published work. In these cases, citation is provided in the figure caption in accordance with copyright laws.

The JM105 mini-Tn7-*gfp* strain was provided by Dr. Ainsley Beaton (John Innes Centre). Strains from the Keio collection were provided by Dr. Manuel Banzaf (University of Birmingham). The pKD46 and pKD4 plasmids were provided by Dr. David Mark (University of Glasgow). The pAJR145 and pACYC184 plasmids were provided by Dr. Rebecca McHugh (University of Glasgow). The gene-specific primers for *amiA*, *cysC*, *minC*, *rodZ* and *ydgD* (Table A.5) were designed by Prof. Paul A. Hoskisson (University of Strathclyde). The schematic diagrams prepared with BioRender were created using license number SR25JKZ3PC (Miss Kay Polland, University of Strathclyde).

Signed: Beatrice Bottura

Date: November 2023

Abstract

The internal structure of biofilms is crucial for their growth and development. In particular, the network of internal channels recently discovered in *Escherichia coli* functions as a nutrient uptake and diffusion system. While mesoscopic imaging of these channels has proven to be a powerful visualisation tool, the lack of a specialised image analysis pipeline has so far prevented an accurate quantitative characterisation of channel morphology. The genetic determinants of channel formation also remain unknown.

This thesis describes the imaging and quantification of the network of nutrient-transporting channels in *E. coli* biofilms through open-source image analysis methods, and presents an experimental framework to perform gene deletions leading to a change in cell shape for the *E. coli* strain JM105 mini-Tn7-*gfp*.

The morphology of bacterial biofilms is strongly affected by environmental growth conditions, with mechanical and biochemical composition of the growth substrate contributing to the formation of complex three-dimensional patterns. Thanks to the combination of mesoscopic fluorescence imaging and open-source image analysis, the width of individual nutrient-transporting channels was measured for biofilms formed by the *E. coli* strain JM105 mini-Tn7-*gfp*, revealing a strong dependence of channel width on both spatial location inside the biofilm and nutrient availability within the substrate. The mechanism of nutrient transport within channels was proposed to follow fluid dynamic behaviour, which would

lead to increased nutrient flow towards the centre of the biofilm, where channels are smaller in diameter.

The use of fractal geometry tools for the quantification of biofilm morphology and expansion patterns is well documented. The network of intra-colony channels in *E. coli* was also originally predicted to exhibit a fractal morphology, and this was verified in this work through fractal analysis of mature *E. coli* biofilm images. A dependence of channel architecture on *E. coli* cell shape was hypothesised due to channel formation being an emergent property of biofilm formation, and this was investigated with four cell shape mutants of *E. coli* obtained from the Keio collection, which is a single-gene knockout library derived from the laboratory strain BW25113. The complexity of internal channels was found to be comparable to that of computer-generated fractals for all strains grown on both rich and minimal medium substrates, though cell shape was not identified as a unique channel morphology descriptor.

The characterisation of nutrient-transporting channels in *E. coli* has so far been performed on the laboratory strain JM105 mini-Tn7-*gfp* thanks to its compatibility with Mesolens imaging, which provides subcellular resolution across whole, multi-millimetre sized biofilms. While the results presented in Chapter 2 of this thesis were obtained with the same strain, the fractal analysis of biofilms formed by cell shape mutants described in Chapter 3 was performed on the strain BW25113, the parental strain for the Keio collection. This was due to the rapid biofilm disruption to planktonic state exhibited by BW25113 during immersion with liquid mounting medium, which was necessary to match the refractive index of the Mesolens used in water immersion mode. A genetic engineering protocol based on Lambda Red recombination was hence designed in order to circumvent this problem and carry out the inactivation of genes involved in the regulation

of cell shape in *E. coli* JM105 mini-Tn7-*gfp*. While testing this method, the resistance of JM105 mini-Tn7-*gfp* to the antibiotic ampicillin was discovered and characterised, leading to a proposed modification of the genetic engineering protocol using traditional cloning methods.

Acknowledgements

There are many people I am grateful to for their help and support in this intense PhD adventure. My family, friends and colleagues are the reason I made it to this incredible finish line, and it will be hard to put in writing how thankful I am to you all. I'll do my best.

First of all, I want to thank Gail. I did not know this at the start of my PhD, but over time I realised how extremely lucky I am to be part of this group. Thank you for always finding the time to show me how to use our many microscopes and to discuss research ideas, and for always being encouraging and supportive even when I wanted to do something completely different from what my project was about at the time (cloning). I wouldn't be the multidisciplinary scientist I am today if it wasn't for you. Thank you for all the support in the conference applications and presentations, and for your (incredibly timely) feedback on manuscripts and experiments. But most of all, thank you for making me feel valued as a person and as a scientist. I do not take any of this for granted, and it has made a real difference during my PhD. It has been a privilege working with you, and it's safe to say I could not have done it without your help and guidance.

I would also like to thank Paul, for giving me guidance on the basics (and beyond!) of microbiology at the start of my PhD. You made me feel part of the microbiology gang since the beginning by introducing me to all the PIs and students on level 6, and you helped me network in a field that was entirely new to me. I am lucky

to have had a second supervisor who taught me so much.

I thank all the PIs from level 6 who helped me during my project, and who made me think about so many different aspects of my research (and of microbiology) which I would not have otherwise encountered. Morgan, your knowledge of *E. coli* genetics will never cease to amaze me, and I aspire one day to be as thorough and systematic as you are in my scientific endeavours. I am tremendously grateful for your guidance during all my cloning and general *E. coli* trouble, for all your invaluable input over these years and for your manuscript contributions. Thank you to Paul Herron, Iain Hunter and Katherine Duncan for your many experimental suggestions, and for not being too harsh on me when I spelled *E. coli* with a capital C during my first microbiology group meeting.

Thank you to my second PhD family on level 6. Becca and John, I will always be grateful for how much you have patiently taught me over the years, for all the protocols you have shown me and for always suggesting sensible controls when my experiments went wrong. I thank Katherine for sharing the Mesolens biofilm journey with me and for always giving me interesting suggestions on literally every aspect of my research. Thank you to Robyn and Elmira for sharing your cloning tricks and sense-checking so many of my gels, and to Ainsley and Dave for listening to my cloning rants. Thanks to Molly, Eilidh and Emily, to my last bench buddies James and Jack, and to the current adults in the Hoskie group, Dan and JB, for keeping the group afloat.

I honestly could not have asked for a better working environment than the Biophotonics/Mesolab group. You have all been very welcoming and understanding of my lack of knowledge of Scottish culture, and while I am not sure I am quite ready to try a fried Mars bar yet, the exclamation “cheese baguette” will forever

be engrained in my brain. I would like to thank Mollie, Lisa and Katrina for the emotional support whenever world politics would come up with something unacceptably unfair. Eliana, thank you for never missing an opportunity to tell off someone who butchered Italian cuisine and for defending the pillars of Italian tradition in the group before me. Thank you to Shannan, for always sharing the cutest dog pictures, for defending me from Liam's mean comments and for tolerating my overuse of the word "Ravintola". Thank you to wee Mollie, for the best pet snail impression I have ever seen, and to Kay, my fellow Fall Out Boy fan, for your life hacks and for introducing me to NY Times crosswords. Thank you to Becca, for listening to my endless drama and somehow managing to lower my stress levels by contributing your own personal shenanigans - I never really understood how that worked really, but I will be forever grateful that it did. Thanks to Jay for coffee recommendations and for being an all round wonderful human. Thank you also to Louise, for sharing yummy media recipes that I definitely don't regret making with you in the media bay (only kidding), and to Laura and Lewis - I'm sad that our paths only crossed for a short time.

Now to Meg, thank you for always listening to my stressed/angry/frustrated rants with no complaints, for all the lifts home and for all the (much needed) emotional support during this PhD journey. I think it's safe to say that we have been through a lot together during these last few years, and I am so glad to have been able to share some of my happiest conference memories with you. More importantly, it has made me incredibly happy to meet someone who could almost match my insanity levels in the office and out (I admit they may have deteriorated in the last month or so), and I am not scared to admit that your Busandals jokes have absolutely, 100% got me through the last few months of my PhD.

I also specifically want to thank Dr. Liam Mark Rooney (FRMS). Ever since you

spent your afternoon waiting in A&E with me after my infamous fainting, it is safe to say that you have been there for me in all my research shenanigans. I still remember you introducing me to everyone on level 6 and making sure I felt part of the group (despite my terrible social skills). I would not have survived my first MicroSoc conference without you and the wine you brought me during the poster presentation. I am grateful for all our breakdowns in the lab (I particularly enjoyed your irrational fear of electroporation), and maybe a little less so for your occasional dubious choices in Italian food preparation. I hope that in those dark moments you will continue to feel my generational disappointment. But most of all, I am glad that I got to work with you on so many cool biofilm projects. I do not mean this lightly when I say that it has been worth all the failed cloning and the shocks of discovering that damned ampicillin resistance. Thanks to you, at the end of all this, on very rare occasions, I might finally be able to say that I am, in fact, a microbiologist.

Thanks to Laura, for all the music recommendations and for all the ghost hugs you sent me during these (objectively) difficult years. I don't say this often enough, but I love you and I hope to go to many more gigs together. Thanks also to the rest of the D&D gang: Ellie, Tom, Vincent and Q. I am sorry for never learning how to play Risk of Rain properly, and thank you for all the adventures.

Thanks to Calum, for supporting me in all the ways a person can. I know I can be a difficult person to be around, and I feel so lucky to have had you by my side in these years. You make me incredibly happy, and I can only hope I make you at least as happy in return. I love you lots and lots and lots.

Grazie a Davide, a cui è dedicata questa tesi. Mi manchi tanto, e anche se non riuscirò mai a pensare a te senza essere triste, spero in qualche modo di averti

resa fiera. Vorrei che tu fossi qui per festeggiare insieme a me questo traguardo, e tutti quelli successivi. A Elena, sei e sarai sempre la mia persona. Ne abbiamo passate di ogni in questi anni, ma uno dopo l'altro abbiamo superato insieme tutti gli ostacoli che ci sono capitati davanti. Non ce l'avrei mai fatta senza di te, spero che tu lo sappia. Ti voglio bene.

Ringrazio anche la mia piccola e disastrata famiglia. Grazie al nonno Luciano e alla nonna Renata, per avermi insegnato a giocare a briscola e ad andare in bicicletta, per i fondini di pane con i pomodori e per avermi sempre supportato negli studi (vedrai nonna, la mia laurea sarà davvero più bella di un matrimonio!). A Laura, anche se ormai siamo lontane, spero che tu sappia che ti voglio e ti vorrò sempre bene, e che sarò qui se mai avrai bisogno o se mi vorrai di nuovo nella tua vita. Infine, a mamma e papà, grazie per avermi supportato nei miei spostamenti verso posti sempre più freddi e piovosi, e per avermi permesso di arrivare fin qui. Grazie per avermi insegnato che con impegno e disciplina si può fare tutto, e per avermi dato fiducia in tutti questi anni, da quando a 17 anni sono partita per questa avventura britannica. Vi voglio bene, e vi devo più di quello che immaginate.

Research outputs

Published and submitted works

- Bottura, B., Rooney, L.M., Hoskisson, P.A., McConnell, G., (2022). Intra-colony channel morphology in *Escherichia coli* biofilms is governed by nutrient availability and substrate stiffness. *Biofilm*, **4**, https://doi.org/10.1016/j.bioflm.2022.100084

- Rooney, L.M., Bottura, B., Baxter, K., Amos, W.B., Hoskisson, P.A., McConnell, G., (2023). Addressing multiscale microbial challenges using the Mesolens. *Journal of Microscopy*, https://doi.org/10.1111/jmi.13172

- Bottura, B., Rooney, L.M., Feeney, M., Hoskisson, P.A., McConnell, G., (2023). Fractal complexity of *Escherichia coli* nutrient transport channels is influenced by cell shape and growth environment. *bioRxiv*, https://www.biorxiv.org/content/10.1101/2023.11.29.569150v1

Oral presentations

- **Microscience Microscopy Congress, virtual, July 2021**

  "Using the Mesolens to observe structural changes in *E. coli* mature colony biofilms under different nutrient availability"

- **Microbiology Society Annual Conference, Belfast, April 2022**

  "Intra-colony channel morphology in *Escherichia coli* biofilms is governed

by nutrient availability and substrate stiffness"

- **Eurobiofilms, Majorca, August 2022**

  "Intra-colony channel morphology in *Escherichia coli* biofilms is governed by nutrient availability and substrate stiffness"

- **Molecular Microbial Ecology Group, Glasgow, December 2022**

  "Intra-colony channel morphology in *Escherichia coli* biofilms is governed by nutrient availability and substrate stiffness"

- **Microscience Microscopy Congress, Manchester, July 2023**

  "Investigating the influence of cell shape on intra-colony channel architecture by fractal analysis of confocal microscopy biofilm images"

- **International Microscopy Congress, Busan, September 2023**

  "Investigating the influence of cell shape on mature biofilm morphology and internal structure by fractal analysis of confocal microscopy images", **Best oral presentation award**

Poster presentations

- **Scottish Universities Physics Alliance (SUPA) Annual gathering, virtual, May 2021**

  "Using the Mesolens to observe structural changes in *E. coli* mature colony biofilms under different nutrient availability"

- **University of Strathclyde Doctoral School Multidisciplinary Symposium, virtual, June 2021**

  "Fractal patterns in *E. coli* biofilms are preserved under various growth conditions"

- **Microscience Microscopy Congress, virtual, July 2021**

  "Using the Mesolens to observe structural changes in *E. coli* mature colony biofilms under different nutrient availability"

- **Microbiology Society Annual Conference, Belfast, April 2022**

  "Intra-colony channel morphology in *Escherichia coli* biofilms is governed by nutrient availability and substrate stiffness"

- **European Light Microscopy Initiative (ELMI), Turku, June 2022**

  "Quantifying the effect of substrate composition on intra-colony channel morphology in *E. coli* biofilms using a custom-made open-source image analysis pipeline"

Contents

List of Figures

List of Tables

List of Abbreviations

2D	**2**-**D**imensional
3D	**3**-**D**imensional
Ag43	**A**nti**g**en 43
ANOVA	**AN**alysis **O**f **VA**riance
BLAST	**B**asic **L**ocal **A**lignment **S**earch **T**ool
CCD	**C**harged **C**oupled **D**evice
CLAHE	**C**ontrast **L**imited **A**dapted **H**istogram **E**qualization
CLSM	**C**onfocal **L**aser **S**canning **M**icroscopy
CRISPR	**C**lustered **R**egularly **I**nterspaced **S**hort **P**alindromic **R**epeats
DAPI	4',6-**DiA**midino-2-**P**henyl**I**ndole
DBC	**D**ifferential **B**ox-**C**ounting
DLA	**D**iffusion-**L**imited **A**ggregation
DNA	**D**eoxyribonucleic **N**ucleic **A**cid
ECM	**E**xtra **C**ellular **M**atrix
EPS	**E**xtracellular **P**olymeric **S**ubstances
FAD	**F**lavin **A**denine **D**inucleotide
FIJI	**F**iji **I**s **J**ust **I**mageJ
FISH	**F**luorescence **I**n **S**itu **H**ybridization
HDM	**H**igh **D**ensity **M**atrix
FITC	**F**luorescein **I**so**T**hio**C**yanate
FWHM	**F**ull **W**idth at **H**alf **M**aximum
GFP	**G**reen **F**luorescent **P**rotein
IQR	**I**nter-**Q**uartile **R**ange
IR	**I**nfra**R**ed

KEGG	**K**yoto **E**ncyclopedia of **G**enes and **G**enomes
LB	**L**ysogeny **B**roth
LED	**L**ight **E**mitting **D**iode
N.A.	**N**umerical **A**perture
NADH	**N**icotinamide **A**denine **D**inucleotide + **H**ydrogen
NCBI	**N**ational **C**enter for **B**iotechnology **I**nformation
OD	**O**ptical **D**ensity
PCR	**P**olymerase **C**hain **R**eaction
PMT	**P**hoto **M**ultiplier **T**ube
PSF	**P**oint **S**pread **F**unction
RD	**R**eaction **D**iffusion
RDBC	**R**elative **D**ifferential **B**ox-**C**ounting
RNA	**R**ibo**N**ucleic **A**cid
rSAP	**S**hrimp **A**lkaline **P**hosphatase
ROI	**R**egion **O**f **I**nterest
SNR	**S**ignal to **N**oise **R**atio
UV	**U**ltra **V**iolet
WGA	**W**heat **G**erm **A**gglutinin
WHO	**W**orld **H**ealth **O**rganisation

Allons-y!

The Doctor

Chapter 1

Introduction

This chapter will introduce the main principles of optical microscopy, and will outline the main microscopy techniques used, or relevant to, this work. In particular, fluorescence microscopy techniques such as widefield and confocal laser scanning microscopy will be discussed, and the Mesolens will be introduced as a novel optical instrument to study bacterial biofilms. Bacterial biofilms, particularly those formed by *Escherichia coli*, will be introduced in terms of their composition and life cycle. Biofilm morphology will be discussed, with emphasis on internal morphological patterns. Next, image analysis tools useful for the characterisation of biological specimens will be presented, with a focus on the techniques applicable to the quantification of biofilm morphology.

1.1 Principles of optical microscopy

The concept of microscopy is best explained by the origin of the word itself: the Greek *mikrós*, "small", and *skopeîn*, "to observe". In essence, the microscope is an instrument used to look at small things. In order to do this, microscopes need to provide magnification, which is the means to optically enlarge originally small objects. This is achieved by a set of lenses, which bend the light rays originating from the object in a process called refraction. Microscopy also requires contrast (the ratio between intensities of different points on the object, or between the object and the background [1]) to facilitate the distinction of features in an image, particularly at borders or edges. In this section, I will describe the principles of image formation along the light path, image resolution and contrast, as well as some microscopy techniques particularly important for this study - widefield epi-fluorescence microscopy, confocal laser scanning fluorescence microscopy, fluorescence mesoscopy and phase-contrast microscopy.

1.1.1 Ray optics and image formation

When light passes through a boundary between two media with different refractive indices (such as air and glass), the portion of the light that passes through to the second medium changes direction in a phenomenon called refraction [2]. Figure 1.1 illustrates the geometry of refraction, where all the rays are assumed to lie on the same plane. The angle of incidence θ_1 and the angle or refraction θ_2 are related by Snell's law [3]

$$n_1 \, sin\theta_1 = n_2 \, sin\theta_2 \tag{1.1}$$

where n_1 and n_2 are the refractive indices of each medium. The principle of

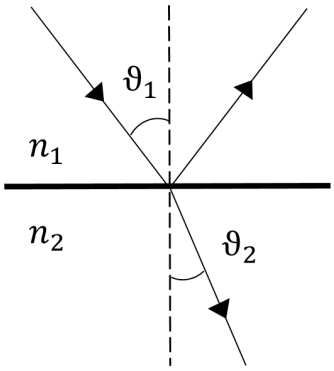

Figure 1.1: Geometry describing Snell's law. The incident beam travels through a medium with refractive index n_1, and crosses the boundary with the second medium (of refractive index n_2) at an angle θ_1 from the normal to the boundary. The beam changes direction and travels through the second medium at an angle θ_2 from the normal to the boundary.

refraction is used in microscopy to focus a beam of light into a specific point, located at a distance f away from the lens. This distance is specific to each lens, and is called focal length [4].

In an optical microscope, images are formed by focusing light rays coming from an object to specific locations thanks to a set of lenses. In the simplest microscope setup, rays from a light source are first focused on the object by the condenser lens, whose axial position and diaphragm aperture are adjusted in such a way to provide uniform illumination to the sample [5]. The beam originating from the object is then focused by a second lens, the objective, onto an intermediate plane. In order to observe the image by eye, the beam is refracted once more inside the eyepiece of the microscope, which allows an image to be formed in focus on the observer's retina [6]. In order to optimise sample illumination while rejecting the image of the light source, the elements forming the microscope must be arranged in what is called "Köhler illumination" [7], [8]. This arrangement creates two sets

of conjugate planes along the beam path (Figure 1.2) where objects are in focus at the same time [9].

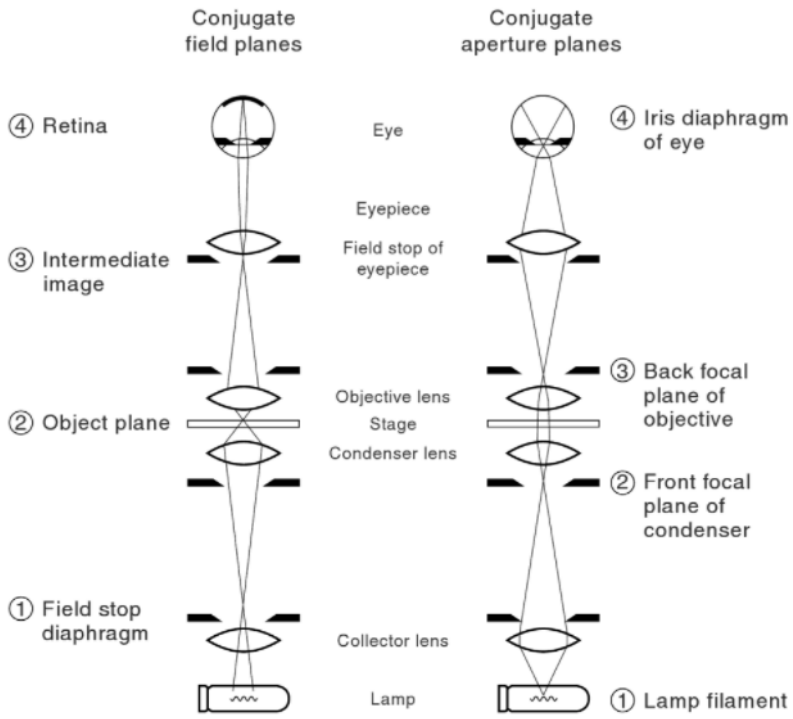

Figure 1.2: Location of the two sets of conjugate planes formed in Köhler illumination. The field (or object) planes include the eyepiece and retina of the eye, whereas the aperture planes host the eye's pupil. Figure reproduced from [9].

1.1.2 Resolution

In a microscope, the image of an object is magnified by a system of lenses, and focused onto a spot on the image plane. Because of the diffraction of light through the optical elements of the microscope, the spot will not be sharp - instead, it will be blurred, and will have an intensity distribution described by the point spread function (PSF) [10]. The image observed at the image plane is given by the convolution of the ideal magnified image and the PSF [11].

The resolution of the imaging system is given by the Rayleigh limit, and corresponds to the full-width at half-maximum (FWHM) of the PSF. More precisely, the image formed on the focal plane will include a central bright spot followed by concentric rings "of rapidly diminishing brightness" [12] called Airy rings, which are separated by dark annuli. The Rayleigh criterion of resolution states that two points can be resolved if centre of the main Airy disk emitted by one object coincides with the first minimum of the Airy disk emitted by the other. This principle is illustrated in Figure 1.3. The distance between these two features, d, is given by [13]

$$d_{xy} = 0.61\frac{\lambda}{N.A.} \tag{1.2}$$

where λ is the excitation wavelength, and the numerical aperture ($N.A.$) is related to the refractive index of the medium, n, and the half-angle of focus, θ, by the equation

$$N.A. = n\ sin\theta \tag{1.3}$$

From Equation 1.2, we see that the size of the smallest features that can be resolved can be reduced by increasing the refractive index of the imaging medium. Typical immersion liquids include water ($n = 1.33$), glycerol ($n = 1.47$) and oil (approximately $n = 1.51$). The lens immersion liquid must be refractive index-matched to the sample in order to minimise spherical aberration. Most biological samples have a refractive index close to that of water [14], which is routinely used in bioimaging.

The considerations above refer to lateral resolution, that is, in the plane of the object. When imaging biological samples, we are also often interested in axial

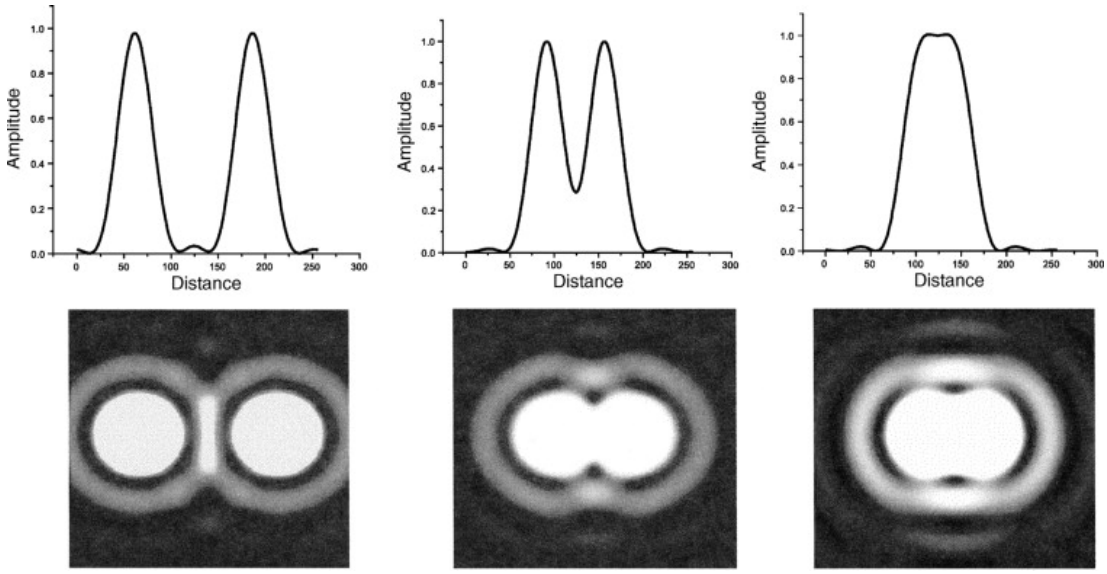

Figure 1.3: The ability to resolve two objects depends on their separation distance, which affects the relative position of their intensity spectra over that distance. When the peak of one of the two spectra coincides with the first minimum of the other spectrum (Rayleigh criterion, centre) the two objects are resolved. Objects are also resolved if the distance between these two features is greater than the Rayleigh criterion (left). If the distance is shorter, on the other hand, the objects are not resolved (right). The bottom panels in the figure show the Airy rings patterns produced by the two object beams. Figure reproduced from [15] with permission from Elsevier (license number 5673801342160).

resolution, which is in the direction perpendicular to the object plane. From Abbe's theory of diffraction, the axial resolution of a system is given by [16]

$$d_z = \frac{2\,\lambda}{N.A.^2} \tag{1.4}$$

1.1.3 Optical aberrations

A perfect objective lens would have a PSF corresponding to the Airy diffraction pattern. In reality, this is difficult to achieve, and the PSF is distorted by a number of aberrations which result from imperfect lens design or suboptimal imaging conditions. Optical aberrations can affect image quality in the axial or lateral direction, and can be either monochromatic - if they do not depend on the wavelength of light used for illumination - or chromatic - if they do.

Chromatic aberrations occur because of dispersion, which is a phenomenon in which different optical wavelengths propagate at different velocities, depending on the refractive index of the material in which they are travelling. This separates the paths of light rays formed by different wavelengths [17], [18]. Spherical aberration results from the spherical nature of optical lenses. Rays hitting the lens at different locations on its surface (along the direction perpendicular to the optical axis) are focused at different positions along the optical axis: in positive spherical aberration, rays hitting the edge of the lens are focused closer to the lens, whereas in negative spherical aberration they are focused further away [19]. Spherical aberrations can also result from a refractive index mismatch between the medium that embeds the specimen and the lens immersion medium. This type of spherical aberration can be corrected with the use of correction collars on some objective lenses, which can adjust the position of the lenses along the optical axis [20].

Coma and astigmatism are off-axis aberrations, which arise from point sources originating away from the optical axis. Coma extends the PSF of point sources in an asymmetric fashion, in a shape resembling a comet [21]. Astigmatism is an optical aberration by which an object off the optical axis is not focused into a

single spot. This can be due to misalignment of optical elements along the optical axis [22].

1.2 Fluorescence microscopy

Fluorescence microscopy is one of the most widely used techniques for the investigation of biological samples, both *in vitro* and *in vivo*. While its achieved resolution is not as high as other techniques (such as electron microscopy), fluorescence imaging allows to target specific molecules inside the sample and image regions at a depth through living cellular specimens in good detail. The emitted fluorescent light signal gives information about the intensity and location of fluorophores in the sample, as well as on the molecular environment and dynamic processes that occur within it. The following sections will describe the principles of image acquisition and analysis in fluorescence microscopy, as well as the particular features needed to take advantage of fluorescence for biological imaging.

1.2.1 Fluorescence

Fluorescence is a radiative process which involves the absorption of a photon by a molecule (fluorophore) followed by the emission, a few nanoseconds later, of a photon with a longer wavelength [23].

The energy transition associated with this process occurs between the lowest energy level of the excited state (S_1) and the ground electronic level (S_0), as shown in Figure 1.4. The extra energy of the absorbed photon is either lost to vibrational relaxation or it is dissipated as heat in a non-radiative process called internal conversion. The resulting difference in energy maxima between the absorption and emission spectra is called the Stokes shift [24]. The number

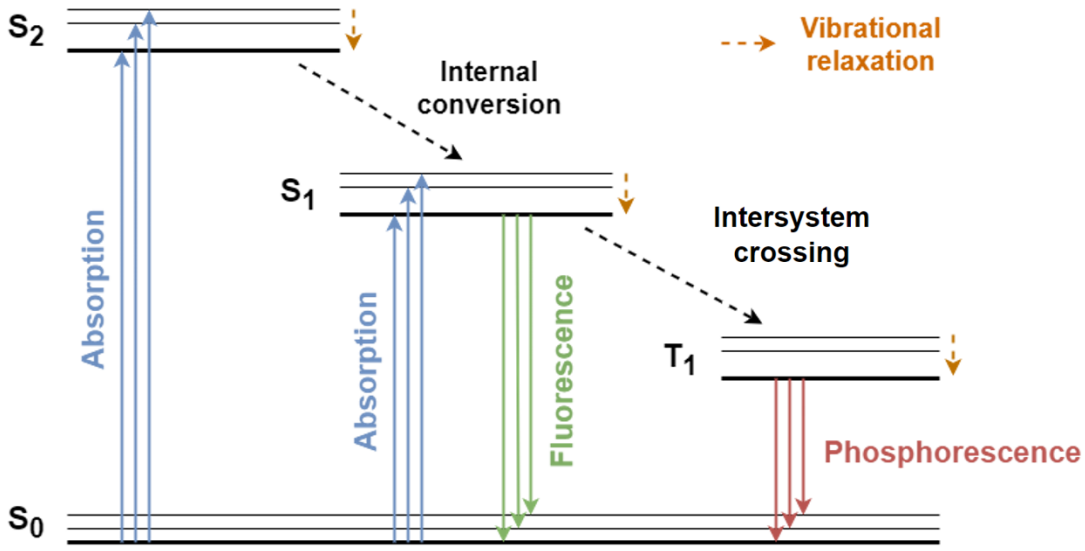

Figure 1.4: Jablonski diagram showing the main transitions between the singlet ground state (S_0), the excited states (S_1 and S_2), and the triplet excited state (T_1). Note that intersystem crossing is non-radiative, since it only involves the transition between states of different spin multiplicity. It can be followed by the slow (ms) emission of a photon via phosphorescence. Image created in draw.io (`https://app.diagrams.net/`, JGraph).

of photons in the excited state, N, decays exponentially with time, t, and follows the equation

$$N(t) = N(0)\ e^{-At} \tag{1.5}$$

where *N(0)* is the initial number of excited photons and A is the Einstein coefficient of spontaneous emission, which represents the rate of fluorescence (the inverse of the fluorescence lifetime τ). Fluorescent intensity also decays exponentially with time, with a rate intrinsic to each fluorophore [25].

1.2.2 Fluorescent probes

Fluorescence microscopy is particularly powerful for biological imaging thanks to its capability to specifically target molecules of interest. In order to achieve this, fluorescent probes must be carefully selected depending on a number of factors. Firstly, their excitation wavelength must match the wavelength of the illumination source of the microscope. The fluorescent molecules themselves have to be bright and with a high quantum yield (number of photons emitted / number of photons absorbed [26]). The fluorescence yield should ideally be independent of external conditions such as temperature, pH or medium composition [27], and the fluorophores should preferably be resistant to photobleaching (chemical degradation of the molecule following prolonged illumination) [28].

Thanks to their molecular and spectral specificity, multiple fluorescent probes can be used simultaneously to investigate different biological components inside the same sample using multichannel fluorescence microscopy [29]. The wide emission spectra of each fluorophore traditionally limits this technique to a few probes per sample, because spectral overlap prevents the precise localisation and signal separation of fluorophores [25]. Nonetheless, image analysis techniques have been developed to separate contributions from different fluorophores post-acquisition. One such example is spectral unmixing, which calculates the contributions of each fluorophore to each pixel intensity using least-square fitting [30]. Crucially, there is now a wide range of fluorophores available to match specific excitation and emission wavelengths. Fluorescent probes can be distinguished in two categories: intrinsic and extrinsic fluorophores, which are described below.

1.2.2.1 Intrinsic fluorophores

Intrinsic fluorophores are biological molecules such as aromatic amino acids (e.g. tryptophan, phenylalanine), organic compounds (e.g. flavins) and coenzymes (NADH, FAD) that naturally emit fluorescent light [31]. Because the emission spectra of intrinsic fluorophores are sensitive to biochemical changes in the local environment [32], these molecules are often used to study protein-protein interactions and protein conformational changes [25]. Intrinsic fluorophores have also been used in conjunction with spectroscopic methods to identify bacterial species [33]–[36] and to study bacterial growth and metabolism [37].

1.2.2.2 Fluorescent proteins

The emission of light by living organisms, called bioluminescence, is a common occurrence, and can be observed in animal and plant kingdoms alike (insects, fungi, seawater organisms, etc.), but also in bacteria [38]. The emission of light is the result of the reaction between a compound named luciferin and the enzyme luciferase, occurring in the presence of oxygen [39]. It was with the intent of purifying luciferase from the bioluminescent hydromedusan *Aequorea victoria* that Shimomura purified the fluorescent protein *aequorin* in 1962 [40]. While purified *aequorin* emits blue light in the presence of calcium ions, *Aequorea victoria* also emits green light. This green light is emitted after energy transfer from *aequorin* to a second protein, later named "green fluorescent protein" (GFP) [41].

The amino acid composition and chemical structure of GFP were soon elucidated [42], [43]. The crystal structure was solved by X-ray crystallography in 1996 [44], [45], revealing a cylindrical shape made of 11 strands of β-sheet with a α-helix chromophore inside them (Figure 1.5). The DNA of the GFP gene was sequenced and cloned in 1992 [46], and was successively expressed in both prokaryotic and

eukaryotic cells [47]. These achievements paved the way for GFP to be used as a marker of gene expression and protein localisation [48].

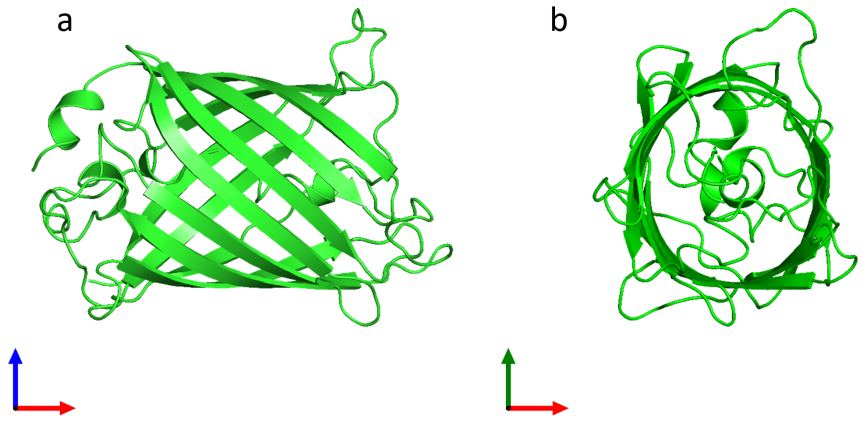

Figure 1.5: Crystal structure of GFP resolved by X-ray crystallography, viewed from the front (a) and from the top (b). The structure was published in [45] and is reproduced here from the Protein Data Bank in Europe [49].

Over the years, fluorescent proteins have been engineered to either enhance their emission intensity [50], or to cover different areas of the visible spectrum [51], [52]. Mutations of GFP were also designed to make it more resistant and less subject to denaturation, resulting in increased fluorescence yield [53]. Thanks to these properties, fluorescent proteins are now routinely used in live fluorescence imaging to study an extensive number of biological phenomena [54], [55], including the morphological study of cellular organelles [56], protein labelling for localisation and tracking [57] and single-molecule localisation [58].

1.2.2.3 Synthetic dyes

Synthetic dyes are extrinsic fluorophores produced through chemical synthesis. The chemical properties of these dyes can be tuned to favour binding to certain

molecules or localisation in specific areas of the sample to be investigated [59]. For example, the lipophilic dye Nile Red is specific to intracellular lipid droplets and it is strongly fluorescent and soluble in hydrophobic environments [60]. The fluorescein derivative fluorescein isothiocyanate (FITC), first synthesised in 1958 [61], is routinely used for antibody labelling [62] and as an intracellular pH probe due to its change in fluorescent spectrum with pH [63]. Finally, the fluorescent stain 4,6-diamidino-2-phenylindole (DAPI) is used as a DNA probe thanks to its strong electrostatic binding to DNA regions rich in adenosine and thymidine [64], and it can be used on fixed samples [65].

Synthetic dyes also include a specific set of molecules, called photoactivatable fluorophores, which can switch from an inactive, non-emitting state to an active, emitting state after illumination by an activation wavelength. Excitation of the molecule with a different, appropriate wavelength can successively cause them to emit fluorescence.

1.2.3 Light sources: broadband, lasers and LEDs

Fluorescence can be excited using various types of light sources. For example, broadband light from an arc lamp can be used in conjunction with emission filters in order to select a particular output wavelength range [27]. More recently, this option has been put aside in favour of laser beams and light-emitting diodes (LEDs), which usually have a narrower bandwidth and hence a higher wallplug efficiency due to the greatly reduced required spectral filtering [66]. In particular, lasers have a bandwidth at least three times smaller than that of LEDs [67].

Lasers are a widely used source of excitation in conventional confocal fluorescence microscopy, and they have a wavelength range covering the ultraviolet (UV), visible, and infrared (IR) parts of the electromagnetic spectrum. Their

output has high temporal coherence, which makes them monochromatic [68]. Unfortunately, laser sources in the visible wavelength regime (needed to excite biologically-relevant fluorophores) are costly. Wavelength-doubling techniques such as second-harmonic generation can be used to bypass this limitation, though this significantly reduces the wallplug efficiency of the laser source [69].

LEDs are increasingly being used for widefield illumination thanks to specific wavelength selection and wide availability of peak emission wavelengths, from UV to IR. Other advantages of LED excitation systems are high stability, efficiency and reduced noise levels [70]. LED systems are also less bulky than laser setups, and are generally cheaper. Nonetheless, LED emission is not monochromatic nor coherent, and requires collimating lenses and filters for tightly-focused outputs [71].

1.2.4 Widefield and confocal laser scanning microscopy

Fluorophore excitation can occur either with widefield illumination (with the light beam covering the field of view of the microscope) or by illuminating a small region at a time and scanning through the sample using confocal microscopy.

While widefield illumination produces a single image of the sample using the eyepiece or camera as a detector, hence reducing the total acquisition time, it also brings out-of-focus light into the image plane [72]. Widefield microscopy requires low beam intensities, meaning that photodamage to the sample is low [73]. Thanks to its simplicity and versatility, widefield fluorescence microscopy is routinely used for studies of biological samples.

The second technique, on the other hand, exploits beam scanning to cover the field of view of the microscope. A light source with a narrow beam (such as a

laser) is required for this purpose. Confocal laser scanning microscopy (CLSM) rejects out-of-focus light by introducing a pinhole aperture before the detector, ensuring that only light from a single focal plane reaches it at any given time [74]. Scanning is usually achieved by changing the focal plane with the aid of movable mirrors [75]. An alternative design for confocal imaging which aims to improve image acquisition rate is the spinning disk setup [76]. In this variant, a disk with multiple pinholes is placed along the beam path, allowing for illumination of the sample with multiple parallel beams at the same time. Confocal microscopy has the advantage of producing slightly higher resolution images with respect to widefield microscopy [77], at the expense of image acquisition time (mainly limited by the movement speed of the scanning mirrors). Laser scanning microscopy can also produce 3D images by stacking images obtained at different sample depths. Another advantage of confocal microscopy is that excitation is provided by lasers, which are monochromatic and thus can specifically match the excitation wavelengths of the chosen fluorophores, and they can be used for simultaneous or sequential excitation of multiple fluorophores for multichannel imaging.

Both widefield and confocal microscopy techniques can be used either in the single-photon or multi-photon regime. In multi-photon microscopy, fluorescence can be excited by the simultaneous absorption of multiple, longer wavelength photons. This has the advantage of increased tissue penetration and reduced photodamage [78], but requires high power, pulsed lasers which are expensive [79].

1.2.5 Detectors

The detection of fluorescence in microscopy is usually performed with high-precision devices such as charged-coupled device (CCD) cameras and photomultiplier tubes (PMTs), and aims to maximise the signal-to-noise ratio (SNR). Wide-field measurements are usually performed using CCD cameras, whereas PMTs are the common choice for confocal laser scanning image acquisition. Both detectors work by converting the incoming photon signal into electric charges [80]. Other factors to consider for the choice of detectors are the response speed (or lag), the detection efficiency variation across the selected wavelength range and the ability to simultaneously detect different fluorescence signals [81].

1.2.5.1 Charge-coupled devices (CCDs)

CCDs are composed of a dense array of photodiodes fabricated from semiconductor materials. When the photodiodes are irradiated with light with energy greater than the band gap energy, they create electron-hole pairs [82]. The pairs can be separated by an applied electric field, leading to the electrons being accumulated at the electrodes [83]. Electrons are sequentially shifted towards the next electrode by changing the electric field. After reaching the last electrode, the charges are amplified and converted to a voltage signal which is stored in the memory of the computer [84].

CCDs have a broad linear dynamic range [32] and great sensitivity in a large portion of the spectrum, from X-rays to near-infrared [82]. Nonetheless, because the absorption depth of silicon decreases steeply for light of wavelength shorter than 400 nm [85], short wavelengths cannot traditionally be used for signal generation in CCDs. This limitation can be overcome by applying an anti-reflection coating to the back of the CCD [86]. The main disadvantages of CCDs are their

high power consumption [87] and smearing and blooming artefacts [88]. CCDs are also particularly sensitive to dark current, a form of noise which originates from thermal excitation of electrons in the semiconductor wells [89].

1.2.5.2 Photomultiplier tubes (PMTs)

In PMTs, shown schematically in Figure 1.6, an incident beam of light enters from a window and causes an electron to be ejected from the cathode through photoelectric effect. The electron is then focused and directed into a vacuum chamber to initiate a cascade of secondary electrons at the electrodes of the PMT, (called dynodes) [90]. This eventually leads to an accumulation of charge at the anode. The intensity of the detected signal is proportional to the incoming photon flux [91].

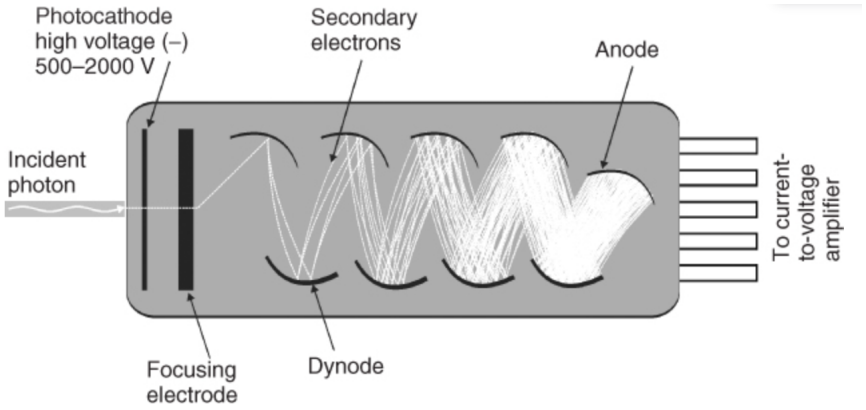

Figure 1.6: Schematic diagram showing a photomultiplier tube (PMT), reproduced from [92]. Reproduced with permission from John Wiley and Sons (license number 5673791158360).

The main advantages of PMTs are high sensitivity, low-noise amplification [32] and fast response time [93]. On the other hand, PMTs generally have a lower quantum efficiency than CCDs [94]. The spectral response of PMTs is also limited,

and multiple PMTs with different optical window materials are required to cover the useful spectral range for fluorescence microscopy [32].

1.3 Phase-contrast microscopy

Phase contrast microscopy was developed by the Dutch physicist Frits Zernike in 1932 as a technique to visualise transparent objects by exploiting small differences in their thickness or refractive index [95]. Light reflected from such objects undergoes a phase change, but this change cannot be visualised by the human eye or by a camera, so it must be converted into an amplitude change [96]. This is achieved by adding a phase plate (also named “Zernike plate") near the back focal plane of the objective lens, which shifts the phase of the light beams passing through it by $\lambda/4$ [97]. The phase plate is used in conjunction with an annulus placed in the front focal plane of the condenser lens, with a shape matching that of the phase plate ring [98]. A schematic diagram of a phase contrast microscope is shown in Figure 1.7 below.

Light is shifted by a factor of $\lambda/4$ when passing through thin transparent specimen [99], and the total phase shift between the light that passes through the phase ring and the light that does not is $\lambda/2$. This leads to destructive interference, which causes the specimen to appear darker than the background [100].

1.4 Optical mesoscopy with the Mesolens

Optical mesoscopy is a technique used to image samples between the microscale and the macroscale (corresponding to sizes between the millimetre and the centimetre), while maintaining high spatial resolution [101]. In this work we have used the Mesolens [102], a bespoke objective lens with a unique combination of

magnification (4×) and numerical aperture (0.47). This lens prescription allows imaging of a field of view of 6 mm × 6 mm in confocal laser scanning mode and of 4.4 mm × 3 mm in widefield epi-fluorescence mode, through a total imaging depth of 3 mm, with a lateral resolution of 700 nm and an axial resolution of 7 μm.

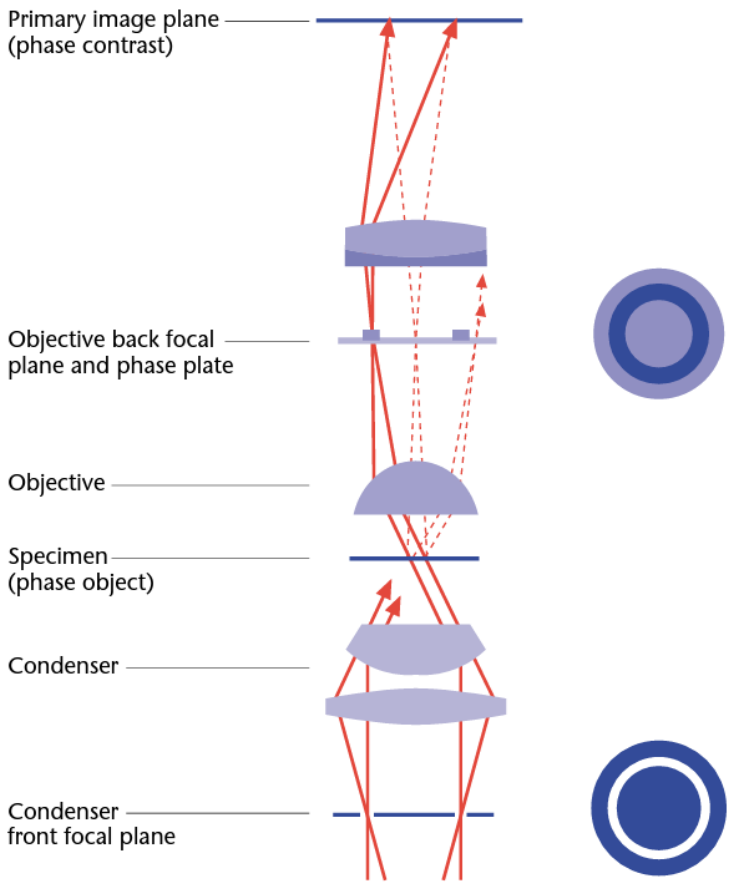

Figure 1.7: Schematic diagram showing a typical phase contrast microscope. An annular phase plate is placed near the back focal plane of the objective to introduce a phase shift of $\lambda/4$ to rays passing through it. A matching annulus is introduced in the illumination path at the front focal plane of the condenser. Image reproduced from [99] with permission from John Wiley and Sons (license number 5673791449329).

The camera used for the detection of widefield epi-fluorescence signal uses a technique called sensor-shifting, which allows the acquisition of 9 images for each pixel (each shifted by 1/3 of a pixel width from the other, forming a square grid). This increases the sampling density, and effectively increases the resolution from the original 29 megapixels to 259.5 megapixels [103]. The ability of the sensor-shifting CCD camera to acquire the full field of view of the Mesolens removes the need for stitching and tiling, an image processing technique which allows to computationally combine individual, high-resolution tile scans of small regions of the sample into a single, larger image in a mosaic fashion [104]. This method usually requires overlap between tiles in order to accurately reconstruct the whole image [105], which significantly increases data acquisition time. Furthermore, stitching artefacts appearing as dark lines at the edges of each tile in the reconstructed image are difficult to remove computationally [104].

The geometry and position of the custom-made lenses and mirrors, shown schematically in Figure 1.8, are designed such as to minimise astigmatism, spherical aberrations and chromatic aberrations across the visible spectrum. Distortions are minimised at the field periphery, and the field flatness is kept below 3 μm in the visible range across the full field of view. The Mesolens can work in both widefield epi-fluorescence and confocal laser scanning modes, and can be adapted to image in water, glycerol, and oil thanks to multiple correction collars which adjust the vertical position of lens groups in the objective barrel. Images can be formed in air, although they are of poorer spatial resolution.

The Mesolens was designed to image whole biological specimens at the early development stage, such as *Drosophila* larvae [106], mouse embryos [102] and zebrafish [103], and it has since been used to image ultrathick tissues including whole mounts of mouse brain [107], pancreas, intestine [108] and lung [109].

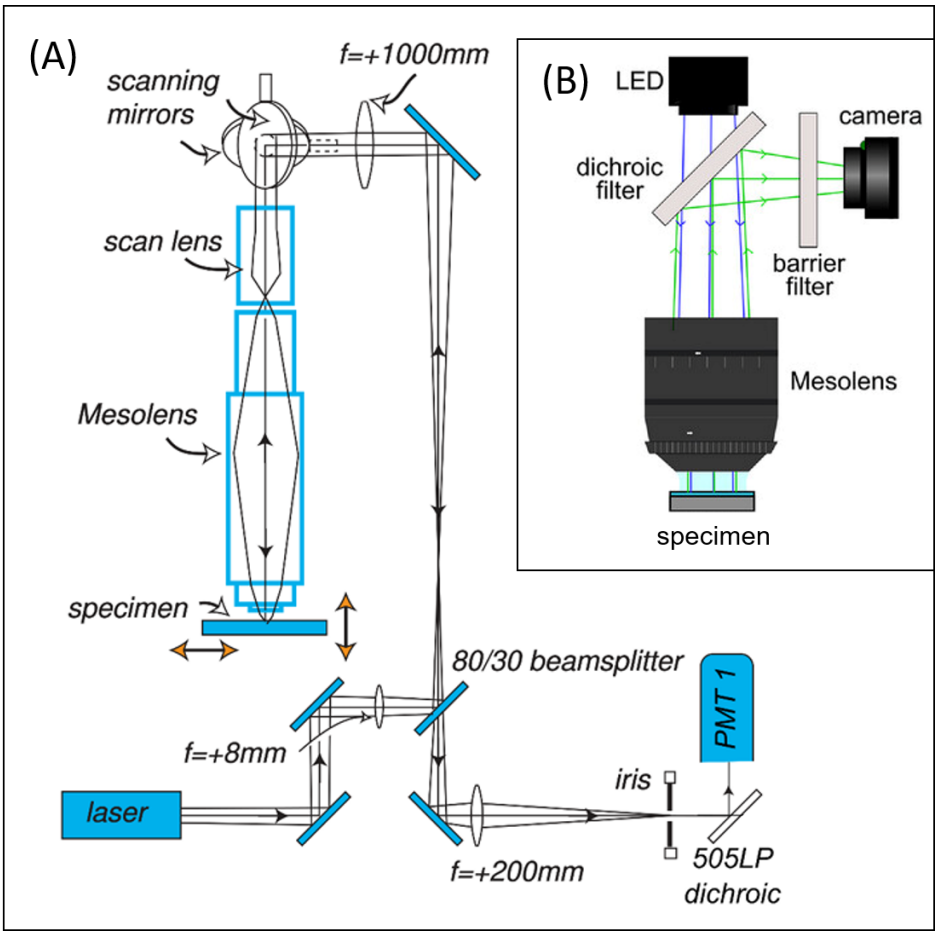

Figure 1.8: Schematic diagram showing the arrangement of optical elements around the Mesolens for confocal laser scanning fluorescence mesoscopy (A) and widefield epi-fluorescence mesoscopy (B). Image adapted from [110] and [111].

1.5 Bacterial biofilms

Biofilms are biological structures formed by microbes to survive in different environments. Bacterial biofilms are aggregates of bacteria, their extracellular matrix and various biological molecules, arranged in a compact but dynamic community which can adapt to external conditions [112]. Biofilms offer protection to mechanical stresses and unfavourable chemical conditions such as nutrient or oxygen deficiency, toxic substances and antibiotics [113]. These properties constitute a

danger for public health because the adaptive capabilities of biofilms can compromise medical equipment and industrial tools, for example by contamination of syringes, catheters [114] and water treatment pipes [115]. In the medical field, biofilm formation on implanted devices can lead to chronic infections which are particularly difficult and costly to cure, and it can promote the emergence of antimicrobial resistance [116]. For these reasons, a deeper understanding of the factors that affect biofilm formation and growth is needed.

While many naturally-occurring biofilms are polymicrobial, research models often focus on monocultures. The traditional model organisms for morphological studies of biofilms are *Pseudomonas aeruginosa* [117], *Bacillus subtilis* [118], and *Vibrio cholerae* [119]. Additionally, the Gram-negative, rod-shaped bacterium *Escherichia coli* is a widely studied and well-characterised organism with many uses in microbiology research thanks to its ability to grow rapidly and strive in a variety of inexpensive media, ease of genetic engineering and availability of a wide range of non-pathogenic strains [120]. In particular, K-12 strains of *E. coli* are the preferred lineage for molecular biology experiments [121]. Because 65% to 80% of infections are estimated to be biofilm-related [122], [123], a quantitative study of biofilm morphologies on a variety of environmental substrates would be beneficial.

1.5.1 Biofilm composition

Biofilms are composed of microbial cells embedded in a self-secreted extracellular matrix (ECM), as shown in Figure 1.9. The latter can be thought of as the scaffolding holding bacteria together, and is responsible for the maturation of the biofilm. It is mainly composed of water (contributing towards up to 97% of the mass of the biofilm [124]), proteins, lipids, nucleic acids, extracellular polymeric

substances such as exopolysaccharides (EPSs) and extracellular DNA (eDNA) [125]. The role of each ECM component in biofilm growth varies depending on the stage of biofilm formation, and its production rate is regulated by both external and internal conditions, which trigger a feedback loop mechanism [126].

EPSs mainly offer structural support to the biofilm, thanks to their ability to retain water, but also participate in signalling mechanisms and internal communication. For example, they contribute to quorum sensing, a collective processing of external signals and information sharing carried out by freely diffusing molecules [127]. They also protect the bacterial community from external stresses, such as antibiotics [128]. Some EPS components, such as colanic acid, are responsible for the resistance of pathogenic *E. coli* strains in the gastro-intestinal acid environment [129].

The main proteinaceous components of biofilms are protein amyloids, which are responsible for cell-to-cell adhesion (self-assembly). The adhesion to external

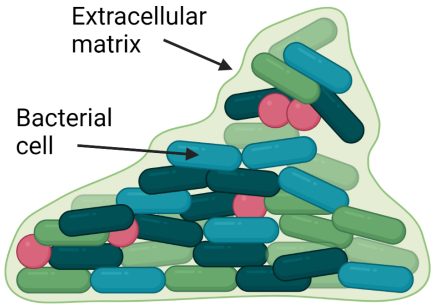

Figure 1.9: Schematic diagram showing the structure and composition of a polymicrobial biofilm. In mature biofilms, bacterial cells are arranged in a closely-packed structure held together by an extracellular matrix, which offers protection from external threats. Image created in BioRender (license number SR25JKZ3PC).

surfaces, on the other hand, is mediated by surface proteins called adhesins. A study by Berk et al. on *V. Cholerae* biofilm formation investigated the role of various matrix proteins using confocal laser scanning microscopy, and found that each contributes to a different assembly process, as well as to the clustering of cells within the biofilm [130].

Extracellular DNA can be released through lysis of dead microbial cells, or during active growth of viable cells [131]. It acts as a nutrient source for bacterial cells within the biofilm, and it strengthens the structure of the biofilm. A study by Okchevsky et al. showed that eDNA removal by DNAse resulted in the dispersal of immature biofilms, and enhanced antibiotic efficacy [132]. eDNA can also act as a shield from antibiotics thanks to its negative charge, which binds to some positively-charged antimicrobial compounds [133]. This property was confirmed by a number of independent studies on both Gram-positive and Gram-negative bacteria. Finally, a study by Gloag et al. [134] found that biofilm growth via independent movement, which takes place as an expanding flow of cells, is facilitated by eDNA. This occurs via guaranteeing the correct alignment of cells that form the expanding edge of the biofilm. In fact, removal of eDNA led to a decrease in distance travelled by individual cells during expansion.

1.5.2 Biofilm growth and maturation

Biofilm formation and growth depends on the ability of the bacteria to clump together and interact with surfaces, overcoming repulsive forces (both electrostatic and hydrodynamic) [112]. Bacteria reproduce by binary fission, which results in two identical daughter cells. This means that during the active growth phase, bacterial growth is exponential over time. Typical growth curves for bacterial

populations (Figure 1.10) involve four phases [135]. The initial phase (lag) corresponds to the initial adaptation of the bacterial colony to the environment, and is characterised by a null growth rate. Following this, an exponential growth phase occurs, where the cells are healthiest (and hence most suitable for studies of their structure and composition). The growth rate depends on nutrient availability, environmental conditions (such as pH) and disposal of toxic by-products. Bacterial growth does not continue indefinitely - it reaches a stationary phase in which the accumulation of waste products and the limitation of nutrients stop cell duplication, although biosynthesis of products still occurs during this phase. The final phase of the bacterial life cycle is the death phase, which also follows an exponential trend but is considerably slower than the exponential growth phase.

Each growth phase is characterised by conformational changes and interactions

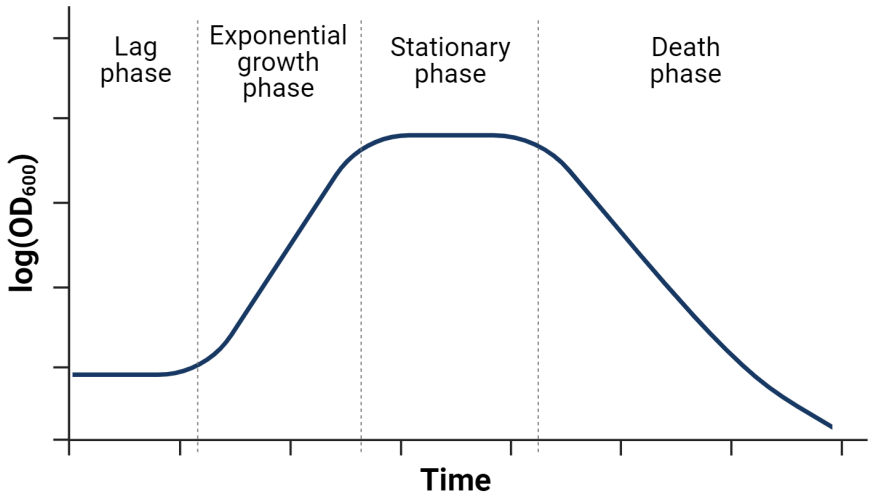

Figure 1.10: Diagram showing the different phases of growth of planktonic bacterial cultures as optical density (OD) against time - note the semi-logarithmic nature of the plot. Figure created in BioRender (license number SR25JKZ3PC).

with the growth substrate. Surface structures such as flagella, fimbriae, and surface proteins all play a role during the various stages of biofilm attachment and growth [136]. For example, the presence and correct functioning of flagella (which are responsible for cell motility) are crucial in the initial stages of *E. coli* biofilm formation [136], and they are linked to increased biofilm formation [137]. The first phase corresponds to a reversible primary adhesion onto a surface, which leads to the formation of a bacterial monolayer [138]. This phase is influenced both by surface properties (roughness, hydrophobicity) and aqueous ambient conditions (pH, ionic strength), and is mainly governed by electrostatic and chemical interactions with the surface [139] which are regulated by sensor membrane proteins [140]. The adhesive organelles fimbriae are required for the initial attachment of bacterial cells to a variety of surfaces and growth media [136]. For this reason, fimbriae are considered an important virulence factor in *E. coli* infections [141].

During biofilm maturation, bacterial cells aggregate and the intracellular space fills with an extracellular matrix. A study by Yan et al. [142] on *V. cholerae* highlighted that this growth initially involves a steady increase in biofilm volume, as cells aggregate and spread onto the surface in a branched pattern. Bacterial cells successively re-orient themselves in the vertical direction due to continuous compression of the surface, and proliferate forming a dome structure which is successively covered by a layer of EPSs. At this stage, the adhesion of bacterial cells onto the surface is irreversible, but the surface of the biofilm undergoes continuous morphological changes in order to adapt to different environmental situations. For example, the bacterial population can rearrange itself to form distinct microcolonies, growing outwards from the biofilm centre [143] - this process is induced by the surface protein Antigen 43 (Ag43) in *E. coli* [144]. Constituent cells exhibit different growth rates and physiology depending on their location

inside the biofilm, as the resources required for biofilm growth are recruited from the surrounding environment over time. This results in the formation of distinct physiological niches, which follow chemical gradients of nutrients and oxygen [145]. In *E. coli* biofilms, cells generally grow faster if they are close to the nutrient-rich agar substrate, and start to die from starvation as they move away from the substrate and the nutrients become limited [146].

Dispersal is the last stage of the life of the biofilm, and it is characterised by bacterial cells leaving the extracellular matrix, which is broken down by enzymes such as dispersins [147], and detaching from the surface. Much is still unknown on the factors triggering this phase, but it is clear that environmental conditions play a role in this process. For example, dramatic changes in carbon or oxygen availability can induce the dispersal of *P. aeruginosa* biofilms [148]. Studies on *Staphylococcus aureus* suggest that ECM production could be responsible for the signalling and regulation of biofilm dispersal [149].

In laboratory experiments, bacterial growth of planktonic cultures is often measured by turbidimetric methods, using a spectrophotometer which measures the amount of light transmitted through the sample at a specific wavelength compared to the amount of incident light. This quantity is named optical density (OD) [150], which is an indirect measure of cell density inside the sample. For most bacterial cells the OD is measured at an incident wavelength 600 nm [151], which does not cause mutations or cellular damage. Biofilm presence, on the other hand, can be quantified using many techniques. For example, bacterial DNA, proteins and EPS present in biofilms can be stained with the crystal violet dye [152] in microtiter plate biofilm formation assays [153]. Biofilms resuspended in liquid cultures can also be quantified using the Coulter method [154], which

indirectly estimates the number of bacterial particles diluted in a sample by calculating the change in impedance that they cause when flowing through a small aperture in a tube [155].

1.5.3 Biofilm morphology

The formation of spatial patterns is ubiquitous in biological systems [156], where simple biological entities, such as cells, come together and form complex structures in a process called "morphogenesis" [157]. In 1952, Alan Turing hypothesised that morphogenesis could be explained by "a system of chemical substances, called morphogens, reacting together and diffusing through a tissue" [158]. So-called Turing patterns would hence arise from a homogeneous population due to the amplification of small, random perturbations to the system. This phenomenon of spontaneous symmetry breaking is also known as reaction-diffusion (RD) model [159].

Bacterial populations are not an exception to this phenomenon: Turing patterns have been observed *in vitro* for *E. coli* biofilms grown inside microfluidic chambers [160], [161], and engineered in isogenic *E. coli* populations tagged with different fluorescent markers [162]. In fact, bacterial biofilms can exhibit a variety of internal patterns, from surface and 3D features to complex fractal shapes [163] (Figure 1.11). As explained in more detail below, these patterns arise from mechanical forces between the expanding biofilm and the substrate (such as friction and cell-surface interactions), which are affected by both the physio-chemical composition of the growth substrate and the properties of component cells [164].

1.5.3.1 Colony growth and expansion patterns

Biofilm growth and expansion on semi-solid surfaces (such as agar) are a result of mechanical forces between the growing cells and the substrate [165], [166]. As such, biofilm shape and three-dimensional (3D) architecture are profoundly affected by the composition of their growth substrate [167]. Colony size is mostly affected by substrate stiffness and nutrient availability, which both affect bacterial growth dynamics [168]. In *E. coli*, soft substrates with a high water content lead to two-dimensional, fast spreading of biofilms across the growth surface, whereas stiff substrates with a lower water concentration are characterised by a slower and smaller expansion, which promotes the formation of wrinkles, crenulations, delamination, and buckling in the axial dimension [169]. The increase in biofilm area with decreasing agar stiffness has also been reported for *V. cholerae* [170], [171], where it is attributed to interfacial energy, which leads to nonuniform expansion across the surface. Similarly, biofilms formed by *B. subtilis* on soft substrates are thicker and expand to larger areas with wrinkled edges [172].

Substrate composition can also affect colony edge morphology. A loss of spatial symmetry in *B. subtilis* colony shape has been observed when growing on nutrient-depleted substrates, leading to irregular edges (Figure 1.11a) [173]. The directional growth of bacterial cells along nutrient concentration gradients can also lead to the formation of highly symmetric spot patterns (Figure 1.11d) [174]. The development of bulges protruding from the edge of the colony can also occur when advantageous mutations arise within the population, as mutants with a fitness advantage over their wild-type counterpart expand more rapidly [175]. Finally, regularly interspaced structures at the edge of *E. coli* colonies can form as a result of filamentous, slow growth of adhesive, signalling cells (Figure 1.11c) [176].

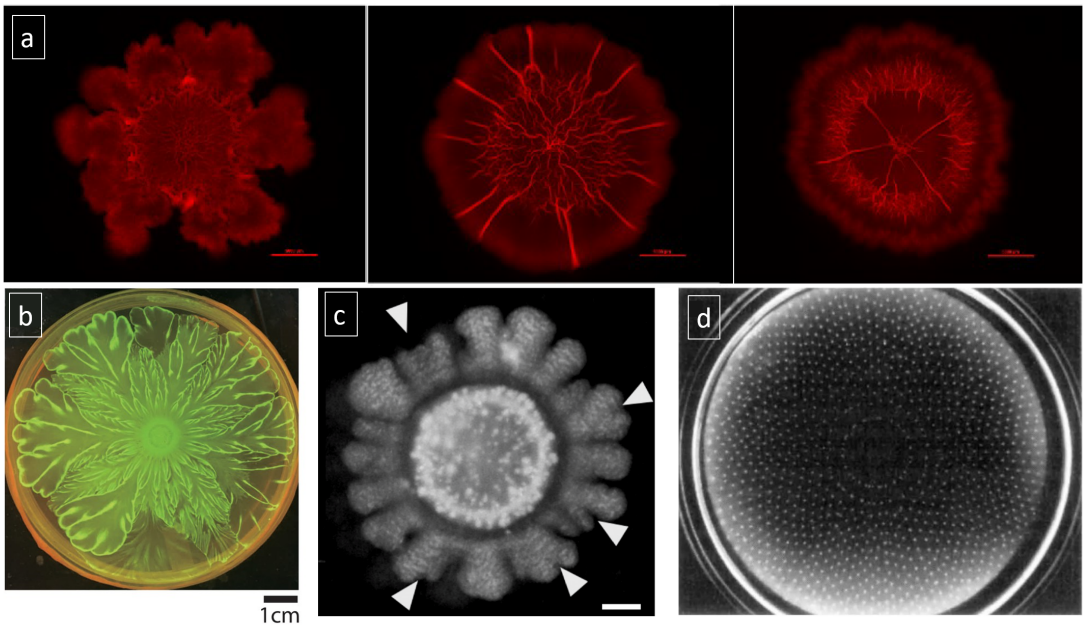

Figure 1.11: (a) Morphological changes on the surface of *B. subtilis* biofilms grown on substrates with different nutrient availability (from left to right, 75%, 50% and 25% nutrient levels). Scale bars: 5 mm. Adapted from [173]. (b) Flower-like patterns in *E. coli* and *Acinetobacter baylyi* multi-species biofilms. Adapted from [177]. (c) Regularly-interspaced edge structures in filamentous, adhesive, signalling *E. coli* biofilms. Branching patterns are shown by arrows. Scale bar 2 mm. Adapted from [176]. (d) Geometric spots formed by *E. coli* biofilms during growth on nutrient-limited substrates. Adapted from [174] and reproduced with permission from Springer Nature (license number 5673800135015).

1.5.3.2 Internal patterns

The 3D organisation adopted by bacterial cells inside a colony biofilm is determined by many factors, including cell shape, motility, distribution of matrix components and interfacial forces [178]. The production and distribution of biofilm structural components, and specifically of the extracellular matrix, determine biofilm structure by affecting intercellular interactions [179] and are crucial for

pattern formation [180]. For example, EPSs such as colanic acid (a structural component of the biofilm matrix) are responsible for the 3D organisation of constituent cells inside the biofilm, resulting in complex three-dimensional patterns [144].

Among the many morphologies that can be observed in mature biofilms, some of the most common are wrinkles, rings and labyrinth patterns. These can arise during biofilm maturation because of the heterogeneous distribution of matrix components [181]. The deletion of genes responsible for the production of these matrix components leads to dramatic changes in biofilm morphology: for example, amyloid curli and cellulose contribute to the formation of concentric rings and wrinkles respectively [182]. Wrinkles are usually formed as a result of buckling instability, which arises when the bacterial cells experience friction with the substrate during their expansion [183]. Buckling instability arises in biofilms where cells are nematically ordered (aligned with their axes parallel to each other) [184] - this type of self-orientation is typical of rod-shaped cells like *E. coli* [164]. Wrinkles can also arise as a result of localised cell death, which increases lateral compressive forces on the surface of the biofilm [185]–[187]. Wrinkle patterns are affected by cell motility, as they are greatly reduced in *E. coli* mutants with reduced or absent flagellar function [146]. It is also possible to observe more than one of these structures within the same biofilm, where they are segregated in different radial regions [170], [188]. In this case, each structure arises during a different stage of biofilm expansion, and the overall morphology is affected by environmental changes.

3D biofilm architecture can also be affected by the shape of individual cells. In the case of a heterogeneous *E. coli* population, exhibiting both rod-shaped and coccal cell phenotypes, the cells adopt a layered structure with coccal cells

on top of rod-shaped cells. When only one phenotype is present, this layering does not occur, and instead coccal cells segregate in vertical bundles and rod-shaped cells mix in a fractal 3D pattern [189]. Cell shape is also important for biofilm axial growth: while longer cells exhibit greater surface expansion, shorter cells experience verticalisation and lead to a thicker biofilm [190]. More recently, a multicellular life cycle has been proposed for *E. coli* [191], where nematically ordered cells assemble in groups of four (forming a "rosette"), and extend along the long axis direction forming chains. Biofilms are formed when these rosette chains attach to one another, and the stability of the final structure is regulated by adhesion and motility proteins. The dependence of chaining on adhesive properties is also observed in *E. coli* microcolonies with diameter of approximately 100 μm [192].

Complex internal patterns can be observed in genetically heterogeneous biofilms, such as multi-species biofilms or biofilms formed by isogenic strains labelled with different fluorescent tags. For example, intricate flower-like patterns (Figure 1.11b) can form inside dual-species biofilms due to the difference in motility between the two strains [177], and similar patterns can form in yeast biofilms during nutrient-limited growth [193]. When isogenic bacterial strains expand on the same substrate, they can have varying degrees of spatial mixing: cooperation tends to increase intermixing, whereas competition leads to segregated domains within the colony [194]. The shape of the boundary between the strains is affected by a number of factors: for example, populations with similar growth properties expand simultaneously, forming radially-segregated sectors, whereas different growth properties lead to successive expansion of one population after the other, creating ring-shaped boundaries [195]. The boundary shape is also affected by the motility of each strain as it expands on the substrate. For example,

the chiral rotation of *E. coli* flagella leads to a clockwise movement of individual cells on the substrate, which in turn results in a chiral-shaped boundary [196]. Differential expression of surface features such as pili and Ag43 leads to a variation in the level of chirality of the boundary, with their removal coinciding with higher boundary chirality [197]. A change in chirality is also associated with increased strain fitness, which results from a greater degree of strain intermixing [198].

Another source of pattern formation is given by spontaneous genetic mutations, which are rare, heritable changes to the genome occurring without selective pressure [199]. The effect of mutations on biofilm morphology can be visualised if they confer a fitness advantage over the wild-type population, as this leads to the formation of morphologically distinct sectors within the colony which can be observed by traditional microscopy techniques [200], [201]. They can be identified by an unusually large width [195] or a significantly reduced fluorescent signal [202].

1.5.3.3 Biofilm nutrient transport channels

The existence of void spaces and channels inside biofilms has been previously demonstrated in biofilms grown in anaerobic fixed film [203] and continuous flow [204] reactors, where they facilitate small-particle transport. Channels can also be found in *P. aeruginosa* biofilms grown in microfluidic devices, where they arise due to compressive stress during biofilm growth [183]. Void channels between individual *E. coli* colonies have also been observed in groundwater reactors: these channels reach deep within the biofilm structure to increase the surface-to-volume ratio of bacterial cells, and persist inside the biofilm even weeks after full growth

conditions are reached [205]. There is evidence from fluorescent particle tracking that these channels participate in nutrient distribution and waste removal between the outer regions of the biofilm and its centre [178]. Laboratory-grown *E. coli* biofilms also exhibit μm-scale channels penetrating the matrix, which support the motion of fluorescent beads [206]. The nutrient-transporting function of these channels has also been observed beneath the wrinkles of *B. subtilis* biofilms, within a network of liquid-filled channels [207]. Filamentous channels are also present throughout *B. subtilis* biofilms, at the interface with the agar growth substrate. In low nutrient conditions, channels become more elongated and directional, and they have an increased ability to transport microspheres to their interior [208].

A recent study by Rooney et al. [209] reported a previously-unseen network of channels inside mature colonies of *E. coli* biofilms, extending throughout their volume (Figure 1.12a). Channels appear dark and form complex patterns. These channels are fundamentally different from those described above, as they are not empty nor filled with liquid. Despite their geometrical arrangement being very similar to the fractal patterns described in the previous section, these intra-colony channels do not constitute a boundary between two isogenic domains, but instead form inside biofilms originating from a single population. Specific fluorescent labelling was used to systematically test for the biochemical component of the channels, which was identified as extracellular protein matrix (Figure 1.12b). The functional role of intra-colony channels was hypothesised to be a nutrient uptake mechanism. This was suggested by their ability to transport fluorescent microspheres to the inside of the biofilm (Figure 1.12c), and by the higher concentration of nutrients observed inside the channels compared to the rest of the biofilm. Furthermore, the channel structures reformed spontaneously after forced

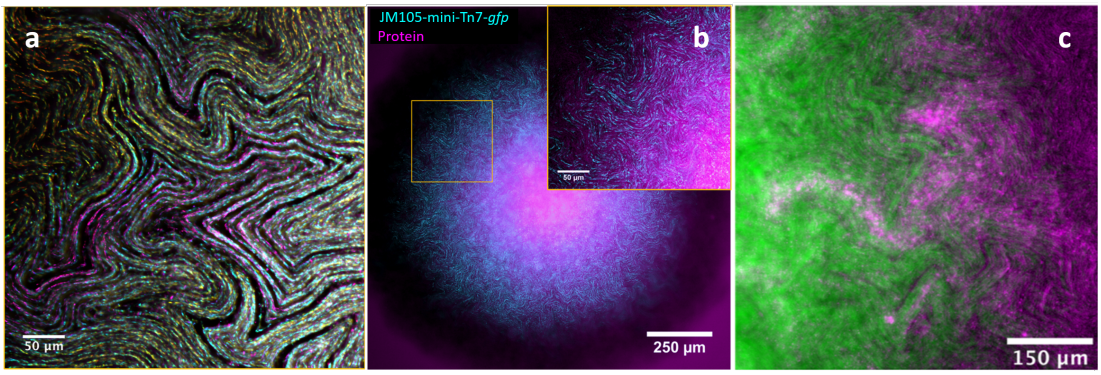

Figure 1.12: Nutrient-transporting channels in mature *E. coli* biofilms. (a) Maximum-intensity projection of a z-stack acquired over 36 μm, colour-coded by depth, showing the 3D organisation of channels. (b) Extracellular protein stain SYPRO Ruby, shown in magenta, is localised inside the channels. (c) Fluorescent microspheres, shown in magenta, can penetrate inside channels. Figures adapted from [209].

biofilm dispersal by mixing. Channel formation is an emergent property of these *E. coli* biofilms; however, the effect of growth medium composition and cell shape on their architecture is unknown.

1.6 Imaging and morphological analysis of bacterial biofilms

1.6.1 Fluorescence microscopy

Interest in biofilms was sparked in the 1970s with the observation of bacterial cells surrounded by polysaccharides in aqueous ambient conditions [210]. Since then, optical microscopy has been used in conjunction with staining techniques to image biofilms *in vitro* [211], and with fluorescent probes for direct counting of bacteria after biofilm disruption [212], to measure biofilm thickness [213] and

to image biofilms in industrial settings [214], [215]. The first 3D high-resolution optical images of biofilms were obtained by Lawrence et al. with confocal laser scanning microscopy [216]. The study involved axial and lateral optical sectioning of *Pseudomonas* and *Vibrio* biofilms, as well as a 3D reconstruction of the biofilm structure. Since then, advances in light source and optical design, image analysis tools, and specialised fluorescent staining techniques have improved the quality of data and allowed a more precise quantification of biofilm growth and morphological parameters [217], [218].

Fluorescence microscopy has been used extensively in microbiology, thanks to its ability to resolve biological phenomena from the subcellular scale up to entire bacterial communities [219], [220] and to its diagnostic capabilities [221], [222]. The fluorescent signal can be provided by immunofluorescence (using fluorescent antibodies to stain proteins in fixed bacterial samples [223]), by fluorescent protein tagging or with fluorescent dyes specific to the desired targets. Fluorescent proteins can be introduced into bacterial genetic material by exploiting horizontal gene transfer, a mechanism by which small, self-replicating genetic elements called plasmids are acquired from the environment (transformation), from other bacteria (conjugation) or from viruses (transduction) [224]. Fluorescence expression from plasmids must be maintained in the host by selective pressure, for example through antibiotic selection [225]. Fluorescent plasmids can contain genes encoding virulence factors [226] and resistance from antimicrobial compounds [227], both of which can be used as a competitive advantage [228]. The expression of these genes can be tracked inside mixed biofilm populations, allowing the visualisation of competitive behaviours in mixed populations over time [229].

Fluorescent proteins can also be inserted directly into the host chromosome, for example through transposition, by which a specific segment of the donor's DNA

is cut and inserted into a specific sequence of the host's DNA [230]. While there are many transposon delivery systems which could be exploited for genetic transfer of fluorescent proteins, the Tn7 transposon mentioned in this work presents significant advantages for microscopy applications. For example, Tn7 transposon insertions occur as a single copy at a specific site of the chromosome [231], without disrupting downstream genes [232]. The mini-Tn7 transposon delivery plasmids are stable in time, they do not affect bacterial growth [233], [234] and do not require antibiotic selection [235].

The improved signal-to-noise ratio of confocal fluorescence microscopy over widefield microscopy enables precise protein localisation as well as protein dynamics studies [236]–[240]. This facilitates the *in vivo* visualisation of fundamental biological processes such as bacterial cell septum formation and division. Among the most significant milestones in this area, we mention the visualisation of the proteins FtsZ [241]–[243] and MinD [244], involved in cell division, and the protein RecA, involved in DNA replication and repair [245]. Fluorescent probes can also be used to visualise RNA [246] and DNA [247] inside bacterial cells, hence providing important insights into gene expression.

At the macroscale, fluorescence microscopy can be used to assess the presence of bacteria on human tissue samples [248], medical devices [26], and industrial equipment [249]. In pathology, it is possible to identify bacterial species participating in human infections [250], [251], visualise infection dynamics [252], [253] and study host-pathogen interactions [254].

The concurrent use of different fluorescent stains enables the quantification of the abundance of biochemical compounds (proteins, carbohydrates, nucleic acids) in biofilm samples [255], and allows for the observation of biofilm matrix structure

and components [256]. Viability stains can also be used to localise and compare the amounts of viable and non-viable bacteria inside biofilms [257], usually by differentiating between cells with intact and damaged membranes. By using fluorescent probes which are specific to predetermined genetic sequences [258], specific bacterial species can also be identified and localised inside fixed biological samples using a technique called fluorescence *in situ* hybridisation (FISH) [259].

The physiological state of bacterial cells in a biofilm can be investigated thanks to enzyme-specific dyes, which can give an indication on the metabolic response to nutrient fluctuations in the growth medium [260], [261]. Fluorescent tagging of antibiotics can be used to assess the penetration of antimicrobial agents in mature biofilms over time [262], and pH-sensitive dyes enclosed in nanosensors allow to quantify pH variations resulting from changes in the chemical environment of the biofilm [263], [264].

Phenotypic changes in biofilm structure are an important marker of environmental changes such as nutrient starvation, temperature or pH changes, antibiotic treatment and competition with other bacterial species. The fluorescent signal from plasmids allows imaging of colony morphogenesis from a single cell to a microcolony [191], [265], [266], as well as the study of three-dimensional development of colonies [267]–[269].

1.6.2 Mesoscopic imaging of bacterial populations with the Mesolens

Thanks to its unique properties, the Mesolens has recently seen applications in the microbiological field, where it has allowed the visualisation of biofilm structures

and processes at a previously unattainable combination of scale and resolution [270]. For example, the presence and 3D organisation of Gram-positive biofilms on fresh excised paediatric tonsils has been quantified using the signal from a fluorescent antibiotic conjugate [110]. Furthermore, the spatio-temporal development of *Candida albicans* and *S. aureus* dual-species biofilms was characterised using time-lapse mesoscopy with the Mesolens [271], revealing the emergence of morphologically distinct sub-populations of each species.

Finally, the Mesolens enabled the discovery and biochemical characterisation of a novel network of nutrient-transporting channels in *E. coli* biofilms [209], which is the focus of this work. Despite the ability to resolve individual channels within the whole biofilm volume, the large size of Mesolens image datasets (up to 20,000 pixels × 20,000 pixels per section, resulting in a total image size of over 600 GB for an acquired volume of 6 mm × 6 mm × 3 mm) and the complex morphology of the channels themselves have so far prevented an accurate quantitative analysis. An appropriate image analysis pipeline is therefore needed to identify morphological changes undergone by channels at different locations or under different growth conditions.

1.6.3 Quantification of microbial populations

Image analysis software can provide quantitative information on bacterial cells and biofilms. Various open-source software such as FIJI [272], ICY [273] and CellProfiler [274] are routinely used to identify and isolate specific biological objects from sample images, and to quantify variables such as cell number, size and position. Among the many tools designed for single-cell morphological analysis (see [275] for a comprehensive review), the FIJI plugin MicrobeJ by Ducret et al. [276] accurately performs bacterial cell segmentation through user-defined parameters,

as well as quantitative morphological analysis. For more specific applications, BacStalk [277] is designed to deal with cells including appendages (e.g. flagella and stalks), and SuperSegger [278] can be used to detect cell division events and track cell lineages in time. While most of these software can be used with little or no programming knowledge, they also allow the user to incorporate plugins and algorithms into the main program's library [279]. This makes image analysis more customisable for researchers and adaptable to a wider range of disciplines.

Image analysis of microbiological specimens can also be performed through programming languages alone. For example, Xavier et al. [280] designed a web interface based on MATLAB coding to extract morphological data such as biovolume, contact surface and average colony height from confocal image sets of bacterial communities. The COMSTAT software [281], initially developed for MATLAB, was also designed to calculate basic 3D properties of biofilms from confocal micrographs, and was since updated to work on open-source software [282]. A more recent example of MATLAB-based software is BiofilmQ [283], which exploits image pre-processing and segmentation techniques to calculate biofilm parameters such as thickness, surface area, and roughness.

1.6.4 Image enhancement and restoration techniques

Image enhancement and restoration are useful tools for improving image quality, which in turn can facilitate image analysis and data presentation. Image enhancement improves the visibility of image features, without increasing the amount of information present [284]. Examples of image enhancement methods are contrast stretching and histogram equalisation. In contrast stretching, pixel grey values are transformed to make bright areas brighter and dark areas darker, thus utilising the whole intensity range available [285]. While this method is useful for

improving the overall visibility of the image, it does not perform well in images with large local intensity fluctuations [286]. For this reason, other methods such as adaptive histogram equalisation are used to locally change the grey value of pixels depending on the the brightness of neighbouring pixels in the image [287].

Image restoration, on the other hand, aims to retrieve information from images that are degraded either by noise or blur [288]. Two common image restoration algorithms are filtering and deconvolution. Image filtering can occur in the spatial domain, for example through median filtering, by which every pixel intensity value is changed to the median intensity value across a predetermined number of its neighbours [289]. This type of filter is useful for reducing (or removing) noise that occurs as small spots through the image [290]. Filtering can also occur in the frequency domain, after applying a Fourier transform to the image to visualise its frequency features. In the frequency domain, the details of the image are described by high frequencies, whereas large, smooth structures correspond to low frequencies [284]. Frequency-domain filters can be applied to specific frequency ranges to obtain different image modifications: for example, high-pass filters improve the sharpness of the image, whereas low-pass filters increase the signal-to-noise ratio [291].

Deconvolution, on the other hand, is an iterative mathematical operation that aims to eliminate the blur inherent to the optical system, through knowledge (or estimation or calculation) of the point spread function [292]. Since the observed image is given by the convolution of the ideal image with the object PSF, the ideal image can be reconstructed through the inverse process - deconvolution. During successive algorithm iterations, the ideal image is guessed, and a convolution with the PSF is performed [80]. The result of this convolution is compared with the blurred image, and a likelihood value for the estimation is calculated. The

iterations continue with updated guesses until the likelihood value is maximised [11], [293]. In deconvolution algorithms, the PSF can be either provided as a separate image file or it can be estimated in a process called blind deconvolution [11]. Crucially, transform analysis can introduce artefacts - features that do not belong to the original image, which are usually more evident at the image borders and can take the form of false texturing [288]. This is to be avoided since it leads to misrepresentation of data and incorrect analysis of image parameters.

1.7 Research aims and objectives

The work presented in this thesis focuses on obtaining a deeper understanding of *E. coli* biofilm morphology, more specifically of the network of intra-colony channels, using quantitative imaging methods.

Firstly, since these channels are known to participate in nutrient transport, I aimed to understand whether their size varied depending on the location within the biofilm (i.e. between zones of varying nutrient accessibility). I aimed also to learn whether the channel morphology changed with respect to the nutritional profile of the growth substrate. To answer these questions, an image analysis pipeline was designed to measure channel width at different radial positions around the centre of the biofilm from microscopy images. This was possible thanks to the subcellular resolution of Mesolens datasets being maintained across whole biofilm micrographs, allowing to identify channels as small as 10 μm.

Secondly, as channel formation is an emergent property of *E. coli* biofilm growth, their morphology is likely to be a result of mechanical forces during expansion across the growth substrate. If this is the case, I aimed to understand whether channel architecture changed depending on the shape of constituent cells. This

was investigated using fractal analysis of images of biofilms formed by cell-shape mutants of *E. coli*. The internal biofilm morphology formed by a normal rod-shaped *E. coli* strain was compared to that formed by four mutant strains with either long or wide cell phenotype by calculating box-counting fractal dimension and lacunarity.

Thirdly, I aimed to investigate whether genetic engineering could be used to elucidate the mechanism of channel formation in *E. coli*. While a single-gene knockout mutant library of *E. coli* exists as the Keio collection, its parent strain BW25113 is not suited for high-throughput mesoscopic imaging with the Mesolens because immersion of biofilms formed by this strain with mounting medium, required for refractive index matching, leads to biofilm dispersal to the planktonic state. For this reason, an experimental framework for single-gene knockouts in the *E. coli* strain JM105 mini-Tn7-*gfp* would be desirable. I conclude my thesis by describing my work that aimed to produce such knockouts.

Chapter 2

Quantification of nutrient-transporting channels in *Escherichia coli* biofilms using an open-source image analysis pipeline

In this Chapter the width of nutrient-transporting channels in mature *E. coli* biofilms was quantified for the first time using a custom image analysis pipeline. The aim of this Chapter was to quantify the impact of environmental growth conditions on the morphology of mature biofilms and on the structure and distribution of intra-colony channels. This was carried out by growing *E. coli* biofilms on rich and minimal medium nutrient substrates with changing agar concentration (stiffness), and on minimal medium with various glucose and ammonium chloride concentrations. A custom-made, open-source image analysis pipeline was designed to measure channel width at different locations inside the biofilms, revealing a non-linear relationship between channel width and radial distance from the centre of the biofilms. Biofilms grown on glucose-limited substrates formed wider biofilms than those grown on ammonium-limited substrates, suggesting that channels might be important for the transport of carbon-based nutrients.

Sections of this Chapter have been adopted from Bottura et al. [294].

2.1 Introduction

2.1.1 Biofilms burden on healthcare

Biofilms are biological structures formed by microorganisms in a variety of environments, and they consist of cells embedded in a self-secreted extracellular matrix [112]. This matrix is mainly composed of EPSs, proteins and eDNA, and offers physical support to the biofilm while protecting its constituent cells from external biological and physio-chemical stresses. For example, biofilms are resistant to mechanical clearance [295], [296] by external applied forces. These factors result in the emergence of populations that exhibit increased resistance to a wide range of deleterious agents when compared to planktonic cells [113]. In fact, a decrease in efficiency of antibiotics for the killing of bacteria in the biofilm form has been observed in various bacterial species such as *S. aureus*, *P. aeruginosa* and *E. coli* [297].

This increased antibiotic tolerance can be attributed to a number of reasons: for example, one of the factors that influences antibiotic uptake is the growth rate, which is considerably slower for biofilms than for planktonic cells. This makes growth-based antibiotics less effective on biofilms. Furthermore, numerous studies have found that antibiotic resistance increases during the exponential growth phase, and is higher for slow growth rates [298]. For example, highest resistance to antibiotics was recorded at the stationary phase for *Burkholderia cepacia* [299]. The abundance of extracellular matrix inside the biofilm also acts as a physical barrier to the diffusion of antimicrobial agents. While the outer cells can be reached by the antibiotic, those lying deeper into the biofilm structure can be spared [300]. Specific niches within the biofilm, such as low oxygen regions or sub-populations that differentiate into antibiotic resisters, also play a role in

antibiotic resistance [301].

All these factors have in time contributed to the rise in antimicrobial resistance, which poses a threat for many standard medical procedures making use of antibiotics. The number of patients infected by strains previously killed by common antibiotics has dramatically increased in the last two decades. For example, a 2014 study by the World Health Organisation (WHO) [302] found that *Streptococcus pneumoniae*'s resistance to penicillin occurred in 25% or more health cases in 67 countries all over the world. Furthermore, 2.8 million antibiotic-resistant infections with resulting 35,000 deaths are recorded every year in the United States alone [303].

2.1.2 Effect of environmental conditions on biofilm growth and architecture

It has long been known that bacterial growth rate and biomass formation depend on the type and concentration of nutrients available, and that altering the nature of growth substrates can influence the growth of planktonic bacteria [304]–[306]. Nutrient availability also has profound effects on the morphology of developing biofilms. For example, growth of *B. subtilis* biofilms occurs following the direction of nutrient gradients [307] and is characterised by a fractal, branched morphology on nutrient-limited substrates [308], [309]. Furthermore, *P. aeruginosa* biofilm dispersal can be induced by a sudden increase in substrate carbon concentration [310], but it can also be a result of carbon-based nutrient depletion [311]. Finally, recent studies on single-species biofilms have identified cross-feeding mechanisms for acetate, alanine, and other nutrients influencing biofilm viability and morphology [312]–[314].

The mechanical properties of the substrate are known to affect the initial stages of biofilm formation, as they determine the extent of frictional forces between the expanding bacterial population and the substrate, and between neighbouring bacterial cells [170]. For example, a reduction in substrate stiffness can lead to increased cell attachment onto hydrogels [315] and silicone polymers [316] by the biofilm-forming model species *E. coli*, *S. aureus* and *P. aeruginosa*. Soft substrates are also colonised more rapidly by *E. coli* cells [317], although this is not due to increased cell motility [318].

The structure of biofilms is integral to their role in infection, with mechanical deformation of soft substrates and epithelial cell monolayers being a major contributor to pathogenicity [319]. The effect of environmental and surface properties on biofilm growth parameters leads to biofilms being a major burden to public health and industry [116]. For these reasons, a more precise understanding of biofilm internal morphology is required.

2.1.3 Experimental aims

The aim of this Chapter was to determine the effect of growth substrate composition (specifically, nutrient availability and substrate stiffness) on mature biofilm morphology and intra-colony channel structure. This question was addressed by growing *E. coli* biofilms on agar substrates with different nutritional profiles, in both nutrient-limited and nutrient-abundant conditions, and on substrates with varying concentrations of agar. Biofilms were then imaged with the Mesolens to capture intra-colony channel networks with sub-cellular resolution across the whole biofilm. The width of individual channels was calculated at different radial positions around the centre of the biofilm using an open-source image analysis pipeline I developed for this purpose.

2.2 Materials and Methods

2.2.1 Bacterial strains and media

The non-pathogenic *E. coli* strain JM105 containing mini-Tn7-*gfp* [234], enabling GFP fluorescence, was used throughout the study. Cultures were grown in either Lysogeny Broth (LB) or M9 minimal medium, with composition as described in Appendix A. Solid substrates were prepared by adding agar in concentrations of 20 g/L (LB agar) and 15 g/L (M9 agar) for nutrient concentration experiments. For agar stiffness experiments, LB and M9 media substrates were prepared with agar concentrations of 5 g/L, 10 g/L and 20 g/L.

2.2.2 *E. coli* liquid culture growth characterisation under different nutrient conditions

2.2.2.1 Liquid culture specimen preparation

Mid-exponential growth phase liquid cultures of *E. coli* JM105 mini-Tn7-*gfp* were prepared in LB medium as described in Appendix A, then washed and resuspended in 1× M9 salts. The cultures were diluted to an OD_{600} of 0.04, split in individual tubes and supplemented with appropriate amounts of the nutrient of interest. For carbon variation growth curves, the concentration of nitrogen was kept constant at 18.7 mM, and for nitrogen variation growth curves the concentration of carbon was kept constant at 66.7 mM. The nutrient concentrations were chosen to be between 0 mM and 80 mM - for comparison, the nominal carbon and nitrogen concentrations in M9 salts are 66.6 mM and 18.7 mM, respectively. 200 μL aliquots of liquid culture of each investigated carbon and nitrogen concentration were analysed in triplicate. Absorbance (OD_{600}) measurements were

performed every 15 minutes for 24 hours using a Synergy HT plate reader (BioTek, USA), with the plate being held at 37°C and shaken continuously.

2.2.2.2 Growth curves

Growth curves were produced for each nutrient concentration thanks to the Gen5 microplate software (BioTek, USA), and exported to MATLAB (MathWorks, USA) for analysis. The average of the first absorbance value for each concentration was used as a baseline and subtracted from each growth curve. The y axis was displayed on a logarithmic scale in order to identify the exponential growth phase (the linear portion of the plot). A linear fit to this region was applied using MATLAB's Curve Fitting Toolbox by selecting an exponential function of the form $y = a\ exp(bx)$, with the specific growth rate corresponding to the coefficient b. Errors on the specific growth rate plots were calculated as the standard deviations across biological repeats for the same nutrient concentration. The duration of the exponential growth phase varied depending on the nutrient concentration, and lasted between 6 and 18 hours, hence the data points corresponding to exponential growth were selected manually as ranging from t_{start} to t_{end}, as shown in Table 2.1. The goodness of the exponential fit was checked for each dataset through the resulting adjusted R-squared value, calculated in MATLAB, which is also shown in Table 2.1. Growth curves and specific growth rates were plotted in Python using matplotlib.

2.2.3 Mesolens imaging

All the data in this work was acquired using the Mesolens in either widefield epi-fluorescence mode (for the rapid acquisition of biofilm images for channel

[C] (mM)	$\mathbf{t}_{start}$	$\mathbf{t}_{end}$	**Adjusted $\mathbf{R}^2$**	**[N] (mM)**	$\mathbf{t}_{start}$	$\mathbf{t}_{end}$	**Adjusted $\mathbf{R}^2$**
5	45	350	>0.925	2.5	255	720	>0.967
10	45	600	>0.989	5	255	720	>0.995
20	45	690	>0.996	10	255	720	>0.997
30	45	750	>0.985	15	255	720	>0.992
40	45	855	>0.998	20	255	720	>0.996
60	45	780	>0.994	25	255	720	>0.993
80	45	1125	>0.995	30	255	720	>0.995

Table 2.1: Table showing the initial and final time points (t_{start} and t_{end}) on the growth curves corresponding to the exponential growth phase for each carbon [C] and nitrogen [N] concentration. The adjusted R-squared values obtained by fitting the exponential function $y = a\ exp(bx)$ to each sub-dataset (corresponding to the exponential growth phase region) are also shown. The exponential growth phase in the growth curves obtained by varying the nitrogen concentration always lasts just under 8 hours, whereas when the carbon concentration is varied the exponential growth phase increases with carbon concentration.

structure quantification) or confocal laser scanning mode (to visualise the three-dimensional architecture of biofilms).

Mesoscopic imaging of biofilms was performed with the lens in water immersion, to match the refractive index of the mounting media (LB and M9), except the 0.5% M9 agar datasets which were acquired in air, with no immersion or mounting liquid. This was needed to preserve biofilm structure, because biofilms grown 0.5% M9 agar were less adherent to the substrate and fully detached after addition of liquid mounting medium. The intra-colony channels formed by these biofilms remained evident even though the lower refractive index resulted in poorer spatial resolution (Figure 2.9d). The Mesolens collars were adjusted to minimise spherical aberrations.

For widefield epi-fluorescence Mesolens imaging, fluorescence from GPF was excited by a 490 nm pE-4000 LED (CoolLED, UK), and emitted fluorescence was directed through a 540 $\pm$ 10 nm bandpass filter before being detected by a VNP-29MC sensor-shifting CCD camera (Vieworks, South Korea). In confocal laser scanning mode, fluorescence from GFP was excited using a 488 nm laser (Multiline Laserbank, Cairn) delivering 5mW of optical power from the laser oscillator. Fluorescence emission was filtered through a 525/39 nm bandpass filter (MF525-39, Thorlabs, USA) before being detected using a PMT (PMM02, Thorlabs, USA). The emission path also included a 505 nm longpass dichroic mirror (DMLP505R, Thorlabs, USA) to further reject backscattered laser light and direct the fluorescence to the PMT.

2.2.4 Image analysis

2.2.4.1 Image processing

Confocal z-stacks were displayed as a maximum intensity projection, colour coded by depth in the z-direction using the "Fire" lookup table from FIJI (ImageJ version 1.53c). Where described, median-filtered widefield epi-fluorescence Mesolens images (filter radius: 2 pixels) were deconvolved using the proprietary Huygens Professional version 19.04 software (Scientific Volume Imaging, Netherlands). Deconvolution was performed after an in-built manual background subtraction and a theoretical PSF estimation on Huygens, using the Classic Maximum Likelihood Estimation method with 50 iterations, a signal-to-noise ratio of 40 and a quality threshold of 0.01.

Mesolens images were brightness-adjusted and contrast-adjusted using FIJI for presentation purposes [272].

2.2.4.2 Biofilm base area calculation

To calculate the base area of the biofilm, widefield epi-fluorescence Mesolens images were opened in FIJI, and thresholded using the "Adjust Threshold" tool, using the mean of grey levels as the threshold value. The "Wand (tracing) tool" was then used to select the biofilm mask, and the area was calculated using the "Measure" function. The base area measurements were systematically underestimated due to the thresholding method used by FIJI to create the binary mask. Nonetheless, by using the same thresholding method on all images I ensured that this limitation had comparable effects on all datasets. Biofilm thickness was calculated by plotting z-axis profiles of confocal z-stacks in FIJI and calculating the distance between the two minima on each profile.

2.2.5 Intra-colony channel width calculation

2.2.5.1 Polar transformation

Intra-colony channel width was calculated using the image analysis workflow outlined in Figure 2.1. The pipeline made use of the FIJI plugin "Polar transformer" [320], which performed an image transformation from polar to cartesian geometry, as well as of two custom Python scripts. Initially, the coordinates of the centre of the biofilm were calculated using the "Measure" function in FIJI applied on an oval selection of the whole biofilm. The Polar Transformer plugin was then launched, and the origin of transformation was manually entered as the coordinates of the centre of the biofilm. The number of pixels for each degree in the original image was set to 7200 within the plugin menu (corresponding to 20 pixels for each degree over one full angular rotation).

2.2.5.2 Absence of distortions from the Polar Transformer plugin

To check that the Polar Transfomer plugin did not distort the original biofilm structure, the plugin was used on a sample image of a bicycle wheel. As shown in Figure 2.2, the bicycle spokes which go out radially from the centre (a) are transformed into straight lines (b). Line profiles were obtained from the inverted, polar-transformed image at radial distances of 100, 150 and 200 pixels from the centre of the wheel (c, d, e), and used within the Python code from Appendix B. The pipeline correctly identified 16 "channels" (indicated by orange crosses) at all three radial positions. Average channel widths were calculated as 6.218 $\pm$ 0.091 μm, 6.229 $\pm$ 0.157 μm and 6.304 $\pm$ 0.098 μm for radial distances of 100, 150 and 200 pixels respectively (f). The uncertainties in this example result from

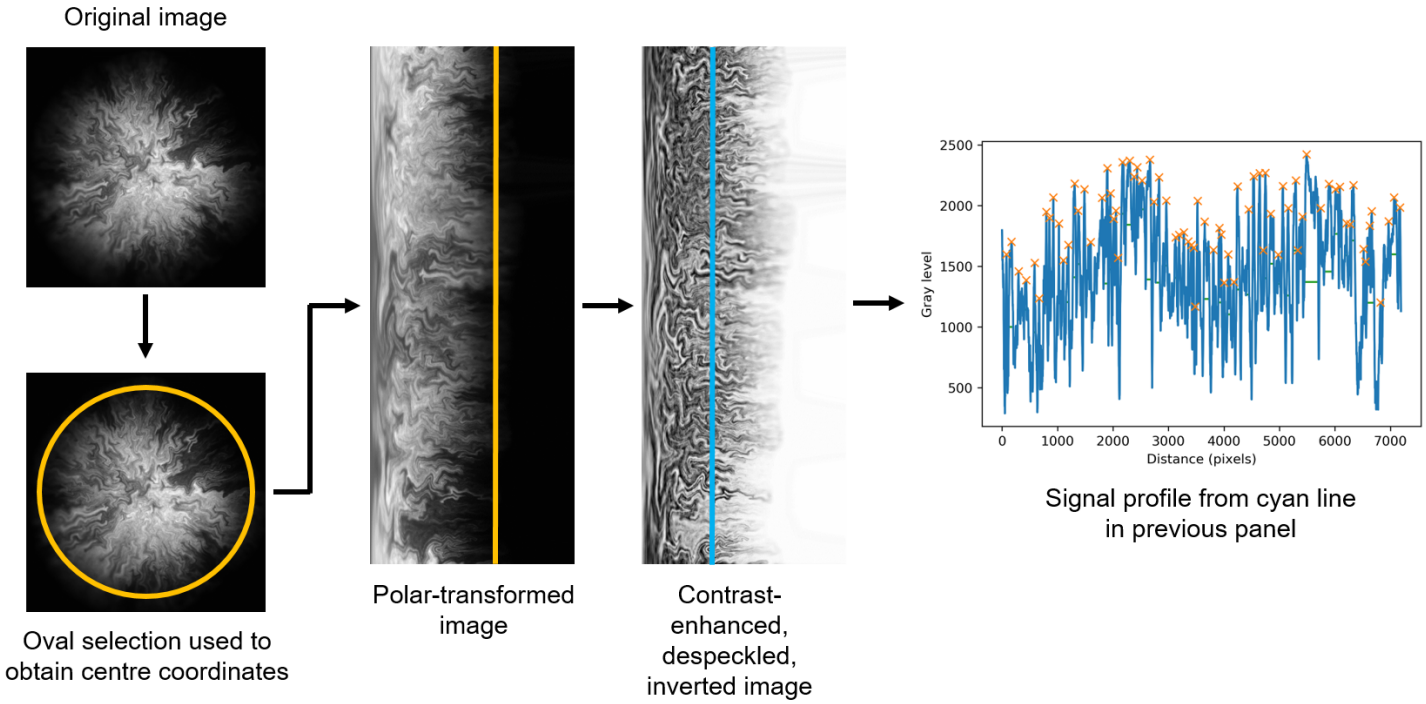

Figure 2.1: Image analysis workflow. A widefield epi-fluorescence Mesolens image was opened in FIJI, where an oval selection was used to obtain the coordinates of the centre of the biofilm. The coordinates were the input into the Polar Transformer FIJI plugin, which performed a transformation from polar to cartesian geometry. The resulting image was locally contrast-enhanced, despeckled and the look-up table was inverted using FIJI. Signal profiles of vertical line selections were exported to Python, where the signal was analysed with a custom script in order to locate the peaks (orange crosses) and calculate the full-width at half-maximum (green horizontal lines) of each peak. The latter quantity corresponded to intra-colony channel width, converted from pixel units to μm using polar geometry.

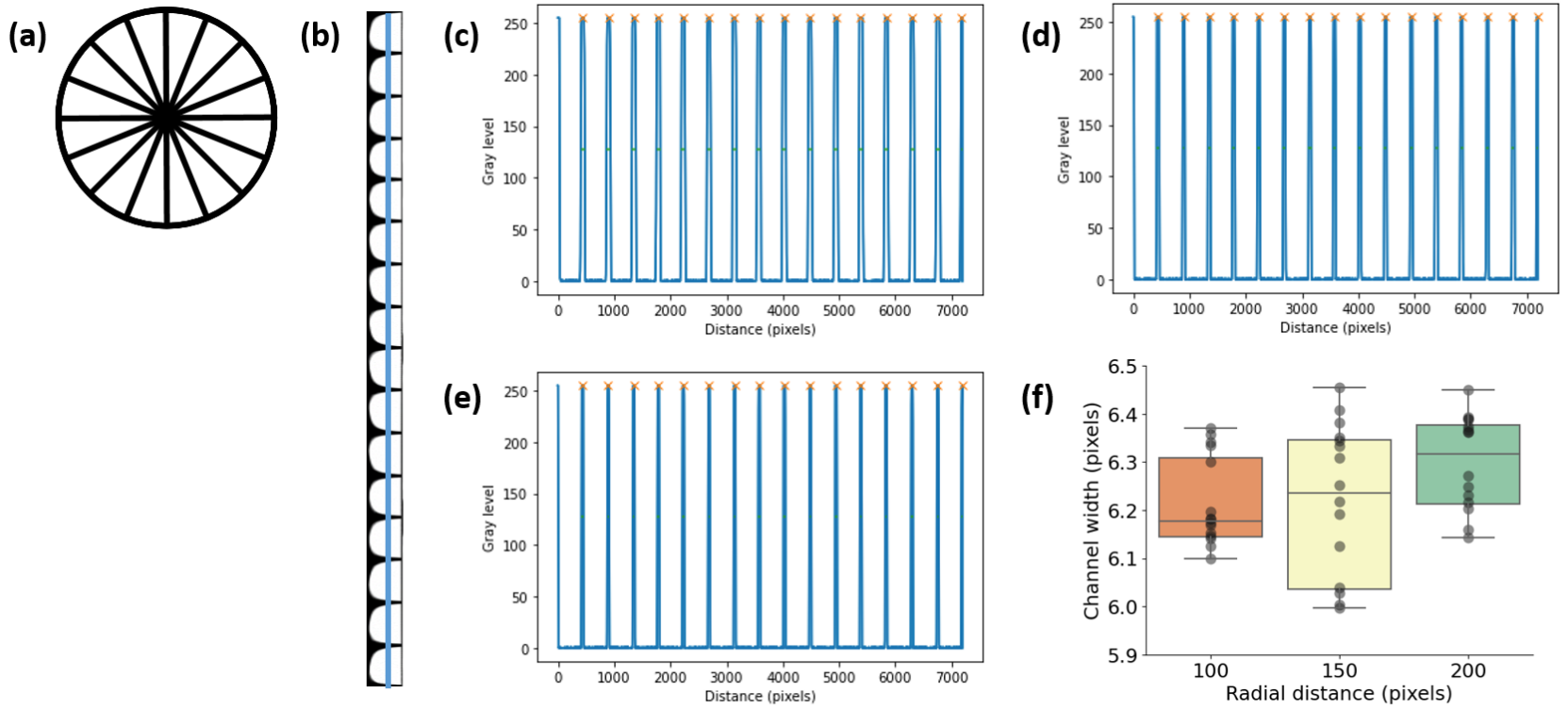

Figure 2.2: Example of Polar Transformer plugin used on the schematic diagram of a bicycle wheel, showing no artefacts are generated. The radially expanding spokes from the original image (a) are transformed into straight vertical lines by polar transformation (b). After inverting the polar-transformed image, line profiles were obtained on FIJI at radial distances of 100 pixels (c), 150 pixels (d) and 200 pixels (e) from the centre of the image. The Python script identified 16 peaks (orange crosses) in each of these images, and the measured channel widths were within a 1.4% variation from each other (f).

the splitting of channels at the edge of each line profile, but the overall variation in calculated channel width is below 1.4%.

2.2.5.3 Image preprocessing

The polar-transformed image was contrast-adjusted using the "CLAHE" (Contrast Limited Adaptive Histogram Equalization, [321]) feature in FIJI with block size 60, maximum slope 3 and 256 histogram bins to facilitate channel identification. The image was then despeckled using the "Despeckle" function in FIJI in order to remove noise. The image was also inverted, making intra-colony channels appear light and cells dark, which facilitated the rest of the analysis.

2.2.5.4 Line profile signal analysis

Vertical line selections were taken at different x positions on the polar-transformed image, corresponding to circumferences around the biofilm taken at different radial distances from its centre. Signal profiles were obtained for each line selection using the "Plot profile" feature in FIJI. The signal was exported as a list of intensity values paired with their position along with the circumference, and was not fitted with a normal distribution. An enlarged image of the signal profile is provided in Figure 2.3 to show this.

2.2.5.5 Python code to calculate channel width

Signal profiles of vertical line selections were exported to Python, where signal peaks were located thanks to a custom script using the `find_peaks()` function (Appendix B). For each For each radial position signal dataset, peak thresholding was performed in order to exclude noise: peak prominence was chosen as 20% of the difference between maximum and minimum signal, and a minimum distance

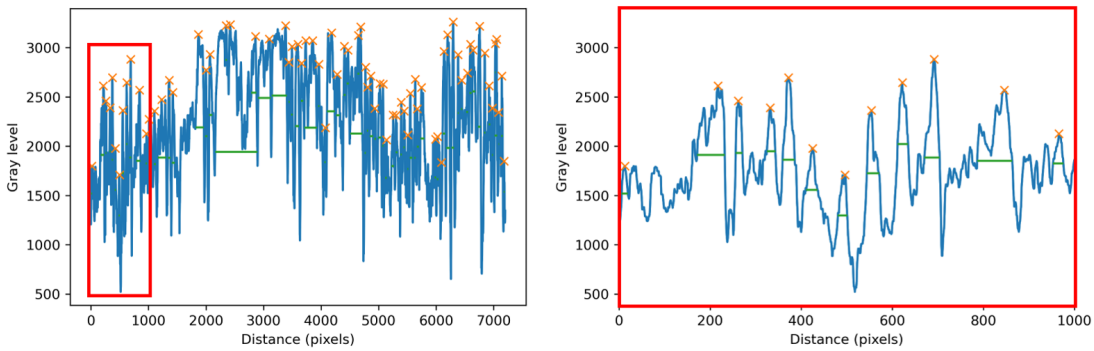

Figure 2.3: Signal line profile showing the identified peaks as orange crosses and full-width at half-maximum as green horizontal lines (left). The section corresponding to the first 1000 pixels along the circumference is enlarged on the right panel, showing the signal is not fitted with a normal distribution.

between adjacent peaks was selected as 9 pixels, which corresponds to the average length of an *E. coli* cell (2 μm) in a Mesolens widefield epifluorescence image. Intra-colony channel widths were then calculated in pixel units as the full-width at half-maximum of each peak, using the `peak_widths()` function. The actual width of the channels in μm was converted according to the radial distance from the centre, using polar coordinate geometry.

2.2.6 Variation of intra-colony channel width along the radial dimension

Intra-colony channel width was measured along whole circumferences at radius intervals of 50 μm, starting from an initial radius of 200 μm. This initial radius value was chosen because at lower values, polar transformed images were distorted and signal analysis was not reliable. Because of the ellipticity of the biofilms, polar-transformed images appeared as rectangles with a non-straight right side

(Figure 2.1), corresponding to the perimeter of the biofilm. Regions beyond which a full circumference could not be obtained for the biofilm were excluded from the analysis.

Channel widths were measured for biofilms grown on the four nutrient conditions and are described in the Results section. Three biological replicates were used for each condition, giving a total sample size of 12 biofilms. An exponential fit was applied to each plot of channel width against radius, and R-squared values for the fit were computed for each dataset. The number of channels identified by the script varied between radial positions, and was highest for the intermediate radii. This is likely due to the fractal nature of intra-colony channels, which have sharp changes in direction and fold on themselves inside the biofilm.

To compare channel widths across different nutrient concentrations of the substrate, intra-colony channel width was calculated at three normalised radial positions (full radius, 50% radius and 20% radius) to investigate the effect of nutrient concentration. Datasets were acquired for each of the following nutrient concentrations: 15 mM carbon (8 biofilms, giving 1062 channels), 200 mM carbon (7 biofilms, giving 1424 channels), 2.5 mM nitrogen (9 biofilms, giving 1524 channels) and 10 mM nitrogen (4 biofilms, giving 507 channels).

2.2.7 Statistical analysis

The comparison of biofilm base areas and channel widths under different nutrient availability and agar concentration was performed by means of a Mann-Whitney U rank test, chosen because datasets were not normally distributed and had unequal sample sizes. The tests were performed using the `scipy.stats.mann whitneyu()` function in Python. P-values smaller than 0.05 were considered statistically significant.

Biofilm base area and intra-colony channel measurements were displayed using Python's `seaborn.boxplot()` and `seaborn.stripplot()` plotting tools, where the first and third quartile of the data (Q1 and Q3) are enclosed by a box which contains 50% of the data (the interquartile range, or IQR). The median is shown as a horizontal line inside each box, whereas the capped bars are the "minimum" and maximum" values, which are found a distance of 1.5*IQR above and below the Q3 and Q1 respectively. Average values for each measurement are shown as white diamonds. Outliers were removed by excluding data points which had a modified z-score greater than 3. The modified z-score was calculated using the median absolute deviation as described in [322] for non-normally distributed data.

2.3 Results

2.3.1 Nutrient availability affects biofilm morphology at the mesoscale

To test how biofilm morphology was affected by nutrient availability, specific carbon and nitrogen limiting conditions were determined for *E. coli* JM105 mini-Tn7-*gfp* (Figure 2.4). Carbon and nitrogen were limited by controlling the nutrient concentrations of the growth media (glucose and ammonium chloride, respectively). The limiting carbon concentration was 15 ± 5 mM (C:N ratio of 1:1.25) and the limiting nitrogen concentration was 2.5 ± 1.5 mM (C:N ratio 27:1). These are broadly comparable with previous *E. coli* growth experiments in minimal medium [323].

The impact of nutrient concentration on biofilm morphology was investigated by measuring the global biofilm property of base area as a proxy for colony size and spreading (Figure 2.5). Biofilms grown on glucose-limited substrates and

those grown on ammonium-limited substrates were similar in size ($p = 0.796$), whereas glucose excess led to larger biofilms than ammonium excess ($p = 8.15 \times 10^{-5}$). As expected, biofilms grown on glucose-rich media were larger than those grown under glucose limitation ($p = 1.97 \times 10^{-5}$). These data show that glucose

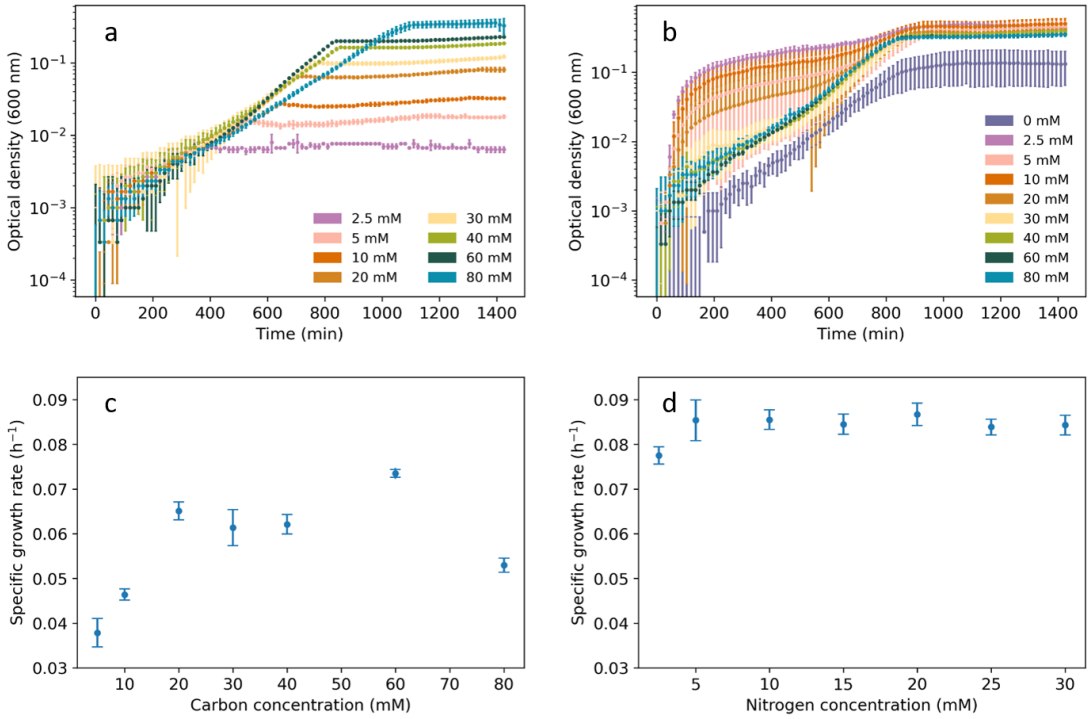

Figure 2.4: Growth curves (top panels) and specific growth rates (bottom panels) of *E. coli* JM105 mini-Tn7-*gfp* liquid cultures grown in M9 minimal medium with various carbon (a, c) and nitrogen (b, d) concentrations, obtained by varying the amounts of glucose or ammonium chloride in the medium. Error bars on growth curve plots represent the standard deviation across three biological repeats. The growth curve for the lowest carbon concentration in a (0 mM) is not shown as it consisted of a baseline of non-growing cells. The data point at 80 mM carbon (c) is likely due to saturation, especially if we consider that the nominal carbon concentration in M9 medium is 67 mM.

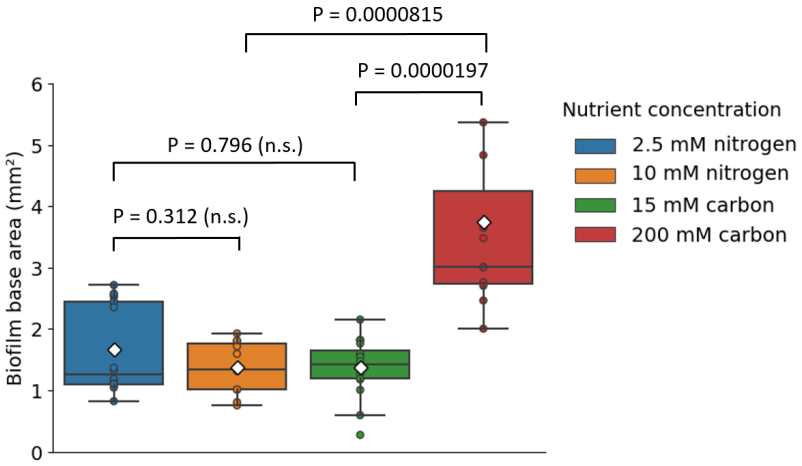

Figure 2.5: Base area of *E. coli* JM105 mini-Tn7-*gfp* biofilms calculated for four nutrient conditions. Average biofilm areas are 1.374 ± 0.118 mm^2 (glucose-limited biofilms, n = 16), 3.738 ± 0.510 mm^2 (glucose-rich biofilms, n = 11), 1.668 ± 0.166 mm^2 (ammonium-limited biofilms, n = 18) and 1.370 ± 0.129 mm^2 (ammonium-rich biofilms, n = 11). Uncertainties correspond to standard errors of the mean across biological repeats (n ≥ 11 for each condition). Mann-Whitney U rank tests were performed on the data, with relevant p-values shown. Average values are shown as white diamonds, whereas boxes represent the interquartile range (with median values shown as horizontal lines inside each box).

availability is the limiting factor governing biofilm base area during growth on minimal medium.

Biofilm maximum intensity projection images (Figure 2.6) which were colour-coded by depth also indicated that not all biofilms had the uniform dome-shaped structure typical of *E. coli* biofilms [324], [325]. Instead, from Figure 2.6c we observed that the thickest region of the biofilm was located at an intermediate radius, between the centre and the edge of the biofilm. A phenomenon similar to colony sectoring was observed on glucose-limited substrates (Figure 2.6a), where

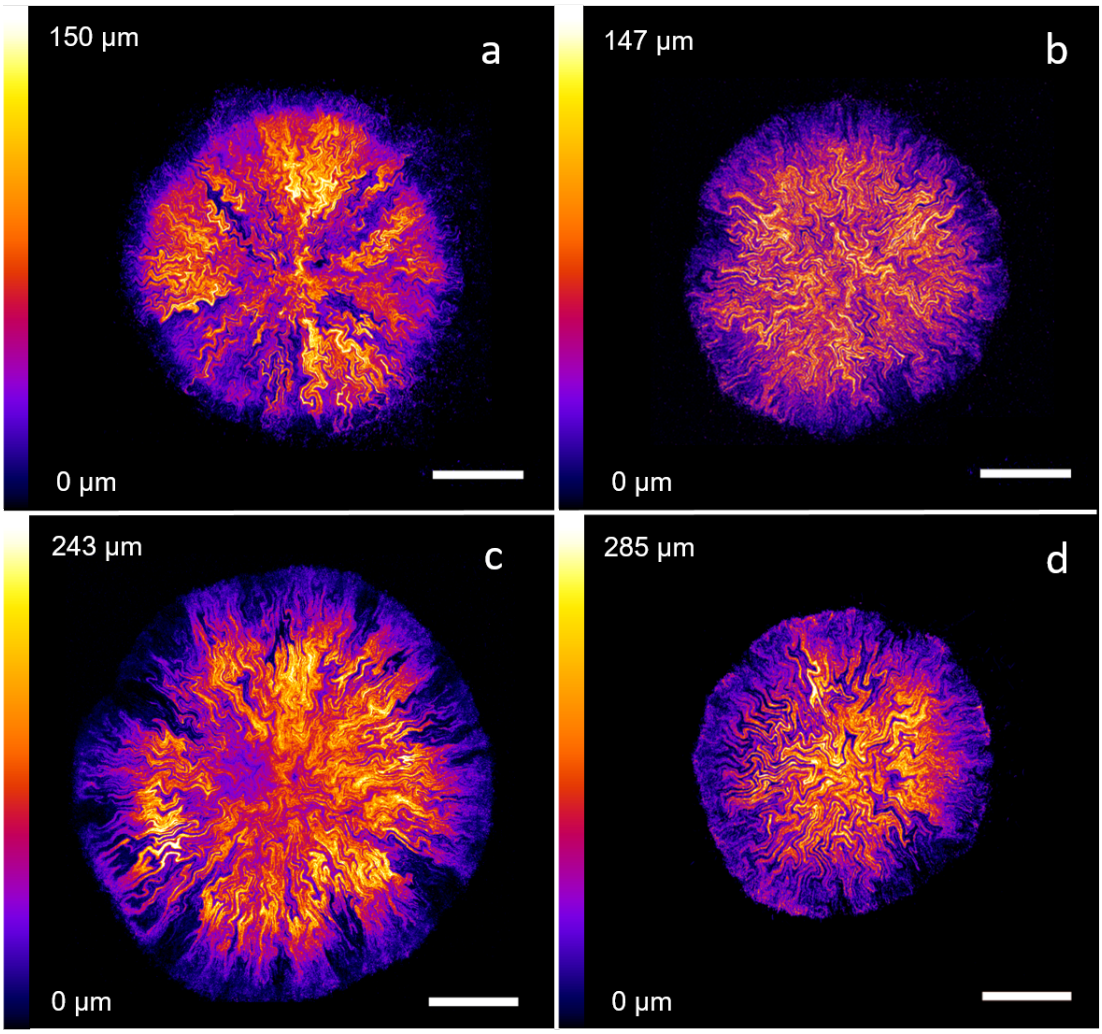

Figure 2.6: *E. coli* JM105 mini-Tn7-*gfp* biofilms grown on M9 minimal medium substrates with 15 mM carbon (a), 200 mM carbon (b), 2.5 mM nitrogen (c) and 10 mM nitrogen (d) concentrations. Intra-colony channel patterns appear radially expanding from the centre on nutrient-limited substrates (a,c), whereas they have a fractal structure with sharp turns on nutrient-sufficient substrates (b,d). Confocal z-stacks made of images separated by 3 μm in the z-direction are displayed as hyperstacks and colour-coded in the axial direction, with purple corresponding to the base of the biofilm and white corresponding to the top. Scale bars: 500 μm.

radial sections of the biofilm had a considerably lower fluorescence signal than the rest of the biofilm. The pattern of intra-colony channels was also distributed heterogeneously inside the biofilm depending on the nutrient availability. Channels grown on nutrient-limited substrates appeared to expand radially outwards from the centre in approximately straight lines, whereas on nutrient-rich substrates the channels often changed direction sharply and did not follow a straight line. These observations confirm that the morphology of *E. coli* biofilms is strongly determined by nutrient availability.

2.3.2 Intra-colony channel width increases non-linearly with radial distance from the centre of the biofilm

Channel width was measured along whole circumferences in *E. coli* JM105 mini-Tn7-*gfp* biofilms grown on M9 minimal medium substrates with limitation and excess of both glucose and ammonium chloride. The average channel width was plotted against radial distance from the centre of the biofilm, revealing a non-linear increase in width with radius. Representative plots of n = 3 repeats for each nutrient condition are shown in Figure 2.7. The minimum observed channel width was between 10 μm and 15 μm, and corresponded to the innermost region of the biofilm (at 200 μm radius). This value was not limited by the spatial resolution of the image datasets, but rather by the smallest radial distance at which channel width could be accurately measured by the image analysis pipeline.

The modality of increase in intra-colony channel width was explored by applying linear and exponential fits to each dataset, and R-squared values were calculated for each fit. Average R-squared values for linear fits were 0.816 for 15 mM carbon, 0.855 for 200 mM carbon, 0.825 for 2.5 mM nitrogen and 0.813 for 10 mM nitrogen. Average R-squared values for exponential fits were 0.845 for 15 mM

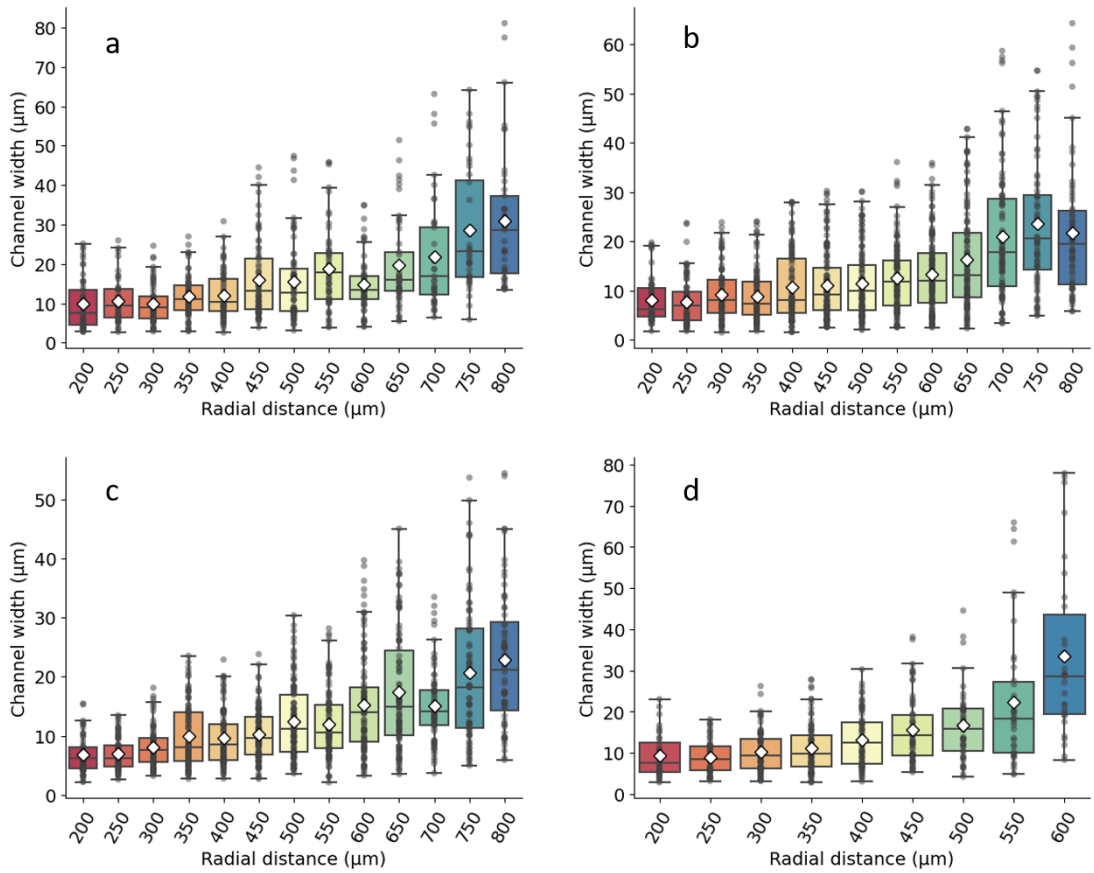

Figure 2.7: Non-linear channel width variation across the radial direction for *E. coli* JM105 mini-Tn7-*gfp* biofilms grown on M9 minimal medium substrates with 15 mM carbon (a), 200 mM carbon (b), 2.5 mM nitrogen (c) and 10 mM nitrogen (d). Each plot is representative of n = 3 biological repeats. Average values are shown as white diamonds, whereas boxes represent the interquartile range (with median values shown as horizontal lines inside each box).

carbon, 0.880 for 200 mM carbon, 0.882 for 2.5 mM nitrogen and 0.892 for 10 mM nitrogen. By verifying that the increase in channel width along the biofilm radius was non-linear, it was concluded that this change was not just a result of polar geometry.

2.3.3 Glucose-limited biofilms possess wider channels than ammonium-limited biofilms

To investigate the effect of nutrient availability on intra-colony channel width, colonial biofilms were grown on substrates with a range of nutrient concentrations: 15 mM carbon (n = 8 biofilms), 200 mM carbon (n = 7 biofilms), 2.5 mM nitrogen (n = 9 biofilms) and 10 mM nitrogen (n = 4 biofilms). Intra-colony channel width was compared across nutrient conditions at three normalised radial positions (Figure 2.8), revealing that channels were approximately 25% wider on glucose-limited substrates than on ammonium-limited substrates inside

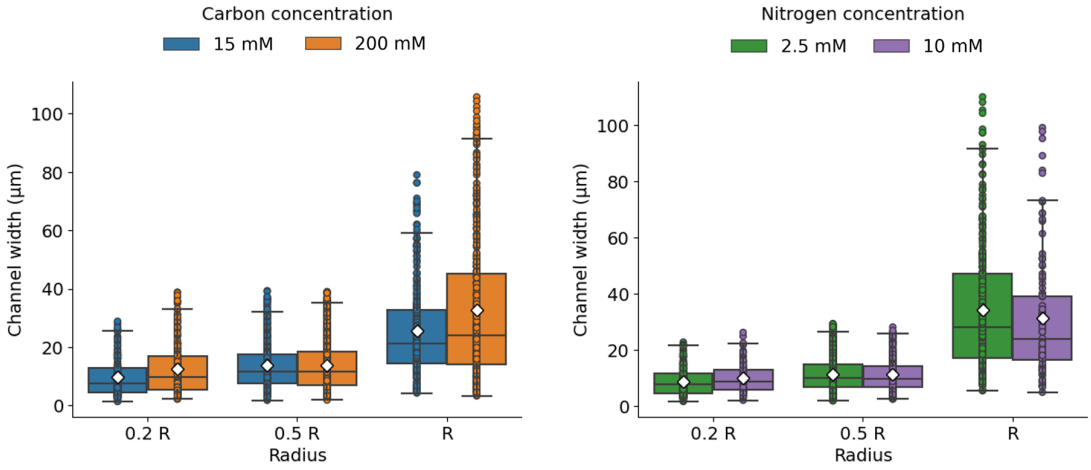

Figure 2.8: Intra-colony channel width calculated at three normalised radial positions (20% radius, 50% radius and full radius, labelled as 0.2 R, 0.5 R and R respectively). Channels were approximately 25% wider on glucose-limited substrates than on ammonium-limited substrates at the mid-radius region of each biofilm, where channel widths measured on average 13.78 μm under glucose limitation and 11.27 μm under ammonium limitation (uncertainties correspond to standard error on the mean across each dataset).

the biofilm. This increase was most significant at the mid-radius region of each biofilm, where channel widths measured on average 21.25 ± 1.26 μm under glucose limitation and 14.38 ± 0.71 μm under ammonium limitation.

These data suggest that carbon- and nitrogen-based nutrients mechanistically affect channel morphology in different manners. The density of channels detected inside the biofilm also varied differently depending on the nutrient source, and was largest at mid-radius.

2.3.4 Substrate stiffness affects channel density and biofilm base area

The effect of substrate stiffness (determined by agar concentration) on internal biofilm morphology was investigated by imaging biofilms grown on soft and hard agar substrates, in both rich and minimal medium (Figure 2.9). An increase in out-of-focus fluorescence for biofilms grown on rich medium substrates was observed compared to biofilms grown on minimal medium substrates. On minimal medium, channel borders were better resolved due to the higher contrast relative to the rest of the biofilm. On rich medium, the density of intra-colony channels increased with decreasing substrate stiffness. On 0.5% agar LB substrates (Figure 2.9a) channels were densely packed in the whole biofilm, while some widely-separated channels progressively appeared on portions of biofilms grown on stiffer substrates (1% and 2% agar concentration, Figure 2.9b and 2.9c respectively).

Varying agar concentration was also associated with a change in biofilm base area for both rich and minimal medium substrates (Figure 2.10). On rich LB medium substrates, decreasing agar concentration resulted in an increase in biofilm base

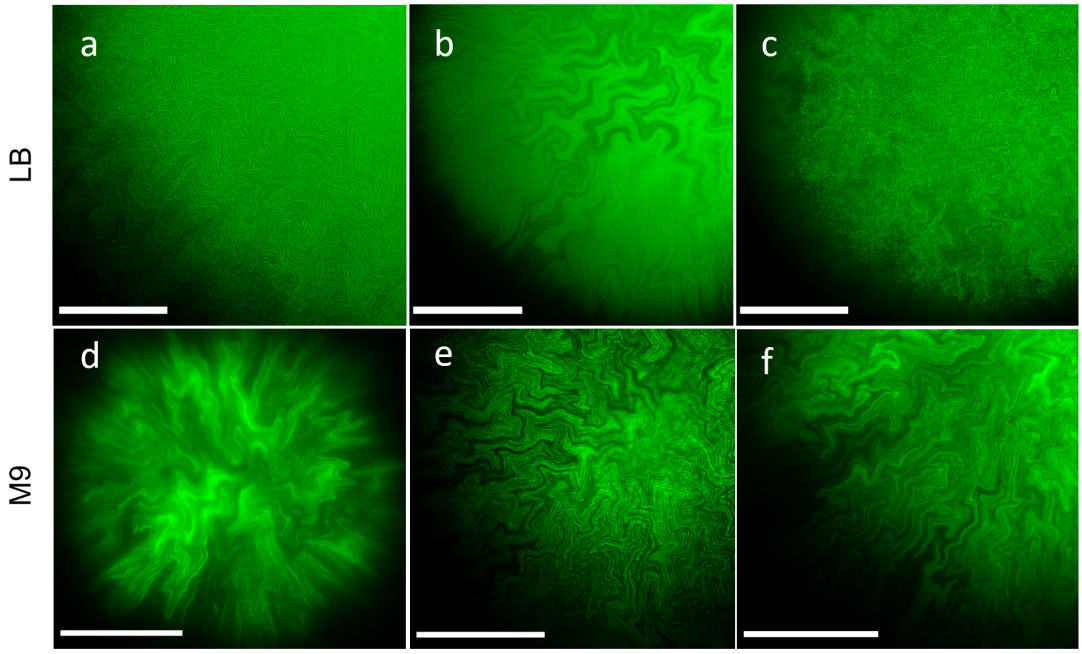

Figure 2.9: Regions of interest (ROIs) showing intra-colony channel morphologies of *E. coli* JM105 mini-Tn7-*gfp* biofilms grown on solid LB rich medium (top) and solid M9 minimal medium (bottom). The agar concentrations of the substrates were 0.5% (a,d), 1% (b,e) and 2% (c,f). All images were acquired using the Mesolens in widefield epi-fluorescence mode. The images were acquired with LB or M9 mounting medium and the Mesolens in water immersion, except for panel d, which was acquired in air with no mounting liquid to prevent the colony from detaching from the substrate. All images were deconvolved using Huygens proprietary software. Scale bars: 500 μm.

area, whereas the effect was opposite on M9 minimal medium substrates. Mann-Whitney U rank tests were performed between the 0.5% and the 2% agar concentration data for both rich and minimal medium, and revealed that increasing agar stiffness had similar effects on biofilm base area for minimal medium ($p = 0.0221$) and rich medium ($p = 0.0180$). However, increasing agar concentration led to an increase in biofilm base area for minimal medium, and a reduction for rich medium. The difference in base area between biofilms grown on rich and

minimal medium substrates was most significant at 0.5% agar concentration (p = 0.0092).

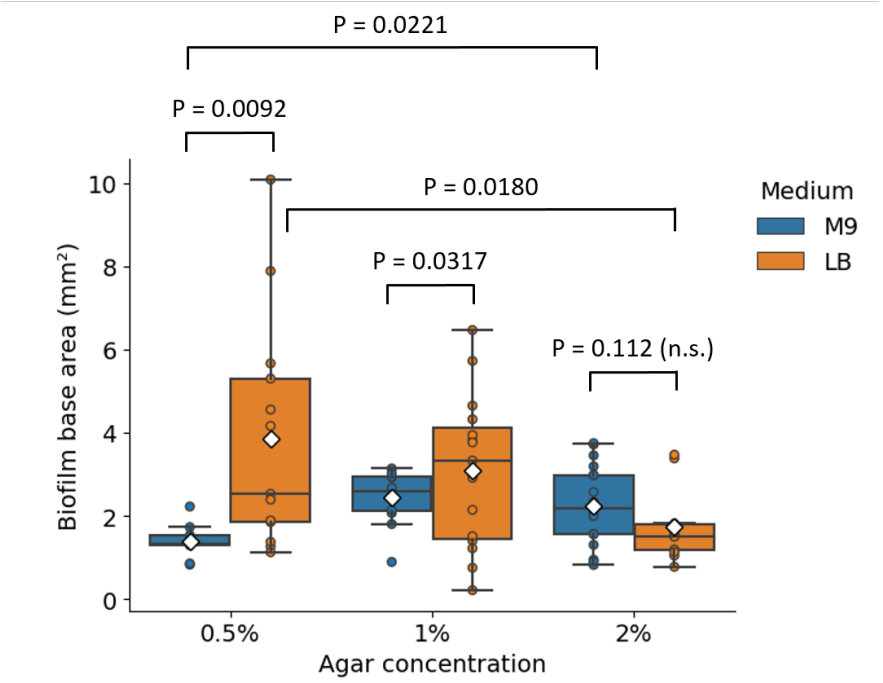

Figure 2.10: *E. coli* JM105 mini-Tn7-*gfp* biofilm base area calculated for three different agar concentrations of the substrate, in both rich (LB) and minimal (M9) medium. Average areas of biofilms grown on rich medium are 3.854 ± 0.772 mm^2 (0.5% agar, n = 13 biofilms), 3.080 ± 0.477 mm^2 (1% agar, n = 15 biofilms) and 1.733 ± 0.245 mm^2 (2% agar, n = 12 biofilms). Average areas of biofilms grown on minimal medium are 1.387 ± 0.142 mm^2 (0.5% agar, n = 9 biofilms), 2.434 ± 0.184 mm^2 (1% agar, n = 12 biofilms) and 2.253 ± 0.224 (2% agar, n = 18 biofilms). Uncertainties correspond to standard errors on the mean across biological repeats. Mann-Whitney U rank tests were performed on the data, with relevant p-values shown. Average values are shown as white diamonds, whereas boxes represent the interquartile range (with median values shown as horizontal lines inside each box).

2.4 Discussion

This study constitutes the first quantitative analysis of intra-colony channels in mature *E. coli* biofilms. Using a simple custom image analysis pipeline developed for the open-source software FIJI and the Python programming language, it was possible to quantify intra-colony channel width subject to various environmental conditions. It was found that channel morphology was affected by both the type of substrate (rich or minimal medium) and by substrate properties (nutrient and agar concentration).

Environmental conditions altered the distribution of intra-colony channels inside biofilms. Channels formed on substrates with limiting carbon or nitrogen concentrations expanded radially outwards, in approximately straight lines. This could be because bacteria growing on nutrient-depleted substrates adhere less strongly on the surface of attachment, and expand more rapidly [208], or may be indicative of nutrient foraging behaviour. Conversely, channels formed on nutrient-rich substrates exhibited complex patterns resembling fractals. It is hypothesised that this type of structure emerges due to rapid cell growth and larger cell dimensions, thereby resulting in a tighter network of channels. This in turn enables a greater proportion of cells to access the nutrients that are transported within the biofilm. A recent study by Fei et al. [170] highlighted two distinct types of patterns forming on the surface of *V. cholerae* biofilms, namely radial stripes and zigzag herringbone patterns. Conversely, the biofilms in our study always involved the same type of fractal patterns: intra-colony channel structures had homogeneous morphology, with only width and spacing varying depending on environmental conditions.

Furthermore, we found that agar concentration in the substrate affected intra-colony channel density on rich medium substrates: channels were tightly packed and had a uniform, narrow width on semi-solid substrates, but as the agar concentration increased, wider channels appeared in portions of the biofilm. This observation appears to be in contrast with previous work on *V. cholerae* biofilms, where homogeneity in radial feature distribution and spacing at the edge of mature biofilms increased with agar stiffness [167].

An increase in out-of-focus fluorescence was also observed in widefield epi-fluorescence images of biofilms grown on rich medium compared to those grown on minimal medium. The fluorescence signal inside channels was likely due to bacterial cells being present inside them, as a result of movement inside the biofilm, collective reorientation [165] or shedding of cells from the inner walls of the channels. Previous studies on *V. cholerae* [326] confirmed that expansion in the depth direction is dependent on friction between the substrate and the expanding cells, with softer substrates leading to flatter biofilms than stiff substrates. This could explain the reduction in contrast between channel border and constituent cells observed on stiff rich medium substrates. A variation in internal biofilm architecture along the depth direction has also previously been reported for *E. coli* growing on agar substrates [327] and was attributed to differences in extracellular matrix components assembly and organisation inside the biofilm volume.

The variation in channel width inside mature biofilms was discovered to increase non-linearly along the radial direction from the centre of the biofilm under all nutrient conditions. Remarkably, channels were on average 25% wider at the centre of glucose-limited media than inside ammonium-limited media, which suggests that they are more important for the transport of carbon-based nutrients. The

increase in channel width at the edge of the biofilm could be due to rapid cell growth in nutrient-rich conditions [328]. This would result in non-uniform radial expansion, as previously observed for *B. subtilis* [208] and *V. cholerae* [170], suggesting that variations in channel width are an emergent property of *E. coli* biofilm growth.

The mesoscopic effects of nutrient limitation were studied by calculating biofilm substrate area. Nutrient abundance in the substrate, achieved by increasing the amounts of either glucose or ammonia, led to larger biofilms than nutrient limitation. Biofilm base area was most significantly affected by the glucose concentration in the growth substrate and was 2.7 times larger for biofilms grown on glucose excess than on glucose limitation. On the other hand, increasing the ammonium concentration on a substrate with sufficient glucose availability did not significantly affect biofilm base area. These findings agree with the reported increase of biofilm formation with glucose concentration in *Staphylococcus* species [329] and the increase in colony size with glucose concentration for *E. coli* [330] and yeast [331]. While it is known that growth rate limitations and carrying capacity limitations differ due to the change in growth condition (homogeneous mixed environment or growth on a solid surface) [332], our data show a similar response to both conditions.

The effect of agar concentration on biofilm base area varied based on the nutritional profile of the substrate. An increase in agar concentration in rich medium was associated with a reduction in biofilm base area, due to slower radial expansion of biofilms on the surface brought by stronger frictional forces [324]. An increase in agar concentration could also affect biofilm base area by decreasing the level of swarming motility [333]. The trend of increased base area with decreased agar stiffness has previously been observed in *V. cholerae* biofilms grown

on LB medium with different agar concentrations [170]. However in this work the opposite trend was observed on minimal medium: biofilms grown on stiff substrates had a base area on average 1.6 times larger than those grown on semi-solid substrates. This could be due to faster assimilation of nutrients occurring on semi-solid minimal media with respect to stiff minimal media, causing a halt to radial expansion. Finally, biofilm base area was on average almost 2.5 times larger on semi-solid rich medium substrates than on semi-solid minimal medium substrates. The slower growth of *E. coli* in minimal medium with respect to rich medium (with average doubling times of 18 $\pm$ 0.5 minutes in LB and 38 $\pm$ 1.1 minutes in M9-glucose [334]) can explain this difference in biofilm base area only in part, since no significant difference in base area between rich and minimal medium substrates was observed at higher agar concentrations of 1% and 2%.

Studying biofilm internal patterns at the cellular level is a task mostly performed using theoretical modelling and computer simulations [324], [335]–[338]. Experimental approaches in imaging biofilms at single-cell resolution [179], [266], [269] have been limited in the total biofilm size that can be imaged at once (under 100 μm^2). The combination of mesoscale imaging and open-source image analysis tools has proven to be an essential platform technology to identify and quantify internal structure in larger biofilms than an ordinary microscope can accommodate. The image analysis pipeline presented in this work provides precise and absolute measurements of intra-colony channel widths in response to specific environmental conditions and gives new insights into the role of nutrient availability in biofilm growth and sustenance. It can also be used without adaptation to validate existing numerical simulations of mature colony biofilm structure, or it can be readily applied for the quantification of any internal patterns and structures in a wide range of biofilms.

2.5 Conclusions

In summary, this Chapter has provided a platform for the identification and quantification of individual nutrient-transporting channels in *E. coli* biofilms from mesoscopic images. Changes in channel architecture observed during growth on various nutritional profiles were ascribed to differences in biofilm expansion rate and cellular adhesion occurring on different growth media. A possible mechanism of nutrient transport through the channel network was proposed to follow fluid dynamics behaviour, leading to increased flow of nutrients at the centre of the biofilm where channels are narrower. This work would benefit from an extension of the image analysis pipeline to accommodate whole confocal z-stacks of biofilms, in order to measure the changes in channel width over the depth direction. Nonetheless, I predict this improvement would result in a significant increase in data size, and would therefore require more computational power.

Chapter 3

Fractal analysis of biofilms formed by cell-shape mutants of *Escherichia coli*

In this Chapter, fractal geometry image analysis tools were used to quantify the morphology of nutrient-transporting channels in *E. coli* biofilms, with the aim of investigating the effect of bacterial cell shape on their architecture. This was achieved by imaging biofilms formed by four *E. coli* bacterial strains with different cell shape mutations and then calculating the fractal geometry quantities of box-counting dimension and lacunarity from each image. While cell shape was found not to be uniquely responsible for the morphological complexity of channel networks, fractal morphometry has proven to be a powerful tool for the comparison of biofilm internal architectures. The analysis presented in this Chapter could be implemented on a larger scale of phenotypic mutations with the aim of elucidating the genetic determinants of channel formation in *E. coli*.

Sections of this Chapter have been adopted from Bottura et al. [339].

3.1 Introduction

3.1.1 Fractal geometry fundamentals

Fractal patterns (from the Latin word *fractus*, "broken") consist of self-similar structures which are repeated at different spatial scales. In computer-generated fractals, the pattern looks the same no matter the scale at which it is observed [340]. One of the most famous examples of fractal patterns is the Koch curve (Figure 3.1), first described by von Koch in 1904 [341]. In fractal geometry, the complexity of the generated shape increases with every iteration step. As such, it can be difficult to quantify. The length of the pattern is infinite (it increases with each iteration step), but the curve itself can fit into a finite space [342]. Mandelbrot showed that the total number of self-similar fragments N in a fractal image is given by $N = 1/S^D$, where S is the scale factor and D is the fractal dimension of the curve. The fractal dimension can then be calculated by [343]

$$D = \frac{log(N)}{log(1/S)} \tag{3.1}$$

In the case of the Koch curve, during each iteration each line is replaced by $N = 4$ lines of length $1/3$ of the original (the scale factor). This means that after n iterations, the total length of the Koch curve $L(n)$ is given by $(4/3)^n$, and the fractal dimension of the Koch curve is $log(4)/log(3) = 1.26$ [344].

While this definition of fractal dimension is useful for mathematical fractals, it is not routinely used to analyse naturally-occurring fractal patterns. In those cases, the box-counting method is used instead [345]. The box-counting algorithm, originally named reticular cell-counting method [346], works by dividing the image containing the fractal pattern into a finite number of boxes of equal size, and

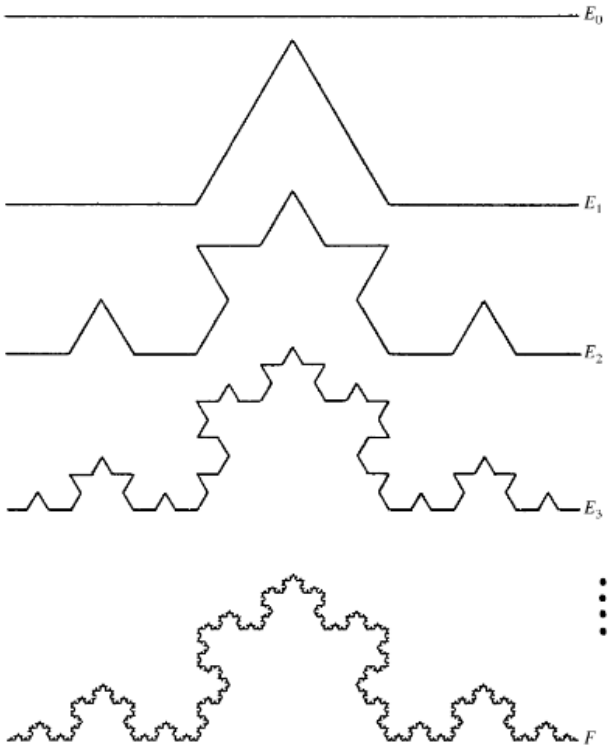

Figure 3.1: Koch curve. Each subsequent form of the curve (E_n) can be generated by adding two sides of an equilateral triangle in the middle of each straight line segment. Figure adapted from [340] and reproduced with permission from John Wiley and Sons (license number 5673800347216).

counting how many boxes contain the pattern outline. The box-counting fractal dimension D_B is then given by

$$D_B = \lim_{\varepsilon \to 0} \frac{logN(\varepsilon)}{log(1/\varepsilon)} \tag{3.2}$$

where ε is the side length of the box and $N(\varepsilon)$ is the number of boxes used to cover the image [347]. In practice, the measurement of the box-counting fractal dimension is achieved by a least-square line fit to the plot of $logN(\varepsilon)$ versus $1/\varepsilon$, with the slope of the fitted line corresponding to the box-counting dimension

[348].

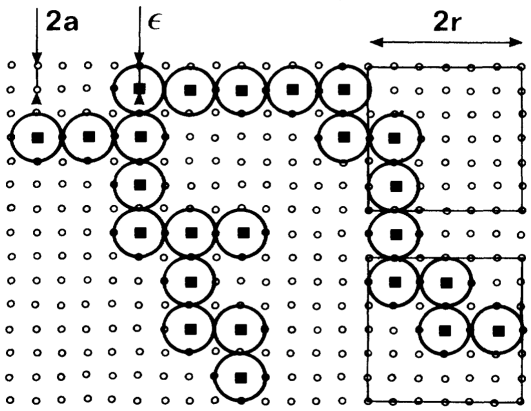

Figure 3.2: Schematic figure showing the quantities involved in the gliding box algorithm proposed by Allain and Cloitre, used to estimate lacunarity from an image. Figure reproduced from [349] with permission from APS (license number RNP/23/NOV/072221).

Another important parameter to describe fractal dimensions is lacunarity (from the Latin word *lacuna*, meaning "cavity" or "emptiness"), which pertains to the holes or empty spaces in a pattern, and is defined as "the deviation of a fractal from being translationally invariant" [350], [351]. Traditionally, lacunarity has been calculated using the gliding box algorithm. Here, the pattern consists of a number of particles of fixed size ε distributed on a lattice of size *2a*, upon which a box of radius r slides in all possible manners from one point to another along the lattice (Figure 3.2) [349]. The lacunarity, Λ of the pattern is proportional to the probability *M(r)* that the sliding box of radius r contains a particle. Mathematically, lacunarity is given by

$$\Lambda = \frac{\sigma^2(M(r))}{[\mu(M)]^2} \tag{3.3}$$

where σ^2 and μ represent the variance and the mean, respectively, of the particle's mass distribution probability [352]. Crucially, lacunarity is also a measure of how diverse the holes are in a pattern: if the holes are all of the same size the lacunarity will be low, whereas if the holes are of different sizes the lacunarity will be much higher [349].

3.1.2 Fractal image analysis algorithms

Fractal geometry has been used extensively to study and quantify many biological structures at various scales [353], through image analysis of microscopy data. In particular, the outline of expanding biofilms has been described in terms of fractal dimension, often through the use of custom-written image analysis programs [354]–[356], whereas other studies [357]–[359] have adopted the box-counting dimension defined in Equation 3.2.

In practice, several algorithms are available to calculate the box-counting dimension from a digital image. Many of these construct a 3D image by keeping the original pattern in the x-y dimension, and adding a z dimension representing the greyscale levels [360]. For example, in the differential box-counting (DBC) method proposed by Sarkar et al. [361], the x-y space is divided into non-overlapping boxes of size r, over which a certain number of $r \times r \times h$ boxes are needed to cover the pattern in the grey-level (z) dimension, as shown in Figure 3.3 [362]. At every $(i, j)^{th}$ box of size r, the number of $r \times r \times h$ boxes required to cover the image pattern is given by

$$n_r(i, j) = \frac{g_{max}}{h} - \frac{g_{min}}{h} + 1 \tag{3.4}$$

where g_{max} and g_{min} are the maximum and minimum greyscale levels present

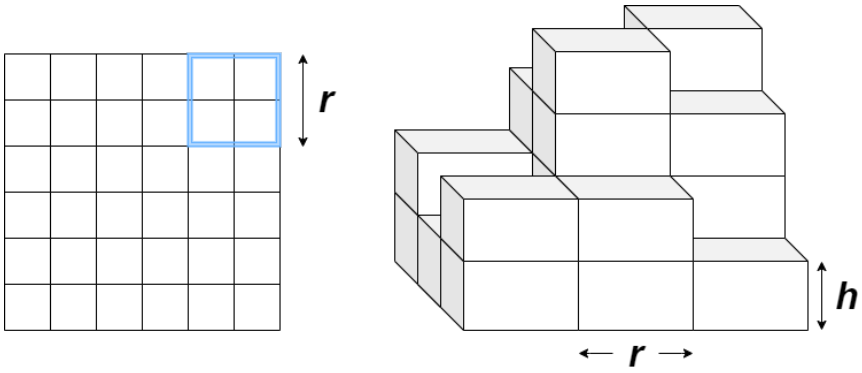

Figure 3.3: Schematic diagram showing the quantities involved in the estimation of the box-counting dimension using the differential box-counting (DBC) algorithm. The image is partitioned in non-overlapping boxes of size r (blue box). In the z direction, the pattern is covered by a number of $r \times r \times h$ boxes dependent on the average greyscale level of each corresponding x-y box. Image created in draw.io (`https://app.diagrams.net/`, JGraph).

on the $(i, j)^{th}$ box [363]. The DBC dimension is then calculated by least-square fitting the log-log plot of N_r versus $1/r$, where N_r is obtained by summing n_r over all (i, j) contributions [361]. A requirement for this algorithm is that the box size should be larger than the resolution limit of the system to avoid non-linear regions in the log-log plot [347]. This version of the box-counting dimension algorithm has been used extensively in feature extraction on a vast sample of images thanks to its low computational complexity and high efficiency [364].

However, the DBC method can lead to incorrect estimates of fractal dimension when the number of boxes used to cover the pattern in either the x-y or z direction is overcounted or undercounted. This is usually due to the fact that in DBC the boxes are applied to the image in a fixed (non-sliding) way [365]. This issue can be overcome for example by modifying the algorithm to allow for the box to shift along the image [366]. An alternative improvement on the DBC algorithm is

given by the relative differential box-counting (RDBC) method, which modifies the upper and lower greyscale limits to which the DBC algorithm is applied [367].

Lacunarity is usually calculated either through the gliding box algorithm presented by Allain and Cloitre [349], or through a modification of the box-counting algorithm. As for fractal dimension estimations, lacunarity algorithms also are modified to account for image greyscale levels [368]. The accuracy of lacunarity estimation algorithms is affected by image resolution and by the choice of algorithm [369].

3.1.3 Fractal patterns in biofilms

Fractal geometry has previously been proposed as a tool for the investigation of microbial growth patterns [370], and it has since been employed to quantify biofilm morphology from microscopy images [358], [371], [372], to describe colony morphogenesis in gram-negative rod-shaped bacteria [373], and to analyse nutrient-limited growth patterns [357].

In *E. coli*, fractal patterns mostly exist as cellular aggregates of co-cultured isogenic strains expressing different fluorescent markers (Figure 3.4), which can be simultaneously expressed in numbers as high as 11 [374]. These types of fractal boundaries can be engineered through stochastic plasmid segregation, achieved by modifying the selective pressure on growing cells [268]. The fractal boundary between isogenic strains is formed during uniaxial cell growth and division, and can be a result of local instabilities [375]. The degree of self-similarity across these boundaries, usually measured through their fractal dimension, depends on the properties of the constituent cells. For example, computer modelling of rigid, dividing rods subject to drag and intercellular forces shows that self-similarity increases with cell length at division [189]. The fractal dimension of strain borders

is much lower for spherical mutant aggregates of *E. coli*, both in modelling and *in vivo*, which suggests that fractal domains are specific to rod-shaped bacterial cells. This is further confirmed by the presence of similar fractal domains in isogenic cocultures of *B. subtilis* [375]. Intercellular adhesion, which is responsible for the adhesion of cells to other cells and to external surfaces, is also associated with increased mixing in isogenic fractal domains [192].

The formation of fractal domains can be also be due to genetic drift. This is the process by which some of the many mutations present in a population are lost in the subsequent generations [376]. Genetic drift often leads to a positive feedback loop, whereby mutant populations with a fitness advantage grow faster and expand more rapidly than the others, hence obtaining greater access to nutrients at the periphery of the colony [377]. This mechanism is called allele surfing, which is a dynamic process that can shape the morphology of the mature biofilm [200]. The same process is responsible for the formation of large mutant sectors inside biofilms [378]: for example, random genetic segregation of fluorescent markers within isogenic bacterial strains can form well-separated, single-colour sectors inside bacterial colonies [201].

Fractal boundaries are also observed in *E. coli* co-cultures of cross-feeding strains. The type of social interaction determines the level of spatial mixing between the two strains: cooperative behaviour leads to high mixing where each strain maintains an approximately constant patch width, whereas in a competitive scenario the strains are well-separated into lager patches [202]. A similar phenomenon is observed in the yeast species *Saccharomyces cerevisiae*, where cooperative behaviour results in a higher degree of population mixing than competitive or commensal behaviour [194]. Metabolic interactions between isogenic strains can lead to different patterns of self-organisation, from uniform radial expansion to the

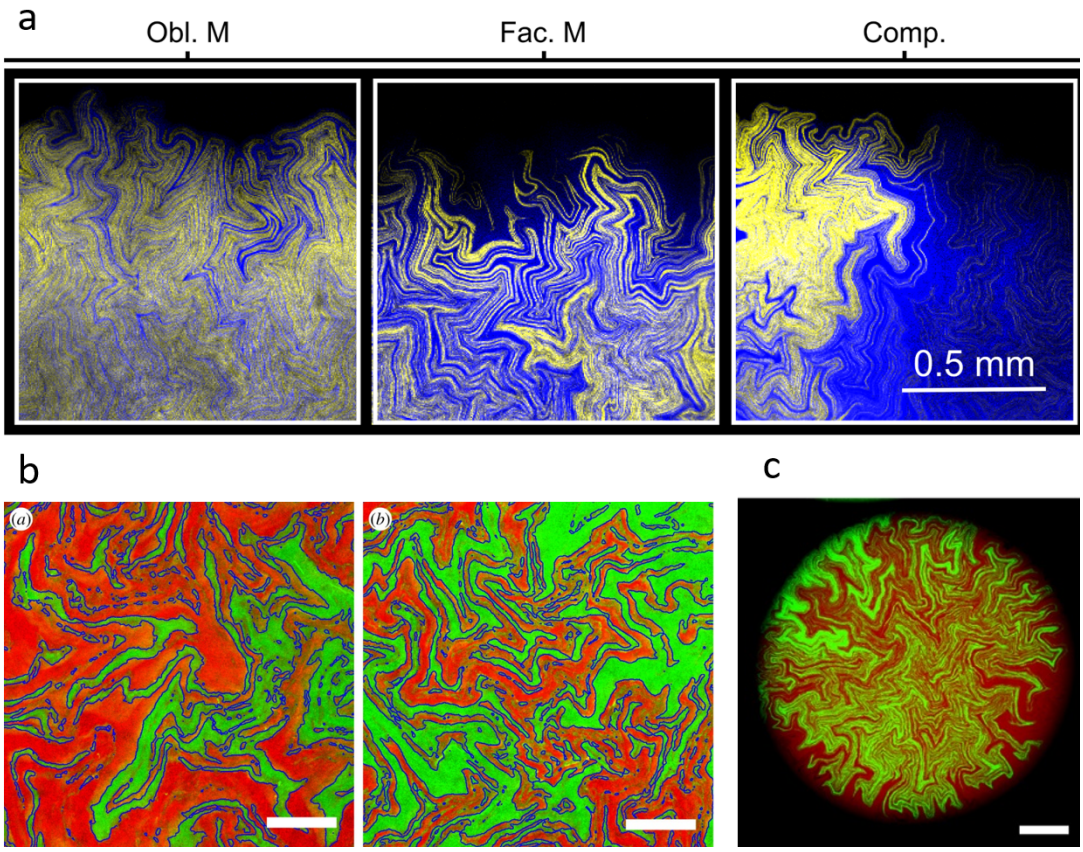

Figure 3.4: Fractal patterns formed during isogenic strain mixing. (a) Cross-feeding strains experiencing obligatory mutualism (Obl. M), facultative mutualism (Fac. M), and competition (Comp). Boundaries have uniform width in the first two cases, whereas the competitive scenario shows an increasing boundary width. Adapted from [202]. (b) Detected boundary mixing is lower for non-adhesive strains (left) than for adhesive strains (right). Scale bars 50 μm. Adapted from [192]. (c) Cell polarity-driven instabilities leading to fractal domain segregation. Scale bar 100 μm. Adapted from [375].

formation of dendritic niches at the colony edge [379].

A different example of fractal pattern formation (Figure 3.5) can be seen during bacterial growth in nutrient-depleted substrates [380]. In this case, bacteria such as *Bacillus subtilis* [381] and *Serratia marcescens* [382], and fungi such as

Aspergillus nidulans [383] adopt a branched morphology as a nutrient scavenging mechanism. These patterns have traditionally been modelled by diffusion-limited growth [384], whereby single particles undergo a random walk on a lattice until they encounter another particle [385]. Given the high dependency of colony morphology on nutrient availability, it is hypothesised that fractal branching patterns are developed to obtain a growth advantage in a nutrient-limited environment [357], [386].

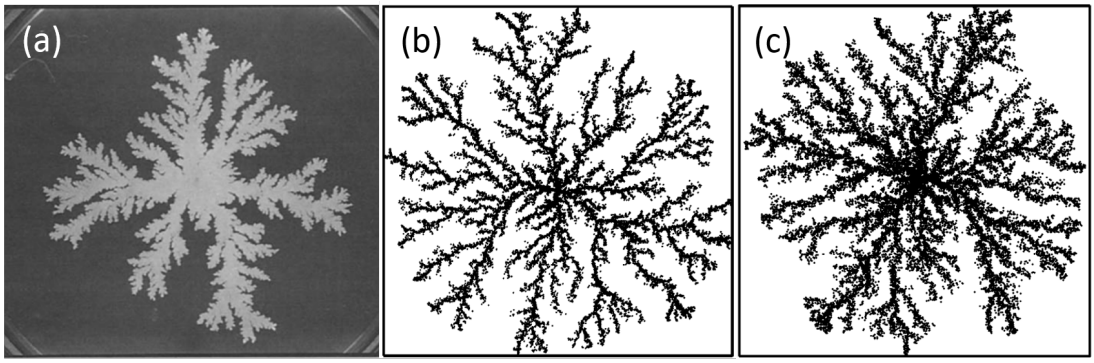

Figure 3.5: (a) Fractal patterns produced during diffusion-limited growth in *B. subtilis* grown on 1 g/l peptone. Figure reproduced from [387] with permission from Elsevier (license number 5673820595999). (b, c) Colony morphologies modelled by diffusion-reaction equations with low (b) and high (c) nutrient diffusivity coefficients. Figures adapted from [388].

The network of nutrient-transporting channels recently identified in *E. coli* biofilms [209] also exhibits a complex 3D morphology. The spatial structure of these emergent channels bears a striking resemblance to the fractal boundary patterning described in multi-strain co-culture biofilms, although these channels are not occupied by cells. In the previous Chapter, I measured the width of individual channels at different locations within the biofilm and showed that the channel

architecture is affected by environmental growth conditions [294], but a quantification of channel morphology at the whole-biofilm scale has not been performed to date.

3.1.4 Cell-shape mutants of *E. coli* and the Keio collection

Bacteria can regulate their cell shape in response to environmental changes, such as changes in nutrient availability, viscosity, external forces, or the presence of predators. They can also change their cell morphology to better perform the fundamental molecular process of division [389]. In rod-shaped bacteria such as *E. coli*, cell division occurs by elongation along the long axis [390] followed by the formation of a septum along the middle of the cell, which progressively tightens and leads to cell splitting. The maintenance of the rod shape is controlled by regulation of cell wall synthesis, which in turn is mainly controlled by the proteins MreB and RodZ [391]. Septation is regulated by the filamentous temperature-sensitive (*fts*) genes [392], [393], which encode for the protein FtsZ, responsible for the formation of the Z ring [394]. Nonetheless, mutations on many other genes have been shown to alter *E. coli* cell length and width, often leading to the formation of spherical cells [395]–[399].

One of the ways to determine the function of a gene is by site-directed mutagenesis, a laboratory technique whereby genetic modifications of the DNA are induced by molecular biology methods such as PCR [400]. The Keio collection [401], a library of knockouts of most non-essential genes in the *E. coli* K-12 strain BW25113, is a prime example of large-scale site-directed mutagenesis. The gene inactivations were performed using the method by Datsenko and Wanner [402], whereby the gene of interest was replaced with a kanamycin resistance cassette.

The Keio collection has been used for phenotypic analysis in various areas of microbiology, including studies of cell morphology and nutrient metabolism [403], [404]. The phenotypic analysis carried out by by Campos et al. [405] showed that approximately 20% of non-essential gene inactivations in the Keio collection led to a variation in cell shape and size, though it is important to note that mutations altering cell shape also affect physiological processes [389].

3.1.5 Experimental aims

The first aim of this chapter was to characterise the cell shape phenotype of the four mutant strains Δ*amiA*::kan, Δ*guaB*::kan, Δ*ompR*::kan and Δ*ydgD*::kan from the Keio collection, hereby named Δ*amiA*, Δ*guaB*, Δ*ompR* and Δ*ydgD* respectively. The genotype of the strains was checked via PCR and amplicon sequencing, and the cell phenotype was confirmed and quantified through phase-contrast microscopy. The second aim of this Chapter was to quantify the morphological complexity of channel networks formed by these strains under different growth conditions. This was achieved through open-source image analysis of confocal micrographs of mature colony biofilms and using the FIJI plugins twombli and ComsystanJ to calculate the fractal geometry quantities of box-counting dimension and lacunarity. The morphology of biofilms formed by the long-cell strain Δ*guaB* and by the wide-cell strain Δ*ompR* were analysed further due to the interesting channel architecture they displayed. The findings of this Chapter are summarised in Figure 3.6.

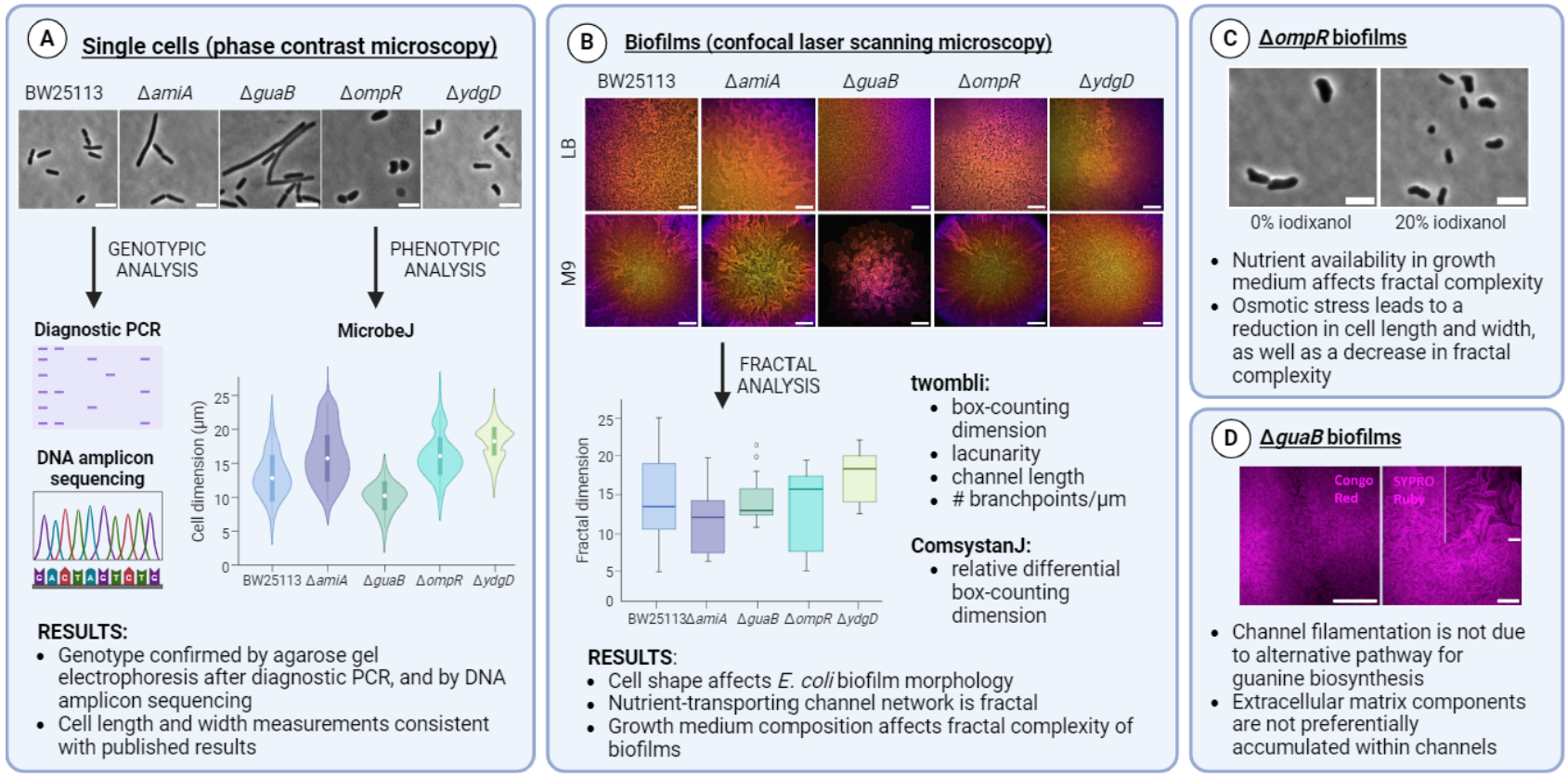

Figure 3.6: Schematic diagram summarising the main methods and results from this Chapter. The four mutant strains Δ*amiA*::kan, Δ*guaB*::kan, Δ*ompR*::kan and Δ*ydgD*::kan from the Keio collection were characterised using genotypic and quantitative phenotypic analysis (A). Biofilms formed by these strains were imaged using confocal laser scanning microscopy, and their morphology was quantified using fractal image analysis (B). The effects of nutrient availability and osmotic stress were investigated for Δ*ompR* biofilms (C). The distribution of biofilm matrix components was investigated for Δ*guaB* biofilms (D). Image created in BioRender (license number SR25JKZ3PC).

3.2 Materials and Methods

3.2.1 Bacterial strains and media

The non-pathogenic *E. coli* strain BW25113 [402] was used throughout this study, alongside the single-gene knockout mutants of the genes *amiA, guaB, ompR* and *ydgD* (genotypes shown in Table A.2 of Appendix A), which were chosen due to the well-documented nature of each gene [406]–[409]. Each gene inactivation led to an objectively recognisable change in cell shape phenotype [401], with cells becoming either longer ($\Delta amiA$, $\Delta guaB$) or wider ($\Delta ompR$, $\Delta ydgD$) than the parental strain phenotype. The inactivated genes are listed in Table 3.1, alongside their function and resulting cell shape phenotype.

Prior to imaging, all strains were transformed by electroporation with the plasmid pAJR145, encoding a constitutively-expressed *gfp* gene thanks to a *rpsM::gfp+* transcriptional fusion to the promoter P*rpsM* [410]. Prior to transformation, liquid cultures of each strain were made electrocompetent through three ice-cold 10% glycerol washes as detailed in Section A.8.2 of Appendix A.

Liquid cultures of each strain were grown in LB and M9 media with the addition

Gene	**Protein function**	**Cell phenotype**	**UniProt ID**
amiA	Cell wall hydrolase	Long	P36548
guaB	Guanine biosynthesis	Long	P0ADG7
ompR	DNA-binding dual transcriptional regulator	Wide	P0AA16
ydgD	Serine protease (putative)	Wide	P76176

Table 3.1: Genes inactivated in the selected *E. coli* strains from the Keio collection used in this work, along with the function of each inactivated gene and the resulting cell phenotype.

of 25 μg/mL chloramphenicol to maintain GFP fluorescence from the pAJR145 plasmid. Keio mutant strains were also grown with the addition of 50 μg/mL kanamycin. All liquid cultures were grown inside a 37°C incubator shaking at 250 rpm. Solid substrates were prepared by adding agar in a final concentration of 20 g/L unless otherwise specified.

3.2.2 Genetic verification of Keio mutants

3.2.2.1 Diagnostic PCRs

The presence of point mutations in mutants from the Keio collection was firstly verified by growth on LB agar medium containing kanamycin. The genotype of the mutants was then checked by two separate PCR experiments, as described in Appendix A, using the primers from Section A.4.1. The reactions are shown schematically in Figure 3.7. The first set of primers, k1 and k2, is specific to the kanamycin resistance cassette and has been previously used to verify its insertion during one-step inactivation of chromosomal genes in *E. coli* [402]. PCR experiments with these primers were carried out with genomic DNA from the parental (wild-type) strain and from each of the mutants. For mutant strains, the amplified PCR product should show as a 1.3 kb band when run on an agarose gel, whereas the DNA of the parental strain, which is not kanamycin-resistant, should not be amplified by these primers.

The second set of primers was designed upstream and downstream to each gene of interest, and was used to verify gene inactivations. PCR experiments with each pair of gene-specific primers were carried out with both the wild-type DNA and the corresponding mutant. These experiments were set up such that a successful reaction would show, for each pair of primers used, bands for both the parental and mutant gDNA. The bands should have different lengths: in the parental

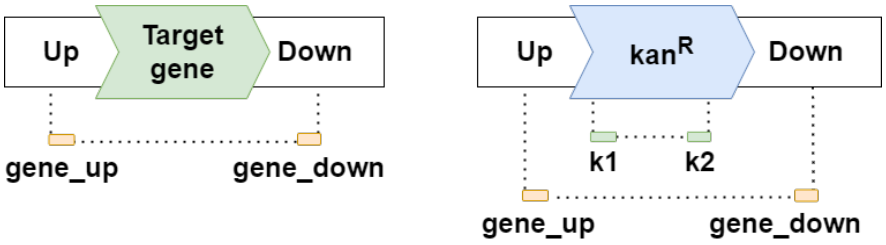

Figure 3.7: Schematic illustration of the PCR experiments used to confirm the genotype of Keio mutant strains. In the parental strain (left), the presence of the gene of interest and the absence of the kanamycin resistance cassette are checked using the gene_up and gene_down primers, designed upstream and downstream of each gene of interest. In the mutant strains (right), the gene of interest is substituted by a kanamycin resistance cassette. The primers k1 and k2 are used to amplify the cassette. The gene-specific primers gene_up and gene_down are also used for sequencing. Image created in draw.io (`https://app.diagrams.net/`, JGraph).

strain, the primers should amplify the whole gene (including the regions upstream and downstream where the primers anneal, as shown in Figure 3.7), whereas in the mutant strains the primers should amplify the kanamycin resistance cassette together with the portions of the gene outside of it. This is because the gene-specific primers occur up and downstream to the gene of interest, and so should always anneal to a portion of DNA, whether or not the gene has been inactivated. The predicted lengths of DNA fragments amplified from both the parental and mutant strains were calculated directly from the genome sequence of the BW25113 strain on NCBI (National Center for Biotechnology Information, GenBank ID: CP009273.1).

PCR reactions were carried out using PCRBIO Taq Mix Red (PCR Biosystems) as described in Section A.5 of Appendix A. Annealing temperatures were optimised for each reaction using a gradient PCR.

3.2.2.2 DNA sequencing

The genetic mutation on each specific gene was then confirmed with Illumina Sanger amplicon sequencing (Eurofins, Germany). PCR experiments were set up using the gene-specific primers for the four mutants, with the same conditions as described above. DNA from PCR products was purified using the Wizard SV Gel & PCR Clean-up System kit (Promega) following manufacturer instructions. The concentration and purity of the DNA products were quantified using a NanoDrop spectrophotometer (Thermo Fisher Scientific, UK). Nucleotide sequencing reads were compared to the target genes or to the kanamycin resistance cassette from plasmid pKD13 (GenBank ID: AY048744.1) using BLAST (Basic Local Alignment Search Tool, NCBI).

3.2.3 Single-cell phase contrast microscopy

Single cell imaging was performed on mid-exponential growth phase liquid cultures of the parental strains and Keio mutants, prepared as described in Appendix A. Single-cell phase contrast images were acquired for both fluorescent and non-fluorescent strains, to ensure that the addition of chloramphenicol required for the maintenance of the pAJR145 plasmid did not affect the cell phenotype of each strain.

Imaging slides were prepared by sandwiching 1 mL of molten 1% agarose between two microscope slides and letting it solidify at room temperature. The top slide was removed, 10 μL of liquid culture was spotted onto the solidified agarose pads, and a 22 mm $\times$ 22 mm borosilicate glass coverslip was added prior to imaging. Single-cell imaging was carried out using an Eclipse E600FN upright widefield microscope (Nikon, Japan) in phase-contrast mode equipped with a 100$\times$/1.30 DLL oil immersion lens (Nikon, Japan). Illumination was provided by a halogen

lamp and detected by a Hamamatsu ORCA 100 digital camera (Hamamatsu, Japan).

3.2.4 Biofilm imaging

3.2.4.1 Specimen preparation

Mid-exponential growth phase liquid cultures of the Keio mutants were prepared as described in Appendix A. At this point, a serial 1:10^{-8} dilution in fresh LB medium with appropriate antibiotics was performed for growth of colony biofilms on LB substrates. For growth on M9/glucose substrates, liquid cultures were washed three times with M9 buffer and resuspended in 1× M9 salts, and diluted 1:10^{-6}. 50 μL of these dilutions were used to inoculate agar plates. Biofilms were grown at 37 °C for 24 hours when using LB medium, and for 48 hours when using M9 medium.

3.2.4.2 Mesolens mesoscopy

While the Mesolens provided a field of view large enough to capture images of entire biofilms, it was not possible to image BW25113-derived strains with the Mesolens correction collars set for imaging with water immersion. This was because mounting biofilm specimens with liquid growth medium, which was needed to match the refractive index of water, led to very rapid disruption of the biofilm structure. The biofilms comprised of cells from BW25113-derived strains were hence imaged in air, with no immersion medium, and this provided too poor a resolution to distinguish individual channels. Mesoscopic imaging of biofilms with the Mesolens was carried out as described in Section 2.2.3 of Chapter 2.

3.2.4.3 Confocal microscopy

Mature biofilm images were acquired on an Olympus IX81 microscope coupled to a FluoView FV1000 confocal laser scanning unit (Olympus, Japan). Fluorescence from GFP was excited using a 488 nm argon laser (GLG3135, Showa Optronics, Japan) and was detected by a PMT with a spectral detection window set between 510 and 560 nm. Samples were imaged using either a 10×/0.4 N.A. or a 4×/0.1 N.A. apochromatic air objective lens (Olympus, Japan).

Three-dimensional z-stacks of biofilms grown on LB and M9 media were acquired with a slice spacing of 25 μm when using a 4×/0.1 lens, and with a slice spacing of 5 μm when using a 10×/0.4 lens for Nyquist sampling in the axial dimension.

3.2.5 Characterisation of the effect of growth medium composition and osmotic stress on the morphology of $\Delta ompR$ cells and biofilms

LB and M9 solid growth substrates were prepared with different chemical compositions to study the resulting change in internal morphology of $\Delta ompR$ biofilms. No-salt substrates were prepared without NaCl, and soft substrates were prepared by reducing the amount of agar to 10 g/L. D-glucose was added to LB and M9 media to final concentrations of 0.02% (w/v), 0.2% (w/v) and 0.5% (w/v) to study the effect of nutrient availability on the morphology of $\Delta ompR$ biofilms.

To study the effect of osmotic stress, growth of the parental strain BW25113 and of the mutant $\Delta ompR$ were first characterised using a plate reader. LB broth was prepared with iodixanol concentrations of 0%, 1%, 2%, 5%, 10% and 20% by adding appropriate amounts of an OptiPrep 60% w/v iodixanol stock solution (Sigma-Aldrich, USA). The amounts of LB salts were increased proportionally to

compensate for this addition. Ten wells of a 96-well plate were then filled with each concentration of iodixanol (five repeats for each strain). Overnight liquid cultures of BW25113 and of the Δ*ompR* strain were prepared in LB broth as described in Appendix A, and diluted to a starting OD_{600} of 0.01. The plate was then loaded onto a Synergy HT plate reader (BioTek, USA), where the OD_{600} of the cultures was measured every 15 minutes for 24 hours with the plate being held at 37°C and shaken continuously.

Growth curves were plotted in Prism by exporting data from the Gen5 microplate software (BioTek, USA), with y axis plotted on a logarithmic scale. Specific growth rates were calculated as the slope of the linear region of the semi-logarithmic plot using the equation

$$\mu = 2.303(log_{10}N - log_{10}N_0)/(t - t_0) \tag{3.5}$$

where N and N_0 are are the cell numbers at the beginning and at the end of the exponential growth phase, respectively, and correspond to optical density readings, and t_0 and t are the times at which exponential growth phase starts and ends, respectively [411].

To compare cell shape phenotype before and after growth in high osmolality medium, BW25113 and Δ*ompR* strains were first grown as liquid cultures overnight in LB broth. They were then diluted 1:100 in both LB broth and LB broth with 20% iodixanol (with LB salts increased proportionally), and incubated further until mid-exponential growth phase before imaging using phase contrast microscopy, as described in Section 3.2.3. Solid LB medium plates were prepared with iodixanol concentrations of 1%, 10% and 20%, and used as substrates for the growth of BW25113 and Δ*ompR* biofilms. Five biofilms were imaged for each condition

using an Olympus IX81 microscope coupled to a FluoView FV1000 confocal laser scanning unit (Olympus, Japan) as described in Section 3.2.4.3. Biofilms grown on each of the different media recipes were imaged on the same day to minimise growth-related effects due to inoculum differences.

3.2.6 Investigation of the effect of guanine complementation in Δ*guaB* mutant strain biofilms

To check whether guanine complementation would revert the phenotype of Δ*guaB* biofilms to that of the parental strain, M9 solid growth medium was supplemented with guanine in concentrations of 2 μg/mL, 20 μg/mL and 200 μg/mL. Biofilm imaging was carried out using an Olympus IX81 microscope coupled to a FluoView FV1000 confocal laser scanning unit (Olympus, Japan) as described in Section 3.2.4.3.

3.2.7 Quantification of matrix components in biofilms formed by the Δ*guaB* mutant strain

The distribution of extracellular matrix components was compared between the parental strain BW25113 and the Δ*guaB* mutant strain by Congo Red assay on LB medium without NaCl as described in [412]. Congo Red stocks were prepared by dissolving 2 g/L Congo Red (Sigma-Aldrich, USA) in 70% ethanol, and Coomassie Blue stocks were prepared by dissolving 1 g/L Coomassie brilliant blue R (Sigma-Aldrich, USA) in 70% ethanol. Solid substrates were prepared with final concentrations of 40 μl/mL Congo Red for visualisation of polysaccharides components of the biofilm matrix, and 20 μl/mL Coomassie Blue for visualisation of matrix proteins.

Biofilms grown on Congo Red-stained plates were imaged with an Olympus IX81 microscope coupled to a FluoView FV1000 confocal laser scanning unit (Olympus, Japan). Fluorescence from GFP and Congo Red were excited using a 488 nm argon laser (GLG3135, Showa Optronics, Japan) and were detected by two PMTs with spectral detection windows set between 520 and 560 nm (GFP) and between 580 and 650 nm (Congo Red). Samples were imaged using a 20×/0.75 N.A. apochromatic air objective lens (Olympus, Japan), with z-stack slice spacing of 2 μm.

The distribution of biofilm matrix components for both the parental strain BW25113 and the $\Delta guaB$ mutant strain was also assessed by staining with the FilmTracer SYPRO Ruby Biofilm Matrix Stain (Thermo Fisher Scientific, UK), which was added in a concentration of 5% (v/v) to solid growth media. Fluorescence from GFP and SYPRO Ruby was excited using a 488 nm argon laser (GLG3135, Showa Optronics, Japan), and was detected using a PMT with spectral detection windows set between 510 and 550 nm (GFP) and between 580 and 680 nm (SYPRO Ruby). The excitation path also included a DM488/561/633 nm dichroic reflector (Olympus, Japan).

3.2.8 Image analysis

Phase-contrast images of both fluorescent and non-fluorescent cells were first pre-processed in FIJI using the background subtraction tool with a rolling ball radius of 15 pixels with, with the "light background" option selected. The images were then analysed using the FIJI plugin MicrobeJ [276] to obtain cell length and width measurements. Segmentation was performed using MicrobeJ with the default settings for a bright background and the medial axis mode of detection. The following changes to the parameter ranges were made: area [1-max] μm^2; width

[0-max] μm with variation [0-0.2]; sinuosity [1-1.2]; angularity [0-0.5] rad; solidity [0.9-max]. For these parameters, a maximum value of "max" signifies that no upper bound is placed on that parameter. The default advanced parameters were changed to have an area cut-off of 1000, and a count cut-off of 250. The options "exclude on edges" and "shape descriptors" were selected. n = 10 phase contrast micrographs were analysed for each strain, with a total number of analysed cells between 202 and 665 (non-fluorescent cells) and between 90 and 524 (fluorescent cells).

Biofilm image z-stacks were displayed as hyperstacks, and colour-coded by depth using the "Fire" lookup table in FIJI. Biofilms images were contrast-adjusted where needed for presentation purposes, using the Contrast Limited Adaptive Histogram Equalization (CLAHE, [321]) feature in FIJI with block size 60, maximum slope 3 and 256 histogram bins. ROIs of biofilm images were despeckled using the "Despeckle" function in FIJI.

3.2.9 Fractal pattern quantification

Fractal analysis of biofilms formed by the Keio mutant strains was carried out with two open-source FIJI plugins, twombli (The Workflow Of Matrix BioLogy Informatics), designed to quantify extracellular matrix patterns in tissue [413] and ComsystanJ (Complex Systems Analysis for ImageJ), a collection of plugins building on existing algorithms for the estimation of morphological complexity [414].

3.2.9.1 twombli

For the analysis of Keio mutant biofilms with twombli, images were first pre-processed with the *Ridge detection* plugin. The FIJI plugin *Ridge detection* [415]

was used to detect channels inside confocal stacks of mature colonies for further analysis. The input images for this analysis were biofilm images acquired with the Olympus IX81 microscope coupled to a FluoView FV1000 confocal laser scanning unit (Olympus, Japan) as described in Section 3.2.4.3. Ten images from each strain were acquired and analysed as follows. The z-stacks were first converted to a maximum intensity projection, then the *Ridge detection* plugin was used to create a binary mask of intra-colony channel architecture (Figure 3.8). The parameters needed to run *Ridge detection* were modified for each image in order to capture the largest amount of channels inside every image. A minimal line length was selected as 10 μm, and the line width was estimated by the plugin for each image. The sigma value, the threshold values and the contrast values were adjusted depending on the contrast levels and channel structure of each image. The output masks were used as input image files for further analysis in the FIJI plugin twombli.

twombli was used to extract a variety of measurements to quantify channel-like structures from input images. Before quantitative analysis, twombli was used to threshold HDM (high-density matrix) from input images, by choosing a maximum pixel value corresponding to matrix fibres (the maximum display HDM) and by specifying a proposed width for the mask (line width), a curvature window (the average length over which matrix fibres are approximately straight), and the minimum branch length (chosen as approximately 10% of the curvature window). These values were chosen iteratively in the pre-processing (mask creation) steps. Box-counting fractal dimension was then calculated according to Equation 3.2, whereas lacunarity was calculated using an alternative version of Equation 3.3 provided by Blackledge [416]. Individual channels were also tracked along their whole length in order to count the number of intersections (branchpoints) and

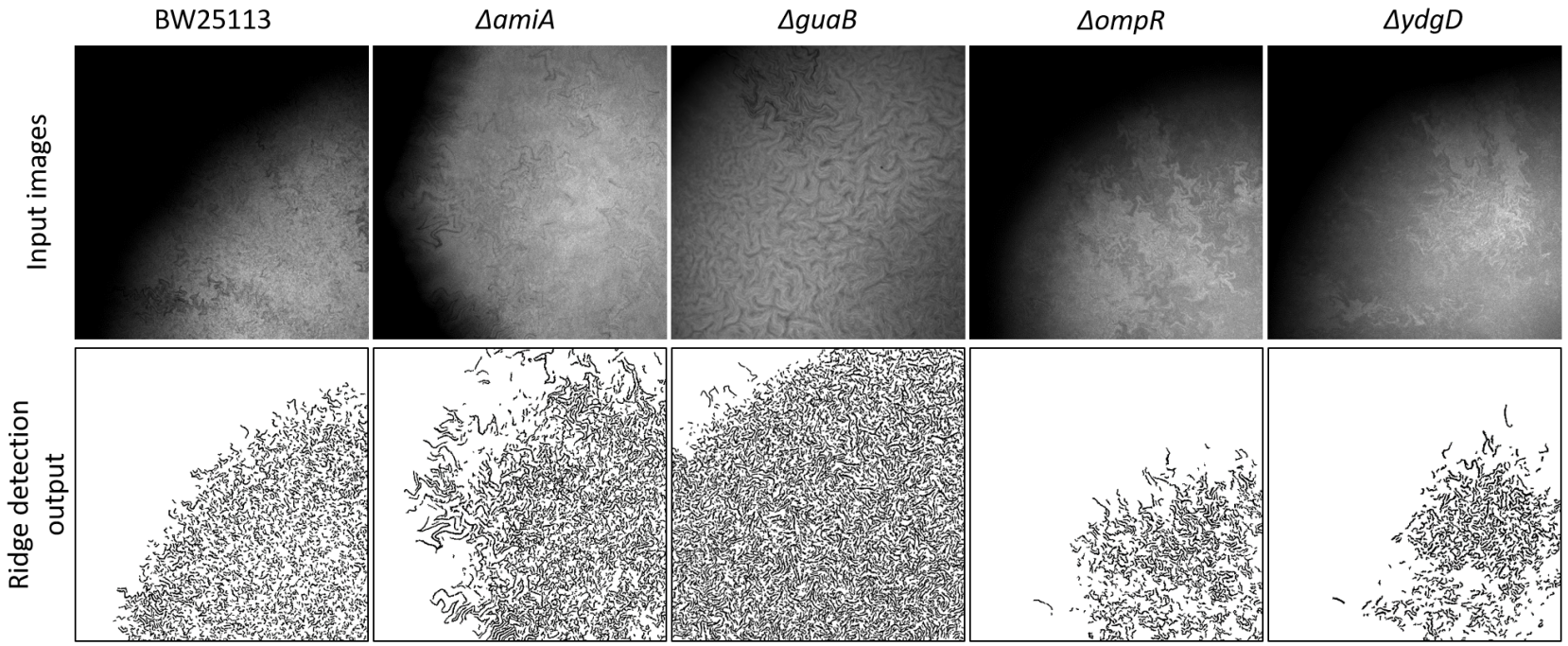

Figure 3.8: Ridge detection performed on a sample set of Keio mutant biofilm images. The input images were acquired on an Olympus IX81 confocal microscope coupled to a FluoView FV1000 confocal laser scanning unit (Olympus, Japan) using a 10×/0.4 objective lens.

endpoints in the image. twombli was run with the following parameters: line width 10, curvature window 50, minimum branch length 10, maximum display HDM 255.

A sample image of a JM105 mini-Tn7-*gfp* biofilm grown on M9 agar was also analysed directly with twombli in order to obtain fractal geometry parameters (Figure 3.9). The image was acquired with the Mesolens in epi-fluorescence mode as described in Section 2.2.3 of Chapter 2. Before the analysis, the image was deconvolved using the proprietary Huygens Professional version 19.04 software

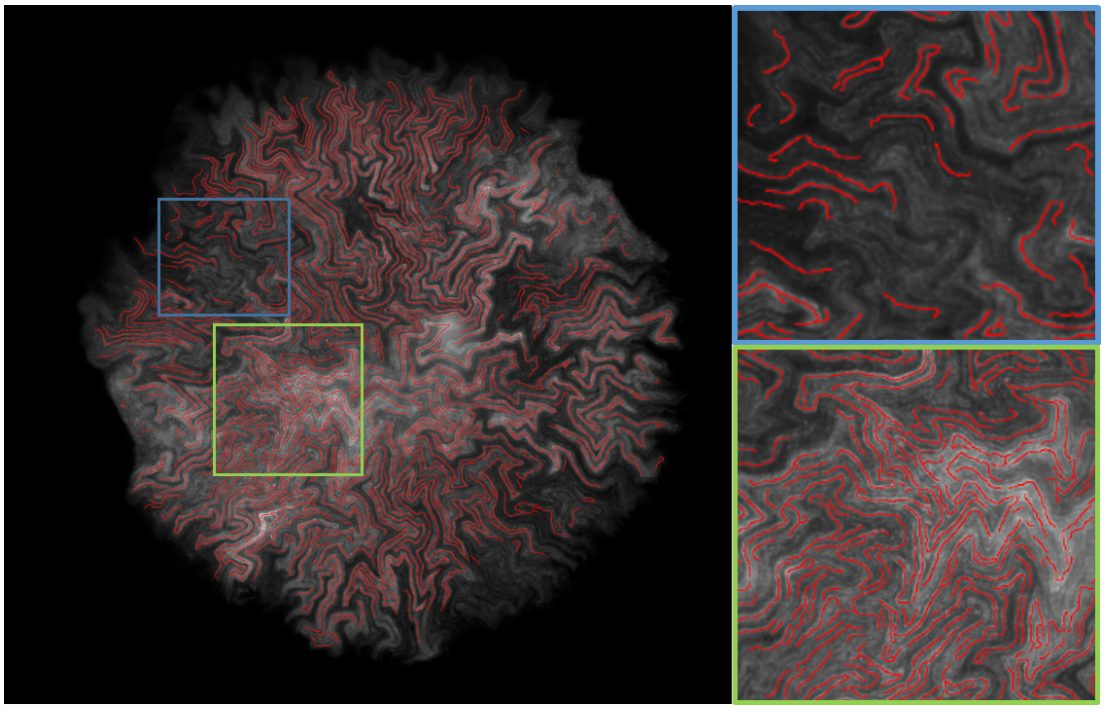

Figure 3.9: twombli mask (red lines) applied to the JM105 mini-Tn7-*gfp* input image. The plugin reliably captures most of the fractal patterns in the biofilm. When the contrast between dark channels and the surrounding bright biofilm cells is low, some channels are missed (blue panel), or broken into multiple channel branches (green panel).

(Scientific Volume Imaging, Netherlands) with Classic Maximum Likelihood Estimation method with 50 iterations, a signal-to-noise ratio of 40 and a quality threshold of 0.01, and despeckled using FIJI.

3.2.9.2 ComsystanJ

Fractal complexity was also quantified using the FIJI plugin ComsystanJ (version 1.0.0). The "2D image" version of the plugin was used on the Olympus IX81 confocal microscopy images acquired with a $10\times/0.4$ lens, all of which had a size of 2048×2048 pixels. Box-counting fractal dimension was calculated using the Relative Differential Box Counting (RDBC) dimension algorithm developed by Jin et al. [367] and described in Section 3.1.2, which uses a raster box scanning method. The plugin was run with 12 boxes and 1-12 regressions.

Firstly, four sets of sample images were analysed (Figure 3.10). Three of the sets were generated as greyscale images through ComsystanJ using the "2D image Image Generator" option, with image types "Constant", "Fractal random shapes – Lines" and "Random". Constant images had a constant pixel intensity value (256) throughout each image. Line images were made of light (pixel intensity = 256) lines with varying thickness randomly intersecting on a dark (pixel intensity = 0) background. Fractal images were obtained from the "Wikimedia commons" open-source image repository [417]–[421]. Finally, in "Random" images every pixel had a random intensity value (between 0 and 256).

Constant images had a RDBC dimension of 0 due to the lack of spatial features, whereas the RDBC dimension of images comprised of straight lines ranged between 2.114 ± 0.032 and 2.213 ± 0.043 (mean $\pm$ standard deviation). The RDBC dimension for computer-generated fractal images were calculated as between 2.329 ± 0.041 and 2.702 ± 0.047, and images of randomised features had

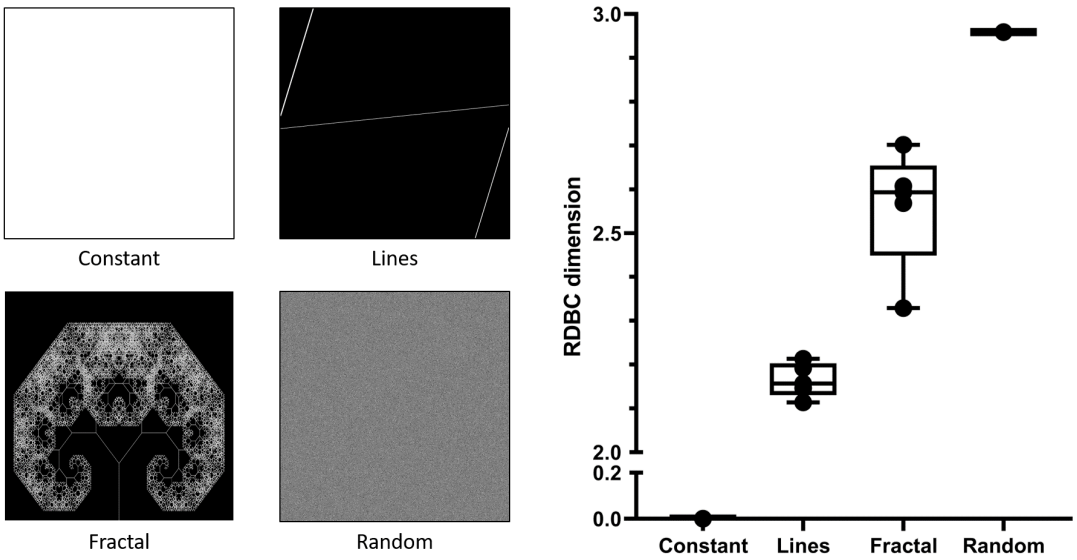

Figure 3.10: (left four panels) Representative images from the sets used for benchmarking of box-counting dimension calculations (right panel). Each set consists of five images, whose fractal complexity is calculated using ComsystanJ. The "Constant", "Lines" and "Random" images are generated from ComsystanJ, whereas the "Fractal" images are reproduced from open-source image repositories [417]–[421]. Increasing complexity in the image sets is reflected by an increase in box-counting dimension, which ranges between 2.329 ± 0.041 and 2.702 ± 0.047 for fractal images.

a RDBC dimension equal to 2.959, which was close to the theoretically possible maximum of 3.000. This is because the RDBC method is sensitive to big changes in greyscale values at very short length scales, which are typical of randomised images.

For biofilm fractal pattern analysis, z-stacks were converted to 8-bit. No contrast-adjustment was used on the images prior to analysis in order to preserve the original greyscale values of each image.

3.2.10 Statistical analysis

Statistical tests were carried out on Prism version 8.0.2 (GraphPad Software, USA). The distribution of each dataset was first checked by plotting a histogram of the data and performing a Normality & Lognormality test, in order to identify the appropriate statistical test to be used.

Cell measurements (length and width) of the mutant strains were compared to those of the parental strain BW25113 using a Kruskal-Wallis nonparametric test, which does not assume a Gaussian distribution of the data, but assumes identical distribution shape between datasets [422]. One-way ANOVA tests were used to compare box-counting dimensions between strains and growth media conditions.

In the main text and figure captions, values are presented as mean ± standard deviation. In all plots, produced using Prism version 8.0.2, p-values are presented as * ($p < 0.05$); ** ($p < 0.005$); *** ($p < 0.0005$); **** ($p < 0.0001$), with specific p-values written in the figure captions.

3.3 Results

3.3.1 The genotype of Keio mutants is confirmed by diagnostic PCR experiments and amplicon sequencing

Agarose gels from PCR experiments performed using the Keio primers k1 and k2 on the DNA extracted from BW25113, $\Delta amiA$ and $\Delta ydgD$ strains are shown in Figure 3.11. The agarose gel pictures showed an anomalous feature: a 1.2 kb portion of the genome of the parental strain BW25113 was amplified by the Keio primers. This was unexpected, since the parental strain is not known to be kanamycin resistant (this was checked by streaking a frozen glycerol stock

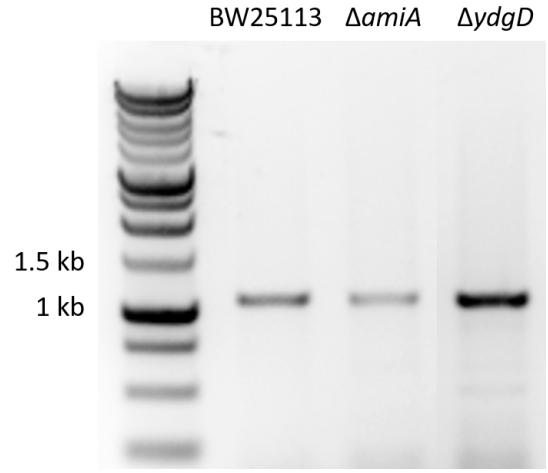

Figure 3.11: Agarose gels obtained from the PCR reactions using the k1 and k2 primers (specific to the kanamycin resistance cassette), with annealing temperature of 65 °C. The genomic DNA used for each reaction is indicated above each band. The parental strain's DNA is unexpectedly amplified by the k1 and k2 primers, resulting in a 1.1 kb band.

on LB solid plates with kanamycin added). Nonetheless, this result was obtained consistently across 10 experimental PCR repeats, carried out with different annealing temperatures. The complete genome of the BW25113 strain (GenBank: CP009273.1) and the sequence of the pAJR145 plasmid DNA (from plasmid pAJR145, [410]) were checked for regions of non-specific binding with the primers, but none were found. The Keio primers were also re-ordered and used in a new PCR experiment, and the genomic DNA was re-extracted from a new sample to rule out contamination.

The agarose gel from PCRs using gene-specific primers is shown in Figure 3.12. The predicted bands were observed for all four mutant strains. *amiA* primers showed a 900 bp band (theoretical: 978 bp) for the parental strain and a 1.5 kb band for the mutant strain. The *guaB* primers showed a 1.4 kb band (theoretical:

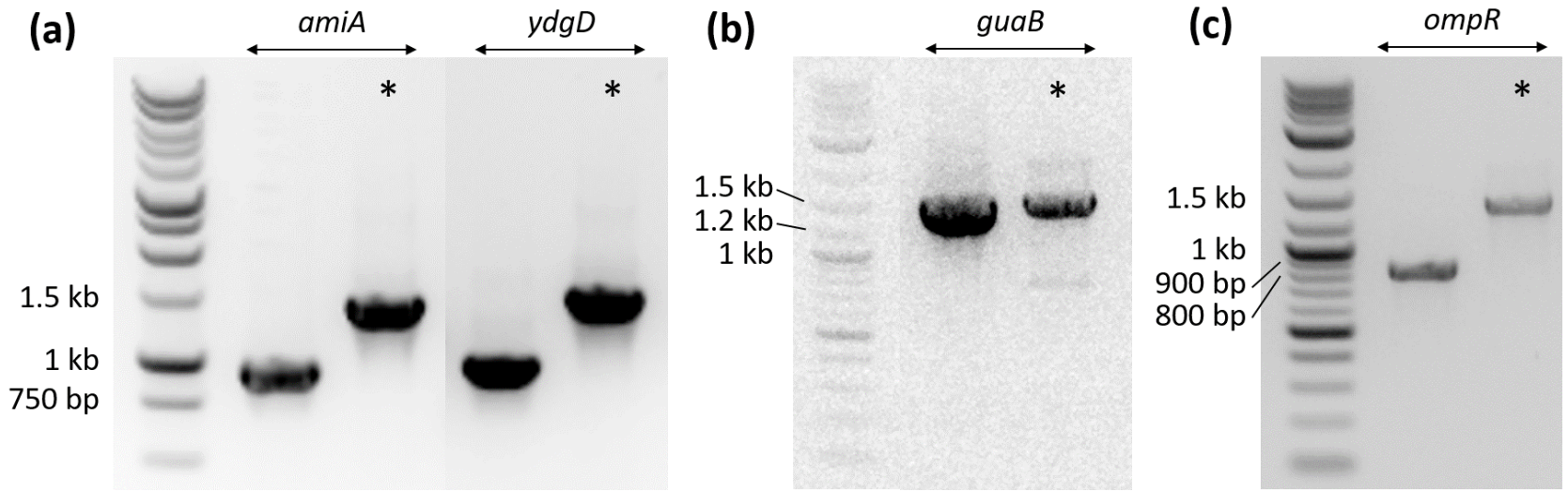

Figure 3.12: Agarose gels obtained from PCR experiments carried out using gene-specific primers *amiA* and *ydgD* (a), *guaB* (b) and *ompR* (c), with annealing temperature 66 °C. The primers used for each reaction are indicated above the gel columns. For each pair of gel columns using the same primer pair, the column on the left corresponds to the BW25113 parental strain gDNA, whereas the column on the right (*) includes gDNA from the corresponding gene knockout strain.

1636 bp) for the parental strain and a 1.5 kb band for the mutant strain, while the *ompR* primers showed a 850 bp band (theoretical: 864 bp) for the parental strain and a 1.4 kb band for the mutant strain. The *ydgD* primers showed a 900 bp band (theoretical: 896 bp) for the parental strain and a 1.3 kb band for the mutant strain.

Amplicon sequencing of the PCR products obtained with gene-specific primers confirmed the deletion of the appropriate DNA fragments within the genes *amiA*, *guaB*, *ompR* and *ydgD* for the strains BW25113 Δ*amiA*, BW25113 Δ*guaB*, BW25113 Δ*ompR* and BW25113 Δ*ydgD* respectively. Gene-specific primers annealed in the correct regions upstream and downstream to each gene of interest in the parental strain, and they amplified the kanamycin resistance cassette disrupting each gene of interest in the mutant strains. The DNA amplicon sequences are provided in Appendix C together with the alignment to the genotype of the BW25113 strain on BLAST.

3.3.2 Phenotypic changes in *E. coli* cell shape are confirmed by cell length and width measurements

Individual cells from each Keio mutant strain were first imaged using phase contrast microscopy to visually confirm their reported morphological phenotype (Figure 3.13). Single cells were analysed with MicrobeJ as described in the Methods to extract length and width of individual segmented cells. For the non-fluorescent strains, the number of segmented cells were 487 (BW25113), 562 (Δ*amiA*), 665 (Δ*guaB*), 238 (Δ*ompR*) and 618 (Δ*ydgD*). For the GFP-fluorescent strains, the number of segmented cells were 214 (BW25113), 90 (Δ*amiA*), 524 (Δ*guaB*), 160 (Δ*ompR*) and 120 (Δ*ydgD*). Cell length and width were compared to the measurements of the parental strain BW25113 for quantitative phenotypic analysis.

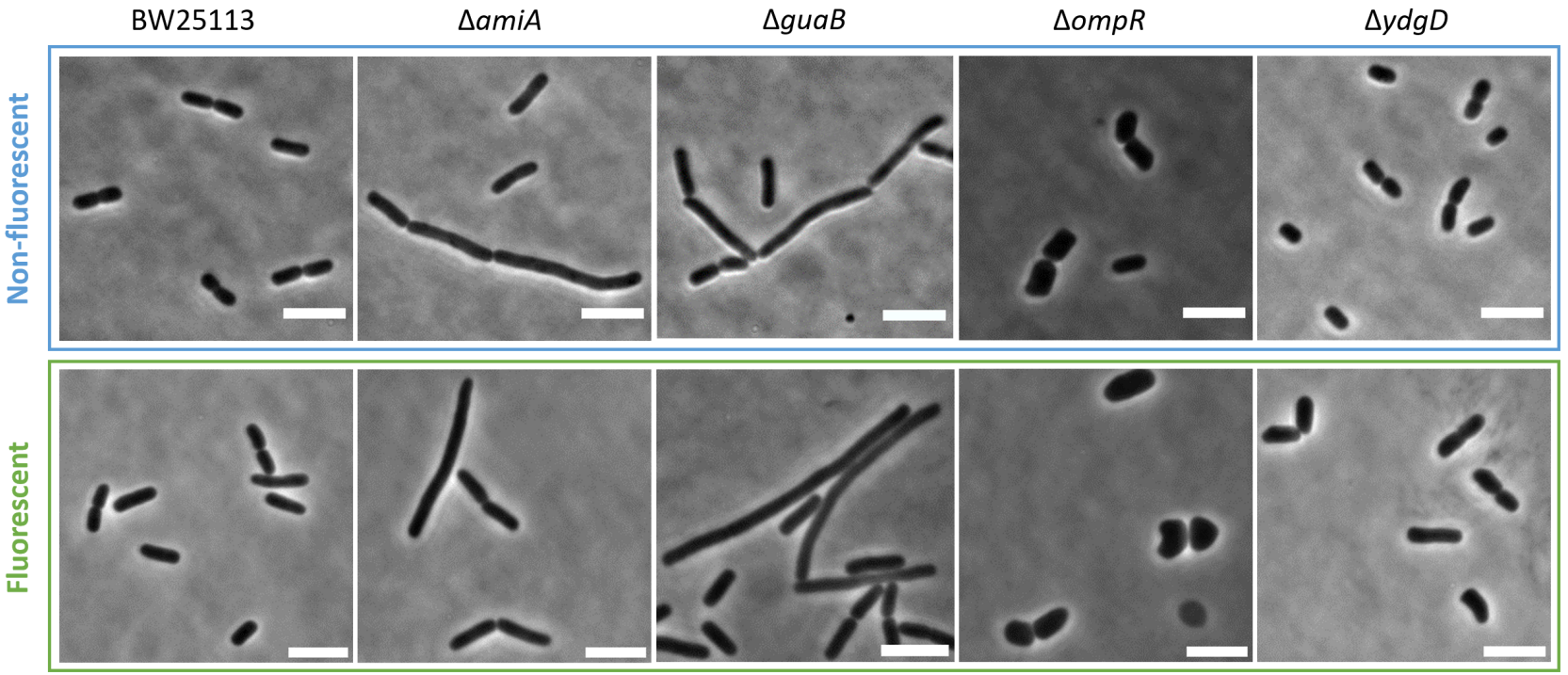

Figure 3.13: Phase contrast single-cell images of the Keio parental strain BW25113 and of four cell-shape mutant strains, showing long ($\Delta amiA$ and $\Delta guaB$) and wide ($\Delta ompR$ and $\Delta ydgD$) phenotypes. Images were acquired with a 100×/1.30 oil immersion lens, for both non-fluorescent and fluorescent strains. Scale bars: 5 μm.

Upon visual inspection of the phase contrast microscopy images, the cell phenotypes appeared consistent with the genotype expectations. Cell length and width, both for the fluorescent and non-fluorescent strains, are shown in Figure 3.14. Δ*amiA* fluorescent cells had an average length of 4.614 ± 1.640 μm, which was longer than that of the parental strain, 3.441 ± 0.803 μm ($p = 3.48 \times 10^{-11}$). Δ*guaB* fluorescent cells were also longer (4.728 ± 5.027 μm) than the parental strain ($p = 2.56 \times 10^{-9}$). Δ*ompR* fluorescent cells had above-average width of 1.582 ± 0.336 μm (compared to the parental strain's 1.066 ± 0.112 μm, $p = 5.16 \times 10^{-39}$). Δ*ydgD* fluorescent cells had a wide phenotype, with average width 1.313 ± 0.221 μm (larger than the width of the parental strain, $p = 3.81 \times 10^{-28}$). Cell measurements are reported here as mean ± standard deviation, and the width of data distribution explains the large uncertainties associated with average measurements. The phenotypes reported in this work are consistent with reports from the Keio collection documentation [401].

3.3.3 Cell shape affects *E. coli* biofilm morphology

Biofilm images of Keio parental and mutant strains acquired with the Mesolens and with an Olympus IX81 confocal microscope using a 4×/0.1 N.A. lens are comparatively shown in Figure 3.15. To resolve nutrient-transporting channels, biofilms formed by the Keio parental strain BW25113, as well as by the mutants Δ*amiA*, Δ*guaB*, Δ*ompR* and Δ*ydgD*, were acquired with an Olympus IX81 confocal microscope on a 10×/0.4 N.A. lens on LB and M9 medium agar substrates (Figure 3.16).

Confocal microscopy of the biofilm structures revealed a complex network of intra-colony channels as previously reported in *E. coli* JM105 [209], [294]. Biofilms

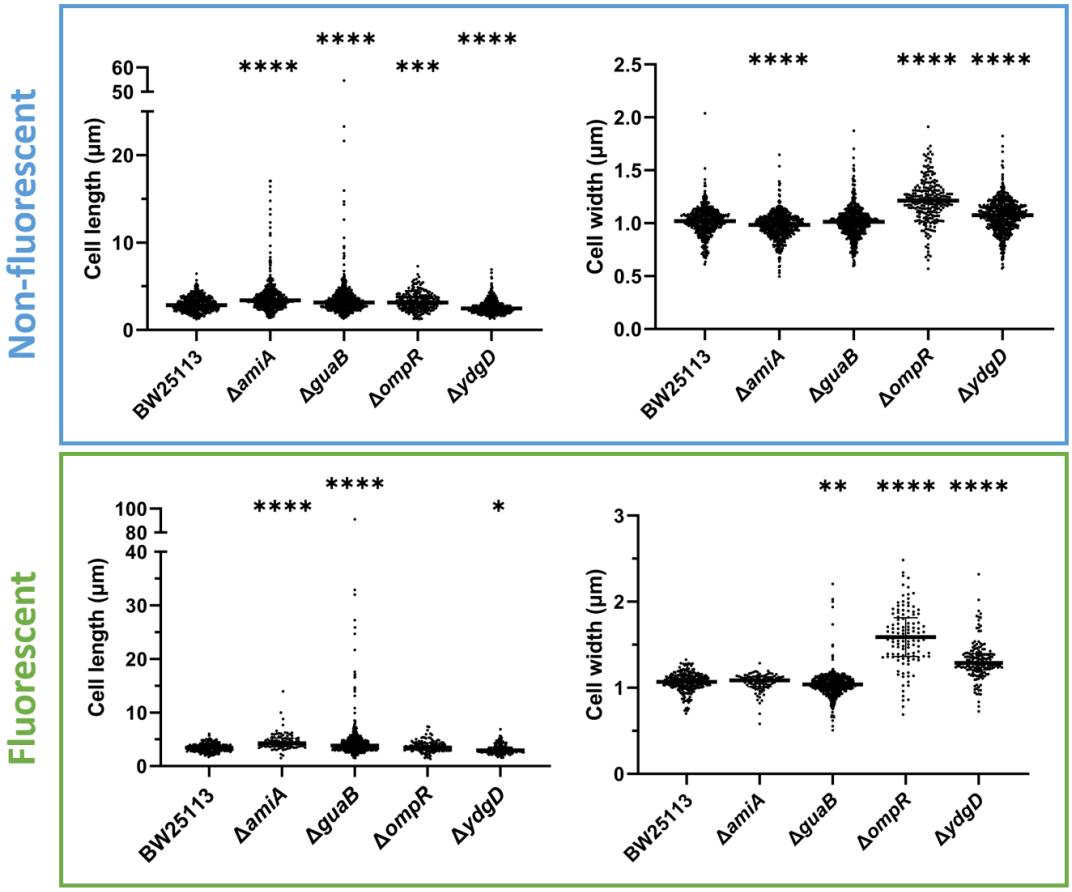

Figure 3.14: Cell length and width measurements of Keio mutant strains obtained from phase contrast images analysed with MicrobeJ. Measurements are shown for fluorescent (green panel) and non-fluorescent (blue panel) strains. Δ*amiA* cells were long (p = 1.34 $\times 10^{-18}$ for non-fluorescent cells and p = 3.48 $\times 10^{-11}$ for fluorescent cells). Δ*guaB* cells were long (p = 3.44 $\times 10^{-7}$ for non-fluorescent cells and p = 2.56 $\times 10^{-9}$ for fluorescent cells). Δ*ompR* cells were wide (p = 3.39 $\times 10^{-42}$ for non-fluorescent cells and p = 5.16 $\times 10^{-39}$ for fluorescent cells). Δ*ydgD* cells were short (p = 2.78 $\times 10^{-11}$ for non-fluorescent cells and p = 0.0134 for fluorescent cells) and wide (p = 1.84 $\times 10^{-10}$ for non-fluorescent cells and p = 3.81 $\times 10^{-28}$ for fluorescent cells). Horizontal lines denote the median of each dataset, and asterisks represent statistical significance between each mutant strain and the parental strain, with average values compared using a Kruskal-Wallis statistical test.

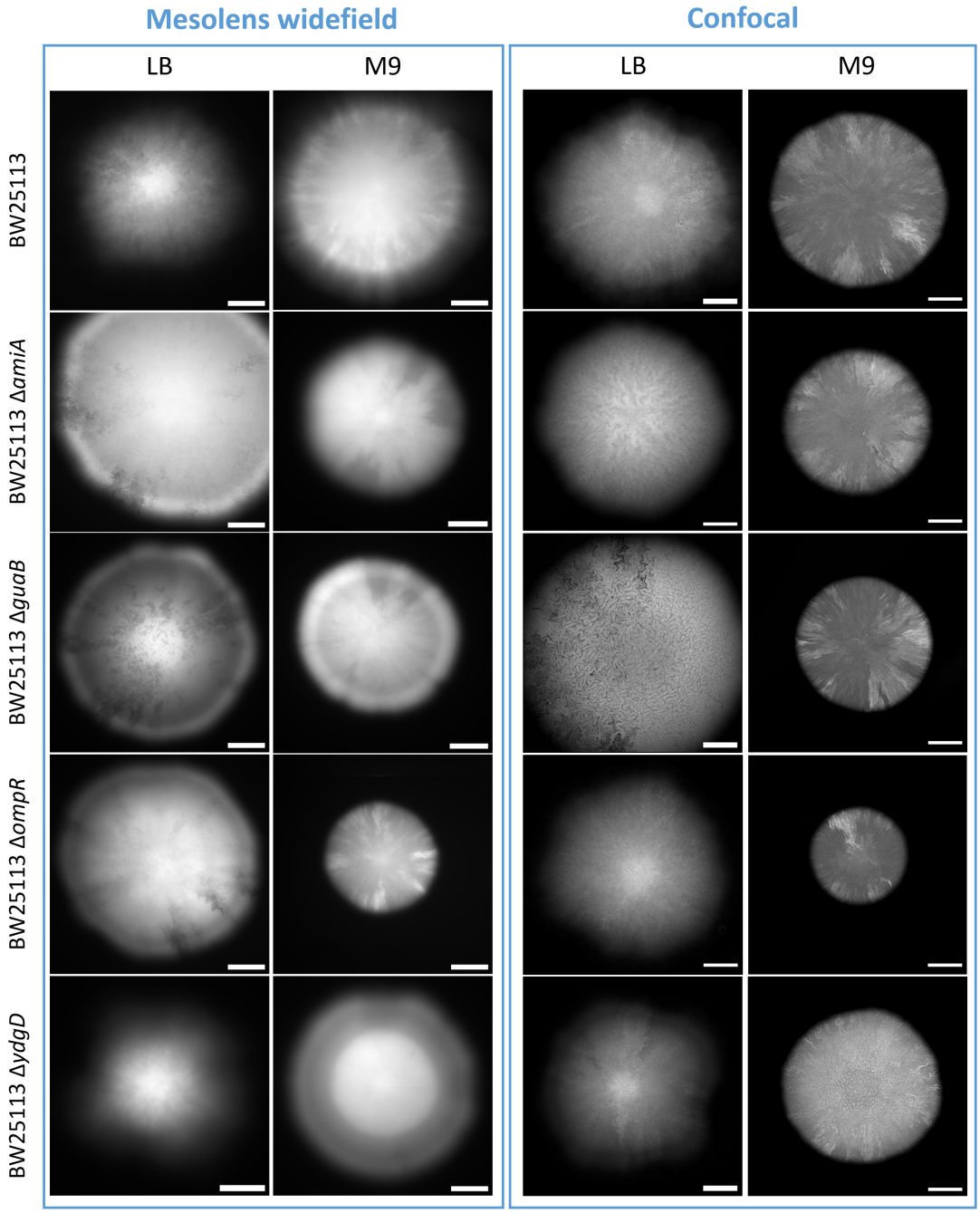

Figure 3.15: Keio mutant biofilms imaged with the Mesolens (left panel) and with an Olympus IX81 confocal microscope (right panel). Images acquired with the Mesolens show poor resolution due to the absence of both mounting medium and lens immersion. Scale bars: 500 μm.

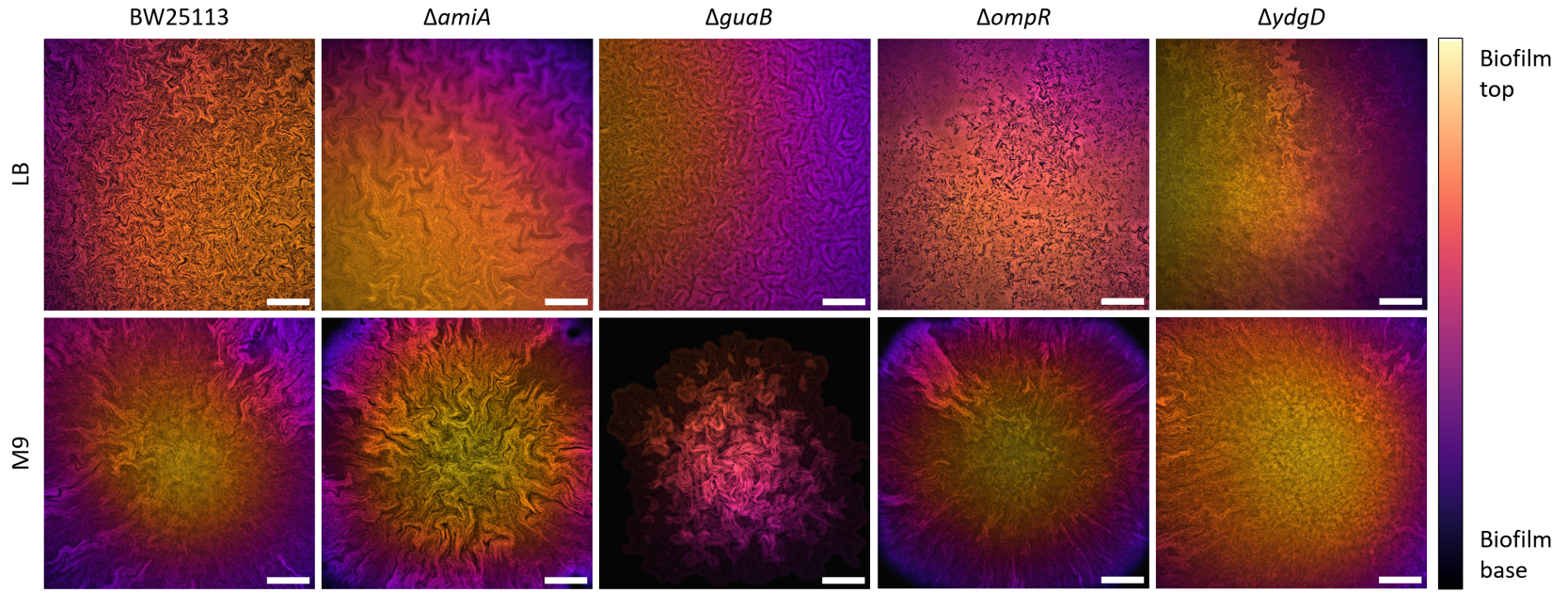

Figure 3.16: Representative confocal microscopy images showing the morphology of biofilms formed by the strains BW25113, Δ*amiA*, Δ*guaB*, Δ*ompR* and Δ*ydgD* when growing on LB (rich) or M9 (minimal) solid medium. Images are projections of z-stacks acquired with 5 μm slice spacing, colour-coded by depth. Scale bars: 200 μm.

formed on minimal medium exhibited sectoring, with large areas of low fluorescence intensity across the biofilm volume, and channels appeared less morphologically complex than in their rich medium counterparts. This was particularly evident in the Δ*ompR* strain, where channels expand radially outwards in approximately straight lines, reminiscent of strain boundaries observed between isogenic domains in biofilms formed by spherical mutants of *E. coli* [375]. On rich medium, channels had more complex arrangements - in particular, channels formed by the Δ*amiA* strain were made up of long (≥10 μm) segments, consistent with the long cell phenotype of the constituent cells. In Δ*amiA* biofilms, channel width appeared uniform and changes in channel direction occurred at regular intervals of approximately 50 to 100 μm. Wide channels also appeared regularly interspaced by at least 50 μm within the biofilm volume, and their density increased towards the edge of the biofilm. Channels formed by the Δ*ompR* mutant strain, on the other hand, appeared fragmented, likely owing to the bulgy morphology of the constituent cells.

Interestingly, while Δ*guaB* exhibited a long cell phenotype similar to that of Δ*amiA*, it formed biofilms with distinctly different morphology, with cells tightly packed together leaving little space for nutrient-transporting channels. On rich medium, Δ*guaB* biofilms were dome-shaped, with uniformly distributed channels. On minimal medium, the biofilms did not exhibit the typical sectoring patterns, and cells were arranged in structures reminiscent of the Van Gogh bundles observed in *B. subtilis* [423], seemingly originating from the centre of each biofilm. Furthermore, the 3D biofilm morphology was irregular, with thicker areas interspersed towards the otherwise thin biofilm edge.

Finally, despite both Δ*ompR* and Δ*ydgD* strains having a wide cell phenotype, their biofilms had different internal morphologies when grown on rich medium.

Δ*ompR* formed darker channels, which were clearly distinguishable from the surrounding cells within the biofilm. On minimal medium, the central region of Δ*ydgD* biofilms appeared devoid of channels, whereas the edges showed radially expanding channels highly similar to those observed at the edges of Δ*ompR* biofilms. Enlarged regions of interest showing channel morphology are shown in Figure 3.17.

3.3.4 Internal patterns in *E. coli* biofilms are fractal

3.3.4.1 twombli

The twombli image analysis pipeline was used on biofilm images of the Keio parental and mutant strains grown on LB medium, acquired with an Olympus IX81 confocal microscope. For each strain, 10 images were used to calculate the following fractal geometry parameters: box-counting dimension, lacunarity, total channel length, and number of branchpoints per unit length (Figure 3.18).

The long-cell strain Δ*guaB* had a significantly higher box-counting dimension (1.423 ± 0.070) than either of the wide-cell strains Δ*ompR* (box-counting dimension: 1.303 ± 0.076, $p = 0.0008$) and Δ*ydgD* (box-counting dimension: 1.334 ± 0.050, $p = 0.0215$). The lacunarity of Δ*guaB* was also considerably lower than the wide-cell strains Δ*ompR* ($p = 0.0002$) and Δ*ydgD* ($p = 0.0009$). The channels formed by the Δ*guaB* strain had the largest total length (87.08 ± 13.68 mm), over 70% longer than channels formed by the parental strain (50.56 ± 24.22 mm, $p = 0.0004$) and by Δ*amiA* (46.23 ± 24.57, $p = 6.50 \times 10^{-5}$), and over three times longer than channels formed by Δ*ompR* (28.70 ± 12.52, $p = 3.98 \times 10^{-8}$) and Δ*ydgD* (28.58 ± 8.79, $p = 3.79 \times 10^{-8}$). Despite this, the number of branchpoints per unit length was approximately constant across all strains, with averages of

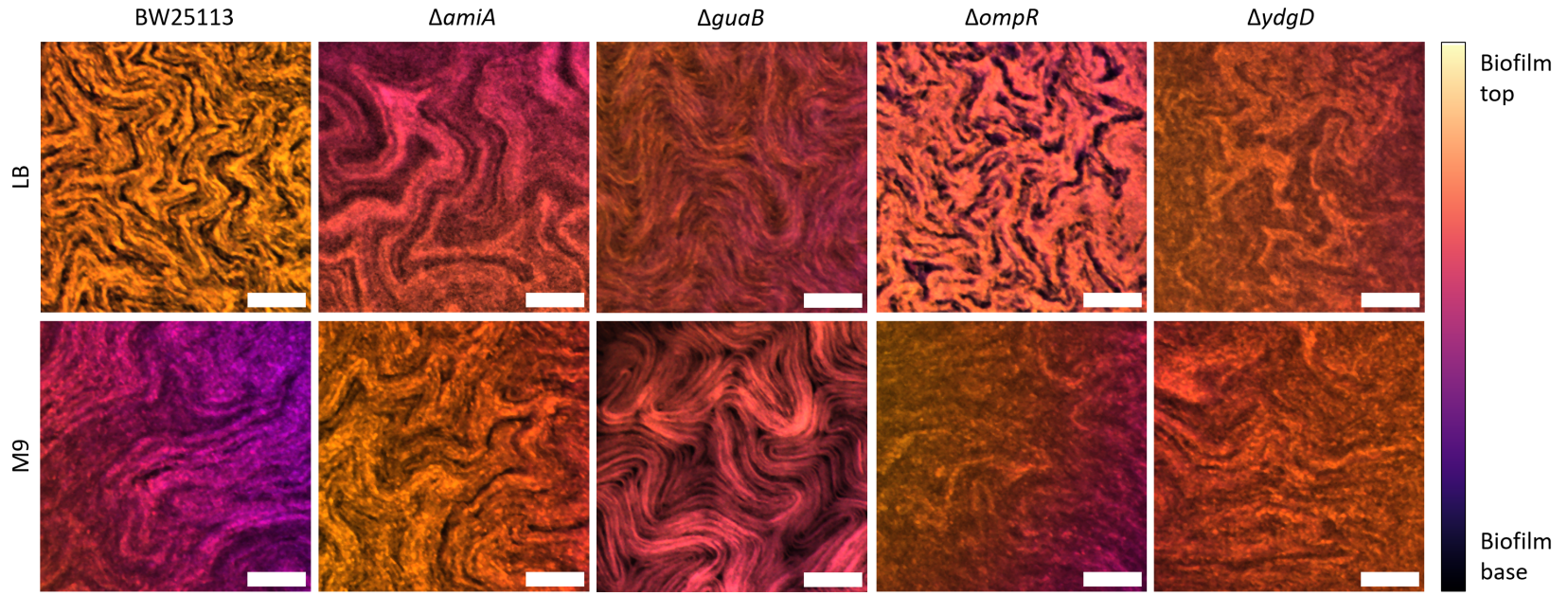

Figure 3.17: Representative regions of interest (ROIs) from the confocal microscopy images shown in Figure 3.16. Scale bars: 50 μm.

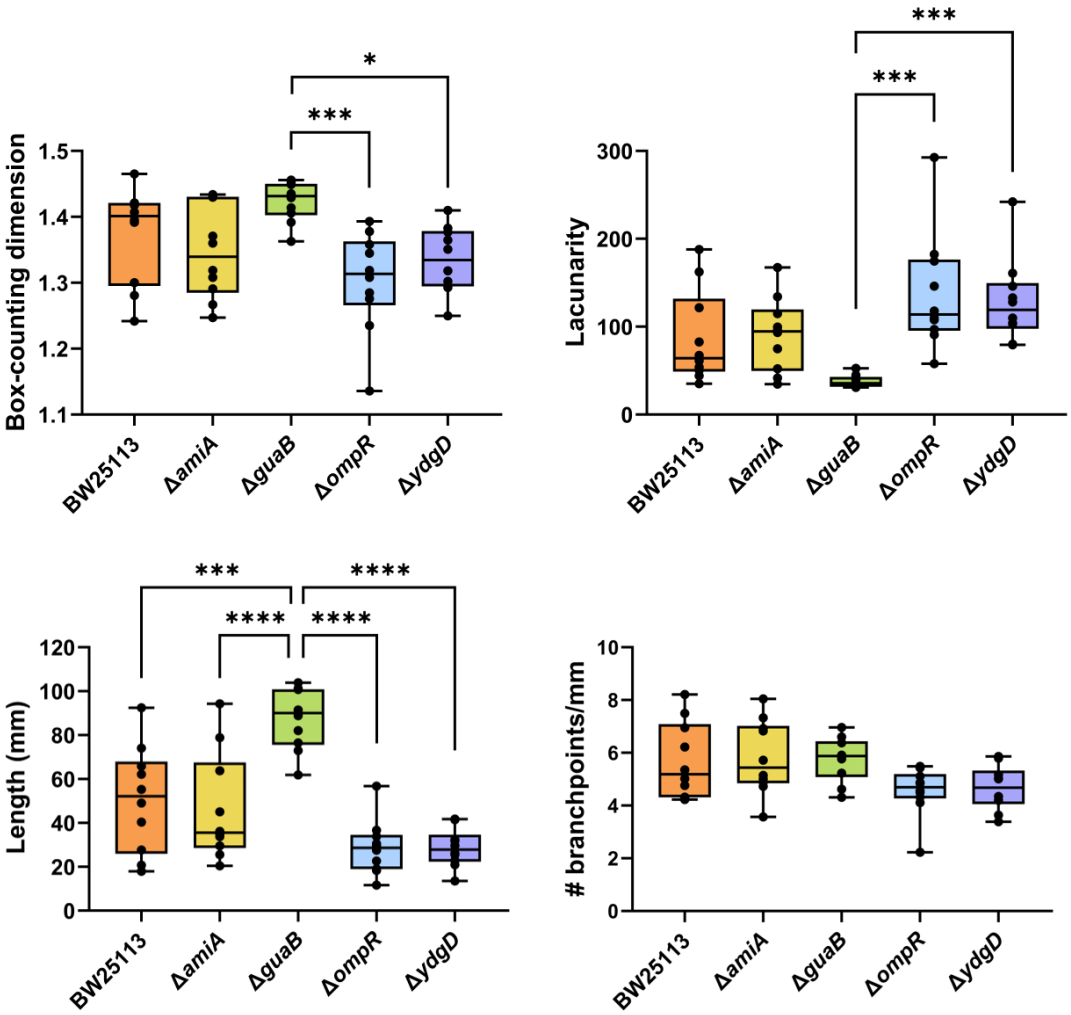

Figure 3.18: Fractal geometry measurements of the *E. coli* strains BW25113, Δ*amiA*, Δ*guaB*, Δ*ompR* and Δ*ydgD* calculated using twombli. Δ*guaB* has higher box-counting dimension than both wide-cell strains Δ*ompR* (p = 0.0008) and Δ*ydgD* (p = 0.0215), and lower lacunarity (p = 0.0002 and 0.0009 respectively). Channels formed by the Δ*guaB* strain are longer than those formed by any other strain (BW25113: p = 0.0004; Δ*amiA*: p = 6.50 $\times 10^{-5}$; Δ*ompR*: p = 3.98 $\times 10^{-8}$; Δ*ydgD*: p = 3.79 $\times 10^{-8}$).

5.687 ± 1.448 (BW25113), 5.819 ± 1.403 (Δ*amiA*), 5.755 ± 0.834 (Δ*guaB*), 4.546 ± 0.932 (Δ*ompR*) and 4.665 ± 0.846 (Δ*ydgD*).

These results suggest that cell shape does not uniquely determine biofilm fractal complexity. While the two strains with a wide-cell phenotype, Δ*ompR* and Δ*ydgD*, form biofilms with comparable fractal geometry descriptors, the strains with a long-shape phenotype, Δ*amiA* and Δ*guaB*, have distinct fractal complexities. In fact, the parental strain BW25113 and the Δ*amiA* mutant produced similar fractal measurement distributions. Interestingly, lacunarity and box-counting fractal dimension appeared to be inversely related. Nonetheless, the lower lacunarity values observed for the Δ*guaB* strain could be explained by the reduced amount of background present in Δ*guaB* biofilm images (Figure 3.8).

3.3.4.2 ComsystanJ

After obtaining benchmark values for fractal complexity on ComsystanJ as described in Section 3.2.9.2, confocal microscopy images of biofilms were analysed using the same image analysis pipeline to investigate the effect of cell shape and growth medium on the complexity of internal biofilm patterns (Figure 3.19). RDBC dimension values obtained from biofilm images fully aligned with those calculated for the set of computer-generated fractal images, with a minimum of 2.488 and a maximum of 2.620. This finding confirms that channel structures in *E. coli* biofilms can be described using fractal geometry.

On rich medium, biofilms formed by the Δ*amiA* mutant strain showed increased fractal complexity (RDBC = 2.578 ± 0.009) when compared to biofilms formed by Δ*ydgD* (RDBC = 2.553 ± 0.009, p = 0.0277). This reflects the peculiar channel architecture exhibited by Δ*amiA* biofilms grown on LB medium (Figure 3.16). On minimal medium, the parental strain BW25113 formed more complex

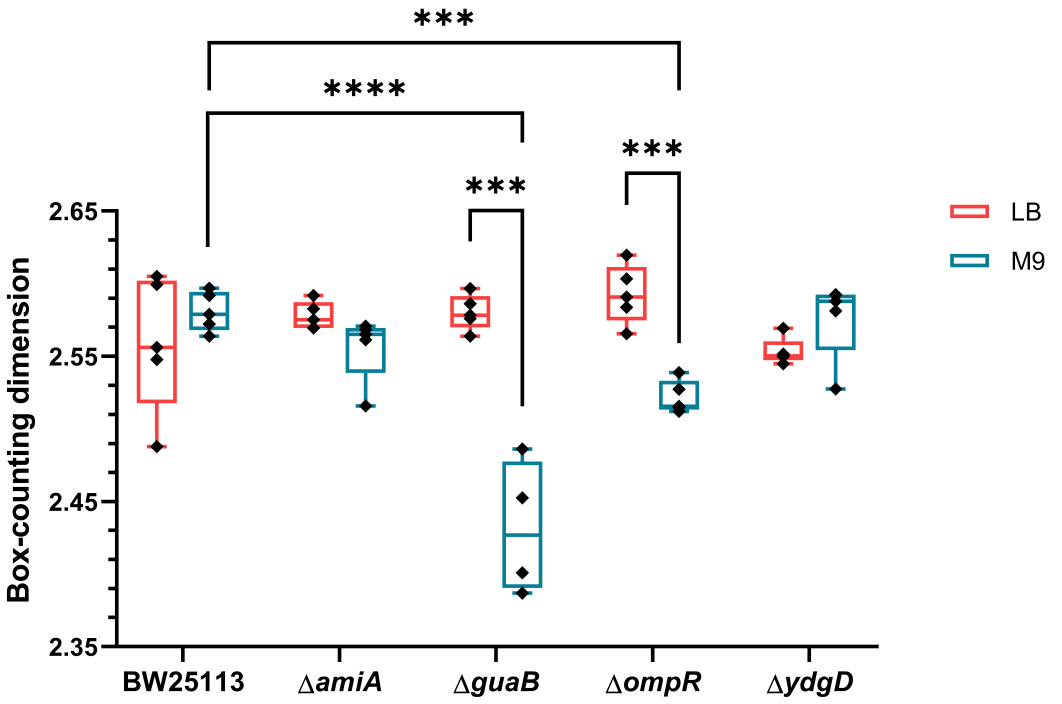

Figure 3.19: Box-counting dimension calculated for each biofilm image (n = 5 for each condition). On minimal medium (M9), biofilms formed by Δ*guaB* and Δ*ompR* mutant strains are less morphologically complex than those formed by the parental strain (p = 4.33×10^{-8} and p = 0.0005 respectively). For the Δ*guaB* and Δ*ompR* mutant strains, the fractal complexity is strongly affected by the growth substrate composition, with biofilms grown on rich medium (LB) showing significantly more complexity than those grown on minimal medium (p = 0.0006, Δ*guaB* and p = 0.0008, Δ*ompR*). Average values are compared using one-way ANOVA tests.

biofilms (RDBC = 2.581 ± 0.014) than both the Δ*guaB* mutant (RDBC = 2.432 ± 0.046, p = 4.33×10^{-8}) and Δ*ompR* mutant (RDBC = 2.522 ± 0.011, p = 0.0005). Biofilms formed by the mutant Δ*ydgD* were also less complex (RDBC = 2.576 ± 0.028) than those formed by Δ*ompR* (p = 0.0013), despite them having the same cell shape phenotype.

From the image data presented in Figure 3.16, growth on minimal media was objectively correlated with large, dark sectors within the biofilm, which was hypothesised to result in a lower fractal complexity. However, quantifying channel morphology through RDBC dimension and comparing each strain grown on the two different growth media revealed no statistical difference. While this was not the case for the Δ*amiA* and Δ*ydgD* strains, growth in minimal medium was associated with significantly lower morphological complexity than growth in rich medium for Δ*guaB* ($p = 0.0006$) and Δ*ompR* ($p = 0.0008$). Possible reasons for these findings are investigated in more detail in the following sections.

3.3.5 Growth medium composition affects the complexity of biofilms formed by the Δ*ompR* mutant strain

The role of medium composition on the internal morphology of biofilms formed by the Δ*ompR* mutant strain was further investigated by comparing biofilms grown on LB and M9 substrates with different chemical compositions (Figure 3.20). The RDBC dimension of biofilms grown in rich medium decreased considerably when the substrate was made softer by halving the amount of agar ($p = 0.0117$). On minimal medium, on the other hand, growth on soft (1% agar) substrates was associated with a significant increase in RDBC dimension, comparable to that of biofilms grown on rich medium ($p = 2.39 \times 10^{-7}$). Secondly, a reduction in RDBC dimension was observed when the osmolality of the medium was reduced by removing salt, both in rich medium ($p = 4.88 \times 10^{-5}$) and in minimal medium ($p = 0.0209$).

Furthermore, increasing glucose amounts in minimal medium led to an increase in RDBC from 2.376 ± 0.007 (0.02% glucose) to 2.503 ± 0.032 (0.2% glucose, $p = 4.81 \times 10^{-11}$) to 2.543 ± 0.005 (0.5% glucose, $p = 0.0478$). In the Δ*ompR* mutant

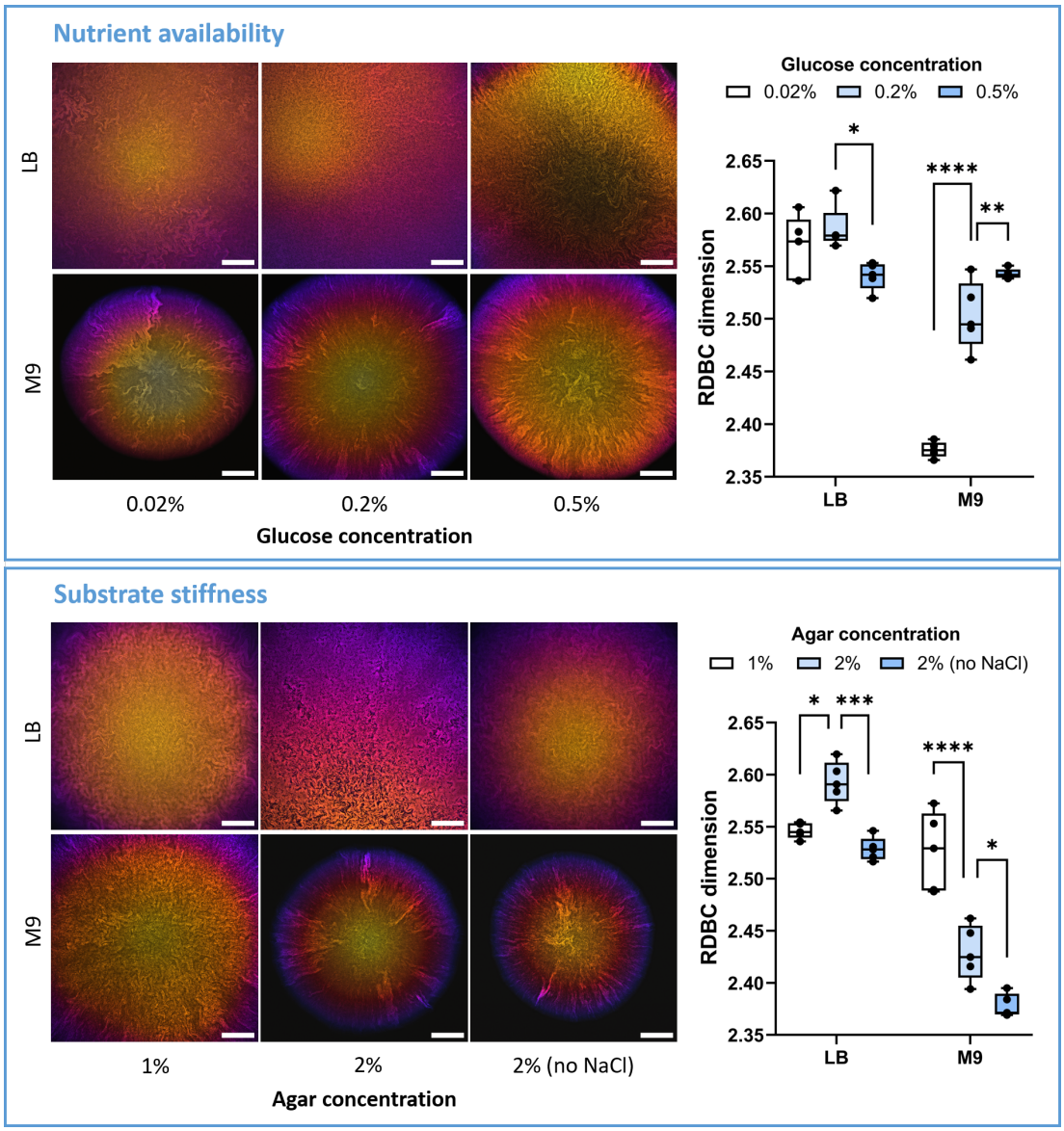

Figure 3.20: Morphology and fractal complexity of biofilms formed by the Δ*ompR* strain grown on solid substrates with different glucose and agar concentrations. Glucose concentration in the medium is particularly important for the complexity of biofilms grown on minimal media (M9): RDBC dimension increases when glucose levels are increased from 0.02% to 0.2% ($p = 4.81 \times 10^{-11}$) and from 0.2% to 0.5% ($p = 0.0478$). On rich medium (LB), conversely, the addition of glucose does not significantly affect biofilm fractal complexity: only a small reduction in RDBC dimension is observed between 0.2% and 0.5% added glucose ($p = 0.0166$). *Continues onto the next page*

Figure 3.20: *(Continued)* The presence of salt in the growth medium increases morphological complexity for both rich and minimal media ($p = 7.34 \times 10^{-4}$ and $p = 0.0209$ respectively). Finally, a reduction in substrate stiffness from 2% to 1% agar concentration leads to a decrease in complexity on rich medium ($p = 0.0365$) and an increase in complexity on minimal medium ($p = 2.39 \times 10^{-7}$). Average values are compared using one-way ANOVA tests. Scale bars: 200 μm.

strain, this increase in RDBC dimension coincides with the gradual disappearance of colony sectoring, as a consequence of the increase in nutrient levels. As expected, the addition of the same amounts of glucose to rich medium did not lead to any significant changes in biofilm morphological complexity, with RDBC dimensions ($2.520 <$ RDBC < 2.622) comparable to those found in normal rich medium with no glucose ($2.566 <$ RDBC dimension < 2.620).

While the diameter of biofilms formed by the $\Delta ompR$ mutant strain increased with glucose concentration and decreased with agar concentration, the presence of dark background in images of smaller biofilms did not significantly affect the resulting RDBC dimension. This was checked by digitally zooming into images of the biofilms grown on 0.02% glucose, which had the smallest area, until they filled the image field of view (corresponding to an area of 1615 $\times$ 1615 pixels in the original images), and calculating their RDBC dimension after re-scaling the images to 2048 $\times$ 2048 pixels. The resulting RDBC value was calculated as 2.373 $\pm$ 0.006, a decrease of only 0.1% compared to the original biofilm images (Figure 3.21).

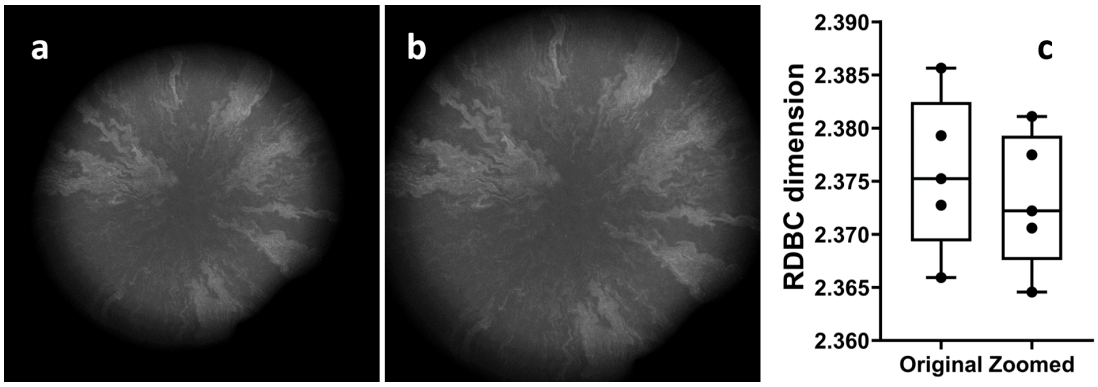

Figure 3.21: Comparison of RDBC dimension values (c) calculated for original $\Delta ompR$ biofilm images (a) and the same images zoomed to fill the image space and re-scaled to 2048 $\times$ 2048 pixels (b). The resulting average decrease in RDBC is only 0.1%.

3.3.6 Osmotic stress partially affects biofilm complexity of $\Delta ompR$

The role of osmotic stress on the growth of the $\Delta ompR$ mutant strain was quantified both the cellular level and at the biofilm level. This was achieved by measuring changes in cell length and width and by measuring the RDBC dimension of biofilm images grown in solid media with different osmolalities, respectively. Changes in growth medium osmolality were induced by adding different amounts of iodixanol, a compound originally designed for density gradient preparations that cannot be metabolised by the bacteria [424]. Iodixanol toxicity in both the parental strain BW25113 and the $\Delta ompR$ mutant strain was checked by growth curve experiments (Figure 3.22).

At the cellular level, an increase in osmotic stress in the liquid growth media led to a reduction in cell size for both strains (Figure 3.23). A significant reduction in cell length with increasing iodixanol concentration was observed in both strains: from 3.520 ± 0.827 μm to 2.205 ± 0.516 μm for BW25113 ($p = 1.32 \times 10^{-167}$), and

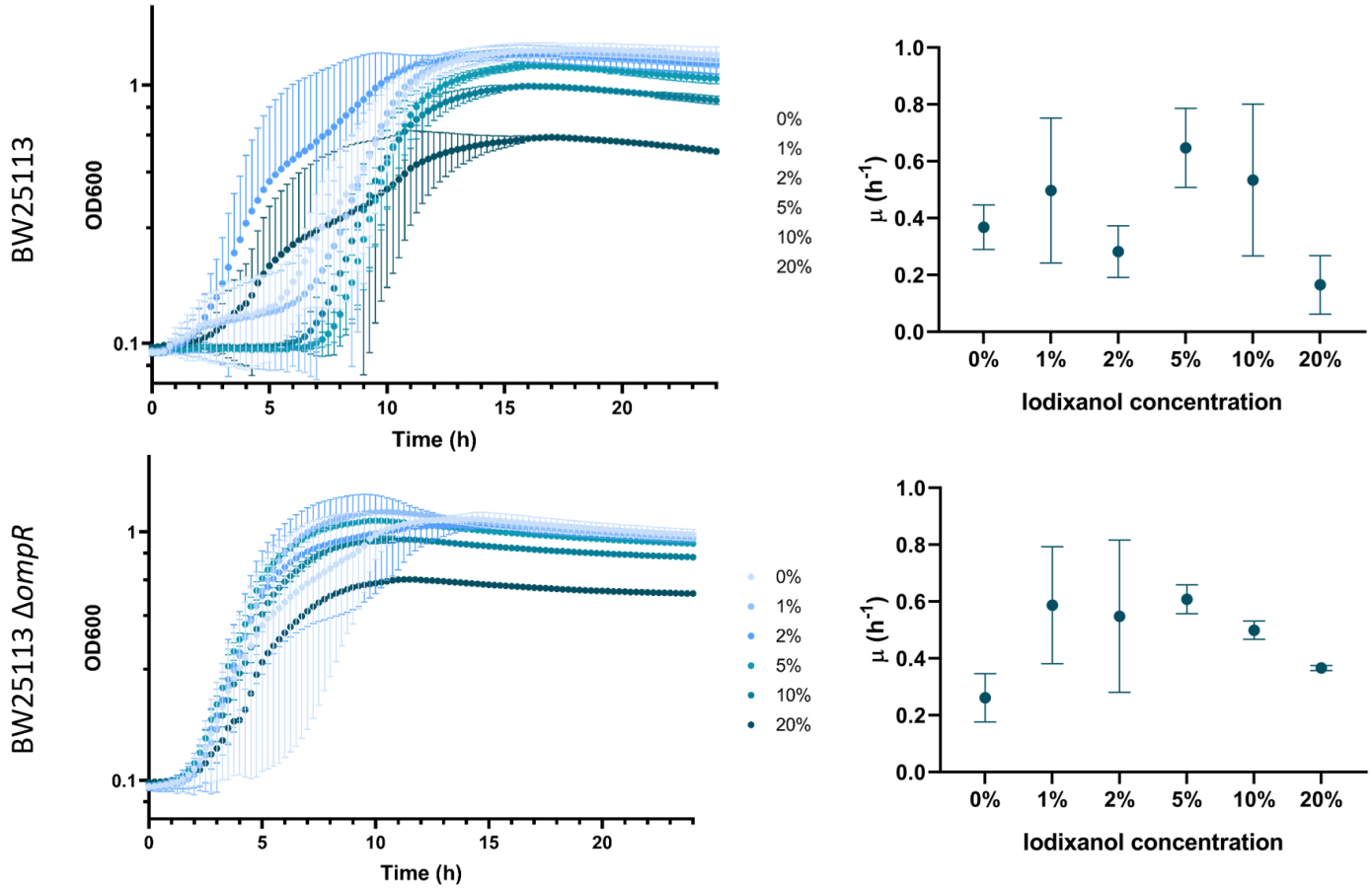

Figure 3.22: Growth curves (left panels) and specific growth rates (right panels) for the parental strain BW25113 and the mutant strain Δ*ompR*, grown on LB broth with increasing concentrations of iodixanol. Growth curves are plotted with the y axis in logarithmic scale. Each data point is an average of 5 repeats, and error bars represent standard deviations.

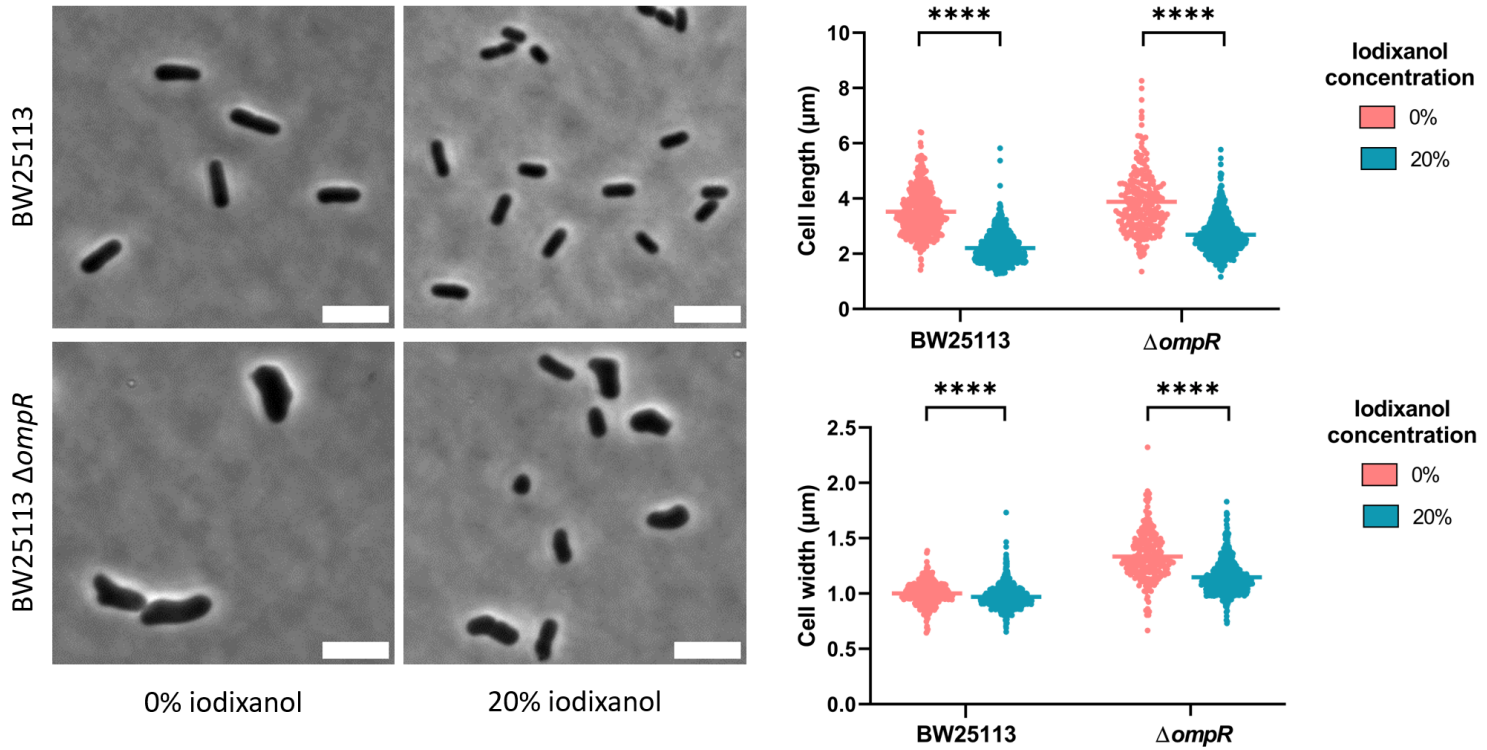

Figure 3.23: Single-cell phenotype of the parental strain BW25113 and of the Δ*ompR* mutant strain, grown in LB broth and in LB broth with 20% iodixanol. A reduction in cell length of more than 30% can be observed for both BW25113 and Δ*ompR* after growth in medium containing iodixanol ($p = 1.32 \times 10^{-167}$ and $p = 6.74 \times 10^{-40}$ respectively). The Δ*ompR* mutant strain also exhibits a 14% reduction in cell width ($p = 1.02 \times 10^{-13}$), almost five times higher than the parental strain's 3% reduction ($p = 8.57 \times 10^{-8}$). Average values are compared using a Kruskal-Wallis statistical test. Scale bars: 5 μm.

from 3.878 ± 1.133 μm to 2.685 ± 0.657 μm for $\Delta ompR$ (p = 6.74 $\times 10^{-40}$). By contrast, the reduction in cell width brought by increasing iodixanol concentration was marginal for BW25113 (from 1.001 ± 0.099 μm to 0.970 ± 0.098 μm, p = 8.57 $\times 10^{-8}$), whereas it was almost five times higher for $\Delta ompR$ (from 1.335 ± 0.219 μm to 1.147 ± 0.149 μm, p = 1.02 $\times 10^{-13}$).

In biofilms, an increase in iodixanol concentration in the solid growth substrate was associated with a small overall reduction in RDBC dimension for both strains (Figure 3.24). This loss of internal complexity could occur because bacterial growth is limited in high osmolality medium, or it could be a result of the cell size reduction following osmotic stress. Alternatively, it could be a pleiotropic effect caused by the presence of iodixanol in the growth medium.

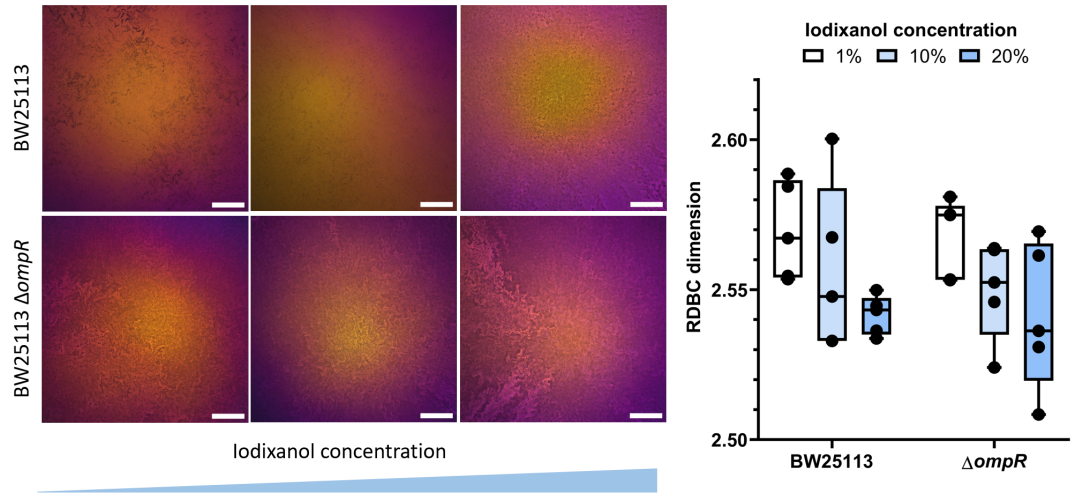

Figure 3.24: Comparison of fractal morphology between biofilms formed by the parental strain BW25113 and the mutant strain $\Delta ompR$ on solid substrates with increasing iodixanol concentrations (1%, 10%, 20%, v/v). Biofilm images are colour-coded by depth. Average RDBC dimension decreases with increasing amounts of iodixanol and is similar between the two strains for each iodixanol concentration. Scale bars: 200 μm.

3.3.7 Guanine complementation of M9 medium does not affect the fractal morphology of biofilms formed by the Δ*guaB* mutant strain

To check whether the peculiar intra-colony channel architecture exhibited by biofilms formed by the Δ*guaB* mutant strain on minimal medium was caused by the activation of an alternative pathway for the biosynthesis of guanine, Δ*guaB* biofilms were grown on M9 medium with increasing levels of guanine (Figure 3.25). However, a comparison of the fractal complexity of these biofilms using

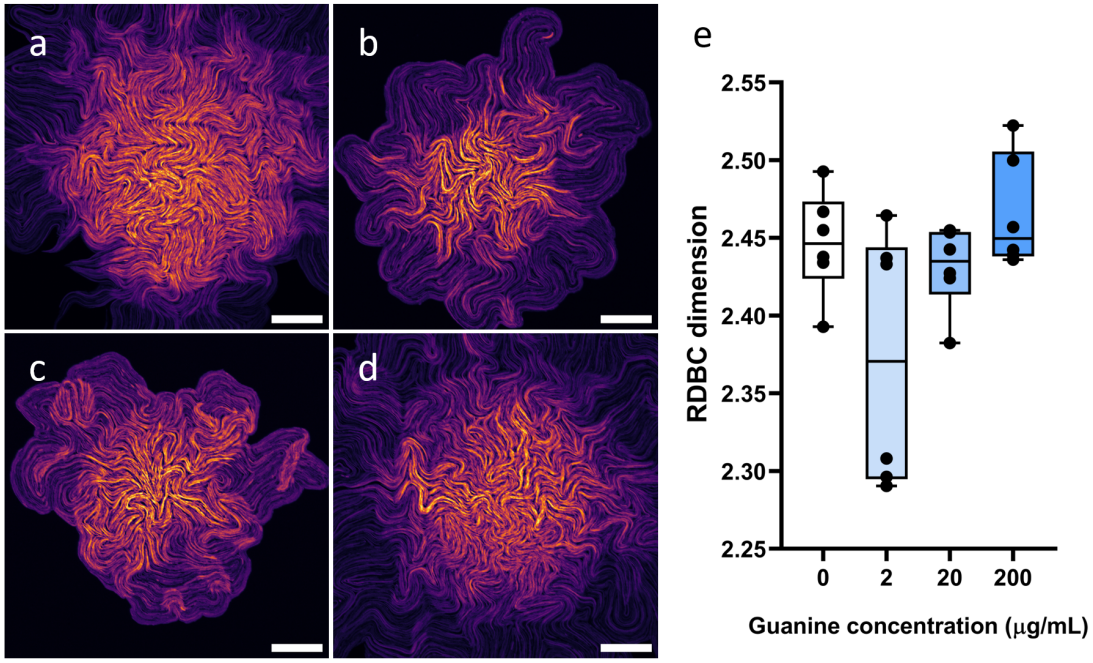

Figure 3.25: Confocal micrographs of Δ*guaB* biofilms grown in M9 minimal medium with guanine added in concentrations of 0 μg/mL (a), 2 μg/mL (b), 20 μg/mL (c) and 200 μg/mL (d). Biofilms grown with low amounts of guanine (b,c) had irregular edges and a smaller diameter. Images are maximum intensity projections of z-stacks, colour-coded using the "Fire" lookup table. Scale bars: 200 μm. (e) RDBC dimension calculated from the biofilms in panels (a-d).

ComsystanJ revealed no significant difference in intra-colony channel architecture. The average RDBC dimension of biofilms grown on nominal M9 substrates (2.444 ± 0.034) was comparable to that of biofilms grown with 2 μg/mL guanine (2.372 ± 0.081), 20 μg/mL guanine (2.431 ± 0.027) and 200 μg/mL guanine (2.466 ± 0.036).

3.3.8 Extracellular matrix distribution in Δ*guaB* biofilms is comparable to that of BW25113

The distribution of extracellular matrix in BW25113 and Δ*guaB* biofilms was visualised by staining LB agar substrates without NaCl with Congo Red and Coomassie Blue dyes (Figure 3.26). The lack of binding to these dyes was an indicator of low production of biofilm matrix polysaccharides and proteins by both strains. Furthermore, no preferential binding to Congo Red or Coomassie

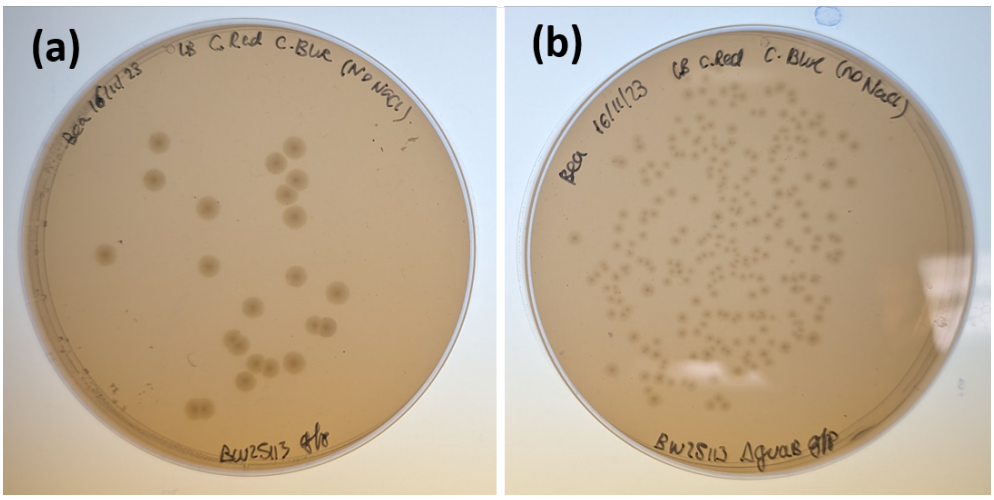

Figure 3.26: Petri dishes images showing the binding of Congo Red and Coomassie Blue dyes to biofilms formed by BW25113 (a) and Δ*guaB* (b) on LB agar substrates with no NaCl. No preferential binding of the Congo Red/Coomassie Blue dye mix is observed between the two strains.

Blue was observed by either strain, suggesting that biofilm matrix components were not responsible for the dense channel architecture exhibited by $\Delta guaB$ on LB medium substrates observed in Figure 3.16.

Biofilms grown on Congo Red-stained LB agar plates were also imaged using fluorescence microscopy to compare the GFP signal originating from the bacterial cells to the signal from the Congo Red dye (Figure 3.27a). GFP and Congo Red signals were spatially overlapping for both BW25113 and $\Delta guaB$ biofilms, and Congo Red was not observed inside nutrient-transporting channels. This indicated that channels were not preferentially filled with biofilm matrix polysaccharides or amyloyd, but did not provide any information on the spatial distribution of proteinaceous matrix components.

The distribution of proteinaceous matrix components was hence investigated in both BW25113 and $\Delta guaB$ biofilms by staining LB agar substrates with the SYPRO Ruby biofilm matrix stain (Figure 3.27b). For both strains, the GFP signal and that from the SYPRO Ruby matrix stain overlapped and did not fill nutrient-transporting channels. This showed that channels were not preferentially filled with proteinaceous matrix in either strain.

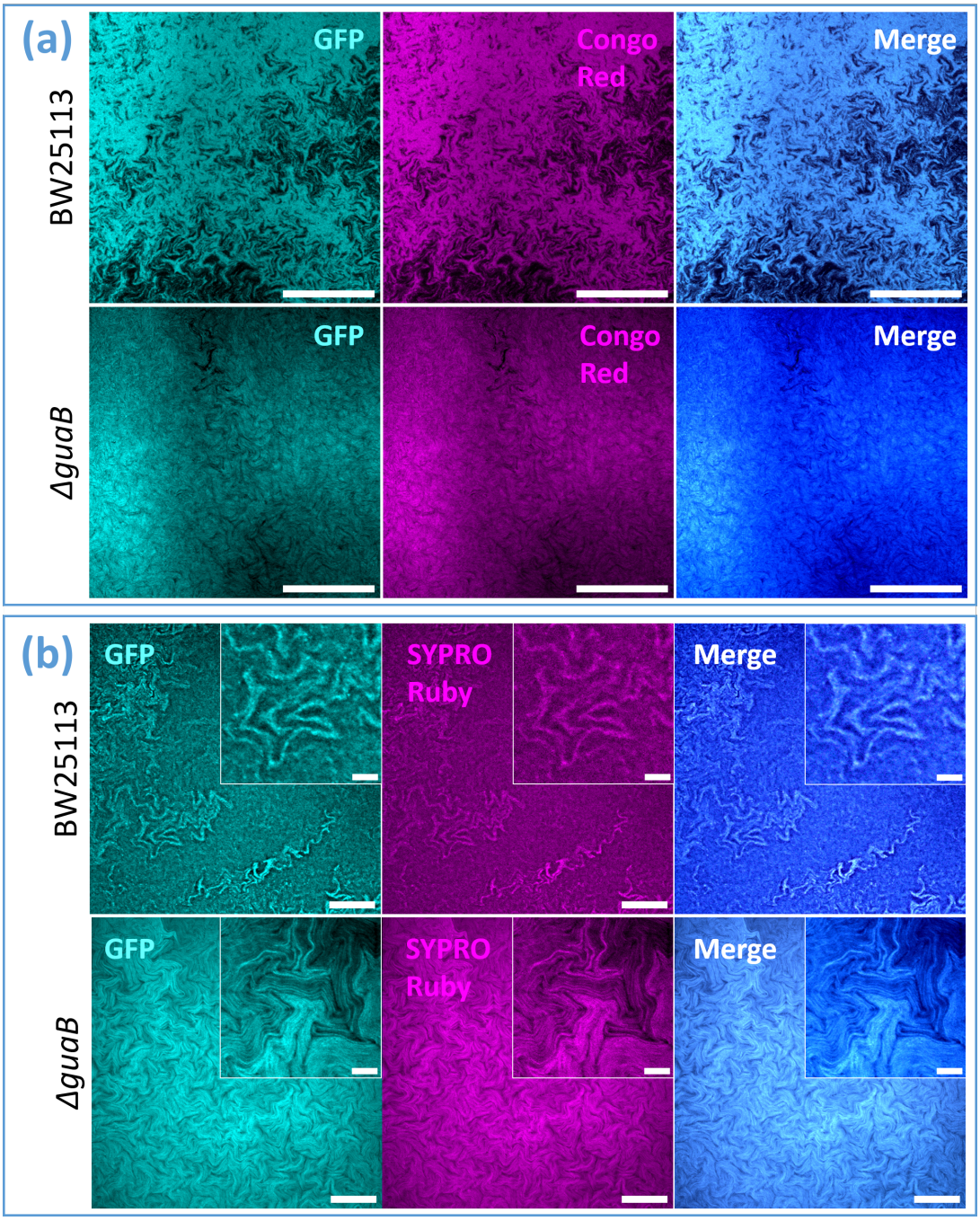

Figure 3.27: Confocal micrographs of biofilms formed by the parental strain BW25113 and by the Δ*guaB* mutant strain when growing on LB medium containing 40 μg/mL Congo Red (a) and 5% (v/v) SYPRO Ruby biofilm matrix stain (b). Scale bars: 200 μm (50 μm in the ROIs).

3.4 Discussion

In this study, the effect of cell shape mutations and growth medium composition on the morphological complexity of *E. coli* biofilms was analysed using confocal microscopy and image analysis. The fractal morphology of *E. coli* nutrient transport channels was comparable to that of computer-generated fractals for all cell shape mutants and growth conditions. While cell shape affected the overall biofilm morphology, this did not lead to a statistically significant change in fractal complexity, as described by the RDBC dimension metric. However, the long-cell mutant strain $\Delta guaB$ and the wide-cell mutant strain $\Delta ompR$ both formed biofilms with a higher RDBC dimension on nutrient excess than in nutrient limited conditions.

The cell shape phenotype of each strain was checked against known phenotypic studies on the Keio collection prior to the investigation of the resulting biofilm fractal morphology. While the presence of the kanamycin resistance cassette can be linked to a phenotypic change in cell shape due to growth with the antibiotic kanamycin, this change is reportedly limited to the specific mutant strains $\Delta croE$ and $\Delta ydaS$ [405]. Furthermore, phenotypic studies of the Keio collection are routinely carried out with the kanamycin cassette present [403], and the phenotypes observed in this work are consistent with the Keio collection documentation [401].

The gene *amiA* controls the cleavage of the peptidoglycan cell wall septum during the last stage of cell division, leading to the physical separation of daughter cells [406]. According to the Keio collection documentation [401], cells from the $\Delta amiA$ mutant strain have a long phenotype, which is consistent with the results presented in this Chapter, though our measured average cell length is considerably higher than that suggested by phase-contrast images provided in the

Keio collection database. The increase in Δ*amiA* cell length, together with the relatively low associated fluctuation in cell length measurements, likely explains the symmetric channel architecture observed within Δ*amiA* biofilms.

guaB is a gene regulating guanine nucleotide biosynthesis [407]. The Δ*guaB* mutant strain is a guanine auxotroph, meaning that it requires the addition of guanine for growth in minimal medium; however xanthine or thiamine complementation can also be used to support growth [425]. This can be seen in the metabolic pathway for guanine ribonucleotide biosynthesis (M00050) on the Kyoto encyclopedia of genes and genomes (KEGG) [426]. Δ*guaB* cells also have a long phenotype, consistently with the documentation from the Keio collection [401]. However, the difference in internal morphology between biofilms formed by the Δ*guaB* and Δ*amiA* mutant strains confirms that channel architecture is not governed exclusively by cell shape phenotype. Instead, complex metabolic factors due to imbalances in nucleotide synthesis [427] and changes in the biofilm matrix components could be the cause of the highly dense internal channel patterns observed in Δ*guaB* biofilms. For example, the abundance of the messenger molecule cyclic di-guanosine monophosphate (c-di-GMP), which promotes the switch from planktonic to motile biofilm form [428] and stimulates the production of EPS [429], is linked to the expression of *guaB* [430].

Deletion of the *ompR* gene in *E. coli* inactivates the expression of the outer membrane porins OmpC and OmpF, which mediate the diffusion of small solutes across the outer membrane [408], [431], [432]. The increase in cell width measured for the Δ*ompR* mutant strain contradicts that calculated by French et al. [433], who did not identify the deletion of *ompR* as a cause for cell phenotype change. This could be due to their use of a 2% glutaraldehyde fixative (pH 6.8) prior to imaging. This fixation method is associated with up to two-fold increase

in PBS osmolality [434], up to 2.5 times higher than that of LB broth [435], as well as with introducing an immediate decrease in cell width of approximately 15% [436]. On the other hand, the cell width of the $\Delta ompR$ mutant strain calculated by Campos et al. [405] concurs with the measurements presented in this Chapter. Furthermore, the wide phenotype observed in the phase contrast images presented in this Chapter is similar to those observed by Ranjit and Young during growth of lysozyme-induced spheroplasts of *E. coli* MG1655 with the same $\Delta ompR$ mutation [437], but it was not observed in the other two phenotypic studies mentioned above. This is not ascribed to differences in immobilisation method (agarose pads for our study and that of Campos; optically clear microplates for the work of French), which is known not to affect cell morphology, changes in intercellular pH or growth in *E. coli* [438].

The gene *ydgD* is a putative periplasmic serine protease [409], and its deletion in *E. coli* is linked to increased sensitivity to some β-lactam antibiotics [439]. The difference in morphology between biofilms formed by $\Delta ompR$ and $\Delta ydgD$ mutant strains could be due to their different constituent cell shape phenotypes, although a more comprehensive knowledge about the function of *ydgD* would be required to inform further analysis.

The effect of growth medium composition on the fractal complexity of biofilms formed by the $\Delta ompR$ mutant strain was investigated in an attempt to identify the components which most affected biofilm fractal dimension. It was found that glucose concentration was particularly important in minimal medium, where it constituted the sole carbon source. Increasing glucose concentrations in minimal medium led to proportionally more complex biofilm channel organisation, eventually reaching a RDBC dimension value close to that of biofilms grown on rich media. This effect is similar to that observed in biofilms formed by *E.*

coli JM105 mini-Tn7-*gfp* [294], which developed more complex channel patterns when grown on minimal medium with an excess of glucose compared to glucose-limited substrates as described in Chapter 2. Furthermore, growth on rich soft substrates reduced biofilm morphological complexity, whereas growth on soft minimal substrates increased it. This is in contrast with previous findings on *E. coli* JM105 mini-Tn7-*gfp*, where channels in biofilms grown on rich, soft substrates were densely packed together [294].

The morphology of cells and biofilms formed by the mutant strain $\Delta ompR$ under growth conditions with varying osmolality was also studied owing to the role of OmpR in regulating the osmotic stress response [440]. Gram-negative bacteria such as *E. coli* respond to an increase in external osmotic pressure by accumulating solutes inside the cell, and by pumping out water through efflux [441]. Hyperosmotic shock also leads to a sudden cell volume shrinkage [442], followed by a gradual recovery [443], and is associated with a reduction in cell elongation rate [444]. The effect of medium osmolality on biofilm morphology was estimated by comparing RDBC dimension values between biofilms grown on solid substrates with and without NaCl, and it was found that low osmolality was associated with a lower fractal complexity on both rich and minimal media. Because NaCl affects not only medium osmolality, but also nutrient metabolism [445], the metabolically inert compound iodixanol was used for subsequent osmotic stress experiments. The observed reduction in $\Delta ompR$ cell width in high osmolality media indicates a possible partial reversion to the parental phenotype, which could equally be driven by *ompR* suppressor mutations. This phenotypic reversion in cell shape may also explain the similarity in absolute RDBC dimension values between biofilms formed by the parental strain BW25113 and the mutant strain $\Delta ompR$ at each iodixanol concentration.

E. coli K-12 strains are generally poor biofilm formers [446], and curli fibres are required for biofilm development in K-12 [447]. The stark difference in morphology between biofilms formed by the strains BW25113 and Δ*guaB* prompted a comparative study of extracellular matrix production. However, no difference was observed in extracellular matrix production when colonies of each strain were grown on agar substrates stained with Congo Red and Coomassie Blue, or with the SYPRO Ruby matrix stain. By imaging these biofilms with fluorescence microscopy, it was also found that extracellular matrix in BW25113-derived strains was not preferentially localised within nutrient-transporting channels, contrary to what was previously observed in JM105 mini-Tn7-*gfp* [209]. Congo Red binding was not observed in either BW25113 or Δ*guaB*, indicating that the peculiar biofilm morphology exhibited by Δ*guaB* was not due to differential production of curli or proteinaceous biofilm matrix components. A comparison with the Van Gogh bundle structures in *B. subtilis* suggests extracellular polysaccharide as a possible candidate for bundle formation in Δ*guaB*, as EPS production is essential for the formation of Van Gogh bundles in *B. subtilis* [448]. This could be verified by biofilm staining with Alexa594-wheat germ agglutinin (WGA) as previously described by Rooney et al. for JM105 mini-Tn7-*gfp* [209].

The extraction of fractal geometry parameters from biofilm micrographs (see for example [449]) is usually achieved by image thresholding, which is a type of image segmentation which isolates an object from its background depending on its greyscale value [450]. While this method can accurately identify the peripheral outline of biofilms [451], it is not effective for the detection of internal channel networks, where the difference in greyscale values between the channels and the rest of the biofilm is small. In this work, this obstacle was overcome using the fractal analysis software ComsystanJ. The use of fractal geometry has proven to

be a simple yet powerful method for the quantification of *E. coli* biofilm internal morphology, formed by cell shape mutants on different growth substrates. Our analysis could help identify the factors controlling the formation and development of nutrient-transporting channels in *E. coli*, and it could be readily applied to other microbial species exhibiting complex biofilm internal patterns.

3.5 Conclusions

In this Chapter, two open-source fractal image analysis methods were applied to microscopy images of *E. coli* biofilms to quantify the morphology of nutrient-transporting channels. The similarity in box-counting dimension calculated for biofilm images to that calculated for computer-generated fractals confirmed that the morphology of nutrient-transporting channels in *E. coli* is fractal. While differences in biofilm internal complexity could not be ascribed to cell shape alone, changes in internal morphology for biofilms formed by the $\Delta guaB$ and $\Delta ompR$ mutant strains were observed with changes in growth conditions. The natural extension of this work would involve the analysis of biofilms formed by other *E. coli* morphotypes, such as chains of cells (obtained for example by inactivating the gene *tolB*) or round cells (through the inactivation of *rodZ*). In particular, the architecture of biofilms formed by round *E. coli* cells would indicate whether nutrient-transporting channels are exclusive to rod-shaped bacteria.

Chapter 4

Design of a Lambda Red recombineering experimental framework for gene inactivations in *Escherichia coli* JM105 mini-Tn7-*gfp*

This Chapter presents an experimental framework designed to disrupt genes in the background strain JM105 mini-Tn7-*gfp* using Lambda Red recombineering, leading to changes in cell shape phenotype. The JM105 mini-Tn7-*gfp* strain was chosen due to its demonstrated compatibility with mesoscopic imaging of biofilm morphology with the Mesolens (as seen in Chapter 2), as opposed to strains derived from BW25113, which are not suitable for Mesolens imaging due to their dispersion to planktonic culture when a liquid mounting medium is added to match the refractive index of the Mesolens used in water immersion mode (as discussed in Chapter 3). During recombineering experiments, JM105 mini-Tn7-*gfp* exhibited unexpected ampicillin resistance. which prompted further genotyping in an attempt to identify a reason for this phenomenon. Modifications to the Lambda Red protocol were subsequently designed to circumvent this issue, but these were unsuccessful. These findings confirmed that the strain BW25113 was the most appropriate model to study the effect of gene inactivations on biofilm morphology during the timeframe of this project.

4.1 Introduction

4.1.1 Fundamentals of genetic engineering in bacteria

Bacterial DNA is mostly arranged into a circular, double-stranded chromosome which contains the majority of genetic information essential for survival and replication [452]. In addition to this, genetic material can be found in separate, smaller, often circular, DNA molecules called plasmids, which can replicate autonomously from the chromosome [453]. The genetic material encoded in plasmids is taken up into the bacterial cell when it confers a fitness or survival advantage [454], for example by countering a selective pressure through resistance to antibiotics [455].

Genetic modification of organisms, also called genetic engineering, is a technique which is used extensively in research, for example to understand metabolic processes, to improve the yield of natural products [456], or to elucidate the function of uncharacterised genes by their addition or deletion/inactivation into the genome and subsequent phenotypic analysis [457]. Genetic modification of bacterial DNA, whereby DNA fragments can be inserted into, or removed from, the genome of a recipient organism, often exploits the rapid self-replication of bacteriophages and plasmids [458]. *E. coli* is one of the best characterised organisms among all biological domains, and it remains the traditional choice for genetic engineering, in part thanks to the availability of complete and annotated genome sequences [121].

4.1.1.1 Lambda Red recombineering

Disruption of target genes can be achieved by PCR methods [459], where DNA fragments containing an antibiotic resistance cassette are amplified using primers

containing homologous regions upstream and downstream of the gene to be disrupted. These fragments are then inserted into the host genome by homologous recombination, a process by which pairs of homologous regions allow for DNA exchange [460]. Many *E. coli* strains are not proficient in recombination, although genetic mutations in the genes *recB*, *recC* and *recD*, which encode for DNA helicases and nucleases [461], can overcome this limitation [462]. Alternatively, homologous recombination can be achieved by replacing the RecBCD function of *E. coli* with the Red recombination machinery from the bacteriophage λ [463]. This forms the basis of Lambda Red recombineering, which can be used in conjunction with PCR amplification of insert DNA fragments with 30-50 bp (base pairs) long homology regions to the gene of interest [464].

Lambda Red recombineering has been successfully used to inactivate genes in *E. coli* K-12 by substituting the gene of interest with a kanamycin resistance cassette from a plasmid [402]. This technique was also used to generate the Keio collection, a single-gene knockout library described in Chapter 3 [401]. Nonetheless, the Keio collection may be impacted by secondary mutations, reversions and handling errors, which could compromise the genotype status. For these reasons, PCR experiments and sequencing are routinely employed to verify each strain, and the removal of the kanamycin resistance cassette by plasmid curing is advisable [465].

4.1.2 Experimental aims

The first aim for this Chapter was to adapt the Lambda Red recombineering protocol designed by Datsenko and Wanner [402] for the inactivation of the genes *amiA*, *cysC*, *guaB*, *minC*, *ompR*, *rodZ*, *tolB* and *ydgD*, which cause changes in *E. coli* cell shape phenotype. The background *E. coli* strain JM105 mini-Tn7-*gfp* was chosen for this experiment instead of the Keio parental strain BW25113

thanks to its proven compatibility with high-throughput microscopy with the Mesolens, as shown in Chapter 2 and discussed in Chapter 3. The failure of the Lambda Red recombineering protocol prompted genotyping of the background strain by diagnostic PCR, restriction enzyme digest and plasmid sequencing, leading to the observation of an unexpected resistance to ampicillin in JM105 mini-Tn7-*gfp*. The second aim of this Chapter was then to modify the Lambda Red recombineering protocol to change the antibiotic selection of the plasmid containing Lambda Red machinery from ampicillin to tetracycline, to which JM105 is susceptible, using Gibson assembly and ligation.

4.2 Materials and Methods

4.2.1 Single-gene inactivation protocol using Lambda Red recombineering

Single-gene inactivations were designed following the method by Datsenko and Wanner [402], where recombination between a region of the target gene and an antibiotic resistance cassette produces the inactivation of that gene (Figure 4.1). In this technique, recombination is carried out using the Lambda Red phage recombinase, which is transformed into the strain of origin using the helper plasmid pKD46 (GenBank accession number: AY048746.1, Figure 4.2). Expression of the recombinase genes is induced by addition of 0.1% L-arabinose into the growth medium, as expression of the recombination components γ, β and *exo* of the Lambda system are controlled by the arabinose-inducible promoter P*araB* [402] (Figure 4.2).

The template plasmid pKD4 (GenBank accession number: AY048743.1, Figure 4.2) carries the kanamycin resistance cassette used to disrupt the target gene,

① Transformation of pKD46 DNA into recipient strain

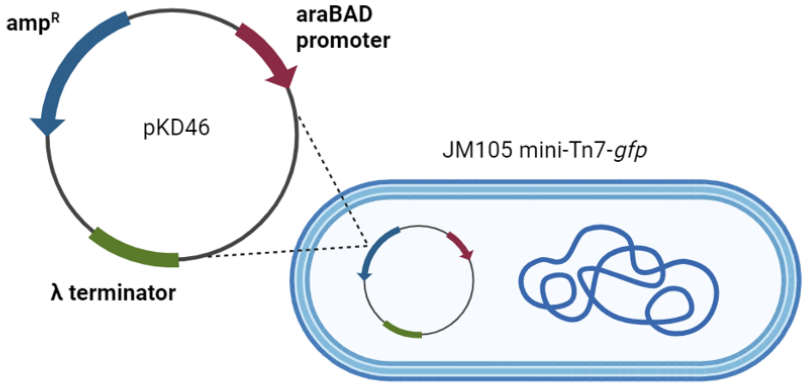

② PCR amplification of antibiotic resistance cassette

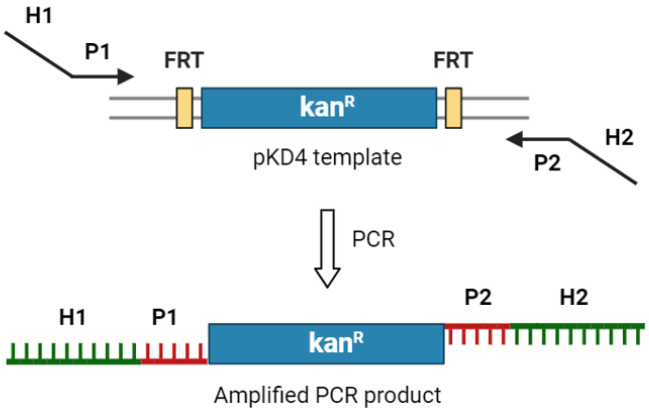

③ Homologous recombination

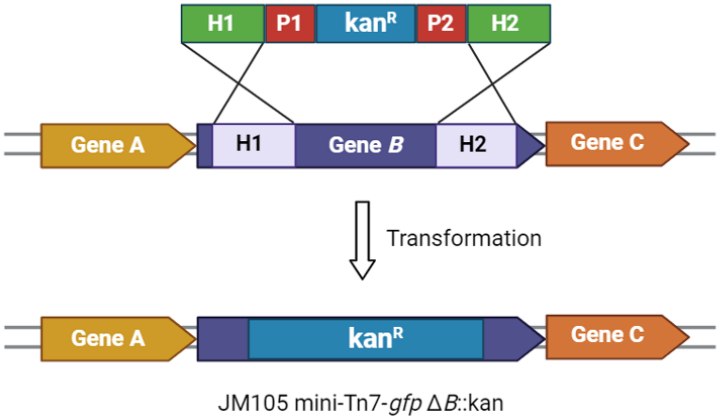

Figure 4.1: Schematic illustration of the single-gene knockout procedure by Datsenko and Wanner. (1) Recombinase genes from the helper plasmid pKD46 are transformed into the recipient strain JM105 mini-Tn7-*gfp*. The plasmid pKD46 contains the ampicillin resistance cassette (amp^R), the promoter of the L-arabinose operon *araBAD*, required for L-arabinose utilisation [466], and the phase Lambda Red recombinase and its transcription terminator (λ terminator). (2) The kanamycin resistance cassette present on the helper plasmid pKD4 is amplified by PCR using primers containing homology regions (H1 and H2) to the target gene to be deleted. The plasmid pKD4 contains two flippase recognition target (FRT) sites. (3) The kanamycin resistance cassette is substituted in the locus of the target gene (B) by homologous recombination, thus inactivating the gene and creating the mutant strain JM105 mini-Tn7-*gfp* ΔB. Image created in BioRender (license number SR25JKZ3PC).

which is amplified via PCR. The primers used for the amplification of the antibiotic resistance cassette contain homologous regions to the target gene, so that when the PCR product is transformed with the recipient strain homologous recombination can occur at the desired locations inside the genome.

4.2.1.1 PCR amplification of the antibiotic resistance cassette

PCR experiments were carried out using Q5 High-fidelity DNA Polymerase (New England Biolabs, USA) with the thermocycling conditions outlined in Section A.5 of Appendix A. The kanamycin resistance cassette from plasmid pKD4 was amplified using primers with homology regions to each gene of interest (Table A.6 in Appendix A) to produce each gene disruption.

A digestion step followed, where 1 μL of DnpI enzyme was added to each 50 μL PCR tube, and incubated at 37 °C for one hour in order to remove methylated

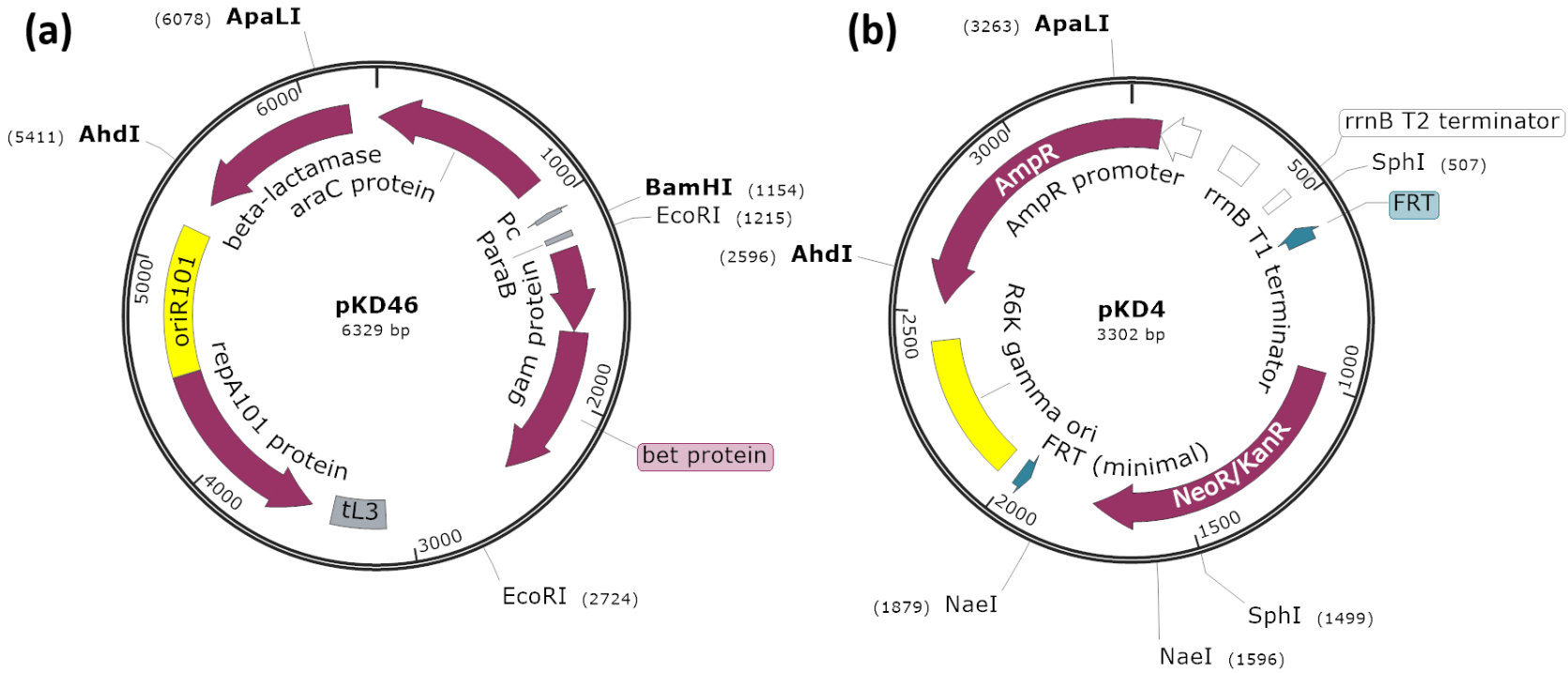

Figure 4.2: Plasmid maps of pKD46 (a) and pKD4 (b) showing the restriction sites used in diagnostic checks. Maps were created in SnapGene Viewer version 6.2.1 (Insightful Science, USA).

DNA from the plasmid template.

Successful amplification of the resistance cassette was checked by agarose gel electrophoresis. The 1.5 kb bands corresponding to the antibiotic resistance cassettes with homology regions were purified using the Wizard SV gel and PCR clean-up system (Promega, UK) following manufacturer protocols.

4.2.1.2 Gene disruptions

Gene disruptions could be obtained by transforming the purified DNA fragments from pKD4 into the JM105 mini-Tn7-*gfp* / pKD46 strain by electroporation. Electrocompetent *E. coli* JM105 mini-Tn7-*gfp* / pKD46 cells were prepared as described in Section A.8.2 of Appendix A in LB broth with 25 μg/mL gentamicin and 100 μg/mL ampicillin. 0.1% L-arabinose was added to the growth medium after 1:100 dilution of overnight cultures of JM105 mini-Tn7-*gfp* / pKD46 to induce expression of the Lambda Red recombinase genes. The cultures were further incubated under the same conditions until they reached mid-exponential growth phase.

After electroporation, a recovery phase was carried out in 1 mL of SOC medium at 30 °C with 300 rpm shaking for one hour. The recovered cultures were inoculated on LB agar plates containing 25 μg/mL gentamicin, 100 μg/mL ampicillin and 50 μg/mL kanamycin. A negative control was established by transforming electrocompetent JM105 mini-Tn7-*gfp* / pKD46 cells with RNAse-free water. A positive control was produced by inoculating electrocompetent JM105 mini-Tn7-*gfp* / pKD46 on LB agar containing 25 μg/mL gentamicin and 100 μg/mL ampicillin. Successful transformants would be streaked once more on LB agar plates containing 25 μg/mL gentamicin, 100 μg/mL ampicillin and 50 μg/mL kanamycin.

4.2.1.3 Verification of gene disruptions by colony PCR and amplicon sequencing

The successful insertion of the antibiotic resistance cassette into the genome was checked by colony PCR. A small section of transformant biomass, taken from re-streaked transformants, was suspended in 15 μL of 50% DMSO (Sigma-Aldrich, USA) with a sterile inoculation loop. The mixture was heated at 65 °C for 30 minutes and used as the DNA template. Diagnostic colony PCR experiments were carried out using the PCRBIO Taq Mix Red (PCR Biosystems, USA) following manufacturer instructions, alongside 2 μL of colony DNA product and 1 μL of each forward and reverse gene-specific primers from Table A.5 in Appendix A. Agarose gel electrophoresis was used to check for successful gene disruption and resistance cassette insertion.

DNA from successful transformants was purified from agarose gels using a Wizard SV Gel and PCR Clean-Up System (Promega, UK) following manufacturer protocol and sequenced by Illumina Sanger amplicon sequencing (Eurofins, Germany) to confirm successful gene disruptions and the presence of the kanamycin resistance cassette.

4.2.2 Characterisation of an unexpected ampicillin resistance mutation in JM105 mini-Tn7-*gfp*

Following the observation of ampicillin resistance in our JM105 mini-Tn7-*gfp* stocks, a phenotypic screening of the strain was carried out based on its genotype. The following properties were verified: resistance to streptomycin, sensitivity to nalidixic acid, thiamine auxotrophy, lactose non-utilisation. These properties were checked by growing the strain on solid LB media plates prepared with the

relevant concentrations of antibiotics as described in Table A.4 in Appendix A, and on solid M9 media plates without thiamine (for thiamine auxotrophy) or with 20 % lactose (w/v) as the sole carbon nutrient source (for lactose non-utilisation).

4.2.2.1 Diagnostic colony PCRs

A diagnostic colony PCR reaction was performed to verify the successful insertion of the mini-Tn7-*gfp* cassette into JM105. The primers glmS and mini-Tn7 were selected to anneal to the *glmS* gene (upstream of the Tn7 insertion site) and to the downstream flanking region of the mini-Tn7 insert [234] respectively (Table A.8 in Appendix A). PCR experiments were performed using PCRBIO Taq Mix Red (PCR Biosystems, USA) following manufacturer's instructions. Template DNA was added by removing a small quantity of biomass from a colony on an agar plate with a sterile pipette tip and swirling it into the PCR tube. The reactions were verified by agarose gel electrophoresis alongside a 50 bp hyperladder (Bioline, USA). The expected DNA fragment size amplified in the context of successful insertion of the mini-Tn7 cassette was 150 bp [209].

4.2.2.2 Diagnostic restriction enzyme digests

Because the mini-Tn7 cassette insertion was originally carried out using the pUC19 delivery plasmid, which confers ampicillin resistance [233], [234], it was hypothesised that some plasmid material could have been left over from the previous cloning steps while constructing the JM105 mini-Tn7-*gfp* strain. This was verified by diagnostic restriction enzyme digests. Plasmid DNA was first purified using a Wizard Plus SV Miniprep DNA Purification System (Promega, UK), following the manufacturer's protocol. The DNA concentration and purity were quantified using a NanoDrop spectrophotometer (Thermo Fisher Scientific, USA),

showing the presence of several micrograms of high-purity DNA. The DNA was digested with the enzymes EcoRI, PvuII, AhdI and NheI (New England Biolabs, USA). Single restriction digests were set up in PCR tubes with 1 μg of plasmid DNA, 5 μL of 10x rCutSmart buffer (New England Biolabs, USA) and 1 μL of each enzyme, and nuclease-free water was added to a total volume of 50 μL. The tubes were incubated for three hours at 37 °C, and the digested DNA was ran on a 1% agarose gel at 80 V for 75 minutes. A separate gel well was also loaded with undigested plasmid DNA for comparison.

Diagnostic restriction double digests were also carried out on the pKD46 and pKD4 plasmids. pKD46 was digested with the enzymes BamHI (unique cutter, producing a 6.6 kb DNA fragment) and EcoRI (dual cutter, producing two DNA fragments of sizes 1.5 kb and 5.1 kb). pKD4 was digested with the enzymes NdeI (unique cutter, producing a 3.3 kb DNA fragment) and SphI (dual cutter, producing two DNA fragments of sizes 1 kb and 2.3 kb).

4.2.2.3 Plasmid sequencing

As a final verification, the plasmid DNA purified from JM105 mini-Tn7-*gfp* was sequenced using Oxford Nanopore long reads by Plasmidsaurus (`https://www.plasmidsaurus.com/`). DNA was diluted in nuclease-free water to a concentration of 30 ng/μL, which was measured with a Qubit 2.0 fluorometer (Thermo Fisher Scientific, USA). The purity of the sample was assessed with a NanoDrop spectrophotometer (Thermo Fisher Scientific, USA), ensuring a 260/280 value greater than 1.8 and a 260/230 value between 2.0 and 2.2. The resulting DNA sequences were analysed using SnapGene Viewer version 6.2.1 (Insightful Science, USA).

4.2.3 Proposed modification of Lambda Red recombineering protocol

The Lambda Red recombineering protocol described in Section 4.2.1 was modified to circumvent the ampicillin resistance identified in JM105 mini-Tn7-*gfp*. Two alternative methods were designed, both relying on the substitution of the ampicillin resistance cassette in pKD46 with a tetracycline resistance cassette from the pACYC184 plasmid (GenBank accession number: X06403.1). The ligation of the two fragments was designed to be carried out by either Gibson assembly or ligation, as discussed in more detail below.

4.2.3.1 Gibson assembly

A Gibson assembly reaction was set up to ligate the backbone sequence of pKD46 (the fragment without the ampicillin resistance cassette) with the tetracycline resistance cassette amplified from pACYC184. The reaction, outlined in Figure 4.3, was designed using NEBuilder Assembly Tool v2.7.1 (New England Biolabs, USA). Plasmid DNA from both pKD46 and pACYC184 was purified from 10 mL overnight cultures in LB30YE (LB broth modified to have 30g/L yeast extract) with appropriate antibiotic using a Wizard Plus SV Miniprep DNA Purification System (Promega, UK), following the manufacturer's protocol. The 5,658 bp backbone sequence from pKD46 was obtained by double restriction digest on pKD46 DNA with the enzymes AhdI and ApaLI. Restriction enzyme digests and agarose gel electrophoresis were carried out as described in Section 4.2.2.2. The 5.6 kb DNA band on the gel corresponding to the backbone sequence (without the ampicillin resistance cassette) was excised and purified using a Wizard SV Gel and PCR Clean-Up System (Promega, UK). The tetracycline resistance cassette fragment from pACYC184 was amplified by PCR, using primers containing at

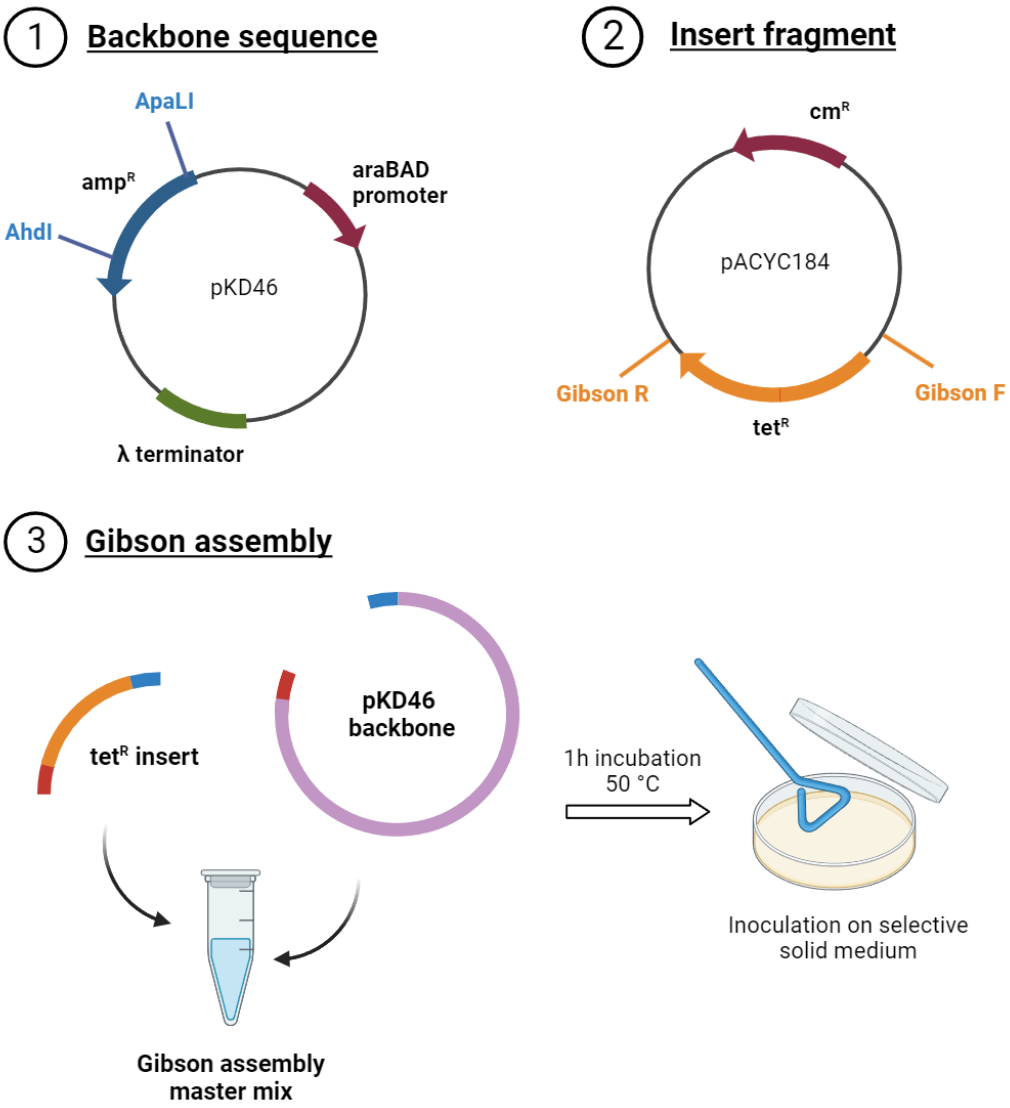

Figure 4.3: Schematic illustration of the Gibson assembly setup. (1) The backbone sequence was isolated by restriction enzyme digest of the plasmid pKD46 with the enzymes AhdI and ApaLI, and agarose gel purification of the 5.6 kb fragment corresponding to the region without the ampicillin resistance cassette. (2) The 1319 bp insert containing the tetracycline resistance cassette (tet^R) was amplified from plasmid pACYC184 using PCR with the primers Gibson F and Gibson R. (3) The two fragments were ligated using the Gibson Assembly Master Mix and incubated at 50 °C for one hour, and the resulting product was streaked on LB agar plates with selective antibiotics. Image created in BioRender (license number SR25JKZ3PC).

least 20 bp overlaps to the annealing region in pKD46 (Gibson F and Gibson R from Table A.7 of Appendix A). Successful DNA amplification was ensured by running the PCR product on 1.5% agarose gel. The 1.3 kb band was excised and purified using a Wizard SV Gel and PCR Clean-Up System (Promega, UK). The remaining contents of the tube were also purified using the same kit.

The Gibson assembly reaction was set up with 0.02 to 0.50 pmols of each fragment, together with 10 μL of Gibson Assembly Master Mix 2$\times$ (New England Biolabs, USA), topped up to a total volume of 20 μL with RNAse-free water. The sample was incubated at 50 °C for one hour, then stored on ice until chemical transformation with Dh5α competent *E. coli* (High Efficiency) (New England Biolabs, USA), which was carried out as described in Section A.8.1 of Appendix A. The cultures were streaked on LB agar plates containing selective antibiotics: tetracycline for the success of the Gibson assembly and ampicillin for a negative control. A single insert in the pUC19 plasmid, conferring ampicillin resistance, was provided in the Gibson assembly kit and was used as a positive control. The resulting 6937 bp-long assembled plasmid, named "pKD46_tet", is shown schematically in Figure 4.4.

Successful assembly was verified by diagnostic colony PCR experiments using primers specific to the tetracycline resistance cassette (tetR_F and tetR_R) and primers annealing just outside of the cassette, on the pKD46 backbone (pKD46_F and pKD46_R). The sequences of these primers are shown in Table A.8 of Appendix A. PCR experiments were designed for the two combinations of tetracycline primer with backbone primer (tetR_F with pKD46_R, forming a 1997 bp product, and pKD46_F with tetR_R, forming a 1682 bp product). The reactions were set up with PCRBIO Taq Mix Red (PCR Biosystems, USA) following manufacturer's instructions. Results of diagnostic colony PCR experiments were

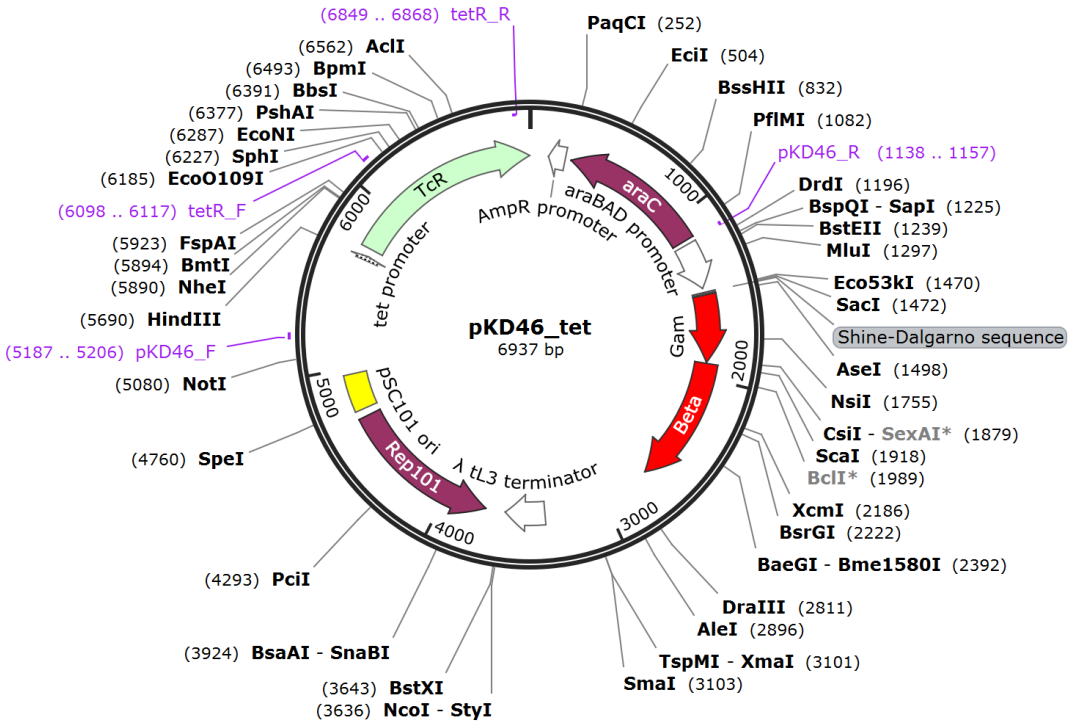

Figure 4.4: Plasmid map of the Gibson-assembled plasmid containing the tetracycline resistance cassette from pACYC184 (TcR) and the backbone sequence of pKD46. The primers used for diagnostic colony PCR experiments (tetR_F, tetR_R, pKD46_F and pKD46_R) are shown in purple along the plasmid map. The presence of the ampicillin resistance promoter (AmpR promoter) should not interfere with the transcription of the tetracycline resistance cassette, which has opposite orientation and includes its own promoter (tet promoter). The map was created in SnapGene Viewer version 6.2.1 (Insightful Science, USA).

checked with agarose gel electrophoresis.

As a second diagnostic check, the Gibson-assembled pKD46_tet plasmid DNA was digested with the single-cutting enzymes NotI and NheI (New England Biolabs, USA), of which the former cut on the pKD46 backbone upstream of the tetracycline resistance cassette, and the latter cut within the resistance cassette. The restriction enzyme digests were run as described in Section 4.2.2.2. The predicted fragment sizes for plasmid DNA digested with both enzymes were 810 bp and 6.1 kb.

4.2.3.2 Ligation

A second method was designed to overcome the ampicillin resistance of JM105 mini-Tn7-*gfp* for gene inactivations with Lambda Red recombineering using ligation. In a similar fashion to Gibson assembly, the aim was to ligate the tetracycline resistance cassette from the pACYC184 plasmid to the backbone of pKD46, which contained the Lambda Red machinery.

The vector fragment was obtained from pKD46 in the same way as for Gibson assembly, by double restriction enzyme digestion with AhdI and ApaLI. The product was run on 1% agarose gel and the 5.6 kb band was gel-purified as described above. 20 μL of the purified DNA was then incubated with 1 μL of Shrimp Alkaline Phosphatase (rSAP, New England Biolabs, USA) and 2 μL of RCutSmart (New England Biolabs, USA). The tube was incubated at 37 °C for 30 minutes and then at 65 °C for 5 minutes for inactivation of rSAP.

The tetracycline resistance cassette insert was amplified from pACYC184 by performing a similar PCR experiment to that described for the Gibson assembly. 20 bp primers were designed to anneal in similar regions of pACYC184, with a

ATG start codon upstream of the cassette and a TGA stop codon downstream of it. To ensure the orientation of the tetracycline resistance cassette was the same as that of the (removed) ampicillin resistance cassette in pKD46 (which is antiparallel to it - see Figure 4.3), the primers were changed to their reverse-complement. To create complementary strands with the pKD46 backbone region of annealing, the ApaLI and AhdI enzyme cut sites (G/TGCAC and GACnnn/n-nGTC respectively) were added before the start codon and after the stop codon respectively. The resulting primer sequences for insert PCR amplification, Ligation F and Ligation R, are shown in Table A.7 of Appendix A.

The PCR experiment for the amplification of the tetracycline resistance cassette from pACYC184 was set up and carried out in the same way as for the Gibson assembly, using Q5 High-Fidelity DNA Polymerase (New England Biolabs, USA). The PCR product was run on a 1.2% agarose gel, and the band at 1.3 kb was purified following gel band excision. The same double restriction enzyme digestion with AhdI and ApaLI was then performed on the purified DNA to create sticky ends compatible with the backbone vector. The correct overlap of the amplified pACYC184 product and the corresponding region of pKD46 was checked on SnapGene version 6.2.1 (Insightful Science, USA) using the "Linear ligation" tool.

Ligation was carried out as a 20 μL reaction containing 2 μL of T4 DNA ligase buffer, 1 μL of T4 DNA ligase (New England Biolabs, USA) and the two DNA fragments in vector to insert ratios of 1:3 and 3:1. A vector-only control was also set up. The tube containing the ligation reaction was left at 5 °C overnight, and was successively transformed into chemically-competent Dh5α competent *E. coli* (High Efficiency) (New England Biolabs, USA) as described in Section A.8.1 of Appendix A. The recovered cultures were streaked on LB agar plates

with 25 μg/mL tetracycline and incubated overnight at the permissive temperature of 30 °C. Cultures were also streaked on LB agar plates with 25 μg/mL chloramphenicol as a negative control.

4.3 Results

4.3.1 Lambda Red recombineering troubleshooting

Digestion of pKD46 plasmid DNA with the restriction enzymes AhdI and ApaLI successfully produced a 5.7 kb fragment corresponding to the desired backbone vector (Figure 4.5). However, the DNA was not fully digested, and a second band was visible just above the 5.7 kb fragment. This prevented accurate excision of the 5.7 kb fragment from the gel for further purification. The correct functioning of the restriction enzymes ApaLI and AhdI was checked on the helper plasmid pKD4, where each successfully cut the plasmid DNA into a linear fragment of 3.3 kb.

The plasmids pKD46 and pKD4 were also verified by restriction enzyme digests to troubleshoot the failure of Lambda Red recombineering experiments (Figure 4.6). In pKD46, agarose gel electrophoresis confirmed that BamHI cut the plasmid DNA into a single 6.3 kb fragment, whereas EcoRI cut at two sites, producing DNA fragments of 4.8 kb and 1.5 kb. In pKD4, agarose gel electrophoresis confirmed that the single cutter NdeI produced a 3.3 kb fragment, and that the double cutter SphI produced two DNA fragments of 1 kb and 2.3 kb.

Despite optimising the restriction enzyme digest protocol for pKD46 for the enzymes AhdI and ApaLI, and successfully purifying approximately 500 ng of high-purity digested DNA, the progress on Lambda Red recombineering experiments

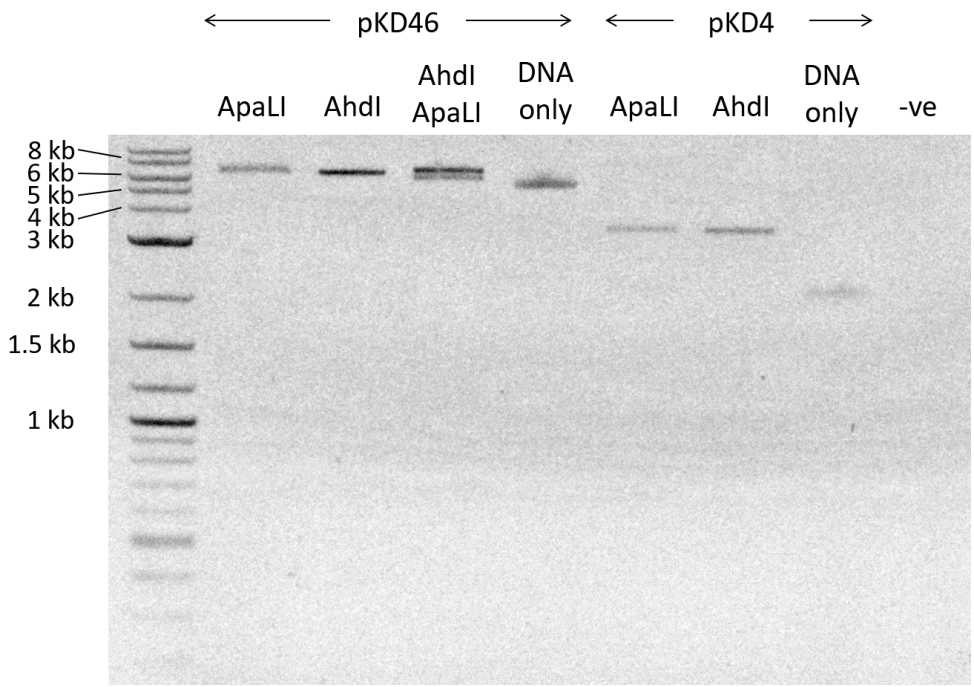

Figure 4.5: Image of the agarose gel showing the DNA fragments formed by digestion of pKD46 and pKD4 with the enzymes ApaLI and AhdI. Digestion of pKD46 with ApaLI and AhdI successfully produced a single 6.3 kb DNA fragment, whereas double digestion with both enzymes should have produced two DNA fragments of 650 bp and 5.7 kb (only the latter was observed). The presence of a 6.3 kb fragment indicated that the digestion of the plasmid DNA was not complete. Digestion of pKD4 with either ApaLI or AhdI successfully produced a single 3.3 kb DNA fragment.

was halted when the negative control plate (JM105 mini-Tn7-*gfp* on LB agar with 100 μg/mL ampicillin) showed extensive growth. This suggested the strain JM105 mini-Tn7-*gfp* was inherently ampicillin resistant, preventing successful transformation of its genomic DNA with the pKD46 plasmid DNA.

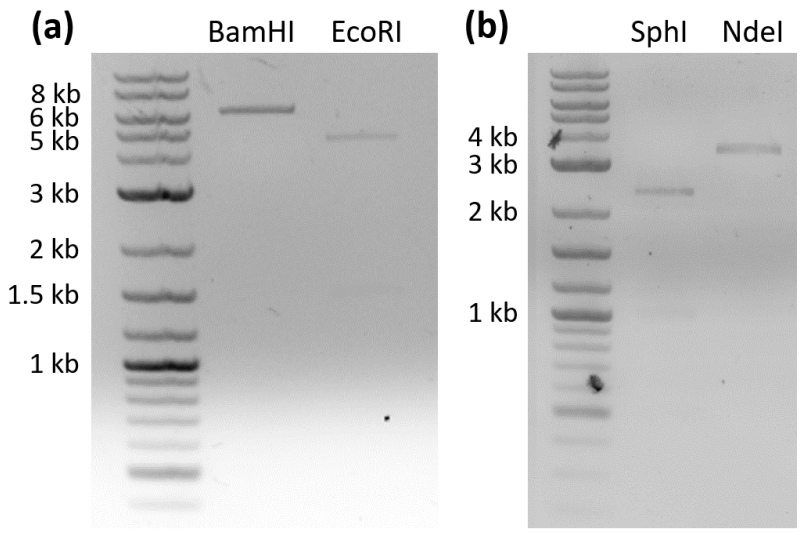

Figure 4.6: Image of the agarose gels showing the DNA fragments formed by digestion of the plasmid pKD46 with the enzymes BamHI and EcoRI (a) and of the plasmid pKD4 with the enzymes SphI and NdeI (b). Digestion of pKD46 with BamHI successfully produced a 6.6 kb DNA fragment, and digestion with EcoRI successfully produced DNA fragments of 1.5 kb and 5.1 kb. Digestion of pKD4 with SphI successfully produced DNA fragments of 1 kb and 2.3 kb, and digestion with NdeI successfully produced a unique 3.3 kb DNA fragment.

4.3.2 The ampicillin resistance of JM105 mini-Tn7-*gfp* is likely to be a leftover from the pUC19 plasmid used for the insertion of the mini-Tn7 cassette

While verifying negative control plates during Lambda Red recombineering experiments, resistance to ampicillin was observed for the strain JM105 mini-Tn7-*gfp*. This observation proved consistent across both solid and liquid media. New media batches, new ampicillin stocks (including a new carbenicillin stock) and new

bacterial stocks stored at -80 °C did not change the results. Because ampicillin resistance was not observed for the JM105 strain without the mini-Tn7 insertion (as expected from the genotype of the JM105 strain [467]), genetic diagnostic checks were designed in an attempt to identify the source of the antibiotic resistance.

Diagnostic colony PCRs were performed on 5 colonies of JM105 mini-Tn7-*gfp* to check for successful insertion of the mini-Tn7 cassette. Colonies were selected from plates streaked with 3 separate glycerol stocks. 150 bp DNA fragments were amplified in each reaction except the negative control (Figure 4.7), showing that the mini-Tn7 cassette was correctly inserted downstream of the *glmS* gene [234].

Diagnostic restriction enzyme digests were carried out on plasmid DNA purified from JM105 mini-Tn7-*gfp* (Figure 4.8). Inspection of the undigested bands revealed multiple DNA fragments, and digested bands also showed large DNA

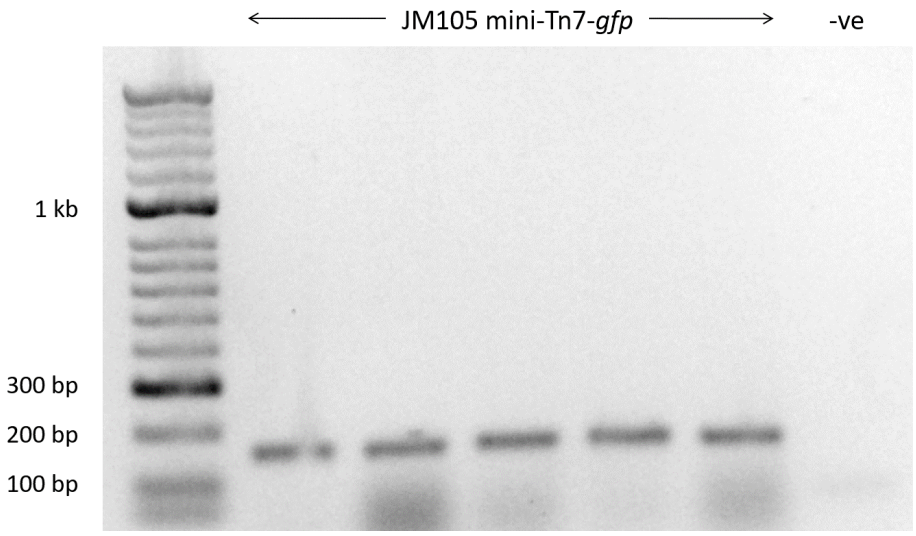

Figure 4.7: Diagnostic colony PCR on JM105 mini-Tn7-*gfp* with template DNA obtained from 5 colonies from 3 different glycerol stocks. Bands at 150 bp indicate the presence of the mini-Tn7 cassette.

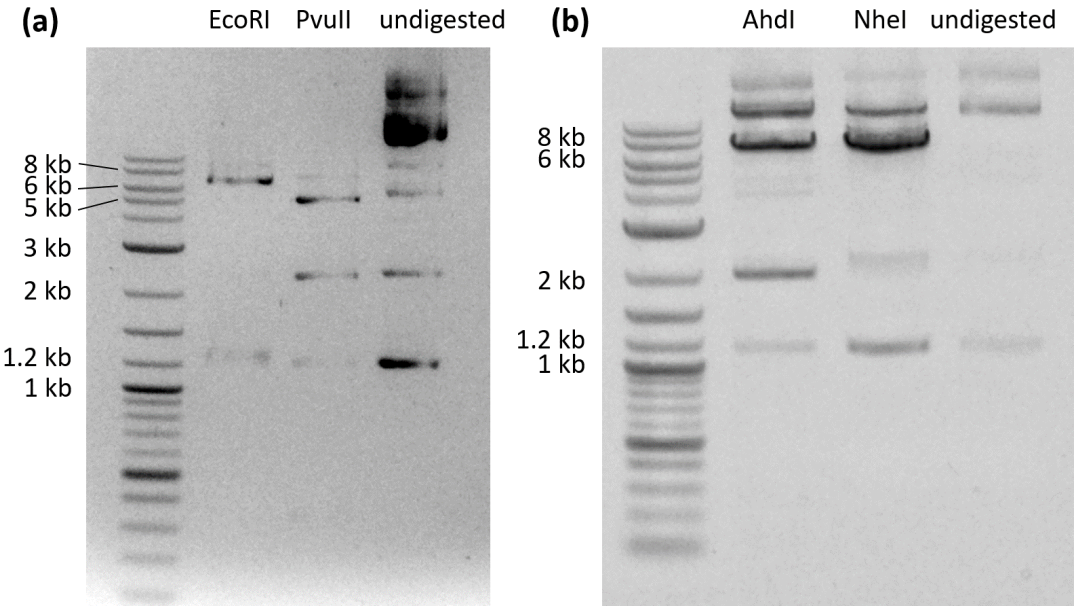

Figure 4.8: Images of agarose gels showing the DNA fragments formed by restriction digest of JM105 mini-Tn7-*gfp* plasmid DNA with the enzymes EcoRI and PvuII (a) and AhdI and NheI (b). Digestion with EcoRI produced DNA fragments of 1.2 kb, 7 kb and 8 kb, the latter of which is consistent with digestion of pUX-BF13 with EcoRI. Digestion with PvuII produced DNA fragments of 1.2 kb, 2.5 kb, 5 kb and 7 kb. The 5 kb and 8 kb fragments are consistent with those formed by digestion of the plasmid pUX-BF13 with PvuII. Digestion with AhdI and NheI both produced a 8 kb DNA fragment (on top of the various DNA fragments present in the undigested DNA). Several bands larger than 10 kb were visible, and were likely due to undigested DNA from the plasmid pUX-BF13 (size: 12.2 kb).

fragments. In particular, the 2.4 kb band obtained by digestion with PvuII was consistent with the pUC19 delivery plasmid (GenBank ID: M77789.2; total size: 2686 bp), on which the mini-Tn7-*gfp* plasmid was originally based [234], and the 8.5 kb band obtained by digestion with EcoRI was consistent with the pUX-BF13 helper plasmid containing Tn7 transposon genes ([468]; total size: 12.256 kb).

Sequencing of the plasmid DNA revealed the presence of 3 distinct plasmids within the JM105 mini-Tn7-*gfp* DNA. The first two plasmids were 4154 bp and 2082 bp long, and only contained the high copy number ColE1 /pMB1/ pBR322/ pUC origin of replication (automatically detected by SnapGene). The third plasmid (shown in Figure 4.9) was 15,649 bp long and included ampicillin, gentamicin and chloramphenicol resistance cassettes, as well as a *gfp* fragment compatible with the GFPmut3 fluorescent protein used in the mini-Tn7-*gfp* transposon delivery system by Lambertsen et al. [234]. The plasmid also included the *traJ* gene, which is used for conjugative transfer of genetic material [469]. This sequence was also present in the helper plasmid pUX-BF13 used for the mini-Tn7-*gfp* insertion. These observations suggested that fragments from the machinery used to construct the JM105 mini-Tn7-*gfp* strain were still present in its genome. This was likely to be the reason why the Lambda Red recombineering approach described previously did not work as intended.

4.3.3 Gibson assembly troubleshooting

Gibson assembly was attempted following the protocol outlined in Section 4.2.3.1. The tetracycline resistance cassette was amplified successfully from pACYC184 (Figure 4.10a), and assembled with the backbone vector from pKD46. Various vector to insert ratios were tested, ranging from 1:3 to 3:1. Seemingly successful Gibson assembly reactions, identified by growth of colonies on LB agar plates with 20 μg/mL tetracycline, were checked by colony PCR as discussed in Section 4.2.3.1, but proved unsuccessful (Figure 4.10b).

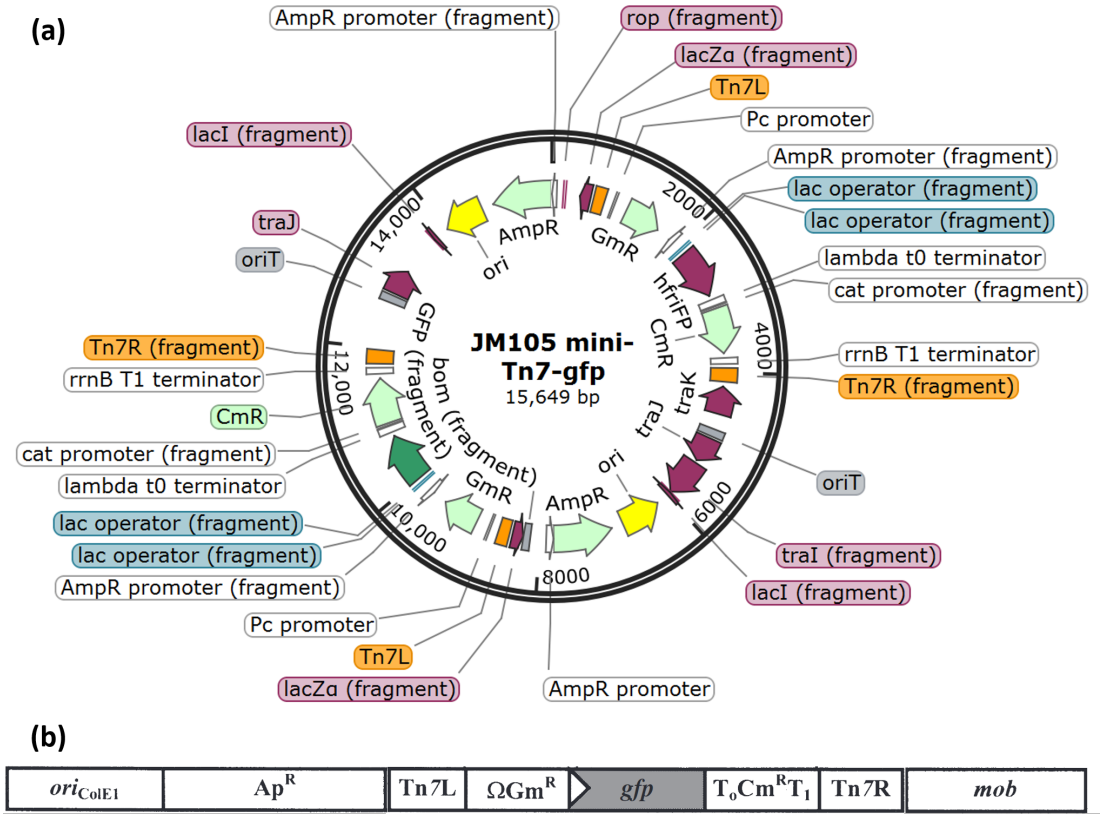

Figure 4.9: (a) Plasmid map of the largest plasmid obtained by sequencing JM105 mini-Tn7-*gfp* plasmid DNA. The 15,549 bp plasmid included resistance cassettes for ampicillin (AmpR), gentamicin (GmR) and chloramphenicol (CmR), GFP coding regions as well as mini-Tn7 elements (Tn7R and Tn7L). The plasmid map was created in SnapGene Viewer version 6.2.1 (Insightful Science, USA). (b) Structure of the mini-Tn7 delivery plasmid used in the JM105 mini-Tn7-*gfp* strain, encoding ampicillin resistance (ApR) and fluorescence from the GFP protein expressed by the constitutive promoter $P_{A1/04/03}$ [470]. Diagram adapted from [234]. The features shown in the plasmid map (a) correspond to those in the mini-Tn7-*gfp* delivery plasmid (b), suggesting the origin of the ampicillin resistance observed in the JM105 mini-Tn7-*gfp* strain.

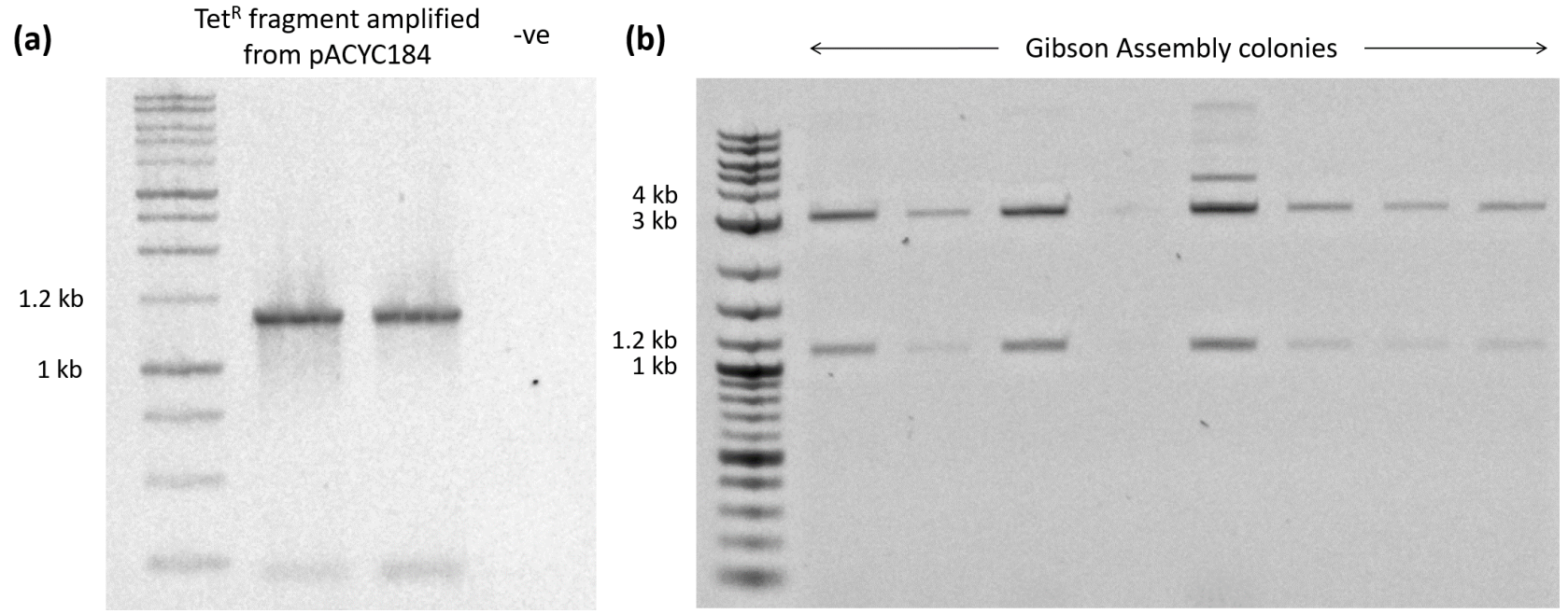

Figure 4.10: (a) Agarose gel showing the DNA fragments containing the tetracycline resistance cassette, amplified from pACYC184 using PCR. (b) Agarose gel showing the DNA fragments produced by restriction digest of the Gibson assembly colonies with the enzymes NotI and NheI. The 1.1 kb and 3.1 kb DNA fragments are compatible with digestion of the plasmid pACYC184 with the enzyme NheI, and were therefore not significant of a successful Gibson assembly reaction.

4.3.4 Ligation troubleshooting

Ligation of the backbone vector from pKD46 with the tetracycline resistance cassette from pACYC184 was also attempted following the protocol in Section 4.2.3.2. The tetracycline resistance cassette amplified by PCR was purified straight from the PCR tube and also after being run on an agarose gel (Figure 4.11a). These purified DNA fragments were digested with AhdI and ApaLI and ligated with the pKD46 backbone vector without success.

Restriction enzyme digests were also set up with pACYC184 fragments purified using both techniques, but this time with whole, undigested DNA from pKD46 (Figure 4.11b). This digest created additional DNA fragments on top of the required 5.6 kb double-digest fragment from pKD46, but the desired fragment could still be purified by excision of the relevant band on agarose gel electrophoresis.

The mixture of pACYC184 amplified fragment and pKD46 whole-plasmid DNA, digested simultaneously with AhdI and ApaLI, was purified from the PCR tube straight after digestion, and digested again with rSAP as described in Section 4.2.3.2. Ligation reactions were set up with vector to insert ratios of 3:1 and 1:3, using insert DNA purified from both PCR tubes and gel band excision. After transformation of the ligated products with both chemically competent and electrocompetent *E. coli*, growth was only observed on plates containing insert DNA purified from PCR tubes. However, a first re-streak on solid medium containing chloramphenicol showed resistance to chloramphenicol exhibited by all colonies, conferred by leftover DNA from pACYC184. This confirmed the failure of the ligation experiment.

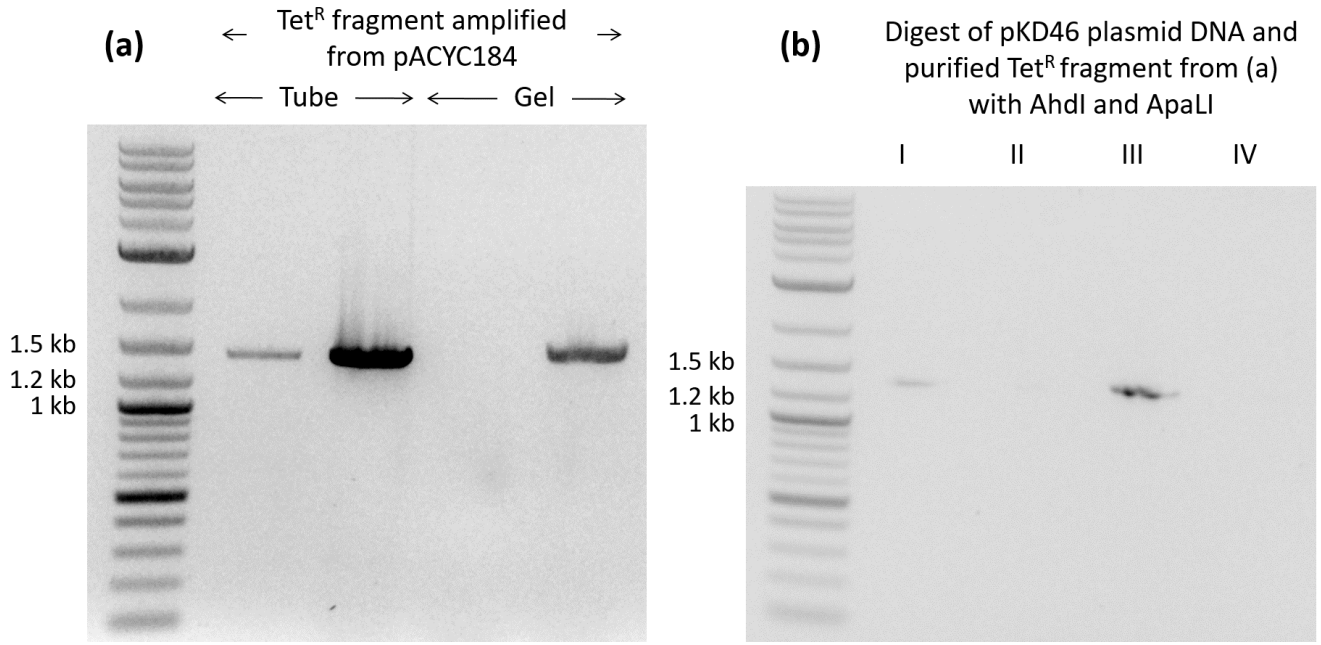

Figure 4.11: (a) Agarose gel showing the tetracycline resistance cassette amplified by PCR from pACYC184 and purified either from the PCR tubes straight after PCR amplification (Tube) or by gel excision after running the DNA on agarose gel (Gel). (b) Agarose gel showing the DNA fragments produced by digestion of the tetracycline resistance cassette from pACYC184 and of pKD46 plasmid DNA. Digest (I) was set up with a vector to insert ratio of 3:1 and column purified insert DNA; digest (II) was set up with a vector to insert ratio of 3:1 and gel purified insert DNA; digest (III) was set up with a vector to insert ratio of 1:3 and column purified insert DNA; digest (IV) was set up with a vector to insert ratio of 1:3 and gel purified insert DNA. The digested DNA was column purified before visualisation with agarose gel electrophoresis.

4.4 Discussion

This work described a genetic engineering platform for single-gene inactivations in the background strain JM105 mini-Tn7-*gfp*. This would have enabled high-resolution imaging of whole biofilms with subcellular resolution using the Mesolens, as well as precise quantification of nutrient-transporting channel width and fractal morphology using the methods described in Chapters 2 and 3. However, the Lambda Red recombineering protocol based on Datsenko and Wanner [402] initially failed due to an unexpected ampicillin resistance observed for JM105 mini-Tn7-*gfp*.

Ampicillin resistance in JM105 mini-Tn7-*gfp* was likely due to leftover of genetic material from the cloning experiments used to insert the mini-Tn7 cassette into the chromosome of JM105 [233], [234]. Attempts to cure the plasmids responsible for this resistance by spontaneous segregation through subsequent sub-culturing on non-selective solid growth medium proved unsuccessful, possibly owing to the high copy number of the plasmid pUC19 [471]. Interestingly, the 15,549 bp plasmid encoding for ampicillin resistance isolated from JM105 mini-Tn7-*gfp* is a dimer, which would theoretically increase the chances of spontaneous loss [472]. Other plasmid curing methods, such as serial batch culture in non-selective growth medium or growth at increased temperatures [473], could possibly eliminate the ampicillin resistance from JM105 mini-Tn7-*gfp*.

During the preparation of the backbone vector from pKD46 by restriction enzyme digestion, the purification of digested DNA from agarose gel slice excision produced extremely low yields. This could be due to the fact that pKD46 is a low copy number plasmid [402]. A number of troubleshooting techniques were employed to overcome this issue, but to no avail. For example, the purification

of plasmid DNA from the Dh5α strain was carried out in modified LB broth containing 30 g/L yeast extract, since high contents of yeast extract in the growth medium are associated with increased plasmid DNA yield [474]. Furthermore, restriction enzyme digests of pKD46 with AhdI and ApaLI were carried out with as much pKD46 plasmid DNA as possible, and were run for extended periods of time (minimum three hours). The addition of restriction enzymes was performed both simultaneously (with both AhdI and ApaLI added to the tube at the start of the reaction) and sequentially (by adding one enzyme, excising and purifying the digested DNA band and adding the second enzyme, or alternatively by adding one enzyme for one 1.5 hours and then the other for a further 2 hours). DNA purification was also performed both directly from PCR tubes (on the whole digested DNA) and after agarose gel electrophoresis after excision of the relevant DNA band. While the former purification method increased the chances of undigested DNA being used in downstream experiments, it was hypothesised that this issue could be circumvented by screening of transformant colonies. Finally, heat inactivation of both AhdI and ApaLI enzymes was performed at both 65 °C and 80 °C for 20 minutes after the double restriction enzyme digest reactions, in an attempt to increase transformation efficiency [475], but without success.

Other changes in the Lambda Red protocol could be implemented, for example by changing the restriction site on pKD46 to include the promoter of ampicillin resistance genes by changing the restriction enzyme from ApaLI to AarI - BfuAI - BspMI, or by isolating the backbone vector from pKD46 using PCR-only methods instead of restriction enzyme digestion. Gene inactivations in the JM105 mini-Tn7-*gfp* strain could also be obtained by P1 phage transduction of the mutated region of the chromosome [476] from the corresponding Keio collection mutant strains, though this method can lead to frequent cross-contamination errors [477].

Finally, gene inactivations could be carried out using the clustered regularly interspaced short palindromic repeats–CRISPR-associated system (CRISPR-Cas9), by which the commonly occurring CRISPR DNA sequences are recognised and split by the enzyme Cas9 [478]. While this technique has been used extensively in genome editing thanks to its simplicity [479], [480], it is also prone to off-target mutations [481], [482].

While Lambda Red recombineering is a fast and reliable method for genetic engineering in *E. coli*, it can often require optimisation. For example, sub-optimal arabinose induction of recombinase genes can reduce recombination efficiency [483]. Successful Lambda Red recombineering for the inactivation of genes in the *E. coli* strain JM105 mini-Tn7-*gfp* would allow for high-throughput phenotypic analysis of mature biofilms using fluorescence mesoscopy. The single-gene inactivations described in this Chapter could be used to study the effect of constituent cell shape on biofilm morphology and intra-colony channel architecture while taking advantage of the increased field of view and resolution offered by the Mesolens. Nonetheless, the results obtained using BW25113 derivative strains described in Chapter 3 offered important insights into the morphological complexity of nutrient-transporting channels in *E. coli*.

4.5 Conclusions

In this Chapter, attempts with Lambda Red recombineering for gene inactivations in the *E. coli* strain JM105 mini-Tn7-*gfp* were characterised. The purification of backbone vector DNA from pKD46 proved to be the biggest hurdle to the success of this experiment, together with the previously uncharacterised ampicillin resistance of the host strain JM105 mini-Tn7-*gfp*. Extensive troubleshooting was

carried out to identify the origin of this resistance, which likely originated from cloning steps used to insert the mini-Tn7-*gfp* cassette into the strain during its construction. Optimisation attempts were also undertaken to improve the yield of backone vector DNA purification, but to no avail. Different gene-inactivation techniques such as CRISPR-Cas9 could be tested instead, but they would require extensive diagnostics to rule out off-target effects.

Chapter 5

Concluding remarks and directions for future work

This Chapter summarises and contextualises the findings presented in Chapters 2, 3 and 4. Recommendations for future work are also provided.

5.1 Summary

The work presented in this thesis was centred on the imaging and quantitative analysis of nutrient-transporting channel networks in *E. coli*. This was achieved by imaging mature biofilms formed by *E. coli* strains with different cell morphologies and on different growth environments with fluorescence microscopy and mesoscopy, and by using image analysis tools to measure the width of individual channels and to quantify their complexity with fractal geometry methods. An experimental framework for individual gene deletions in an *E. coli* strain optimised for high-throughput mesoscopy was also proposed in an attempt to investigate the genetic determinants of channel formation.

In Chapter 2, a quantification of the recently discovered nutrient-transporting channel network in *E. coli* was provided. The Mesolens was used to image *E. coli* JM105 mini-Tn7-*gfp* biofilms grown under different environmental conditions of nutrient availability and substrate stiffness, and an open-source image analysis pipeline was developed to measure channel width at different positions within the biofilm. The pipeline combined elements from the FIJI image analysis software with a Python programming script, allowing for the identification and measurement of hundreds of individual channels, with widths as narrow as 10 μm. The width of these nutrient-transporting channels was on average 25% larger for biofilms grown on glucose-limited substrates than for those grown on ammonium-limited substrates, suggesting that channels might be particularly important for the transport of carbon-based nutrients. Channel density in biofilms grown on soft, nutrient-rich medium was considerably higher than that of biofilms grown on stiffer substrates. Further analysis also revealed that channel width increased non-linearly from the centre to the edge of the biofilms under all growth conditions, possibly in an attempt to maximise fluid flow of nutrients from the

surrounding growth environment towards the innermost regions of the biofilm.

In Chapter 3, the morphological complexity of nutrient-transporting channels was quantified for the first time using fractal geometry. The effect of constituent cell shape on channel architecture was investigated by imaging mature biofilms formed by the *E. coli* BW25113 mutant strains Δ*amiA*, Δ*guaB*, Δ*ompR* and Δ*ydgD*, whose single-gene deletions affected the cell phenotype. Biofilms formed by all strains had a fractal complexity comparable to that of computer-generated fractals, but cell shape alone could not explain the differences in channel architecture observed between different strains. For the long-cell mutant strain Δ*guaB* and the wide-cell mutant strain Δ*ompR*, biofilm fractal complexity was significantly higher when the biofilms were grown on nutrient-rich substrates than when they were grown on nutrient-limited conditions. The peculiar biofilm morphology exhibited by the Δ*guaB* mutant strain was investigated by staining of the extracellular matrix, but no difference in matrix production was identified between the mutant strain and the parental strain, BW25113. Channel architecture in the mutant strain Δ*ompR* was affected by nutrient availability on nutrient-limited growth medium, and by the presence of salt. Due to the role of *ompR* in osmotic stress response, the architecture of channel networks in growth substrates with different osmolalities were also investigated, but the reduction in complexity observed for Δ*ompR* biofilms was comparable to that observed for the parental strain, BW25113.

Finally, Chapter 4 presented an experimental genetic engineering framework designed to combine the high-throughput imaging capabilities of the Mesolens with the morphological properties of biofilms formed by cell-shape mutant strains. Gene knockout experiments were designed in the background strain JM105 mini-Tn7-*gfp*, which is more suitable for Mesolens imaging than BW25113 thanks to

its superior structural resilience to immersion with mounting medium. Genetic engineering experiments were firstly performed using the Lambda Red-mediated recombineering method proposed by Datsenko and Wanner, but this route was abandoned when ampicillin resistance was unexpectedly observed for JM105 mini-Tn7-*gfp*. Plasmid DNA sequencing revealed that the resistance was likely to be a remnant of cloning experiments performed to insert the mini-Tn7 cassette into the host chromosome. The Lambda Red gene-knockout framework was then modified to substitute the ampicillin resistance cassette in the helper plasmid pKD46 with a tetracycline resistance from a different plasmid, but Gibson assembly and ligation attempts at this modification were unsuccessful.

5.2 Recommendations for future work

The central theme of this work is the quantitative characterisation of the recently-discovered network of nutrient-transporting channels in *E. coli*. The width and fractal complexity of these channels were quantified for the first time in Chapters 2 and 3 using fluorescence imaging and image analysis. Preliminary checks towards the investigation of genetic determinants of channel formation using genetic engineering were also introduced in Chapter 4.

The channel width measurements presented in Chapter 2 could be further improved by imaging biofilms with the Mesolens in confocal laser scanning mode, which would reject out-of-focus light originating from different axial planes and improve the sharpness of nutrient-transporting channels. This method would also allow to track individual channels in the axial dimension, and allow to study the variation in channel width depending on the distance from the growth substrate (and, therefore, the nutrient source). At the time of investigation, this avenue was

not pursued due to the considerably longer image acquisition time required for confocal laser scanning mode (several hours for a single biofilm z-stack) compared to widefield epi-fluorescence (approximately two minutes per biofilm). However, during my work, a lightsheet mode was developed for the Mesolens [108]. This would provide optical sectioning for high-resolution 3D imaging of these large biofilms, with sub-cellular resolution throughout, at speeds much higher than the confocal laser scanning mode can generate.

The study on the effect of bacterial cell shape on the fractal complexity of nutrient-transporting channels presented in Chapter 3 would benefit from the complementation of each mutant strain with the corresponding deleted gene. This would allow for the precise attribution of the observed biofilm phenotypes to the loss of the disrupted coding sequences, and rule out polar effects on downstream genes or extragenic mutations. It would also be interesting to study biofilms formed by different *E. coli* cell phenotypes, such as chains of cells and round cells. Furthermore, there are many more molecular and physiochemical mechanisms which could be responsible for channel formation and architecture. These could be investigated for example by imaging biofilms formed by *E. coli* strains involving mutations in genes affecting biofilm formation and surface features. In addition to this, a library of strains containing transcriptional GFP fusions could be used to detect the activity of promoters of genes involved in biofilm formation in real time using fluorescence microscopy, in order to investigate whether these genes are involved in channel formation. This would constitute an important step towards elucidating the genetic determinants of channel formation in *E. coli*.

The disruption of genes involved in biofilm formation within the host strain JM105 mini-Tn7-*gfp* would provide a platform for the quantitative analysis of biofilm morphology with the Mesolens, which provides subcellular resolution across whole

mature biofilms. While the Lambda Red-based recombineering techniques explored in Chapter 4 were not successful for the inactivation of genes which affect cell shape phenotype, a number of alternative methods were suggested that may achieve this aim, including P1 phage transduction and CRISPR-Cas9.

While the work presented in this thesis is specific to *E. coli*, the presence of complex patterns is ubiquitous in biofilms. The methods described here form an important addition to the arsenal of image analysis tools available to quantify these patterns in any microbiological genus. Finally, the findings presented in these chapters further our understanding of the principles governing channel formation and development, and could inform the investigation of similar morphological structures in other bacterial species.

That's plenty!

Victor McDade

Appendix A

Materials and methods

A.1 Growth media

Molecular grade reagents were purchased from Merck (Germany), Thermo Fisher Scientific (USA) and Melford (UK) unless otherwise specified. Liquid and solid media were prepared in Duran bottles using distilled water (for LB and SOC media) and distilled deionised water (for M9-based media) as described in Table A.1. Media pH was adjusted to 7.0 using 1M NaOH solution. Media was sterilised by autoclaving at 121 °C at 100 kPA. Minimal M9 medium was prepared in a 5× concentrated solution then diluted to 1× with distilled deionised water. The 1× solution was then supplemented with 1 mM $MgSO_4 \cdot 7H_2O$, 0.2% (w/v) glucose

Name	**Components**
Lysogeny Broth (LB)	tryptone 10 g/L, yeast extract 5 g/L, NaCl 10 g/L
SOC	tryptone 20 g/L, yeast extract 5 g/L, NaCl 0.6 g/L, KCl 0.2 g/L
M9 medium (5×)	Na_2HPO_4 30 g/L, KH_2PO_4 15 g/L, NH_4Cl 5 g/L, NaCl 2.5 g/L

Table A.1: Growth media recipes used in this work.

and 0.00005% (w/v) thiamine. For plasmid DNA purification, the recipe for LB medium was modified to include 30 g/L yeast extract.

Solid substrates were made by adding 20 g/L of agar prior to autoclaving unless otherwise specified. Solid media was melted using a microwave and stored in a 55 °C water bath prior to use.

A.2 Strains and plasmids

A.2.1 Bacterial strains

The two principal strains used in this work are *E. coli* JM105 mini-Tn7-*gfp* and BW25113, both K-12 derivatives. Details of the strains are given in Table A.2. JM105 mini-Tn7-*gfp* is based on the K-12 derivative JM105, and contains a *gfp* insertion within a mini-Tn7 transposon system, providing GFP fluorescence [234]. BW25113 is the parental strain for the Keio collection. Strains containing single-gene knockouts of the genes *amiA, guaB, ompR* and *ydgD* (referred to as "Keio mutants" throughout this thesis) were selected from the Keio collection [401]. Strains were stored as 25% glycerol stocks at -80 °C.

A.2.2 Plasmids

The plasmids used in this work are listed in Table A.3. The pAJR145 plasmid was transformed into BW25113 and the Keio mutant strains to provide GFP fluorescence, whereas the plasmids pKD46, pKD4 and pACYC184 were used in cloning experiments for Lambda Red recombination.

Name	**Genotype**	**Reference**
JM105	*endA1, glnV44, sbcB15, rpsL, thi-1,* Δ*(lac-proAB), [F´ traD36, proAB*$^{+}$*, lacI*^{q} *lacZ*Δ*M15] hsdR4* (r_K^- m_K^+)	[467]
BW25113	*F-,* Δ*(araD-araB)567,* Δ*lacZ4787*(::rrnB-3), λ-, *rph-1,* Δ*(rhaD-rhaB)568, hsdR514*	[402]
BW25113 / pAJR145		This study
BW25113 Δ*amiA*::kan	BW25113 Δ*amiA764::kan*	[401]
BW25113 Δ*guaB*::kan	BW25113 Δ*guaB757::kan*	[401]
BW25113 Δ*ompR*::kan	BW25113 Δ*ompR739::kan*	[401]
BW25113 Δ*ydgD*::kan	BW25113 Δ*ydgD746::kan*	[401]
BW25113 Δ*amiA*::kan / pAJR145		This study
BW25113 Δ*guaB*::kan / pAJR145		This study
BW25113 Δ*ompR*::kan / pAJR145		This study
BW25113 Δ*ydgD*::kan / pAJR145		This study
DH5α	F' *endA1, glnV44, thi-1, recA1, relA1, gyrA96, deoR, nupG, purB20* φ80d*lacZ*ΔM15 Δ(*lacZYA-argF*)U169, *hsdR17*(r_K^- m_K^+), λ^-	[484]

Table A.2: Bacterial strains used in this work.

Name	Description	Antibiotic selection	Reference
pAJR145	pACYC184 *rpsM::gfp+* transcriptional fusion	chloramphenicol	[410]
pKD46	Lambda Red recombinase machinery	ampicillin	[402]
pKD4	FRT-flanked kanamycin cassette	ampicillin, kanamycin	[402]
pACYC184	Cloning vector	chloramphenicol, tetracycline	[485]

Table A.3: Plasmids used for genetic manipulation in this work.

A.2.3 Growth conditions

The BW25113 strain was grown in LB broth at 37 °C, and Keio mutant strains were grown in LB broth with 50 μg/mL kanamycin. After transformation with the pAJR145 plasmid, strains were grown with the addition of 25 μg/mL chloramphenicol. The JM105 mini-Tn7-*gfp* strain was grown at 37 °C in LB broth with 25 μg/mL gentamicin. Strains containing the pKD46 plasmid were grown in LB broth with 100 μg/mL ampicillin at the permissive temperature of 30 °C, to avoid plasmid curing. Strains containing the pKD4 plasmid were grown at 37 °C in LB with 50 μg/mL kanamycin.

Liquid cultures were prepared by inoculating a single colony from an agar plate into 5-10 mL of LB broth containing the appropriate antibiotics. Cultures were grown overnight at 37 °C (unless otherwise specified) in an aerated shaking incubator with shaking speed of 225 rpm. Mid-exponential growth phase cultures were obtained by diluting overnight cultures 1:100 into 5 mL of fresh LB broth containing the appropriate antibiotics, and incubating this new culture in the conditions specified above until the optical density (OD) reached a value between

0.4 and 0.6.

A.2.4 Bacterial growth curves

Growth curves were acquired on a BioTek Synergy HT plate reader (Agilent Technologies, USA) from 200 μL aliquots of diluted liquid culture. Aliquots were added in triplicate to a black Nunc MicroWell 96-well optical-bottom plate with polymer base (Thermo Fisher Scientific, USA). Absorbance (OD_{600}) measurements were performed every 15 minutes for 24 hours, with the plate being held at 37 °C and shaken continuously.

A.3 Antibiotics

Antibiotics were added to liquid media and molten solid media where required in the final concentrations shown in Table A.4. Antibiotic stocks were prepared in small 1 mL aliquots in a 1000x concentration and stored at -20 °C. They were thawed before use and added in the appropriate concentration.

Name	**Description**	**Solvent**	**Concentration**
ampicillin	β-lactam	water	100 μg/mL
chloramphenicol	aminoglycoside	ethanol	25 μg/mL
gentamicin	aminoglycoside	water	25 μg/mL
kanamycin	aminoglycoside	water	50 μg/mL
nalidixic acid	DNA gyrase inhibitor	1M NaOH	30 μg/mL
stremptomycin	aminoglycoside	water	100 μg/mL
tetracycline	tetracycline	water	25 μg/mL

Table A.4: Antibiotic stocks and concentrations.

A.4 Primers

All primers were purchased as 25 nmole DNA oligos from IDT (Integrated DNA Technologies, USA), and diluted to 100 μM and 10 μM stock solutions using RNAse-free water. Melting temperatures for each primer sequence were checked using the New England Biolabs Tm calculator website [486]. Primers were designed to have a GC (guanine-cytosine) content between 40% and 60%, and melting temperatures within 5 °C of each other for plasmids constructed for the same gene.

A.4.1 Genetic check of Keio mutant strains

Primers used for genetic check of the Keio mutants are shown in Table A.5. They were designed to anneal upstream and downstream to each gene of interest, or inside the kanamycin resistance cassette.

A.4.2 Gene knockouts by Lambda Red recombineering

Primers for Lambda Red recombineering experiments are shown in Table A.6. In particular, each primer consisted of two regions. The 5' ends consisted of 36-50 nucleotide regions of homology to the target gene. The 3' ends consisted of 20 nucleotides used as priming sites for amplification of the ampicillin resistance cassette on pKD4. These were P1 (GTGTAGGCTGGAGCTGCTTC) for the reverse primers and P2 (ATGGGAATTAGCCATGGTCC) for the forward primers. Melting temperatures for the priming sites, which anneal to the pKD4 plasmid, are 68 °C for P1 and 65 °C for P2. The P1 and P2 priming sites were taken from Datsenko and Wanner [402].

Name	**Primer sequence (5' - 3')**	**Tm (°C)**
k1	CAGTCATAGCCGAATAGCCT	64
k2	CGGTGCCCTGAATGAACTGC	69
amiA F	TCTCAACAGCAAACCGTCGT	67
amiA R	GTTTAACCTGGTGTGCGTCG	67
cysC F	TCTGGTTCGTCGCCACTTTC	68
cysC R	TTACTTTGACGAACCGGGCA	67
guaB F	GATGCAATCGGTTACGCTCT	65
guaB R	GGATGCGATGCTTATGAATG	61
minC F	CGCGCTGGCGATGATTAATAG	66
minC R	CCCTTTGCCCGAAGTAACAAC	66
ompR F	TAGCTGGTGACGAACGTGAG	67
ompR R	GCGAACAGCAAGGTGACGAT	68
rodZ F	GATGGTTCACCGGCATCTCA	67
rodZ R	CAATCGGCACATTCCCAACG	67
tolB F	CAGGCAGAGCAATCATCAGC	66
tolB R	TGGGCCATCGGTCCAGATAA	68
ydgD F	ACTTTCATCCCGTCCCGTCT	68
ydgD R	ATTGGCCTGGTCTTGCTGTT	67

Table A.5: Primers used for the genetic check of Keio mutant strains. The k1 and k2 primers [402] anneal upstream and downstream of the kanamycin resistance cassette inserted in the place of each knocked-out gene. The other primers are designed to anneal upstream (F) and downstream (R) to the gene of interest.

Name	Primer sequence (5' - 3')
amiA_del F	CTCACTTCGCGCCGCCAGGTGCTGAAAGCCGGTTTGGCTGatgggaattagccatggtcc
amiA_del R	ATCTGTTTGCACCAGATCAAACAGCACTTGTTGCAATAGGgtgtaggctggagctgcttc
cysC_del F	CGTCGTCTGGCATAGCCATCCGGTCACTGTGCAACAACGCatgggaattagccatggtcc
cysC_del R	ATTGAGATGAATTTCTGCCGATTCAGGCGCTTCGTAAACGgtgtaggctggagctgcttc
guaB_del F	GCTAAAGAAGCTCTGACGTTTGACGACGTTCTCCTCGTTCCTGCatgggaattagccatggtcc
guaB_del R	CTCTTTAGTAATGGTCACGTCGTGAACGTGGCTTTCCTGAATGCgtgtaggctggagctgcttc
minC_del F	CCAATCGAGCTTAAAGGCAGTAGCTTCACTTTATCTGTGGTTCATCTGCatgggaattagccatggtcc
minC_del R	CGCCGCTTTGCCATAAAATTCTGCTGGGATTTGATCACTCAGCCAGTATgtgtaggctggagctgcttc
ompR_del F	TACAAGATTCTGGTGGTCGATGACGACATGCGCCTGCGatgggaattagccatggtcc
ompR_del R	GCCGTCCGGTACAAAGACGTAGCCCAGACCCCAGACGGgtgtaggctggagctgcttc
rodZ_del F	GCTCGCCTGCGTAATGCTCGCGAACAACTAGGACTTAGTCatgggaattagccatggtcc
rodZ_del R	GGCATTGAGGGTCAGACGCGCAACCTGGTTAGTTCTGATAgtgtaggctggagctgcttc
tolB_del F	CGACCAGGCAGGGAATTTGACCTGTCCATCAGTTGCCGatgggaattagccatggtcc
tolB_del R	CTCATACTGTGGGCATCAGTTCTGCATGCTGAAGTCCGgtgtaggctggagctgcttc
ydgD_del F	ATTGCTGTAGTGTTGGGTGCAATTAGTTTGACGTCTGCatgggaattagccatggtcc
ydgD_del R	GGTAACAGAAATGGCCCGGTTATCGGCGCGCCAGCGATgtgtaggctggagctgcttc

Table A.6: Primers used for the amplification of the kanamycin reistance cassette from the plasmid pKD4 for Lambda Red recombineering. Lowercase nucleotide sequences correspond to the priming sites P1 and P2 on the plasmid pKD4. Uppercase nucleotide sequences correspond to homology regions upstream and downstream of the gene of interest.

A.4.3 Cloning

Primers were designed for Gibson assembly and ligation experiments to substitute the ampicillin resistance cassette in plasmid pKD46 with a tetracycline resistance cassette from plasmid pACYC184. The primers used to amplify the tetracycline resistance cassette in these experiments are shown in Table A.7.

A.4.4 Diagnostic colony PCR experiments

Colony PCR experiments were used as a diagnostic tool to check some specific regions in the genome of the strains used in this study, or to investigate the success of cloning experiments. The primers used to check successful insertion of the mini-Tn7 cassette into JM105 were taken from Lambertsen et al. [234]. The other primers were designed using the Eurofins Primer Design Tool (`https://eurofinsgenomics.eu/en/ecom/tools/pcr-primer-design/`). The primer sequences are shown in Table A.8.

Name	**Primer sequence (5' - 3')**	**Tm (°C)**
Gibson F	atccatagttgcctgactccTAATTCTCATGTTTGACAG CTTATCATCGATAAGCTTTAATGCGGTAGTT TATCACAG	67
Gibson R	gatgctgaagatcagttgggTCAGGTCGAGGTGGCCCG GC	68
Ligation F	GACTACGAGTCTCACAGTTCTCCGCAAGAAT	56
Ligation R	CGGCCGTGCACATGTAGCACCTGAAGTCAGC	55

Table A.7: Primers used for Gibson assembly and ligation cloning experiments. Lowercase nucleotide sequences in the Gibson primers correspond to the fragments annealing to pACYC184.

Name	Primer sequence (5' - 3')	Tm (°C)
glmS	AACCTGGCAAATCGGTTAC	63
mini-Tn7	CAGCATAACTGGACTGATTTCAG	63
tetR_F	GCCTATATCGCCGACATCAC	65
tetR_R	GCCTACAATCCATGCCAACC	67
ampR_R	CAACTTTATCCGCCTCCATC	53
ampR_R	CGCCGCATACACTATTCTCA	53
pKD46_F	CAGTGAATGGGGGTAAATGG	63
pKD46_R	AATGGCGGGAGTATGAAAAG	62

Table A.8: Primers used for diagnostic colony PCR experiments.

A.5 Polymerase Chain Reaction

PCR experiments were carried out following manufacturer's protocols in 0.2 mL PCR tubes (VWR, USA) using a DNA Engine Thermal Cycler (BioRad, USA) for routine PCR experiments and with an Applied Biosystems Veriti Dx Thermal Cycler (Thermo Fisher Scientific, USA) for temperature gradient PCR experiments. Thermolycling conditions used in PCR experiments are shown in Table A.9.

A.6 DNA sequencing

A.6.1 Sanger amplicon sequencing

For Sanger amplicon DNA sequencing, purified PCR products were diluted to 10 ng/μL using nuclease-free water. For the sequencing of each product, 15 μL of purified diluted DNA was added to 2 μL of primer, giving two tubes for each DNA (one with forward primer, and one with reverse primer). Samples were sequenced

PCRBIO Taq Mix Red

Reaction Setup	**Thermocycling conditions**
2x PCRBIO Taq Mix Red 25 μL	Denaturation (95 °C, 1 min)
10 μM Forward primer 1 μL	Denaturation (95 °C, 30 s)
10 μM Reverse primer 1 μL	Annealing (Tm -5 °C, 30 s)
Template DNA <100 ng	Extension (72 °C, 1-2 min)
RNAse free water (to 50 μL)	[*30 cycles*]
	Extension (72 °C, 3 min)

Q5 High-fidelity DNA Polymerase

Reaction Setup	**Thermocycling conditions**
5x Q5 Buffer 10 μL	Denaturation (98 °C, 30 s)
5x GC Enhancer 10 μL	Denaturation (98 °C, 10 s)
10 mM dNTPs 1 μL	Annealing (* °C, 20 s)
10 μM Forward primer 2.5 μL	Extension (72 °C, 20-30 s/kbp)
10 μM Reverse primer 2.5 μL	[*30 cycles*]
Template DNA <100 ng	Extension (72 °C, 2 min)
Q5 DNA Polymerase 0.5 μL	
RNAse free water (to 50 μL)	

Table A.9: Reaction setup and thermocycling conditions for PCR experiments carried out with PCRBIO Taq Mix Red (PCR Biosystems, USA) and Q5 High-fidelity DNA Polymerase (New England Biolabs, USA). Tm refers to the melting temperature of the primers. Annealing temperatures (*) for PCR experiments using Q5 polymerase were obtained from the New England Biolabs Tm calculator website [486].

by Eurofins (Germany), and successful sequencing was checked by ensuring the chromatogram was made of well-separated, non-overlapping peaks.

A.6.2 Plasmid DNA sequencing

plasmid DNA was sequenced using Oxford Nanopore long reads by Plasmidsaurus (`https://www.plasmidsaurus.com/`). DNA was diluted in nuclease-free water to a concentration of 30 ng/μL, which was checked with a Qubit 2.0 fluorometer (Thermo Fisher Scientific, USA). The purity of the sample was assessed with a NanoDrop spectrophotometer (Thermo Fisher Scientific, USA), ensuring a 260/280 value greater than 1.8 and a 260/230 value between 2.0 and 2.2. DNA sequences were checked, and plasmid maps were visualised, using SnapGene Viewer version 6.2.1 (Insightful Science).

A.7 Agarose gel electrophoresis

Agarose gels were prepared with 1.5% agarose concentration (unless otherwise specified) by dissolving agarose in TAE buffer. TAE buffer was prepared as a 50× stock solution by adding 242.2 g/L tris base and 57.1 mL/L glacial acetic acid to 18.612 g/L EDTA disodium salt (previously adjusted to pH 8.0 using NaOH). This solution was stored at room temperature, and diluted to 1× with distilled water before use. The agarose gel was heated in a microwave until liquid and allowed to cool to 50 °C at room temperature. Ethidium bromide was added to a final concentration of 100 μg/mL and the mixture was poured into GT Cell gel tanks (Bio-Rad, USA) to solidify. After adding 1× TAE buffer to the tanks, wells were loaded with 10 μL of the appropriate DNA ladder (Promega, UK) and 2-10 μL of DNA mixed with Purple 6× loading dye (New England Biolabs, USA).

Electrophoresis was carried out at voltages between 60 and 90 V for 1-1.5 hours - low voltages and high running times were preferred for small DNA fragments. The resulting bands on the gel were imaged using UV light from an Azure c200 gel imager (Azure Biosystems, USA).

A.8 Bacterial transformation

A.8.1 Chemically competent cells

Transformation into chemically competent High Efficiency NEB 5-alpha competent *E. coli* cells (New England Biolabs, USA) was carried out according to manufacturer's protocol. Briefly, after adding 1-5 μL of DNA to 50 μL of thawed cells, the mixture was put on ice for 30 minutes, then heat shocked in a 42 °C dry bath for 30 seconds and put on ice for another 5 minutes. The cells were then mixed gently with 950 μL of room temperature LB broth or SOC medium and put in a dry 37 °C shaking bath for one hour. The resulting culture was plated, both in normal and 100x concentration, on LB agar plates with selective antibiotics. A negative control with no DNA was also plated in both normal and 10x concentration. Both sets were incubated overnight at permissive temperatures. The presence of colonies in the plates (and their absence in the negative control plates) ensured the transformation was successful.

A.8.2 Electrically competent cells

To prepare electrocompetent cells, overnight cultures were diluted 1:100 into a total volume of 50 mL of sterile LB (plus relevant antibiotics). The culture was left to grow for about 3 hours, until the optical density (OD_{600}) reached a value of 0.4 - 0.6. The culture was then transferred into a sterile 50 mL tube, chilled

on ice for 5 minutes and then centrifuged at 4000 ×g for 10 minutes at 4 °C. After discarding the supernatant, three washes were performed with 10 mL of ice-cold 10% glycerol solution. After the last centrifugation step, the pellet was resuspended in the required amount of ice-cold 10% glycerol solution and mixed by gentle pipetting.

For transformation, freezer-cold 1 mm gap electroporation cuvettes (Bio-Rad, USA) were filled with 100 μL of electrocompetent cells, to which 100 ng of DNA was added. The contents of the cuvettes were shocked with a 1.8 kV electric pulse lasting around 5 ms. 900 μL of room temperature LB broth or SOC medium were then added to the cuvettes and mixed by pipetting, and the cultures were transferred to sterile eppendorf tubes. The cultures were recovered by incubation in a dry shaking bath for one hour at permissive temperatures, and then streaked both in normal and 10x concentrations on LB agar plates with the appropriate selection antibiotics. Plates were incubated overnight and checked for the presence of colonies the following morning.

A.9 DNA purification

Plasmid DNA was purified from 10 mL overnight cultures using a Wizard Plus SV Miniprep DNA Purification System (Promega, UK), following the manufacturer's protocol. Genomic DNA was purified from 1 mL of overnight culture using a Wizard Genomic DNA Purification Kit (Promega, UK). Amplified DNA from PCR products and excised gel bands containing DNA were purified using a Wizard SV Gel and PCR Clean-Up System (Promega, UK).

The concentration of purified DNA was quantified using a NanoDrop spectrophotometer (Thermo Fisher Scientific, USA) or a Qubit 2.0 fluorometer (Thermo

Fisher Scientific, USA). DNA samples were stored at -20 °C.

A.10 Biofilm specimen preparation

A.10.1 Imaging chamber design and 3D-printing

The imaging chamber to be used with the Mesolens was designed on AutoCAD (Autodesk, USA) by modifying the original design of Rooney et al. [209]. The chamber was designed to mimic a Petri dish, and consisted of a 120 mm × 100 mm × 12 mm plate with a 60 mm diameter, 10 mm deep well at its centre to hold the agar substrate (Figure A.1). After 3D printing the chamber in black ABS plastic (FlashForge, Hong Kong) using a FlashForge Dreamer 3D printer (FlashForge, Hong Kong), the corners were smoothed out using a scalpel. This reduced the movement of the imaging chamber inside the square plate. The chamber was sterilised with a 70% (v/v) ethanol solution, and then under UV light for 20 minutes immediately before the addition of sterile solid growth medium.

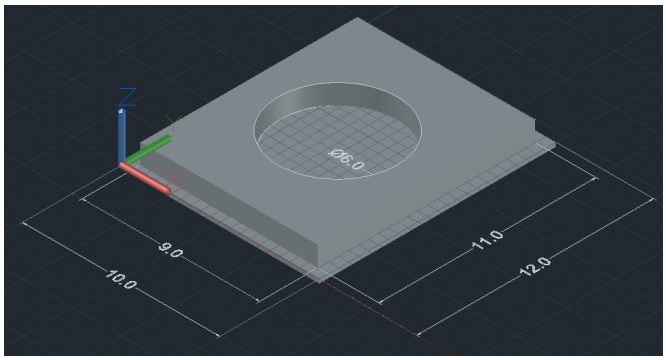

Figure A.1: 3D-printed imaging chamber used with the Mesolens. Measurements are given in cm.

A.10.2 Mature biofilm specimen preparation

Liquid cultures of *E. coli* JM105-mini-Tn7-*gfp* at mid-exponential growth phase were prepared as described previously. To grow biofilms on rich medium, 100 μL of a liquid culture with density 1×10^4 colony-forming units (CFUs) per mL was inoculated on the 10 mm-thick LB agar substrate inside the imaging chamber. The specimen was incubated at 37 °C for 24 hours in darkened condition prior to imaging. For minimal medium with varying nutrient concentration, mid-exponential phase liquid cultures were washed three times with 1× M9 salts. They were then resuspended in M9 medium with appropriate amounts of glucose and ammonium chloride (for carbon and nitrogen variation, respectively). M9 agar substrates cast into the 3D-printed imaging chambers were inoculated at a concentration of 1×10^4/mL. Based on the dimensions of the imaging chamber (Supplementary Figure A.1), this corresponds to a seeding density of 1 cell per mm^2, which ensured biofilms were sufficiently spaced out and did not have to compete for nutrients with others in their proximity. It was also ensured that only one biofilm was visible in the field of view of the Mesolens at once, which prevented background signal from nearby biofilms from reaching the detectors.

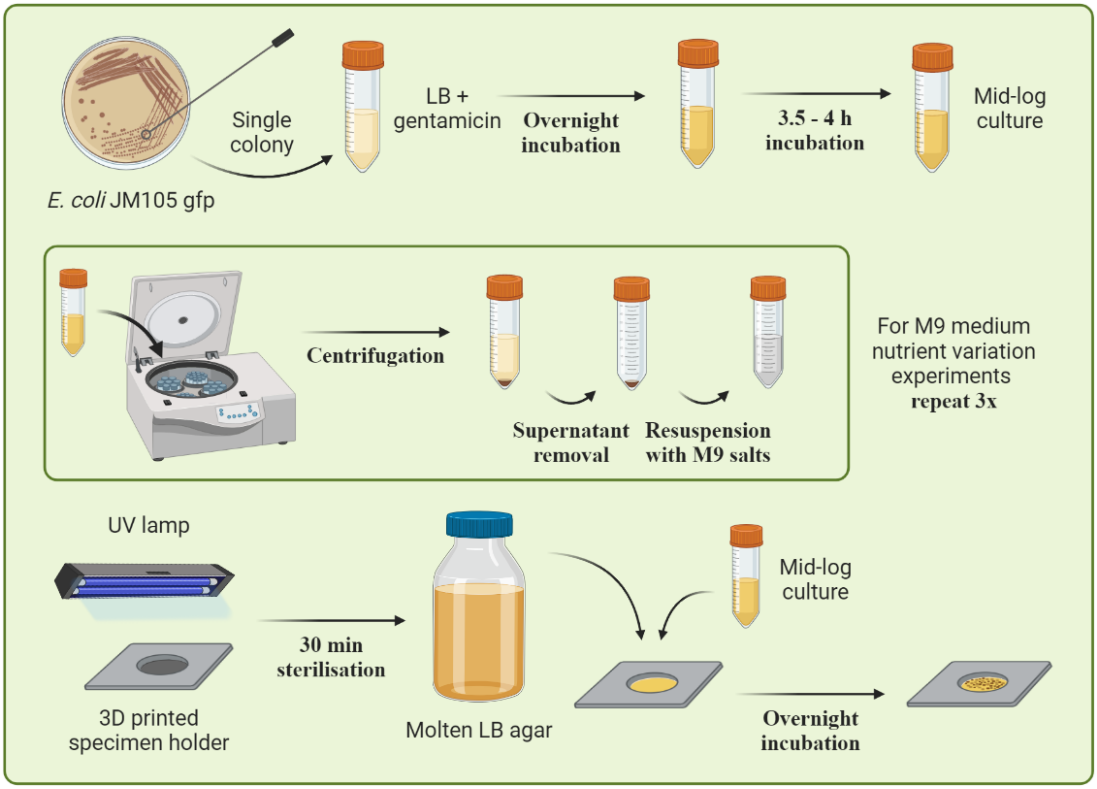

Figure A.2: Specimen preparation for Mesolens imaging, as described by Rooney et al. [209]. Overnight liquid cultures are first prepared in LB medium, then diluted and incubated until mid-exponential growth phase. For experiments carried out with M9 minimal medium, the cultures are pelleted and resuspended with 1× M9 salts 3 times. The cultures are then spread on solidified agar substrates (either LB or M9) on the 3D-printed plastic specimen holder. Image created in BioRender (license number SR25JKZ3PC).

Appendix B

Python scripts used to calculate and plot intra-colony channel width at different radial distances from the centre of the biofilm

B.1 Channel width calculation

This Python script is used to measure channel width at different radial distances from the centre of the biofilm using the `find_peaks()` function from the `scipy.signal` signal processing library.

After transforming the geometry of biofilm images from polar to Cartesian, line profiles are taken along the full circumference of biofilms as described in Section 2.2.5 of Chapter 2. Line profile data contains two variables: the grey level of each pixel (`df.grey`) and its corresponding distance along the circumference in pixels (`distance`). Line profile data at each radial distance is saved as an Excel file, which is read in as a dataframe by the script (line 9). The number of pixels per degree (in polar coordinates) and the radial distance at which the line profile is obtained are entered manually in lines 12 and 13. The peaks are identified on line 25 from the by the `find_peaks()` function, which is called with the following arguments: a minimum `height` for each peak is selected as 50 pixels;

the minimum `distance` between neighbouring peaks is selected as 9 pixels; the `prominence` of each peak is selected as 20% of the total range of pixel intensities in the line profile. The full-width at half-maximum of each peak is then calculated on line 28 using the `peak_widths()` function, and it is converted to μm units using polar geometry on line 30.

The final lines of the code are used to plot the signal as a blue line, to denote the identified peaks with orange crosses and their full-width at half-maximum with green horizontal lines, as shown in Figure 2.3 in Chapter 2. The full-width at half-maximum values computed using this script, which correspond to intra-colony channel widths, are saved in a separate file for plotting.

```
1  # imports
2  import math
3  import numpy as np
4  import pandas as pd
5  import matplotlib.pyplot as plt
6  from scipy.signal import find_peaks, peak_widths
7
8  # read in data file containing peak intensity values
9  df = pd.read_excel(r'file_name.xlsx')
10
11 # assign values for pixel to micrometer conversion
12 num_pixels_y = 7200          # from polar transformer plugin
13 radius = 300                # radial distance from the centre (um)
14
15 # plot signal (by extracting data from excel sheet)
16 plt.plot(df.distance, df.grey, c='#0087BD')
17 plt.xlabel('Distance (pixels)')
18 plt.ylabel('Grey level')
19
```

```
20 # find minimum and maximum of signal
21 max_signal = np.max(df.grey)
22 min_signal = np.min(df.grey)
23
24 # find peaks (returns indices of data array at which peaks occur)
25 peaks, _ = find_peaks(df.grey, height=50, distance=9, prominence
       =0.2*(np.max(df.grey)-np.min(df.grey)))
26
27 # calculate FWHMs and convert to micrometer units
28 peaks_half = peak_widths(df.grey, peaks, rel_height=0.5)
29 FWHM = peaks_half[0]
30 FWHM_um = FWHM*2*math.pi*radius/num_pixels_y
31
32 # plot peaks and FWHM lines
33 plt.plot(df.grey)
34 plt.plot(peaks, df.grey[peaks], "x")
35 plt.hlines(*peaks_half[1:], color="C2")
36 plt.show()
```

B.2 Channel width plotting

This Python script is used to plot channel width against radial distance from the centre of the biofilm as box plots with scatter points using the `seaborn` library.

The data file containing intra-colony channel widths (`width`) calculated at different radial distances from the centre of the biofilm (`radius`) is read in as a dataframe at line 11. The mean absolute deviation (`MAD`) of channel widths at each radial distance is calculated on line 16, and used to calculate a modified z-score on line 17. Data points are removed if their modified z-score is greater than 3 (line 20).

Box plots for the data are plotted using the `boxplot()` function (lines 23-28), and individual data points are added using the `stripplot()` function (lines 32-34). This generates the plots constituting Figure 2.7 in Chapter 2. Average channel width values are also calculated for each radial distance on line 37 and saved for further analysis.

```
1  # imports
2  import pandas as pd
3  from scipy import stats
4  import seaborn as sns
5  import matplotlib.pyplot as plt
6
7  sns.reset_defaults()
8  plt.rcParams.update({'font.size': 14})
9
10 # read in data file containing channel widths vs radius
11 data = pd.read_excel(r'file_name.xlsx')
12
13 # NON NORMAL DISTRIBUTION #
14 # calculate modified Z-score and add it to dataframe
15 data["width_median"] = data.groupby('radius')["width"].transform(
       'median')
16 data["MAD"] = data.groupby('radius')["width"].transform(stats.
       median_abs_deviation)
17 data["modified_zscore"] = 0.6745*(data["width"]-data["
       width_median"])/data["MAD"]
18
19 # filter outliers (remove values that are more than 3 "modified
       stdevs" away)
20 data_no_outliers_non_normal = data[data["modified_zscore"] < 3]
21
```

```
22 # boxplots showing median, 25% and 75% quartiles (box edges)),
       errorbars and means (white diamonds)
23 ax = sns.boxplot(x="radius", y="width", data=
       data_no_outliers_non_normal, showmeans=True,
24                 meanprops={"marker":"D",
25                            "markerfacecolor":"white",
26                            "markeredgecolor":"black",
27                            "markersize":"7"},
28                 showfliers=False, fliersize=1, zorder=2,
       palette="Spectral")
29
30
31 # stripplot showing individual datapoints
32 ax = sns.stripplot(x="radius", y="width", data=
       data_no_outliers_non_normal,
33                    dodge=True, jitter=False, zorder=1,
34                    color=".25", alpha=0.5)
35
36 # Calculate averages
37 average_widths = data_no_outliers_non_normal.groupby('radius')["
       width"].mean()
38
39 # Hide the right and top spines
40 ax.spines['right'].set_visible(False)
41 ax.spines['top'].set_visible(False)
42
43 plt.xticks(rotation = 60)
44 plt.xlabel('Radial distance (um)')
45 plt.ylabel('Channel width (um)')
46
47 plt.show()
```

Appendix C

Genetic checks of Keio mutant strains by DNA sequencing

Amplicon sequences obtained for the parental strain were aligned against the full-genome sequence of the parental strain BW25113 (GenBank ID: CP009273.1) to identify the corresponding gene of interest. Amplicon sequences obtained for the mutant strains were aligned against the sequence of the plasmid pKD13 (GenBank ID: AY048744.1) encoding the kanamycin resistance cassette [402].

C.0.1 *amiA* gene region

The *amiA* region of the parental strain's genome (`>amiA_wt`) and of the mutant strain Δ*amiA* (`>amiA_mut`) were sequenced using the primers amiA F and amiA R from Table A.5 in Appendix A. The sequences are reported below, together with the corresponding BLAST alignments. `N` bases signify an ambiguous nucleotide identification by the sequencing software.

```
>amiA_wt
NNNNNANATCTGGGANCTTTATTATTACAACTCAGGCCGTATGAGCACTTTTAAACC
ACTAAAAACACTCACTTCGCGCCGCCAGGTGCTGAAAGCCGGTTTGGCTGCCCTGAC
```

GTTGTCAGGAATGTCGCAAGCCATCGCCAAAGACGAACTTTTAAAAACCAGCAACGG

ACACAGCAAGCCGAAAGCCAAAAAATCTGGCGGCAAACGTGTCGTTGTTCTCGATCC

AGGTCACGGCGGAATTGATACCGGAGCGATCGGACGCAACGGTTCGAAAGAAAAACA

TGTGGTGCTGGCGATTGCTAAAAACGTCCGTTCCATTTTGCGTAATCATGGGATTGA

TGCGCGTTTAACGCGTTCTGGCGATACGTTTATCCCACTTTACGATCGCGTTGAAAT

CGCCCATAAACATGGCGCAGATCTGTTTATGTCAATTCATGCCGATGGCTTTACCAA

CCCGAAAGCTGCCGGTGCTTCGGTATTTGCCCTCTCTAACCGTGGGGCAAGTAGCGC

AATGGCGAAATACCTGTCTGAACGCGAAAACCGCGCCGATGAAGTTGCCGGTAAAAA

GGCGACTGACAAGGATCACCTATTGCAACAAGTGCTGTTTGATCTGGTGCAAACAGA

TACCATTAAAAATAGTCTGACGCTCGGCTCGCATATTCTGAAGAAGATTAAGCCGGT

GCATAAACTGCACAGCCGCAACACCGAACAAGCGGCATTTGTGGTGTTGAAATCACC

GTCGGTTCCTTCGGTGCTGGTGGAAACCTCGTTTATCACCAACCCGGAAGAAGAACG

GCTGTTAGGCACGGCGGCGTTTCGTCAGAAAATCGCCACAGCGATTGCTGAAGGCGT

GATCAGTTATTTCCACTGGTTCGACAACCAGAAAGCACATTCGAAAAAGCGATAAGT

TATGAAACCGANNNN

>amiA_mut

NGNNNNACATCTGGNANCTTTATTATTACAACTCAGGCCGTATGATTCCGGGGATCC

GTCGACCTGCAGTTCGAAGTTCCTATTCTCTAGAAAGTATAGGAACTTCAGAGCGCT

TTTGAAGCTCACGCTGCCGCAAGCACTCAGGGCGCAAGGGCTGCTAAAGGAAGCGGA

ACACGTAGAAAGCCAGTCCGCAGAAACGGTGCTGACCCCGGATGAATGTCAGCTACT

GGGCTATCTGGACAAGGGAAAACGCAAGCGCAAAGAGAAAGCAGGTAGCTTGCAGTG

GGCTTACATGGCGATAGCTAGACTGGGCGGTTTTATGGACAGCAAGCGAACCGGAAT

TGCCAGCTGGGGCGCCCTCTGGTAAGGTTGGGAAGCCCTGCAAAGTAAACTGGATGG

CTTTCTTGCCGCCAAGGATCTGATGGCGCAGGGGATCAAGATCTGATCAAGAGACAG

GATGAGGATCGTTTCGCATGATTGAACAAGATGGATTGCACGCAGGTTCTCCGGCCG

CTTGGGTGGAGAGGCTATTCGGCTATGACTGGGCACAACAGACAATCGGCTGCTCTG

ATGCCGCCGTGTTCCGGCTGTCAGCGCAGGGGCGCCCGGTTCTTTTTGTCAAGACCG

ACCTGTCCGGTGCCCTGAATGAACTGCAGGACGAGGCAGCGCGGCTATCGTGGCTGG

CCACGACGGGCGTTCCTTGCGCAGCTGTGCTCGACGTTGTCACTGAAGCGGGAAGGG

ACTGGCTGCTATTGGGCGAAGTGCCGGGGCAGGATCTCCTGTCATCTCACCTTGCTC

CTGCCGAGAAAGTATCCATCATGGCTGATGCAATGCGGCGGCTGCATACGCTTGATC

CGGCTACCTGCCCATTCGACCACCAAGCGAAACATCGCATCGAGCGAGCACGTACTC

GGATGGAAGCCGGTCTTGTCGATCAGGATGATCTGGACGAAGAGCATCAGGGGCTCG

CGCCAGCNGAACTGTTCGCCAGGCTCAAGGCGCGCATGCCCGACGGCGAGGATCTCG

TCGTGACCCATGGCGATGCCTGCTTGCCGAATATCATGNNGGAAANTGGCCGCTTTN

CTGGATTCATCGACTGTNGCCNNCTGGNNGNGGCGGACNGCTATCAGGNNNNNGCGT

TGGCTACCCGTGNNNNTGCTGANNNNTTG

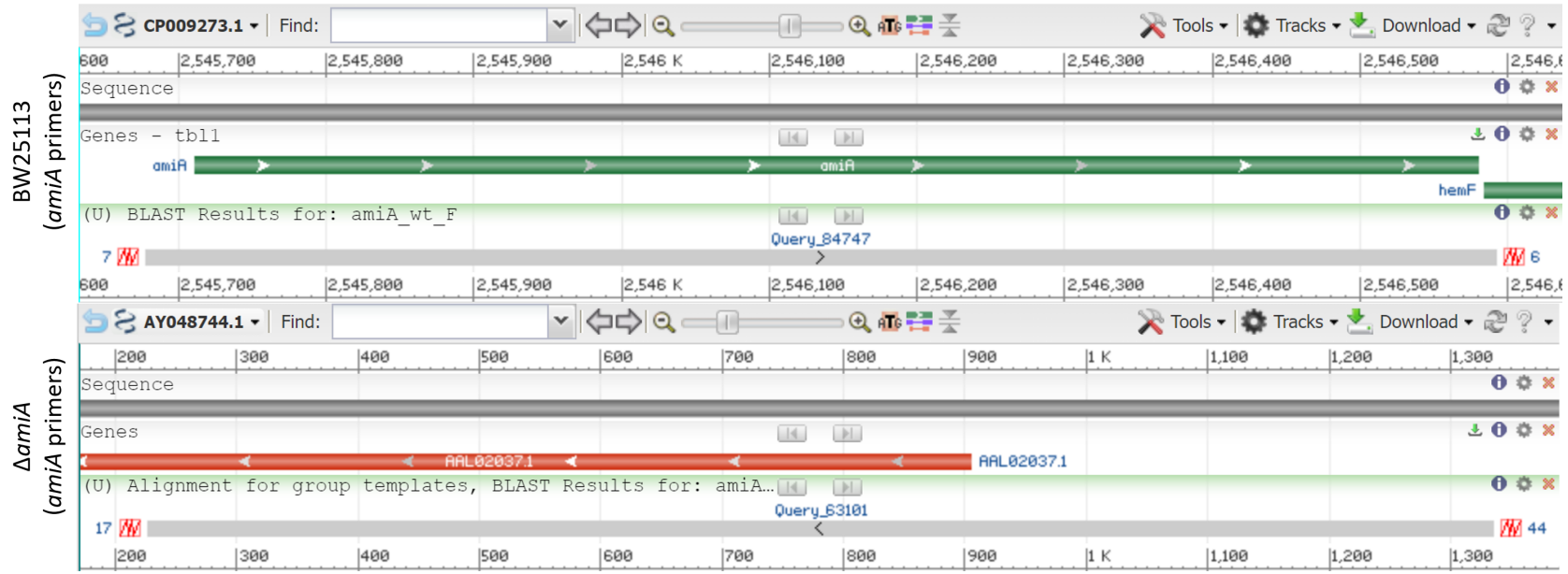

Figure C.1: Screengrabs obtained on BLAST after aligning amplicon sequences of the parental strain BW25113 and of the Δ*amiA* mutant strain obtained using *amiA* primers from Appendix A Section A.4.1. The feature AAL02037.1 identified on the alignment with Δ*amiA* corresponds to the Tn5 neomycin phosphotransferase, which is encoded by the kanamycin resistance transposon Tn5 [487].

C.0.2 *guaB* gene region

The *guaB* region of the parental strain's genome (>guaB_wt) and of the mutant strain Δ*guaB* (>guaB_mut) were sequenced using the primers guaB F and guaB R from Table A.5 in Appendix A. The sequences are reported below, together with the corresponding BLAST alignments. N bases signify an ambiguous nucleotide identification by the sequencing software.

>guaB_wt

NNNCNNNTCTGGNTCGAGATATTGCCCATGCTACGTATCGCTAAAGAAGCTCTGACG
TTTGACGACGTTCTCCTCGTTCCTGCTCACTCTACCGTTCTGCCGAATACTGCTGAC
CTCAGCACCCAGCTGACGAAAACTATTCGTCTGAATATCCCTATGCTTTCCGCAGCA
ATGGATACCGTAACGGAAGCGCGCCTGGCTATTGCTCTGGCTCAGGAAGGCGGTATC
GGCTTTATCCACAAAAACATGTCCATTGAACGCCAGGCAGAAGAAGTTCGCCGTGTG
AAAAAACACGAATCTGGTGTGGTGACTGATCCGCAGACTGTTCTGCCAACCACGACG
CTGCGCGAAGTGAAAGAACTGACCGAGCGTAACGGTTTTGCGGGCTATCCGGTCGTT
ACCGAAGAAAACGAACTGGTGGGTATTATCACCGGTCGTGACGTGCGTTTTGTTACC
GACCTGAACCAGCCGGTTAGCGTTTACATGACGCCGAAAGAGCGTCTGGTCACCGTG
CGTGAAGGTGAAGCCCGTGAAGTGGTGCTGGCAAAAATGCACGAAAAACGCGTTGAA
AAAGCGCTGGTGGTTGATGACGAATTCCACCTGATCGGCATGATCACCGTGAAAGAC
TTCCAGAAAGCGGAACGTAAACCGAACGCCTGTAAAGACNANCAAGGCCGTCTGCGT
GTTGGTGCAGCGGTTGGCGCAGGTGCGGGTAACGAAGAGCGTGTTGACGCGCTGGTT
GCCGCAGGCGTTGACGTTCTGCTGATCGACTCCTCCCACGGTCACTCAGAAGGTGTA
CTGCAACGTATCCGTGAAACCCGTGCTAAATATCCGGATCTGCAAATTATCGGCGGC
AACGTGGCAACAGCTGCAGGTGCACGCGCTCTGGCNNAAGCTGGTTGCAGTGCGGTT
AAAGTCGGCATTGGCCCTGGCTCTATCTGTACAACTCGTATCGTGACTGNNGTCGGT
GTTCCGCANATTACCGCTGTTGCTGACGCAGTNNNAGCCCTGGAAGGCNCCGGTATT

CCGGTTATCGNTGATGNNGGN

>guaB_mut

CNNNTCTGNNTCGAGATATTGCCCATGATTCCGGGGATCCGTCGACCTGCAGTTCGA
AGTTCCTATTCTCTAGAAAGTATAGGAACTTCAGAGCGCTTTTGAAGCTCACGCTGC
CGCAAGCACTCAGGGCGCAAGGGCTGCTAAAGGAAGCGGAACACGTAGAAAGCCAGT
CCGCAGAAACGGTGCTGACCCCGGATGAATGTCAGCTACTGGGCTATCTGGACAAGG
GAAAACGCAAGCGCAAAGAGAAAGCAGGTAGCTTGCAGTGGGCTTACATGGCGATAN
CTAGACTGGGCGGTTTTATGGACAGCAAGCGAACCGGAATTGCCAGCTGGGGCGCCC
TCTGGTAAGGTTGGGAAGCCCTGCAAAGTAAACTGGATGGCTTTCTTGCCGCCAAGG
ATCTGATGGCGCAGGGGATCAAGATCTGATCAAGAGACAGGATGAGGATCGTTTCGC
ATGATTGAACAAGATGGATTGCACGCAGGTTCTCCGGCCGCTTGGGTGGAGAGGCTA
TTCGGCTATGACTGGGCACAACAGACAATCGGCTGCTCTGATGCCGCCGTGTTCCGG
CTGTCAGCGCAGGGGCGCCCGGTTCTTTTTGTCAAGACCGACCTGTCCGGTGCCCTG
AATGAACTGCAGGACGAGGCAGCGCGGCTATCGTGGCTGGCCACGACGGGCGTTCCT
TGCGCAGCTGTGCTCGACGTTGTCACTGAAGCGGGAAGGGACTGGCTGCTATTGGGC
GAAGTGCCGGGGCAGGATCTCCTGTCATCTCACCTTGCTCCTGCCGAGAAAGTATCC
ATCATGGCTGATGCAATGCGGCGGCTGCATACGCTTGATCCGGCTACCTGCCCATTC
GACCACCAAGCGAANCATCGCATCGAGCGAGCACGTACTCGGATGGAAGCCGGTCTT
GTCGATCAGGNNGATCTGGNNNN

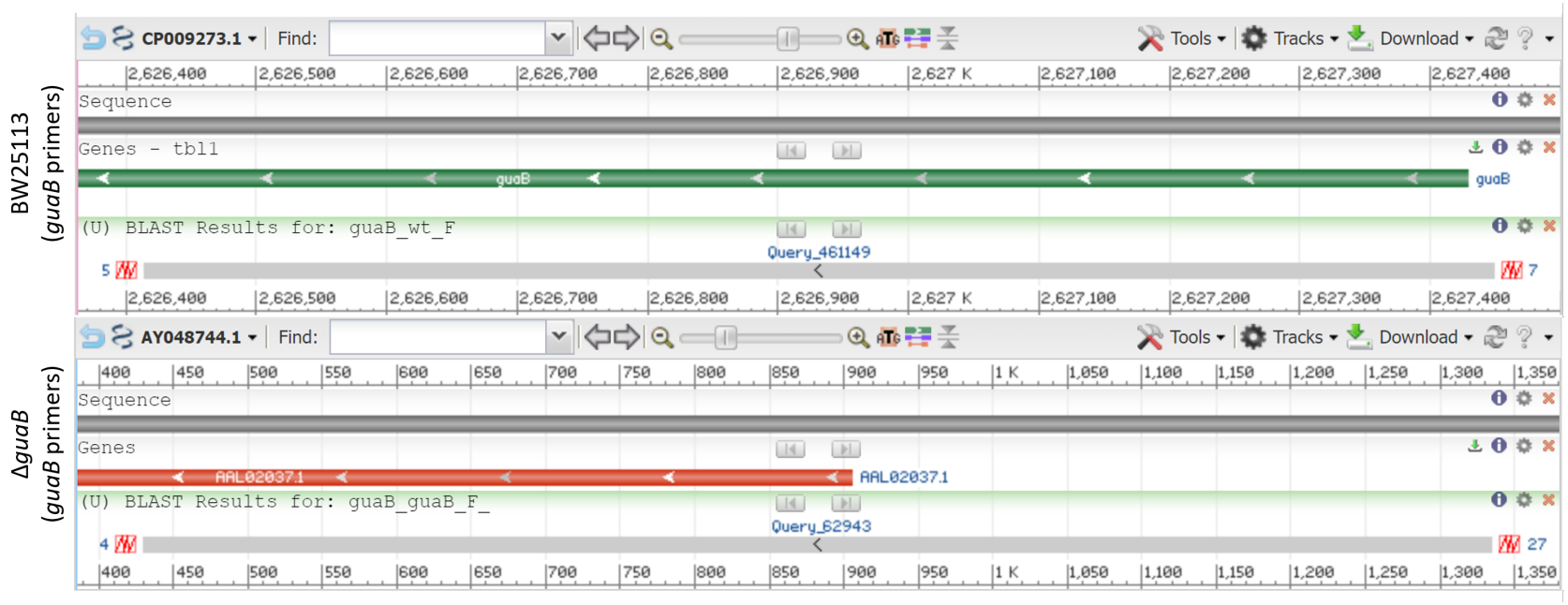

Figure C.2: Screengrabs obtained on BLAST after aligning amplicon sequences of the parental strain BW25113 and of the Δ*guaB* mutant strain obtained using *guaB* primers from Appendix A Section A.4.1. The feature AAL02037.1 identified on the alignment with Δ*guaB* corresponds to the Tn5 neomycin phosphotransferase, which is encoded by the kanamycin resistance transposon Tn5 [487].

C.0.3 *ompR* gene region

The *ompR* region of the parental strain's genome (>ompR_wt) and of the mutant strain $\Delta ompR$ (>ompR_mut) were sequenced using the primers ompR F and ompR R from Table A.5 in Appendix A. The sequences are reported below, together with the corresponding BLAST alignments. N bases signify an ambiguous nucleotide identification by the sequencing software.

>ompR_wt

TNNNNATTGTTGCGNACCTTTGGGAGTACAAACAATGCAAGAGAACTACAAGATTCT
GGTGGTCGATGACGACATGCGCCTGCGTGCGCTGCTGGAACGTTATCTCACCGAACA
AGGCTTCCAGGTTCGAAGCGTCGCTAATGCAGAACAGATGGATCGCCTGCTGACTCG
TGAATCTTTCCATCTTATGGTACTGGATTTAATGTTACCTGGTGAAGATGGCTTGTC
GATTTGCCGACGTCTTCGTAGTCAGAGCAACCCGATGCCGATCATTATGGTGACGGC
GAAAGGGGAAGAAGTGGACCGTATCGTAGGCCTGGAGATTGGCGCTGACGACTACAT
TCCAAAACCGTTTAACCCGCGTGAACTGCTGGCCCGTATCCGTGCGGTGCTGCGTCG
TCAGGCGAACGAACTGCCAGGCGCACCGTCACAGGAAGAGGCGGTAATTGCTTTCGG
TAAGTTCAAACTTAACCTCGGTACGCGCGAAATGTTCCGCGAAGACGAGCCGATGCC
GCTCACCAGCGGTGAGTTTGCGGTACTGAAGGCACTGGTCAGCCATCCGCGTGAGCC
GCTCTCCCGCGATAAGCTGATGAACCTTGCCCGTGGTCGTGAATATTCCGCAATGGA
ACGCTCCATCGACGTGCAGATTTCGCGTCTGCGCCGCATGGTGGAAGAAGATCCAGC
GCATCCGCGTTACATTCAGACCGTCTGGGGTCTGGGCTACGTCTTTGTACCGGACGG
CTCTAAAGCATGAGGCGATTGCGCTTCTCGCCACGAAGTTCATTTGCCCGTACGTTA
T

>ompR_mut

NNNCTNNNNATTGTTGCGAACCTTTGGGAGTANAAACAATGATTCCGGGGATCCGTC

GACCTGCAGTTCGAAGTTCCTATTCTCTAGAAAGTATAGGAACTTCAGAGCGCTTTT

GAAGCTCACGCTGCCGCAAGCACTCAGGGCGCAAGGGCTGCTAAAGGAAGCGGAACA

CGTAGAAAGCCAGTCCGCAGAAACGGTGCTGACCCCGGATGAATGTCAGCTACTGGG

CTATCTGGACAAGGGAAAACGCAAGCGCAAAGAGAAAGCAGGTAGCTTGCAGTGGGC

TTACATGGCGATAGCTAGACTGGGCGGTTTTATGGACAGCAAGCGAACCGGAATTGC

CAGCTGGGGCGCCCTCTGGTAAGGTTGGGAAGCCCTGCAAAGTAAACTGGATGGCTT

TCTTGCCGCCAAGGATCTGATGGCGCAGGGGATCAAGATCTGATCAAGAGACAGGAT

GAGGATCGTTTCGCATGATTGAACAAGATGGATTGCACGCAGGTTCTCCGGCCGCTT

GGGTGGAGAGGCTATTCGGCTATGACTGGGCACAACAGACAATCGGCTGCTCTGATG

CCGCCGTGTTCCGGCTGTCAGCGCAGGGGCGCCCGGTTCTTTTTGTCAAGACCGACC

TGTCCGGTGCCCTGAATGAACTGCAGGACGAGGCAGCGCGGCTATCGTGGCTGGCCA

CGACGGGCGTTCCTTGCGCAGCTGTGCTCGACGTTGTCACTGAAGCGGGAAGGGACT

GGCTGCTATTGGGCGAAGTGCCGGGGCAGGATCTCCTGTCATCTCACCTTGCTCCTG

CCGAGAAAGTATCCATCATGGCTGATGCAATGCGGCGGCTGCATACGCTTGATCCGG

CTACCTGCCCATTCGACCACCAAGCGAAACATCGCATCGAGCGAGCACGTACTCGGA

TGGAAGCCGGTCTTGTCGATCAGGATGATCTGGACGAAGAGCATCAGGGGCTCGCGC

CAGCCGAACTGTTCGCCAGGCTCAAGGCGCGCATGCCCGACGGCGAGGATCTCGTCG

TGACCCATGGCGATGCCTGCTTGCCGAANATCATGGTGGAAANTGGCCGCTTTNCTG

GATTCATCGACNNNNG

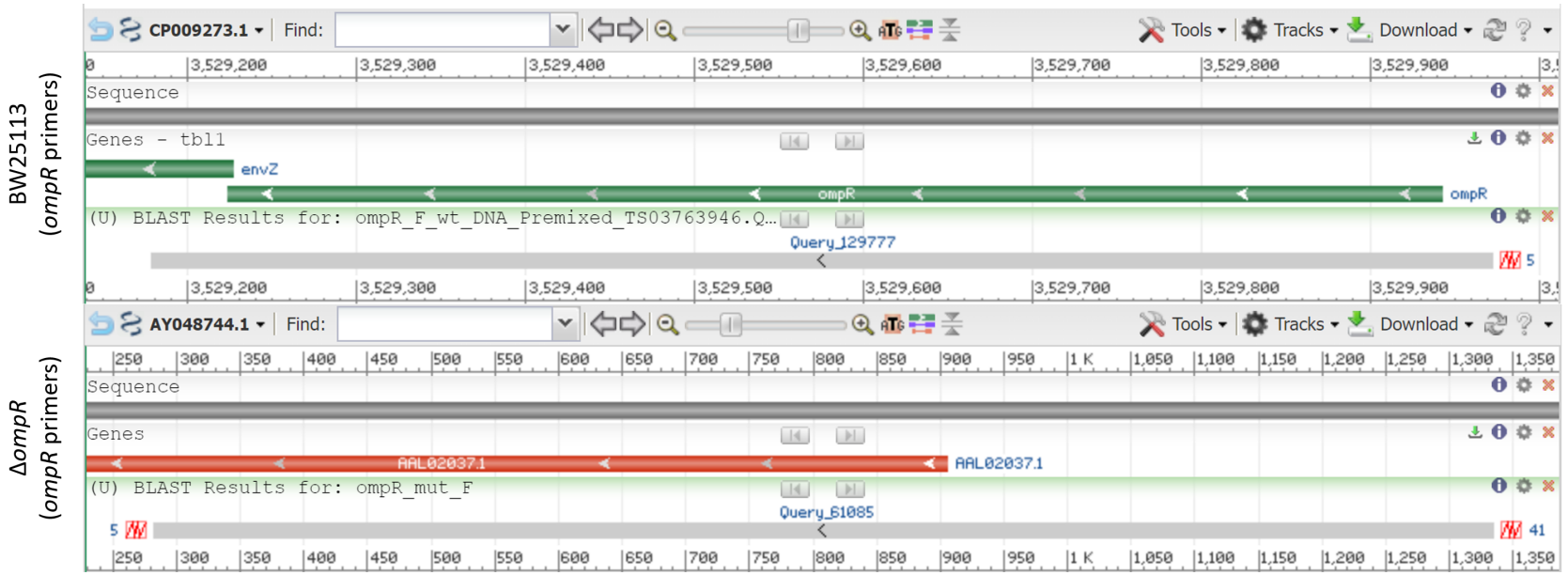

Figure C.3: Screengrabs obtained on BLAST after aligning amplicon sequences of the parental strain BW25113 and of the Δ*ompR* mutant strain obtained using *ompR* primers from Appendix A Section A.4.1. The feature AAL02037.1 identified on the alignment with Δ*ompR* corresponds to the Tn5 neomycin phosphotransferase, which is encoded by the kanamycin resistance transposon Tn5 [487].

C.0.4 *ydgD* gene region

The *ydgD* region of the parental strain's genome (>ydgD_wt) and of the mutant strain Δ*ydgD* (>ydgD_mut) were sequenced using the primers ydgD F and ydgD R from Table A.5 in Appendix A. The sequences are reported below, together with the corresponding BLAST alignments. N bases signify an ambiguous nucleotide identification by the sequencing software.

>ydgD_wt

NNNNNGTTGCTTTTNNNNATCATAATTACCCACCAGAGTGTGATATGCGTACAACCA
TTGCTGTAGTGTTGGGTGCAATTAGTTTGACGTCTGCTTTTGTGTTTGCAGATAAAC
CAGACGTTGCCAGATCGGCAAACGATGAGGTCAGCACCCTGTTTTTTGGTCATGATG
ATCGTGTGCCAGTGAATGACACGACCCAATCACCGTGGGATGCGGTTGGGCAACTGG
AAACGGCCAGCGGCAATTTATGTACGGCGACGCTGATTGCACCCAATCTGGCATTAA
CGGCAGGACACTGTTTATTGACACCTCCAAAGGGTAAAGCCGATAAAGCAGTGGCGC
TGCGTTTTGTGTCAAATAAAGGTCTTTGGCGCTATGAGATCCACGACATAGAAGGCC
GCGTTGATCCGACACTGGGAAAGCGGTTAAAAGCAGATGGGGATGGTTGGATTGTAC
CTCCCGCAGCCGCGCCGTGGGACTTCGGATTGATTGTGCTACGTAATCCCCCTTCTG
GCATTACGCCGTTGCCGTTATTTGAGGGAGATAAAGCCGCGCTTACCGCCGCATTAA
AAGCGGCAGGTCGTAAAGTGACTCAGGCAGGCTACCCTGAAGATCATCTCGATACGT
TGTACAGTCATCAAAACTGTGAAGTGACTGGCTGGGCGCAAACGTCGGTGATGTCAC
ATCAGTGCGATACCTTGCCGGGTGACAGCGGTTCGCCTCTGATGTTGCATACCGATG
ACGGCTGGCAATTAATTGGGGTGCAAAGTTCGGCTCCTGCCGCGAAAGATCGCTGGC
GCGCCGATAACCGGGCCATTTCTGTTACCGGTTTTCGCGACAAGCTGGATCAACTGT
CGCAAAAATAATGTTCAAACGCTGCCCGACAGCGCGGGCAGCGTCTTCATCAGGCAA
GTTTCACCATGATCATTCCNNCNN

>ydgD_mut

NNNTNNTAATTACCCACCAAAGTGTGATATGATTCCGGGGATCCGTCGACCTGCAGT

TCGAAGTTCCTATTCTCTAGAAAGTATAGGAACTTCAGAGCGCTTTTGAAGCTCACG

CTGCCGCAAGCACTCAGGGCGCAAGGGCTGCTAAAGGAAGCGGAACACGTAGAAAGC

CAGTCCGCAGAAACGGTGCTGACCCCGGATGAATGTCAGCTACTGGGCTATCTGGAC

AAGGGAAAACGCAAGCGCAAAGAGAAAGCAGGTAGCTTGCAGTGGGCTTACATGGCG

ATAGCTAGACTGGGCGGTTTTATGGACAGCAAGCGAACCGGAATTGCCAGCTGGGGC

GCCCTCTGGTAAGGTTGGGAAGCCCTGCAAAGTAAACTGGATGGCTTTCTTGCCGCC

AAGGATCTGATGGCGCAGGGGATCAAGATCTGATCAAGAGACAGGATGAGGATCGTT

TCGCATGATTGAACAAGATGGATTGCACGCAGGTTCTCCGGCCGCTTGGGTGGAGAG

GCTATTCGGCTATGACTGGGCACAACAGACAATCGGCTGCTCTGATGCCGCCGTGTT

CCGGCTGTCAGCGCAGGGGCGCCCGGTTCTTTTTGTCAAGACCGACCTGTCCGGTGC

CCTGAATGAACTGCAGGACGAGGCANCGCGGCTATCGTGGCTGGCCACGACGGGCGT

TCCTTGCGCAGCTGTGCTCGACGTTGTCACTGAAGCGGGAAGGGACTGGCTGCTATT

GGGCGAAGTGCCGGGGCAGGATCTCCTGTCATCTCACCTTGCTCCTGCCGAGAAAGT

ATCCATCATGGCTGATGCAATGCGGCGGCTGCATACGCTTGATCCGGCTACCTGCCC

ATTCGACCACCAAGCAAAACATCGCATCGAGCGAGCACGTACTCGGATGGAAGCCGG

TCTTGTCGATCAGGATGATCTGGACGAAGAGCATCAGGGGCTCGCGCCAGCCGAACT

GTTCGCCAGGCTCAAGGCGCGCATGCCCGACGGCNAGGNNNTCGTNNNGACCCATGN

CGATGCCTGCTTGCCGAANNTCATGNNNGAAANTGGCCGCTTTTCTGGATTNNNCGA

CTNNNGCCGGCTGGNNNN

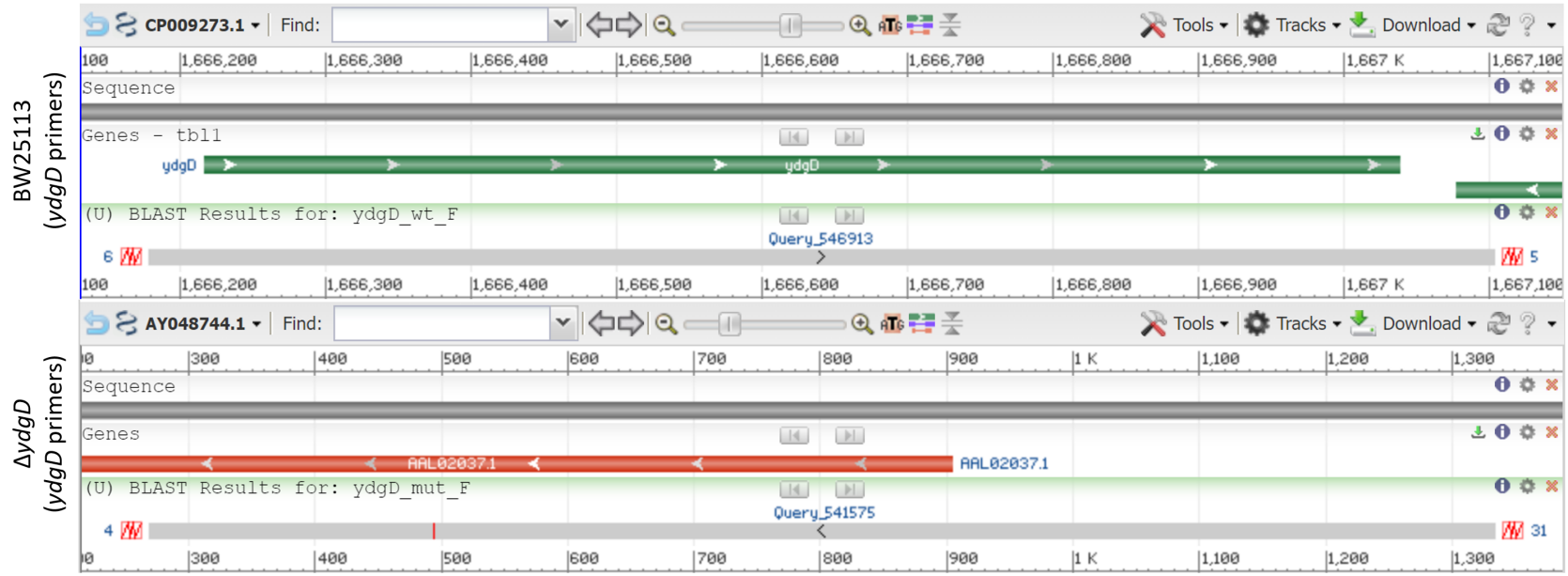

Figure C.4: Screengrabs obtained on BLAST after aligning amplicon sequences of the parental strain BW25113 and of the Δ*ydgD* mutant strain obtained using *ydgD* primers from Appendix A Section A.4.1. The feature AAL02037.1 identified on the alignment with Δ*ydgD* corresponds to the Tn5 neomycin phosphotransferase, which is encoded by the kanamycin resistance transposon Tn5 [487].

Bibliography

[1] B. R. Masters, *Confocal microscopy and multiphoton excitation microscopy: the genesis of live cell imaging*. SPIE, 2006.

[2] J. Hecht, *Optics: light for a new age*. Macmillan/McGraw-Hill School Publishing Company, 1987.

[3] R. S. Quimby, *Photonics and lasers: an introduction*. John Wiley & Sons, 2006.

[4] R. Winston, J. C. Miñano, P. G. Benitez, *et al.*, *Nonimaging optics*. Elsevier, 2005.

[5] M. A. Hayat *et al.*, *Principles and techniques of electron microscopy. Biological applications*. Cambridge University Press, 1981.

[6] U. Kubitscheck, "Principles of light microscopy," *Fluorescence Microscopy: From Principles to Biological Applications*, 2017. DOI: https://doi.org/10.1002/9783527687732.ch2.

[7] A. Köhler, "New method of illumination for photomicrographical purposes," *Journal of the Royal Microscopical Society*, vol. 14, 1894.

[8] G. W. Gill, "Köhler illumination," in *Cytopreparation. Essentials in Cytopathology*, vol. 12, Springer, 2013. DOI: https://doi.org/10.1007/978-1-4614-4933-1_19.

[9] D. B. Murphy, *Fundamentals of light microscopy and electronic imaging*. John Wiley & Sons, 2002.

[10] M. J. Nasse and J. C. Woehl, "Realistic modeling of the illumination point spread function in confocal scanning optical microscopy," *Journal of the Optical Society of America A*, vol. 27, no. 2, 2010. DOI: https://doi.org/10.1364/JOSAA.27.000295.

[11] D. Kundur and D. Hatzinakos, "Blind image deconvolution," *IEEE signal processing magazine*, vol. 13, no. 3, 1996. DOI: https://doi.org/10.1109/79.489268.

[12] L. Rayleigh, "XXXI. Investigations in optics, with special reference to the spectroscope," *The London, Edinburgh, and Dublin Philosophical Magazine and Journal of Science*, vol. 8, no. 49, 1879. DOI: https://doi.org/10.1080/14786447908639684.

[13] J. Pawley, *Handbook of biological confocal microscopy*. Springer Science & Business Media, 2006, vol. 236.

[14] S. F. Gibson and F. Lanni, "Experimental test of an analytical model of aberration in an oil-immersion objective lens used in three-dimensional light microscopy," *Journal of the Optical Society of America A*, vol. 9, 1992. DOI: https://doi.org/10.1364/JOSAA.8.001601.

[15] D. E. Wolf, "The optics of microscope image formation," *Methods in cell biology*, vol. 81, 2007. DOI: https://doi.org/10.1016/S0091-679X(06)81002-2.

[16] M. Born and E. Wolf, *Principles of optics: electromagnetic theory of propagation, interference and diffraction of light*. Elsevier, 2013.

[17] M. Kozubek and P. Matula, "An efficient algorithm for measurement and correction of chromatic aberrations in fluorescence microscopy," *Journal of Microscopy*, vol. 200, no. 3, 2000. DOI: https://doi.org/10.1046/j.1365-2818.2000.00754.x.

[18] N. Ji, "Adaptive optical fluorescence microscopy," *Nature methods*, vol. 14, no. 4, 2017. DOI: https://doi.org/10.1038/nmeth.4218.

[19] H. E. Keller, "Objective lenses for confocal microscopy," in *Handbook of biological confocal microscopy*, Springer, 2006, ch. 7. DOI: https://doi.org/10.1007/978-0-387-45524-2_7.

[20] H. Itoh, N. Matsumoto, and T. Inoue, "Spherical aberration correction suitable for a wavefront controller," *Optics express*, vol. 17, no. 16, 2009. DOI: https://doi.org/10.1364/OE.17.014367.

[21] S. Deng, L. Liu, Y. Cheng, R. Li, and Z. Xu, "Effects of primary aberrations on the fluorescence depletion patterns of STED microscopy," *Optics express*, vol. 18, no. 2, 2010. DOI: https://doi.org/10.1364/OE.18.001657.

[22] A. Lahiri, *Basic optics: principles and concepts*. Elsevier, 2016, ch. 2.

[23] B. Valeur and M. N. Berberan-Santos, "Absorption of ultraviolet, visible and near-infrared radiation," in *Molecular fluorescence: principles and applications*, John Wiley & Sons, 2012.

[24] J. R. Albani, "Fluorescence spectroscopy principles," in *Principles and applications of fluorescence spectroscopy*, John Wiley & Sons, 2007.

[25] A. Jain, C. Blum, and V. Subramaniam, "Fluorescence lifetime spectroscopy and imaging of visible fluorescent proteins," in *Advances in Biomedical Engineering*, Elsevier, 2009, ch. 4. DOI: https://doi.org/10.1016/B978-0-444-53075-2.00004-6.

[26] K.-L. Wong, J.-C. G. Bünzli, and P. A. Tanner, "Quantum yield and brightness," *Journal of Luminescence*, vol. 224, 2020. DOI: https://doi.org/10.1016/j.jlumin.2020.117256.

[27] M. J. Sanderson, I. Smith, I. Parker, and M. D. Bootman, "Fluorescence microscopy," *Cold Spring Harbor Protocols*, vol. 2014, no. 10, 2014. DOI: https://doi.org/10.1101/pdb.top071795.

[28] F. W. Rost, *Quantitative fluorescence microscopy*. Cambridge University Press, 1991.

[29] P. Rodrıguez-Sevilla, S. A. Thompson, and D. Jaque, "Multichannel fluorescence microscopy: Advantages of going beyond a single emission," *Advanced NanoBiomed Research*, vol. 2, no. 5, 2022. DOI: https://doi.org/10.1002/anbr.202100084.

[30] T. Zimmermann, "Spectral imaging and linear unmixing in light microscopy," *Microscopy Techniques*, 2005. DOI: https://doi.org/10.1007/b102216.

[31] M. S. Ammor, "Recent advances in the use of intrinsic fluorescence for bacterial identification and characterization," *Journal of fluorescence*, vol. 17, 2007. DOI: https://doi.org/10.1007/s10895-007-0180-6.

[32] J. R. Lakowicz, *Principles of fluorescence spectroscopy*. Springer, 2004.

[33] H. Bhatta, E. M. Goldys, and R. P. Learmonth, "Use of fluorescence spectroscopy to differentiate yeast and bacterial cells," *Applied microbiology and biotechnology*, vol. 71, 2006. DOI: https://doi.org/10.1007/s00253-005-0309-y.

[34] L. Leblanc and E. Dufour, "Monitoring the identity of bacteria using their intrinsic fluorescence," *FEMS microbiology letters*, vol. 211, no. 2, 2002. DOI: https://doi.org/10.1111/j.1574-6968.2002.tb11217.x.

[35] H. E. Giana, L. Silveira, R. A. Zângaro, and M. T. T. Pacheco, "Rapid identification of bacterial species by fluorescence spectroscopy and classification through principal components analysis," *Journal of Fluorescence*,

vol. 13, 2003. DOI: https://doi.org/10.1023/B:JOFL.0000008059.74052.3c.

[36] B. C. Spector, L. Reinisch, D. Smith, and J. A. Werkhaven, "Noninvasive fluorescent identification of bacteria causing acute otitis media in a chinchilla model," *The Laryngoscope*, vol. 110, no. 7, 2000. DOI: https://doi.org/10.1097/00005537-200007000-00009.

[37] H. Wang, J. Wang, J. Xu, and R.-X. Cai, "Study on the influence of potassium iodate on the metabolism of Escherichia coli by intrinsic fluorescence," *Spectrochimica Acta Part A: Molecular and Biomolecular Spectroscopy*, vol. 64, no. 2, 2006. DOI: https://doi.org/10.1016/j.saa.2005.07.025.

[38] W. McElroy and B. Strehler, "Bioluminescence," *Bacteriological reviews*, vol. 18, no. 3, 1954.

[39] E. N. Harvey, "Studies on bioluminescence: VII. Reversibility of the photogenic reaction in Cypridina.," *The Journal of General Physiology*, vol. 1, no. 2, 1918.

[40] O. Shimomura, F. H. Johnson, and Y. Saiga, "Extraction, purification and properties of aequorin, a bioluminescent protein from luminous hydromedusan, Aequorea," *Journal of Cellular and Comparative Physiology*, vol. 59, no. 3, 1962. DOI: https://doi.org/10.1002/jcp.1030590302.

[41] J. G. Morin and J. W. Hastings, "Energy transfer in a bioluminescent system," *Journal of cellular physiology*, vol. 77, no. 3, 1971. DOI: https://doi.org/10.1002/jcp.1040770305.

[42] H. Morise, O. Shimomura, F. H. Johnson, and J. Winant, "Intermolecular energy transfer in the bioluminescent system of Aequorea," *Biochemistry*, vol. 13, no. 12, 1974.

[43] O. Shimomura, "Structure of the chromophore of Aequorea green fluorescent protein," *FEBS letters*, vol. 104, no. 2, 1979. DOI: https://doi.org/10.1016/0014-5793(79)80818-2.

[44] F. Yang, L. G. Moss, and G. N. Phillips Jr, "The molecular structure of green fluorescent protein," *Nature biotechnology*, vol. 14, no. 10, 1996. DOI: https://doi.org/10.1038/nbt1096-1246.

[45] M. Ormö, A. B. Cubitt, K. Kallio, L. A. Gross, R. Y. Tsien, and S. J. Remington, "Crystal structure of the Aequorea victoria green fluorescent protein," *Science*, vol. 273, no. 5280, 1996. DOI: https://doi.org/10.1126/science.273.5280.1392.

[46] D. C. Prasher, V. K. Eckenrode, W. W. Ward, F. G. Prendergast, and M. J. Cormier, "Primary structure of the Aequorea victoria green-fluorescent protein," *Gene*, vol. 111, no. 2, 1992. DOI: https://doi.org/10.1016/0378-1119(92)90691-H.

[47] M. Chalfie, Y. Tu, G. Euskirchen, W. W. Ward, and D. C. Prasher, "Green fluorescent protein as a marker for gene expression," *Science*, vol. 263, no. 5148, 1994. DOI: https://doi.org/10.1126/science.8303295.

[48] R. Niedenthal, L. Riles, M. Johnston, and J. Hegemann, "Green fluorescent protein as a marker for gene expression and subcellular localization in budding yeast," *Yeast*, vol. 12, no. 8, 1996. DOI: https://doi.org/10.1002/(SICI)1097-0061(19960630)12:8<773::AID-YEA972>3.0.CO;2-L.

[49] EMBL-EBI, *Protein data bank in europe*, https://www.ebi.ac.uk/pdbe/entry/pdb/1ema, 2012. (visited on 02/22/2023).

[50] R. A. Cinelli, A. Ferrari, V. Pellegrini, M. Tyagi, M. Giacca, and F. Beltram, "The enhanced green fluorescent protein as a tool for the analysis of

protein dynamics and localization: Local fluorescence study at the single-molecule level," *Photochemistry and Photobiology*, vol. 71, no. 6, 2000. DOI: https://doi.org/10.1562/0031-8655(2000)0710771TEGFPA2.0.CO2.

[51] S. G. Olenych, N. S. Claxton, G. K. Ottenberg, and M. W. Davidson, "The fluorescent protein color palette," *Current protocols in cell biology*, vol. 33, no. 1, 2007. DOI: https://doi.org/10.1002/0471143030.cb2105s36.

[52] N. C. Shaner, G. H. Patterson, and M. W. Davidson, "Advances in fluorescent protein technology," *Journal of cell science*, vol. 124, no. 13, 2011. DOI: https://doi.org/10.1242/jcs.094722.

[53] J.-D. Pédelacq, S. Cabantous, T. Tran, T. C. Terwilliger, and G. S. Waldo, "Engineering and characterization of a superfolder green fluorescent protein," *Nature biotechnology*, vol. 24, no. 1, 2006. DOI: https://doi.org/10.1038/nbt0906-1170d.

[54] J. March, G. Rao, and W. Bentley, "Biotechnological applications of green fluorescent protein," *Applied microbiology and biotechnology*, vol. 62, no. 4, 2003. DOI: https://doi.org/10.1007/s00253-003-1339-y.

[55] T. Misteli and D. L. Spector, "Applications of the green fluorescent protein in cell biology and biotechnology," *Nature biotechnology*, vol. 15, no. 10, 1997. DOI: https://doi.org/10.1038/nbt1097-961.

[56] N. Kato, D. Reynolds, M. L. Brown, *et al.*, "Multidimensional fluorescence microscopy of multiple organelles in Arabidopsis seedlings," *Plant Methods*, vol. 4, no. 1, 2008. DOI: https://doi.org/10.1186/1746-4811-4-9.

[57] S. Wang and T. Hazelrigg, "Implications for bcd mRNA localization from spatial distribution of exu protein in Drosophila oogenesis," *Nature*, vol. 369, no. 6479, 1994. DOI: https://doi.org/10.1038/369400a0.

[58] R. Henriques, C. Griffiths, E. Hesper Rego, and M. M. Mhlanga, "PALM and STORM: Unlocking live-cell super-resolution," *Biopolymers*, vol. 95, no. 5, 2011. DOI: https://doi.org/10.1002/bip.21586.

[59] L. M. Wysocki and L. D. Lavis, "Advances in the chemistry of small molecule fluorescent probes," *Current opinion in chemical biology*, vol. 15, no. 6, 2011. DOI: https://doi.org/10.1016/j.cbpa.2011.10.013.

[60] P. Greenspan, E. P. Mayer, and S. D. Fowler, "Nile red: A selective fluorescent stain for intracellular lipid droplets," *The Journal of cell biology*, vol. 100, no. 3, 1985. DOI: https://doi.org/10.1083/jcb.100.3.965.

[61] J. Riggs, R. J. Seiwald, J. Burckhalter, C. M. Downs, and T. Metcalf, "Isothiocyanate compounds as fluorescent labeling agents for immune serum," *The American journal of pathology*, vol. 34, no. 6, 1958.

[62] T. The and T. Feltkamp, "Conjugation of fluorescein isothiocyanate to antibodies: I. Experiments on the conditions of conjugation," *Immunology*, vol. 18, no. 6, 1970.

[63] E. Lanz, M. Gregor, J. Slavık, and A. Kotyk, "Use of FITC as a fluorescent probe for intracellular pH measurement," *Journal of Fluorescence*, vol. 7, 1997. DOI: https://doi.org/10.1023/A:1022586127784.

[64] B. I. Tarnowski, F. G. Spinale, and J. H. Nicholson, "DAPI as a useful stain for nuclear quantitation," *Biotechnic & histochemistry*, vol. 66, no. 6, 1991. DOI: https://doi.org/10.3109/10520299109109990.

[65] F. Otto, "DAPI staining of fixed cells for high-resolution flow cytometry of nuclear DNA," in *Methods in cell biology*, vol. 33, Elsevier, 1990. DOI: https://doi.org/10.1016/S0091-679X(08)60516-6.

[66] B. Hohman, "LED light source: Major advance in fluorescence microscopy," *Biomedical Instrumentation & Technology*, vol. 41, no. 6, 2007. DOI: https://doi.org/10.1017/S1551929500061733.

[67] L. Cohen, "Comparison of single-mode fiber dispersion measurement techniques," *Journal of lightwave technology*, vol. 3, no. 5, 1985.

[68] H. Cao, R. Chriki, S. Bittner, A. A. Friesem, and N. Davidson, "Complex lasers with controllable coherence," *Nature Reviews Physics*, vol. 1, no. 2, 2019. DOI: https://doi.org/10.1038/s42254-018-0010-6.

[69] J. Sipior, G. M. Carter, J. R. Lakowicz, and G. Rao, "Blue light-emitting diode demonstrated as an ultraviolet excitation source for nanosecond phase-modulation fluorescence lifetime measurements," *Review of scientific instruments*, vol. 68, no. 7, 1997. DOI: https://doi.org/10.1063/1.1148177.

[70] K. Aswani, T. Jinadasa, and C. M. Brown, "Fluorescence microscopy light sources," *Microscopy today*, vol. 20, no. 4, 2012. DOI: https://doi.org/10.1017/S1551929512000399.

[71] J. S. Kuo, C. L. Kuyper, P. B. Allen, G. S. Fiorini, and D. T. Chiu, "High-power blue/UV light-emitting diodes as excitation sources for sensitive detection," *Electrophoresis*, vol. 25, no. 21-22, 2004. DOI: https://doi.org/10.1002/elps.200406118.

[72] M. G. Gustafsson, L. Shao, P. M. Carlton, *et al.*, "Three-dimensional resolution doubling in wide-field fluorescence microscopy by structured illumination," *Biophysical journal*, vol. 94, no. 12, 2008. DOI: https://doi.org/10.1529/biophysj.107.120345.

[73] V. Magidson and A. Khodjakov, "Circumventing photodamage in live-cell microscopy," *Methods in cell biology*, vol. 114, 2013. DOI: https://doi.org/10.1016/B978-0-12-407761-4.00023-3.

[74] Z. Földes-Papp, U. Demel, and G. P. Tilz, "Laser scanning confocal fluorescence microscopy: An overview," *International immunopharmacology*, vol. 3, no. 13-14, 2003. DOI: https://doi.org/10.1016/S1567-5769(03)00140-1.

[75] R. H. Webb, "Confocal optical microscopy," *Reports on progress in physics*, vol. 59, no. 3, 1996. DOI: https://doi.org/10.1088/0034-4885/59/3/003.

[76] R. C. Mellors and R. Silver, "A microfluorometric scanner for the differential detection of cells: Application to exfoliative cytology," *Science*, vol. 114, no. 2962, 1951.

[77] C. Sheppard and A. Choudhury, "Image formation in the scanning microscope," *Optica Acta: International Journal of Optics*, vol. 24, no. 10, 1977. DOI: https://doi.org/10.1080/713819421.

[78] C. Macias-Romero, V. Zubkovs, S. Wang, and S. Roke, "Wide-field medium-repetition-rate multiphoton microscopy reduces photodamage of living cells," *Biomedical optics express*, vol. 7, no. 4, 2016. DOI: https://doi.org/10.1364/BOE.7.001458.

[79] B. Li, C. Wu, M. Wang, K. Charan, and C. Xu, "An adaptive excitation source for high-speed multiphoton microscopy," *Nature methods*, vol. 17, no. 2, 2020. DOI: https://doi.org/10.1038/s41592-019-0663-9.

[80] J. R. Swedlow, "Quantitative fluorescence microscopy and image deconvolution," in *Methods in cell biology*, vol. 114, Elsevier, 2013. DOI: https://doi.org/10.1016/B978-0-12-407761-4.00017-8.

[81] X. Michalet, R. Colyer, G. Scalia, *et al.*, "Development of new photon-counting detectors for single-molecule fluorescence microscopy," *Philosophical Transactions of the Royal Society B: Biological Sciences*, vol. 368, no. 1611, 2013. DOI: https://doi.org/10.1098/rstb.2012.0035.

[82] R. Aikens, D. Agard, and J. Sedat, "Solid-state imagers for microscopy," *Methods in cell biology*, vol. 29, 1988. DOI: https://doi.org/10.1016/S0091-679X(08)60199-5.

[83] B. Burke, P. Jorden, and P. Vu, "CCD technology," *Experimental Astronomy*, vol. 19, 2005. DOI: https://doi.org/10.1007/s10686-005-9011-4.

[84] S. Inoue and K. Spring, "Video microscopy, plenum press," *New York*, 1997.

[85] F. M. Li and A. Nathan, *CCD Image Sensors in Deep-Ultraviolet: Degradation Behavior and Damage Mechanisms*. Springer, 2005.

[86] M. Lesser, "Antireflection coatings for silicon charge-coupled devices," *Optical Engineering*, vol. 26, no. 9, 1987. DOI: https://doi.org/10.1117/12.7974170.

[87] M. Bigas, E. Cabruja, J. Forest, and J. Salvi, "Review of CMOS image sensors," *Microelectronics journal*, vol. 37, no. 5, 2006. DOI: https://doi.org/10.1016/j.mejo.2005.07.002.

[88] L. Thorpe, E. Tamura, and T. Iwasaki, "New advances in CCD imaging," *SMPTE journal*, vol. 97, no. 5, 1988.

[89] R. Widenhorn, M. M. Blouke, A. Weber, A. Rest, and E. Bodegom, "Temperature dependence of dark current in a CCD," in *Sensors and Camera Systems for Scientific, Industrial, and Digital Photography Applications III*, SPIE, vol. 4669, 2002. DOI: https://doi.org/10.1117/12.463446.

[90] L. Austin and H. Starke, "Ueber die Reflexion der Kathodenstrahlen und eine damit verbundene neue Erscheinung secundärer Emission," *Annalen der Physik*, vol. 314, no. 10, 1902. DOI: https://doi.org/10.1002/andp.19023141003.

[91] K. R. Spring, "Detectors for fluorescence microscopy," in *Methods in Cellular Imaging*, 2001. DOI: https://doi.org/10.1007/978-1-4614-7513-2_3.

[92] N. Naredi-Rainer, J. Prescher, A. Hartschuh, and D. C. Lamb, "Confocal microscopy," in *Fluorescence Microscopy*. John Wiley Sons, Ltd, 2013, ch. 3. DOI: https://doi.org/10.1002/9783527671595.ch5.

[93] E. Sánchez-Ortiga, C. J. Sheppard, G. Saavedra, M. Martınez-Corral, A. Doblas, and A. Calatayud, "Subtractive imaging in confocal scanning microscopy using a CCD camera as a detector," *Optics letters*, vol. 37, no. 7, 2012. DOI: https://doi.org/10.1364/OL.37.001280.

[94] P. O. Bayguinov, D. M. Oakley, C.-C. Shih, D. J. Geanon, M. S. Joens, and J. A. Fitzpatrick, "Modern laser scanning confocal microscopy," *Current protocols in cytometry*, vol. 85, no. 1, 2018. DOI: https://doi.org/10.1002/cpcy.39.

[95] F. Zernike, "Phase contrast, a new method for the microscopic observation of transparent objects part II," *Physica*, vol. 9, no. 10, 1942. DOI: https://doi.org/10.1016/S0031-8914(42)80079-8.

[96] H. Komatsu and G. Sazaki, "Differential interference contrast microscopy / phase-contrast microscopy," *Compendium of Surface and Interface Analysis*, 2018. DOI: https://doi.org/10.1007/978-981-10-6156-1_10.

[97] C. Burch and J. Stock, "Phase-contrast microscopy," *Journal of Scientific Instruments*, vol. 19, no. 5, 1942. DOI: https://doi.org/10.1088/0950-7671/19/5/302.

[98] C. Maurer, A. Jesacher, S. Bernet, and M. Ritsch-Marte, "Phase contrast microscopy with full numerical aperture illumination," *Optics express*, vol. 16, no. 24, 2008. DOI: https://doi.org/10.1364/OE.16.019821.

[99] J. B. Sanderson, "Phase contrast microscopy," *Encyclopedia of Life Sciences*, 2001. DOI: https://doi.org/10.1038/npg.els.0002635.

[100] B. Payne, "Image formation in phase-contrast microscopy," *Journal of Scientific Instruments*, vol. 24, no. 6, 1947. DOI: https://doi.org/10.1088/0950-7671/24/6/308.

[101] S. Munck, C. Cawthorne, A. Escamilla-Ayala, *et al.*, "Challenges and advances in optical 3D mesoscale imaging," *Journal of Microscopy*, vol. 286, no. 3, 2022. DOI: https://doi.org/10.1111/jmi.13109.

[102] G. McConnell, J. Trägårdh, R. Amor, J. Dempster, E. Reid, and W. B. Amos, "A novel optical microscope for imaging large embryos and tissue volumes with sub-cellular resolution throughout," *Elife*, vol. 5, e18659, 2016. DOI: 10.7554/eLife.18659.

[103] J. Schniete, A. Franssen, J. Dempster, T. J. Bushell, W. B. Amos, and G. McConnell, "Fast optical sectioning for widefield fluorescence mesoscopy with the mesolens based on hilo microscopy," *Scientific reports*, vol. 8, no. 1, 2018. DOI: 10.1038/s41598-018-34516-2.

[104] F. B. Legesse, O. Chernavskaia, S. Heuke, *et al.*, "Seamless stitching of tile scan microscope images," *Journal of microscopy*, vol. 258, no. 3, 2015. DOI: https://doi.org/10.1111/jmi.12236.

[105] S. Preibisch, S. Saalfeld, and P. Tomancak, "Globally optimal stitching of tiled 3D microscopic image acquisitions," *Bioinformatics*, vol. 25, no. 11, 2009. DOI: https://doi.org/10.1093/bioinformatics/btp184.

[106] G. McConnell and W. B. Amos, "Application of the Mesolens for subcellular resolution imaging of intact larval and whole adult Drosophila," *Journal of microscopy*, vol. 270, no. 2, 2018. DOI: https://doi.org/10.1111/jmi.12693.

[107] E. Battistella, J. F. Quintana, and G. McConnell, "Application of light-sheet mesoscopy to image host-pathogen interactions in intact organs," *Frontiers in Cellular and Infection Microbiology*, 2022. DOI: https://doi.org/10.3389/fcimb.2022.903957.

[108] E. Battistella, J. Schniete, K. Wesencraft, J. F. Quintana, and G. McConnell, "Light-sheet mesoscopy with the Mesolens provides fast subcellular resolution imaging throughout large tissue volumes," *Iscience*, vol. 25, no. 9, 2022. DOI: https://doi.org/10.1016/j.isci.2022.104797.

[109] R. J. Francis, G. Robb, L. McCann, *et al.*, "Three-dimensional in situ morphometrics of mycobacterium tuberculosis infection within lesions by optical mesoscopy and novel acid-fast staining," *Scientific reports*, vol. 10, no. 1, 2020. DOI: https://doi.org/10.1038/s41598-020-78640-4.

[110] M. Clapperton, T. Kunanandam, C. D. Florea, C. M. Douglas, and G. McConnell, "Multimodal optical mesoscopy reveals the quantity and spatial distribution of Gram-positive biofilms in ex vivo tonsils," *Journal of Microscopy*, 2024. DOI: https://doi.org/10.1111/jmi.13266.

[111] S. Foylan, J. K. Schniete, L. S. Kölln, *et al.*, "Mesoscale standing wave imaging," *Journal of Microscopy*, 2023. DOI: https://doi.org/10.1111/jmi.13189.

[112] R. M. Donlan, "Biofilms: Microbial life on surfaces," *Emerging infectious diseases*, vol. 8, no. 9, 2002. DOI: 10.3201/eid0809.020063.

[113] W. Yin, Y. Wang, L. Liu, and J. He, "Biofilms: The microbial "protective clothing" in extreme environments," *International journal of molecular sciences*, vol. 20, no. 14, 2019. DOI: 10.3390/ijms20143423.

[114] P. Stewart and T. Bjarnsholt, "Risk factors for chronic biofilm-related infection associated with implanted medical devices," *Clinical Microbiology and Infection*, vol. 26, no. 8, 2020. DOI: https://doi.org/10.1016/j.cmi.2020.02.027.

[115] D. Van der Kooij, J. Vrouwenvelder, and H. Veenendaal, "Elucidation and control of biofilm formation processes in water treatment and distribution using the unified biofilm approach," *Water Science and Technology*, vol. 47, no. 5, 2003. DOI: https://doi.org/10.2166/wst.2003.0287.

[116] J. D. Bryers, "Medical biofilms," *Biotechnology and bioengineering*, vol. 100, no. 1, 2008. DOI: https://doi.org/10.1002/bit.21838.

[117] A. Reisner, J. A. Haagensen, M. A. Schembri, E. L. Zechner, and S. Molin, "Development and maturation of Escherichia coli K-12 biofilms," *Molecular microbiology*, vol. 48, no. 4, 2003. DOI: https://doi.org/10.1046/j.1365-2958.2003.03490.x.

[118] S. Arnaouteli, N. C. Bamford, N. R. Stanley-Wall, and Á. T. Kovács, "Bacillus subtilis biofilm formation and social interactions," *Nature Reviews Microbiology*, vol. 19, no. 9, 2021. DOI: https://doi.org/10.1038/s41579-021-00540-9.

[119] J. K. Teschler, D. Zamorano-Sánchez, A. S. Utada, *et al.*, "Living in the matrix: Assembly and control of Vibrio cholerae biofilms," *Nature Reviews Microbiology*, vol. 13, no. 5, 2015. DOI: https://doi.org/10.1038/nrmicro3433.

[120] Z. D. Blount, "The natural history of model organisms: The unexhausted potential of E. coli," *Elife*, vol. 4, 2015. DOI: https://doi.org/10.7554/eLife.05826.

[121] F. R. Blattner, G. Plunkett III, C. A. Bloch, *et al.*, "The complete genome sequence of Escherichia coli K-12," *Science*, vol. 277, no. 5331, 1997. DOI: https://doi.org/10.1126/science.277.5331.1453.

[122] C. Potera, "Forging a link between biofilms and disease," *Science*, vol. 283, 1999. DOI: 10.1126/science.283.5409.1837.

[123] G. Sharma, S. Sharma, P. Sharma, *et al.*, "Escherichia coli biofilm: Development and therapeutic strategies," *Journal of applied microbiology*, vol. 121, no. 2, 2016. DOI: https://doi.org/10.1111/jam.13078.

[124] D. G. Allison, "The biofilm matrix," *Biofouling*, vol. 19, no. 2, 2003. DOI: https://doi.org/10.1080/0892701031000072190.

[125] H.-C. Flemming, J. Wingender, U. Szewzyk, P. Steinberg, S. A. Rice, and S. Kjelleberg, "Biofilms: An emergent form of bacterial life," *Nature Reviews Microbiology*, vol. 14, no. 9, 2016. DOI: https://doi.org/10.1038/nrmicro.2016.94.

[126] N. Steinberg and I. Kolodkin-Gal, *The matrix reloaded: How sensing the extracellular matrix synchronizes bacterial communities*, 2015. DOI: https://doi.org/10.1128/jb.02516-14.

[127] A. Ueda and T. K. Wood, "Connecting quorum sensing, c-di-GMP, pel polysaccharide, and biofilm formation in Pseudomonas aeruginosa through

tyrosine phosphatase TpbA (PA3885)," *PLoS pathogens*, vol. 5, no. 6, 2009. DOI: https://doi.org/10.1371/journal.ppat.1000483.

[128] N. P. Ivleva, M. Wagner, H. Horn, R. Niessner, and C. Haisch, "Towards a nondestructive chemical characterization of biofilm matrix by Raman microscopy," *Analytical and bioanalytical chemistry*, vol. 393, no. 1, 2009. DOI: https://doi.org/10.1007/s00216-008-2470-5.

[129] Y. Mao, M. Doyle, and J. Chen, "Role of colanic acid exopolysaccharide in the survival of enterohaemorrhagic Escherichia coli O157: H7 in simulated gastrointestinal fluids," *Letters in applied microbiology*, vol. 42, no. 6, 2006. DOI: https://doi.org/10.1111/j.1472-765X.2006.01875.x.

[130] V. Berk, J. C. Fong, G. T. Dempsey, *et al.*, "Molecular architecture and assembly principles of Vibrio cholerae biofilms," *Science*, vol. 337, no. 6091, 2012. DOI: https://doi.org/10.1126/science.1222981.

[131] A. L. Ibanez de Aldecoa, O. Zafra, and J. E. González-Pastor, "Mechanisms and regulation of extracellular DNA release and its biological roles in microbial communities," *Frontiers in microbiology*, vol. 8, 2017. DOI: https://doi.org/10.3389/fmicb.2017.01390.

[132] M. Okshevsky, V. R. Regina, and R. L. Meyer, "Extracellular DNA as a target for biofilm control," *Current opinion in biotechnology*, vol. 33, 2015. DOI: https://doi.org/10.1016/j.copbio.2014.12.002.

[133] W.-C. Chiang, M. Nilsson, P. Ø. Jensen, *et al.*, "Extracellular DNA shields against aminoglycosides in Pseudomonas aeruginosa biofilms," *Antimicrobial agents and chemotherapy*, vol. 57, no. 5, 2013. DOI: https://doi.org/10.1128/aac.00001-13.

[134] E. S. Gloag, L. Turnbull, A. Huang, *et al.*, "Self-organization of bacterial biofilms is facilitated by extracellular DNA," *Proceedings of the National*

Academy of Sciences, vol. 110, no. 28, 2013. DOI: https://doi.org/10.1073/pnas.121889811.

[135] J. Monod, "The growth of bacterial cultures," *Annual Reviews in Microbiology*, 1949.

[136] R. Van Houdt and C. W. Michiels, "Role of bacterial cell surface structures in Escherichia coli biofilm formation," *Research in microbiology*, vol. 156, no. 5-6, 2005. DOI: https://doi.org/10.1016/j.resmic.2005.02.005.

[137] T. K. Wood, A. F. G. Barrios, M. Herzberg, and J. Lee, "Motility influences biofilm architecture in Escherichia coli," *Applied microbiology and biotechnology*, vol. 72, no. 2, 2006. DOI: 10.1007/s00253-005-0263-8.

[138] C. Beloin, A. Roux, and J.-M. Ghigo, "Escherichia coli biofilms," in *Bacterial Biofilms*, Springer, 2008. DOI: https://doi.org/10.1007/978-3-540-75418-3_12.

[139] T. R. Garrett, M. Bhakoo, and Z. Zhang, "Bacterial adhesion and biofilms on surfaces," *Progress in natural science*, vol. 18, no. 9, 2008. DOI: https://doi.org/10.1016/j.pnsc.2008.04.001.

[140] G. A. O'Toole and G. C. Wong, "Sensational biofilms: Surface sensing in bacteria," *Current opinion in microbiology*, vol. 30, 2016. DOI: https://doi.org/10.1016/j.mib.2016.02.004.

[141] R. R. Spurbeck, A. E. Stapleton, J. R. Johnson, S. T. Walk, T. M. Hooton, and H. L. Mobley, "Fimbrial profiles predict virulence of uropathogenic Escherichia coli strains: Contribution of ygi and yad fimbriae," *Infection and immunity*, vol. 79, no. 12, 2011. DOI: https://doi.org/10.1128/iai.05621-11.

[142] J. Yan, B. Sabass, H. Stone, N. Wingreen, and B. Bassler, "Biofilm growth program and architecture revealed by single-cell live imaging," *Bulletin of the American Physical Society*, vol. 62, 2017.

[143] R. Roy, M. Tiwari, G. Donelli, and V. Tiwari, "Strategies for combating bacterial biofilms: A focus on anti-biofilm agents and their mechanisms of action," *Virulence*, vol. 9, no. 1, 2018. DOI: https://doi.org/10.1080/21505594.2017.1313372.

[144] P. N. Danese, L. A. Pratt, and R. Kolter, "Exopolysaccharide production is required for development of Escherichia coli K-12 biofilm architecture," *Journal of bacteriology*, vol. 182, no. 12, 2000. DOI: https://doi.org/10.1128/jb.182.12.3593-3596.2000.

[145] P. S. Stewart and M. J. Franklin, "Physiological heterogeneity in biofilms," *Nature Reviews Microbiology*, vol. 6, no. 3, 2008. DOI: https://doi.org/10.1038/nrmicro1838.

[146] D. O. Serra and R. Hengge, "Stress responses go three dimensional–the spatial order of physiological differentiation in bacterial macrocolony biofilms," *Environmental microbiology*, vol. 16, no. 6, 2014. DOI: https://doi.org/10.1111/1462-2920.12483.

[147] D. McDougald, S. A. Rice, N. Barraud, P. D. Steinberg, and S. Kjelleberg, "Should we stay or should we go: Mechanisms and ecological consequences for biofilm dispersal," *Nature Reviews Microbiology*, vol. 10, no. 1, 2012. DOI: https://doi.org/10.1038/nrmicro2695.

[148] J. B. Kaplan, "Biofilm dispersal: Mechanisms, clinical implications, and potential therapeutic uses," *Journal of dental research*, vol. 89, no. 3, 2010. DOI: https://doi.org/10.1177/0022034509359403.

[149] J. L. Lister and A. R. Horswill, "Staphylococcus aureus biofilms: Recent developments in biofilm dispersal," *Frontiers in cellular and infection microbiology*, vol. 4, 2014. DOI: https://doi.org/10.3389/fcimb.2014.00178.

[150] K. Stevenson, A. F. McVey, I. B. Clark, P. S. Swain, and T. Pilizota, "General calibration of microbial growth in microplate readers," *Scientific reports*, vol. 6, no. 1, 2016. DOI: https://doi.org/10.1038/srep38828.

[151] C. Begot, I. Desnier, J. D. Daudin, J. C. Labadie, and A. Lebert, "Recommendations for calculating growth parameters by optical density measurements," *Journal of Microbiological Methods*, vol. 25, no. 3, 1996. DOI: https://doi.org/10.1016/0167-7012(95)00090-9.

[152] B. M. Coffey and G. G. Anderson, "Biofilm formation in the 96-well microtiter plate," *Pseudomonas methods and protocols*, 2014. DOI: https://doi.org/10.1007/978-1-4939-0473-0_48.

[153] G. A. O'Toole, "Microtiter dish biofilm formation assay," *JoVE (Journal of Visualized Experiments)*, no. 47, 2011. DOI: https://doi.org/10.3791/2437.

[154] E. M. Swanton, W. A. Curby, and H. E. Lind, "Experiences with the coulter counter in bacteriology," *Applied Microbiology*, vol. 10, no. 5, 1962. DOI: https://doi.org/10.1128/am.10.5.480-485.1962.

[155] W. Zhang, E. S. McLamore, N. Garland, J. C. Leon, and M. K. Banks, "A simple method for quantifying biomass cell and polymer distribution in biofilms," *Journal of microbiological methods*, vol. 94, no. 3, 2013. DOI: https://doi.org/10.1016/j.mimet.2013.07.022.

[156] V. Isaeva, "Self-organization in biological systems," *Biology Bulletin*, vol. 39, 2012. DOI: https://doi.org/10.1134/S1062359012020069.

[157] B. L. Hogan, "Morphogenesis," *Cell*, vol. 96, no. 2, 1999. DOI: https://doi.org/10.1016/S0092-8674(00)80562-0.

[158] A. M. Turing, "The chemical basis of morphogenesis," *Philosophical Transactions of the Royal Society B*, vol. 237, 1953. DOI: https://doi.org/10.1007/BF02459572.

[159] S. Kondo and T. Miura, "Reaction-diffusion model as a framework for understanding biological pattern formation," *Science*, vol. 329, no. 5999, 2010. DOI: https://doi.org/10.1126/science.1179047.

[160] N. Cogan, M. Donahue, M. Whidden, and L. De La Fuente, "Pattern formation exhibited by biofilm formation within microfluidic chambers," *Biophysical journal*, vol. 104, no. 9, 2013. DOI: https://doi.org/10.1016/j.bpj.2013.03.037.

[161] P. Thomen, J. D. Valentin, A.-F. Bitbol, and N. Henry, "Spatiotemporal pattern formation in E. coli biofilms explained by a simple physical energy balance," *Soft Matter*, vol. 16, no. 2, 2020. DOI: https://doi.org/10.1039/C9SM01375J.

[162] D. Karig, K. M. Martini, T. Lu, N. A. DeLateur, N. Goldenfeld, and R. Weiss, "Stochastic Turing patterns in a synthetic bacterial population," *Proceedings of the National Academy of Sciences*, vol. 115, no. 26, 2018. DOI: https://doi.org/10.1073/pnas.172077011.

[163] L. Eigentler, F. A. Davidson, and N. R. Stanley-Wall, "Mechanisms driving spatial distribution of residents in colony biofilms: An interdisciplinary perspective," *Open Biology*, vol. 12, no. 12, 2022. DOI: https://doi.org/10.1098/rsob.220194.

[164] D. Volfson, S. Cookson, J. Hasty, and L. S. Tsimring, "Biomechanical ordering of dense cell populations," *Proceedings of the National Academy*

of Sciences, vol. 105, no. 40, 2008. DOI: https://doi.org/10.1073/pnas.0706805105.

[165] J. Nijjer, C. Li, Q. Zhang, H. Lu, S. Zhang, and J. Yan, "Mechanical forces drive a reorientation cascade leading to biofilm self-patterning," *Nature communications*, vol. 12, no. 1, 2021. DOI: https://doi.org/10.1038/s41467-021-26869-6.

[166] S. Trinschek, K. John, S. Lecuyer, and U. Thiele, "Continuous versus arrested spreading of biofilms at solid-gas interfaces: The role of surface forces," *Physical review letters*, vol. 119, no. 7, 2017. DOI: https://doi.org/10.1103/PhysRevLett.119.078003.

[167] J. Yan, C. Fei, S. Mao, *et al.*, "Mechanical instability and interfacial energy drive biofilm morphogenesis," *Elife*, vol. 8, 2019. DOI: 10.7554/eLife.43920.

[168] K. Manickam, R. R. Machireddy, and S. Seshadri, "Characterization of biomechanical properties of agar based tissue mimicking phantoms for ultrasound stiffness imaging techniques," *Journal of the mechanical behavior of Biomedical Materials*, vol. 35, 2014. DOI: https://doi.org/10.1016/j.jmbbm.2014.03.017.

[169] R. Ziege, A.-M. Tsirigoni, B. Large, *et al.*, "Adaptation of Escherichia coli biofilm growth, morphology, and mechanical properties to substrate water content," *ACS biomaterials science & engineering*, vol. 7, no. 11, 2021. DOI: https://doi.org/10.1021/acsbiomaterials.1c00927.

[170] C. Fei, S. Mao, J. Yan, *et al.*, "Nonuniform growth and surface friction determine bacterial biofilm morphology on soft substrates," *Proceedings of the National Academy of Sciences*, vol. 117, no. 14, pp. 7622–7632, 2020. DOI: 10.1073/pnas.1919607117.

[171] J. Yan, C. D. Nadell, H. A. Stone, N. S. Wingreen, and B. L. Bassler, "Extracellular-matrix-mediated osmotic pressure drives vibrio cholerae biofilm expansion and cheater exclusion," *Nature communications*, vol. 8, no. 1, 2017. DOI: https://doi.org/10.1038/s41467-017-00401-1.

[172] X. Wang, S. Meng, and J. Han, "Morphologies and phenotypes in Bacillus subtilis biofilms," *Journal of Microbiology*, vol. 55, no. 8, 2017. DOI: https://doi.org/10.1007/s12275-017-7041-z.

[173] S. Gingichashvili, D. Duanis-Assaf, M. Shemesh, J. D. Featherstone, O. Feuerstein, and D. Steinberg, "The adaptive morphology of Bacillus subtilis biofilms: A defense mechanism against bacterial starvation," *Microorganisms*, vol. 8, no. 1, 2019. DOI: https://doi.org/10.3390/microorganisms8010062.

[174] E. O. Budrene and H. C. Berg, "Dynamics of formation of symmetrical patterns by chemotactic bacteria," *Nature*, vol. 376, no. 6535, 1995. DOI: https://doi.org/10.1038/376049a0.

[175] K. S. Korolev, M. J. Müller, N. Karahan, A. W. Murray, O. Hallatschek, and D. R. Nelson, "Selective sweeps in growing microbial colonies," *Physical biology*, vol. 9, no. 2, 2012. DOI: 10.1088/1478-3975/9/2/026008.

[176] S. Duran-Nebreda, J. Pla, B. Vidiella, J. Pinero, N. Conde-Pueyo, and R. Solé, "Synthetic lateral inhibition in periodic pattern forming microbial colonies," *ACS Synthetic Biology*, vol. 10, no. 2, 2021. DOI: https://doi.org/10.1021/acssynbio.0c00318.

[177] L. Xiong, Y. Cao, R. Cooper, W.-J. Rappel, J. Hasty, and L. Tsimring, "Flower-like patterns in multi-species bacterial colonies," *Elife*, vol. 9, 2020. DOI: https://doi.org/10.7554/eLife.48885.

[178] T. Tolker-Nielsen and S. Molin, "Spatial organization of microbial biofilm communities," *Microbial ecology*, vol. 40, no. 2, 2000. DOI: 10.1007/s002480000057.

[179] R. Hartmann, P. K. Singh, P. Pearce, *et al.*, "Emergence of three-dimensional order and structure in growing biofilms," *Nature physics*, vol. 15, no. 3, pp. 251–256, 2019. DOI: 10.1038/s41567-018-0356-9.

[180] H.-C. Flemming and J. Wingender, "The biofilm matrix," *Nature reviews microbiology*, vol. 8, no. 9, 2010. DOI: https://doi.org/10.1038/nrmicro2415.

[181] D. O. Serra, G. Klauck, and R. Hengge, "Vertical stratification of matrix production is essential for physical integrity and architecture of macrocolony biofilms of Escherichia coli," *Environmental microbiology*, vol. 17, no. 12, 2015. DOI: https://doi.org/10.1111/1462-2920.12991.

[182] D. O. Serra, A. M. Richter, G. Klauck, F. Mika, and R. Hengge, "Microanatomy at cellular resolution and spatial order of physiological differentiation in a bacterial biofilm," *MBio*, vol. 4, no. 2, 2013. DOI: https://doi.org/10.1128/mbio.00103-13.

[183] S. Geisel, E. Secchi, and J. Vermant, "The role of surface adhesion on the macroscopic wrinkling of biofilms," *Elife*, vol. 11, 2022. DOI: https://doi.org/10.7554/eLife.76027.

[184] D. Boyer, W. Mather, O. Mondragón-Palomino, *et al.*, "Buckling instability in ordered bacterial colonies," *Physical biology*, vol. 8, no. 2, 2011. DOI: https://doi.org/10.1088/1478-3975/8/2/026008.

[185] M. Asally, M. Kittisopikul, P. Rué, *et al.*, "Localized cell death focuses mechanical forces during 3D patterning in a biofilm," *Proceedings of the*

National Academy of Sciences, vol. 109, no. 46, 2012. DOI: https://doi.org/10.1073/pnas.1212429109.

[186] B. Aguilar, A. Ghaffarizadeh, C. D. Johnson, G. J. Podgorski, I. Shmulevich, and N. S. Flann, "Cell death as a trigger for morphogenesis," *PLoS One*, vol. 13, no. 3, 2018. DOI: https://doi.org/10.1371/journal.pone.0191089.

[187] M. Trejo, C. Douarche, V. Bailleux, *et al.*, "Elasticity and wrinkled morphology of Bacillus subtilis pellicles," *Proceedings of the National Academy of Sciences*, vol. 110, no. 6, 2013. DOI: https://doi.org/10.1073/pnas.1217178110.

[188] X. Wang, Y. Tan, J. Liu, S. Hu, and H. Zhao, "The evolving wrinkle pattern of the Bacillus subtilis biofilm providing more living space for cells," *Journal of Mechanics in Medicine and Biology*, vol. 20, no. 07, 2020. DOI: https://doi.org/10.1142/S0219519420500487.

[189] W. P. Smith, Y. Davit, J. M. Osborne, W. Kim, K. R. Foster, and J. M. Pitt-Francis, "Cell morphology drives spatial patterning in microbial communities," *Proceedings of the National Academy of Sciences*, vol. 114, no. 3, 2017. DOI: 10.1073/pnas.1613007114.

[190] F. Beroz, J. Yan, Y. Meir, *et al.*, "Verticalization of bacterial biofilms," *Nature physics*, vol. 14, no. 9, 2018. DOI: https://doi.org/10.1038/s41567-018-0170-4.

[191] D. Puri, X. Fang, and K. R. Allison, "Evidence of a possible multicellular life cycle in Escherichia coli," *Iscience*, vol. 26, no. 1, 2023. DOI: https://doi.org/10.1016/j.isci.2022.105795.

[192] A. Kan, I. Del Valle, T. Rudge, F. Federici, and J. Haseloff, "Intercellular adhesion promotes clonal mixing in growing bacterial populations," *Journal of The Royal Society Interface*, vol. 15, no. 146, 2018. DOI: https://doi.org/10.1098/rsif.2018.0406.

[193] A. Tam, J. E. F. Green, S. Balasuriya, *et al.*, "Nutrient-limited growth with non-linear cell diffusion as a mechanism for floral pattern formation in yeast biofilms," *Journal of theoretical biology*, vol. 448, 2018. DOI: https://doi.org/10.1016/j.jtbi.2018.04.004.

[194] B. Momeni, K. A. Brileya, M. W. Fields, and W. Shou, "Strong inter-population cooperation leads to partner intermixing in microbial communities," *elife*, vol. 2, 2013. DOI: https://doi.org/10.7554/eLife.00230.

[195] F. Goldschmidt, R. R. Regoes, and D. R. Johnson, "Successive range expansion promotes diversity and accelerates evolution in spatially structured microbial populations," *The ISME journal*, vol. 11, no. 9, 2017. DOI: https://doi.org/10.1038/ismej.2017.76.

[196] W. R. DiLuzio, L. Turner, M. Mayer, *et al.*, "Escherichia coli swim on the right-hand side," *Nature*, vol. 435, no. 7046, 2005. DOI: https://doi.org/10.1038/nature03660.

[197] L. Jauffred, R. M. Vejborg, K. S. Korolev, S. Brown, and L. B. Oddershede, "Chirality in microbial biofilms is mediated by close interactions between the cell surface and the substratum," *The ISME journal*, vol. 11, no. 7, 2017. DOI: 10.1038/ismej.2017.19.

[198] A. B. George and K. S. Korolev, "Chirality provides a direct fitness advantage and facilitates intermixing in cellular aggregates," *PLoS computational biology*, vol. 14, no. 12, 2018. DOI: https://doi.org/10.1371/journal.pcbi.1006645.

[199] J. W. Schroeder, P. Yeesin, L. A. Simmons, and J. D. Wang, "Sources of spontaneous mutagenesis in bacteria," *Critical reviews in biochemistry and molecular biology*, vol. 53, no. 1, 2018. DOI: https://doi.org/10.1080/10409238.2017.1394262.

[200] I. Golding, I. Cohen, and E. Ben-Jacob, "Studies of sector formation in expanding bacterial colonies," *Europhysics Letters*, vol. 48, no. 5, 1999. DOI: 10.1209/epl/i1999-00524-7.

[201] O. Hallatschek, P. Hersen, S. Ramanathan, and D. R. Nelson, "Genetic drift at expanding frontiers promotes gene segregation," *Proceedings of the National Academy of Sciences*, vol. 104, no. 50, 2007. DOI: https://doi.org/10.1073/pnas.0710150104.

[202] D. R. Amor, R. Montañez, S. Duran-Nebreda, and R. Solé, "Spatial dynamics of synthetic microbial mutualists and their parasites," *PLoS computational biology*, vol. 13, no. 8, 2017. DOI: https://doi.org/10.1371/journal.pcbi.1005689.

[203] M. S. Switzenbaum and R. B. Eimstad, "Analysis of anaerobic biofilms," *Environmental Technology*, vol. 8, no. 1-12, 1987. DOI: https://doi.org/10.1080/09593338709384460.

[204] W. J. Drury, W. G. Characklis, and P. S. Stewart, "Interactions of 1 μm latex particles with Pseudomonas aeruginosa biofilms," *Water Research*, vol. 27, no. 7, 1993. DOI: https://doi.org/10.1016/0043-1354(93)90003-Z.

[205] A. A. Massol-Deyá, J. Whallon, R. F. Hickey, and J. M. Tiedje, "Channel structures in aerobic biofilms of fixed-film reactors treating contaminated groundwater," *Applied and Environmental Microbiology*, vol. 61, no. 2, 1995. DOI: https://doi.org/10.1128/aem.61.2.769-777.1995.

[206] A. Birjiniuk, N. Billings, E. Nance, J. Hanes, K. Ribbeck, and P. S. Doyle, "Single particle tracking reveals spatial and dynamic organization of the Escherichia coli biofilm matrix," *New journal of physics*, vol. 16, no. 8, 2014. DOI: 10.1088/1367-2630/16/8/085014.

[207] J. N. Wilking, V. Zaburdaev, M. De Volder, R. Losick, M. P. Brenner, and D. A. Weitz, "Liquid transport facilitated by channels in Bacillus subtilis biofilms," *Proceedings of the National Academy of Sciences*, vol. 110, no. 3, 2013. DOI: https://doi.org/10.1073/pnas.1216376110.

[208] S. Gingichashvili, O. Feuerstein, and D. Steinberg, "Topography and expansion patterns at the biofilm-agar interface in bacillus subtilis biofilms," *Microorganisms*, vol. 9, no. 1, 2021. DOI: 10.3390/microorganisms9010084.

[209] L. M. Rooney, W. B. Amos, P. A. Hoskisson, and G. McConnell, "Intracolony channels in E. coli function as a nutrient uptake system," *The ISME journal*, vol. 14, no. 10, 2020. DOI: 10.1038/s41396-020-0700-9.

[210] J. W. Costerton, G. Geesey, and K.-J. Cheng, "How bacteria stick," *Scientific American*, vol. 238, no. 1, 1978.

[211] R. Murga, P. S. Stewart, and D. Daly, "Quantitative analysis of biofilm thickness variability," *Biotechnology and bioengineering*, vol. 45, no. 6, 1995. DOI: https://doi.org/10.1002/bit.260450607.

[212] J. E. Hobbie, R. J. Daley, and S. Jasper, "Use of nuclepore filters for counting bacteria by fluorescence microscopy," *Applied and environmental microbiology*, vol. 33, no. 5, 1977. DOI: https://doi.org/10.1128/aem.33.5.1225-1228.1977.

[213] R. Bakke and P. Olsson, "Biofilm thickness measurements by light microscopy," *Journal of microbiological methods*, vol. 5, no. 2, 1986. DOI: https://doi.org/10.1016/0167-7012(86)90005-9.

[214] J. Walker and C. Keevil, "Study of microbial biofilms using light microscope techniques," *International biodeterioration & biodegradation*, vol. 34, no. 3-4, 1994. DOI: https://doi.org/10.1016/0964-8305(94)90084-1.

[215] T. Ladd, J. Costerton, and G. Geesey, "Determination of the heterotrophic activity of epilithic microbial populations," *Native aquatic bacteria: Enumeration, activity and ecology*, 1979.

[216] J. Lawrence, D. Korber, B. Hoyle, J. W. Costerton, and D. Caldwell, "Optical sectioning of microbial biofilms," *Journal of bacteriology*, vol. 173, no. 20, 1991. DOI: https://doi.org/10.1128/jb.173.20.6558-6567.1991.

[217] T. R. Neu, B. Manz, F. Volke, J. J. Dynes, A. P. Hitchcock, and J. R. Lawrence, "Advanced imaging techniques for assessment of structure, composition and function in biofilm systems," *FEMS microbiology ecology*, vol. 72, no. 1, 2010. DOI: https://doi.org/10.1111/j.1574-6941.2010.00837.x.

[218] J. Azeredo, N. F. Azevedo, R. Briandet, *et al.*, "Critical review on biofilm methods," *Critical reviews in microbiology*, vol. 43, no. 3, 2017. DOI: https://doi.org/10.1080/1040841X.2016.1208146.

[219] D. Caldwell, D. Korber, and J. Lawrence, "Imaging of bacterial cells by fluorescence exclusion using scanning confocal laser microscopy," *Journal of Microbiological Methods*, vol. 15, no. 4, 1992. DOI: https://doi.org/10.1016/0167-7012(92)90045-6.

[220] D. C. Fung and J. A. Theriot, "Imaging techniques in microbiology," *Current opinion in microbiology*, vol. 1, no. 3, 1998. DOI: https://doi.org/10.1016/S1369-5274(98)80040-4.

[221] H. Kobayashi, M. Ogawa, R. Alford, P. L. Choyke, and Y. Urano, "New strategies for fluorescent probe design in medical diagnostic imaging," *Chemical reviews*, vol. 110, no. 5, 2010. DOI: https://doi.org/10.1021/cr900263j.

[222] K. K. Jain, "Applications of nanobiotechnology in clinical diagnostics," *Clinical chemistry*, vol. 53, no. 11, 2007. DOI: https://doi.org/10.1373/clinchem.2007.090795.

[223] J. Heesemann and R. Laufs, "Double immunofluorescence microscopic technique for accurate differentiation of extracellularly and intracellularly located bacteria in cell culture," *Journal of clinical microbiology*, vol. 22, no. 2, 1985. DOI: https://doi.org/10.1128/jcm.22.2.168-175.1985.

[224] C. M. Thomas and K. M. Nielsen, "Mechanisms of, and barriers to, horizontal gene transfer between bacteria," *Nature reviews microbiology*, vol. 3, no. 9, 2005. DOI: https://doi.org/10.1038/nrmicro1234.

[225] A. Karsi and M. L. Lawrence, "Broad host range fluorescence and bioluminescence expression vectors for Gram-negative bacteria," *Plasmid*, vol. 57, no. 3, 2007. DOI: https://doi.org/10.1016/j.plasmid.2006.11.002.

[226] A. Caratooli, "Evolution of plasmids and evolution of virulence and antibiotic-resistance plasmids," in *Evolutionary Biology of Bacterial and Fungal Pathogens*. ASM Press, 2008, ch. 15. DOI: https://doi.org/10.1128/9781555815639.ch15.

[227] D. E. Taylor, A. Gibreel, T. D. Lawley, and D. M. Tracz, "Antibiotic resistance plasmids," in *Plasmid biology*. Wiley Online Library, 2004, ch. 23. DOI: https://doi.org/10.1128/9781555817732.ch23.

[228] O. Rendueles and J.-M. Ghigo, "Mechanisms of competition in biofilm communities," in *Microbial biofilms*. Wiley Online Library, 2015, ch. 16. DOI: https://doi.org/10.1128/9781555817466.ch16.

[229] D. A. Mavridou, D. Gonzalez, W. Kim, S. A. West, and K. R. Foster, "Bacteria use collective behavior to generate diverse combat strategies," *Current Biology*, vol. 28, no. 3, 2018. DOI: https://doi.org/10.1016/j.cub.2017.12.030.

[230] W. S. Reznikoff, "The Tn5 transposon," *Annual review of microbiology*, vol. 47, no. 1, 1993. DOI: 10.1146/annurev.mi.47.100193.004501.

[231] G. J. McKenzie and N. L. Craig, "Fast, easy and efficient: Site-specific insertion of transgenes into Enterobacterial chromosomes using Tn7 without need for selection of the insertion event," *BMC microbiology*, vol. 6, no. 1, 2006. DOI: https://doi.org/10.1186/1471-2180-6-39.

[232] M. N. Remus-Emsermann, P. Gisler, and D. Drissner, "Mini Tn 7-transposon delivery vectors for inducible or constitutive fluorescent protein expression in Enterobacteriaceae," *FEMS Microbiology Letters*, vol. 363, no. 16, 2016. DOI: https://doi.org/10.1093/femsle/fnw178.

[233] B. Koch, L. E. Jensen, and O. Nybroe, "A panel of Tn7-based vectors for insertion of the gfp marker gene or for delivery of cloned DNA into Gram-negative bacteria at a neutral chromosomal site," *Journal of microbiological methods*, vol. 45, no. 3, 2001. DOI: https://doi.org/10.1016/S0167-7012(01)00246-9.

[234] L. Lambertsen, C. Sternberg, and S. Molin, "Mini-Tn7 transposons for site-specific tagging of bacteria with fluorescent proteins," *Environmental microbiology*, vol. 6, no. 7, 2004. DOI: 10.1111/j.1462-2920.2004.00605.x.

[235] K.-H. Choi and H. P. Schweizer, "Mini-tn 7 insertion in bacteria with single att tn 7 sites: Example pseudomonas aeruginosa," *Nature protocols*, vol. 1, no. 1, 2006. DOI: https://doi.org/10.1038/nprot.2006.24.

[236] Z. Gitai, "New fluorescence microscopy methods for microbiology: Sharper, faster, and quantitative," *Current opinion in microbiology*, vol. 12, no. 3, 2009. DOI: https://doi.org/10.1016/j.mib.2009.03.001.

[237] P. Meyer and J. Dworkin, "Applications of fluorescence microscopy to single bacterial cells," *Research in microbiology*, vol. 158, no. 3, 2007. DOI: https://doi.org/10.1016/j.resmic.2006.12.008.

[238] S. van Teeffelen, J. W. Shaevitz, and Z. Gitai, "Image analysis in fluorescence microscopy: Bacterial dynamics as a case study," *Bioessays*, vol. 34, no. 5, 2012. DOI: https://doi.org/10.1002/bies.201100148.

[239] D. Z. Rudner and R. Losick, "Protein subcellular localization in bacteria," *Cold Spring Harbor perspectives in biology*, vol. 2, no. 4, 2010. DOI: 10.1101/cshperspect.a000307.

[240] G. J. Phillips, "Green fluorescent protein–a bright idea for the study of bacterial protein localization," *FEMS microbiology letters*, vol. 204, no. 1, 2001. DOI: https://doi.org/10.1111/j.1574-6968.2001.tb10854.x.

[241] H. P. Erickson, "Ftsz, a tubulin homologue in prokaryote cell division," *Trends in cell biology*, vol. 7, no. 9, 1997. DOI: https://doi.org/10.1016/S0962-8924(97)01108-2.

[242] P. C. Jennings, G. C. Cox, L. G. Monahan, and E. J. Harry, "Super-resolution imaging of the bacterial cytokinetic protein FtsZ," *Micron*, vol. 42, no. 4, 2011. DOI: https://doi.org/10.1016/j.micron.2010.09.003.

[243] A. W. Bisson-Filho, Y.-P. Hsu, G. R. Squyres, *et al.*, "Treadmilling by FtsZ filaments drives peptidoglycan synthesis and bacterial cell division,"

Science, vol. 355, no. 6326, 2017. DOI: https://doi.org/10.1126/science.aak9973.

[244] D. M. Raskin and P. A. De Boer, "Rapid pole-to-pole oscillation of a protein required for directing division to the middle of Escherichia coli," *Proceedings of the National Academy of Sciences*, vol. 96, no. 9, 1999. DOI: https://doi.org/10.1073/pnas.96.9.4971.

[245] C. Lesterlin, G. Ball, L. Schermelleh, and D. J. Sherratt, "RecA bundles mediate homology pairing between distant sisters during DNA break repair," *Nature*, vol. 506, no. 7487, 2014. DOI: https://doi.org/10.1038/nature12868.

[246] J. Fei and C. M. Sharma, "RNA localization in bacteria," *Microbiology spectrum*, vol. 6, no. 5, 2018. DOI: https://doi.org/10.1128/microbiolspec.rwr-0024-2018.

[247] J. K. Fisher, A. Bourniquel, G. Witz, B. Weiner, M. Prentiss, and N. Kleckner, "Four-dimensional imaging of E. coli nucleoid organization and dynamics in living cells," *Cell*, vol. 153, no. 4, 2013. DOI: https://doi.org/10.1016/j.cell.2013.04.006.

[248] H. Frickmann, A. E. Zautner, A. Moter, *et al.*, "Fluorescence in situ hybridization (FISH) in the microbiological diagnostic routine laboratory: A review," *Critical reviews in microbiology*, vol. 43, no. 3, 2017. DOI: https://doi.org/10.3109/1040841X.2016.1169990.

[249] J. Maukonen, J. Mättö, G. Wirtanen, L. Raaska, T. Mattila-Sandholm, and M. Saarela, "Methodologies for the characterization of microbes in industrial environments: A review," *Journal of Industrial Microbiology and Biotechnology*, vol. 30, 2003. DOI: https://doi.org/10.1007/s10295-003-0056-y.

[250] S. Krishnamurthy, A. Cortes, M. Lopez, *et al.*, "Ex vivo confocal fluorescence microscopy for rapid evaluation of tissues in surgical pathology practice," *Archives of pathology & laboratory medicine*, vol. 142, no. 3, 2018. DOI: https://doi.org/10.5858/arpa.2017-0164-OA.

[251] M. Ragazzi, S. Piana, C. Longo, *et al.*, "Fluorescence confocal microscopy for pathologists," *Modern Pathology*, vol. 27, no. 3, 2014. DOI: https://doi.org/10.1038/modpathol.2013.158.

[252] M. Sheppard, C. Webb, F. Heath, *et al.*, "Dynamics of bacterial growth and distribution within the liver during salmonella infection," *Cellular microbiology*, vol. 5, no. 9, 2003. DOI: https://doi.org/10.1046/j.1462-5822.2003.00296.x.

[253] E. J. Pollitt, P. T. Szkuta, N. Burns, and S. J. Foster, "Staphylococcus aureus infection dynamics," *PLoS pathogens*, vol. 14, no. 6, 2018. DOI: https://doi.org/10.1371/journal.ppat.1007112.

[254] J. L. Coombes and E. A. Robey, "Dynamic imaging of host–pathogen interactions in vivo," *Nature Reviews Immunology*, vol. 10, no. 5, 2010. DOI: https://doi.org/10.1038/nri2746.

[255] O. Nosyk, E. ter Haseborg, U. Metzger, and F. H. Frimmel, "A standardized pre-treatment method of biofilm flocs for fluorescence microscopic characterization," *Journal of Microbiological methods*, vol. 75, no. 3, 2008. DOI: https://doi.org/10.1016/j.mimet.2008.07.024.

[256] T. R. Neu and J. R. Lawrence, "Advanced techniques for in situ analysis of the biofilm matrix (structure, composition, dynamics) by means of laser scanning microscopy," *Microbial biofilms: methods and protocols*, 2014. DOI: https://doi.org/10.1007/978-1-4939-0467-9_4.

[257] C. Hope, D. Clements, and M. Wilson, "Determining the spatial distribution of viable and nonviable bacteria in hydrated microcosm dental plaques by viability profiling," *Journal of applied microbiology*, vol. 93, no. 3, 2002. DOI: https://doi.org/10.1046/j.1365-2672.2002.01703.x.

[258] Y. Aoi, "In situ identification of microorganisms in biofilm communities," *Journal of bioscience and bioengineering*, vol. 94, no. 6, 2002. DOI: https://doi.org/10.1016/S1389-1723(02)80194-3.

[259] T. Thurnheer, R. Gmür, and B. Guggenheim, "Multiplex FISH analysis of a six-species bacterial biofilm," *Journal of microbiological methods*, vol. 56, no. 1, 2004. DOI: https://doi.org/10.1016/j.mimet.2003.09.003.

[260] L. E. Chávez de Paz, I. R. Hamilton, and G. Svensäter, "Oral bacteria in biofilms exhibit slow reactivation from nutrient deprivation," *Microbiology*, vol. 154, no. 7, 2008. DOI: https://doi.org/10.1099/mic.0.2008/016576-0.

[261] L. E. Chávez de Paz, "Image analysis software based on color segmentation for characterization of viability and physiological activity of biofilms," *Applied and environmental microbiology*, vol. 75, no. 6, 2009. DOI: https://doi.org/10.1128/AEM.02000-08.

[262] S. Daddi Oubekka, R. Briandet, M.-P. Fontaine-Aupart, and K. Steenkeste, "Correlative time-resolved fluorescence microscopy to assess antibiotic diffusion-reaction in biofilms," *Antimicrobial agents and chemotherapy*, vol. 56, no. 6, 2012. DOI: https://doi.org/10.1128/aac.00216-12.

[263] C. Kromer, K. Schwibbert, A. K. Gadicherla, *et al.*, "Monitoring and imaging pH in biofilms utilizing a fluorescent polymeric nanosensor," *Scientific Reports*, vol. 12, no. 1, 2022. DOI: https://doi.org/10.1038/s41598-022-13518-1.

[264] G. Hidalgo, A. Burns, E. Herz, *et al.*, "Functional tomographic fluorescence imaging of ph microenvironments in microbial biofilms by use of silica nanoparticle sensors," *Applied and environmental microbiology*, vol. 75, no. 23, 2009. DOI: https://doi.org/10.1128/AEM.01220-09.

[265] P.-T. Su, C.-T. Liao, J.-R. Roan, S.-H. Wang, A. Chiou, and W.-J. Syu, "Bacterial colony from two-dimensional division to three-dimensional development," *PloS one*, vol. 7, no. 11, 2012. DOI: https://doi.org/10.1371/journal.pone.0048098.

[266] J. Yan, A. G. Sharo, H. A. Stone, N. S. Wingreen, and B. L. Bassler, "Vibrio cholerae biofilm growth program and architecture revealed by single-cell live imaging," *Proceedings of the National Academy of Sciences*, vol. 113, no. 36, 2016. DOI: https://doi.org/10.1073/pnas.1611494113.

[267] Q. Zhang, J. Li, J. Nijjer, *et al.*, "Morphogenesis and cell ordering in confined bacterial biofilms," *Proceedings of the National Academy of Sciences*, vol. 118, no. 31, 2021. DOI: https://doi.org/10.1073/pnas.2107107118.

[268] I. N. Nuñez, T. F. Matute, I. D. Del Valle, *et al.*, "Artificial symmetry-breaking for morphogenetic engineering bacterial colonies," *ACS synthetic biology*, vol. 6, no. 2, 2017. DOI: https://doi.org/10.1021/acssynbio.6b00149.

[269] K. Drescher, J. Dunkel, C. D. Nadell, *et al.*, "Architectural transitions in Vibrio cholerae biofilms at single-cell resolution," *Proceedings of the National Academy of Sciences*, vol. 113, no. 14, 2016. DOI: 10.1073/pnas.1601702113.

[270] M. Krsmanovic, D. Biswas, H. Ali, A. Kumar, R. Ghosh, and A. K. Dickerson, "Hydrodynamics and surface properties influence biofilm proliferation," *Advances in Colloid and Interface Science*, vol. 288, 2021. DOI: https://doi.org/10.1016/j.cis.2020.102336.

[271] K. J. Baxter, F. A. Sargison, J. R. Fitzgerald, G. McConnell, and P. A. Hoskisson, "Time-lapse mesoscopy of Candida albicans and Staphylococcus aureus dual-species biofilms reveals a structural role for the hyphae of C. albicans in biofilm formation," *Microbiology*, vol. 170, no. 1, 2024. DOI: https://doi.org/10.1099/mic.0.001426.

[272] J. Schindelin, I. Arganda-Carreras, E. Frise, *et al.*, "Fiji: An open-source platform for biological-image analysis," *Nature methods*, vol. 9, no. 7, 2012. DOI: 10.1038/nmeth.2019.

[273] F. de Chaumont, S. Dallongeville, and J.-C. Olivo-Marin, "ICY: A new open-source community image processing software," in *2011 IEEE International Symposium on Biomedical Imaging: From Nano to Macro*, IEEE, 2011. DOI: 10.1109/ISBI.2011.5872395.

[274] M. R. Lamprecht, D. M. Sabatini, and A. E. Carpenter, "CellProfiler™: Free, versatile software for automated biological image analysis," *Biotechniques*, vol. 42, no. 1, 2007. DOI: https://doi.org/10.2144/000112257.

[275] H. Jeckel and K. Drescher, "Advances and opportunities in image analysis of bacterial cells and communities," *FEMS Microbiology Reviews*, vol. 45, no. 4, 2021. DOI: https://doi.org/10.1093/femsre/fuaa062.

[276] A. Ducret, E. M. Quardokus, and Y. V. Brun, "MicrobeJ, a tool for high throughput bacterial cell detection and quantitative analysis," *Nature microbiology*, vol. 1, no. 7, 2016. DOI: https://doi.org/10.1038/nmicrobiol.2016.77.

[277] R. Hartmann, M. C. van Teeseling, M. Thanbichler, and K. Drescher, "BacStalk: A comprehensive and interactive image analysis software tool for bacterial cell biology," *Molecular microbiology*, vol. 114, no. 1, 2020. DOI: https://doi.org/10.1111/mmi.14501.

[278] S. Stylianidou, C. Brennan, S. B. Nissen, N. J. Kuwada, and P. A. Wiggins, "SuperSegger: Robust image segmentation, analysis and lineage tracking of bacterial cells," *Molecular microbiology*, vol. 102, no. 4, 2016. DOI: https://doi.org/10.1111/mmi.13486.

[279] W. Burger and M. J. Burge, *Principles of digital image processing: fundamental techniques*. Springer Science & Business Media, 2010.

[280] J. Xavier, D. White, and J. Almeida, "Automated biofilm morphology quantification from confocal laser scanning microscopy imaging," *Water Science and Technology*, vol. 47, no. 5, 2003. DOI: https://doi.org/10.2166/wst.2003.0273.

[281] A. Heydorn, A. T. Nielsen, M. Hentzer, *et al.*, "Quantification of biofilm structures by the novel computer program COMSTAT," *Microbiology*, vol. 146, no. 10, 2000. DOI: https://doi.org/10.1099/00221287-146-10-2395.

[282] M. Vorregaard, "Comstat2 - a modern 3D image analysis environment for biofilms," M.S. thesis, Technical University of Denmark, DTU, DK-2800 Kgs. Lyngby, Denmark, 2008.

[283] R. Hartmann, H. Jeckel, E. Jelli, *et al.*, "Quantitative image analysis of microbial communities with BiofilmQ," *Nature microbiology*, vol. 6, no. 2, 2021. DOI: 10.1038/s41564-020-00817-4.

[284] F. Merchant and K. Castleman, *Microscope image processing*. Academic press, 2022.

[285] R. C. Gonzalez, R. E. Woods, and S. L. Eddins, "Intensity transformations and spatial filtering," in *Digital Image Processing using MATLAB*. Pearson, 2018, ch. 3.

[286] B. Xu, Y. Zhuang, H. Tang, and L. Zhang, "Object-based multilevel contrast stretching method for image enhancement," *IEEE transactions on consumer electronics*, vol. 56, no. 3, pp. 1746–1754, 2010. DOI: 10.1109/TCE.2010.5606321.

[287] S. M. Pizer, E. P. Amburn, J. D. Austin, *et al.*, "Adaptive histogram equalization and its variations," *Computer vision, graphics, and image processing*, vol. 39, no. 3, 1987. DOI: https://doi.org/10.1016/S0734-189X(87)80186-X.

[288] M. R. Banham and A. K. Katsaggelos, "Digital image restoration," *IEEE signal processing magazine*, vol. 14, no. 2, 1997. DOI: 10.1109/79.581363.

[289] S.-J. Ko and Y. H. Lee, "Center weighted median filters and their applications to image enhancement," *IEEE transactions on circuits and systems*, vol. 38, no. 9, pp. 984–993, 1991. DOI: 10.1109/31.83870.

[290] S. H. Teoh and H. Ibrahim, "Median filtering frameworks for reducing impulse noise from grayscale digital images: A literature survey," *International Journal of Future Computer and Communication*, vol. 1, no. 4, 2012. DOI: 10.7763/IJFCC.2012.V1.87.

[291] N. Bonnet, "Some trends in microscope image processing," *Micron*, vol. 35, no. 8, 2004. DOI: https://doi.org/10.1016/j.micron.2004.04.006.

[292] J.-B. Sibarita, "Deconvolution microscopy," in *Microscopy Techniques*, Springer, 2005. DOI: https://doi.org/10.1007/b102215.

[293] T. J. Holmes, "Blind deconvolution of quantum-limited incoherent imagery: Maximum-likelihood approach," *JOSA A*, vol. 9, no. 7, 1992. DOI: https://doi.org/10.1364/JOSAA.9.001052.

[294] B. Bottura, L. M. Rooney, P. A. Hoskisson, and G. McConnell, "Intracolony channel morphology in Escherichia coli biofilms is governed by nutrient availability and substrate stiffness," *Biofilm*, vol. 4, 2022. DOI: https://doi.org/10.1016/j.bioflm.2022.100084.

[295] P. S. Stewart, "Biophysics of biofilm infection," *Pathogens and disease*, vol. 70, no. 3, 2014. DOI: https://doi.org/10.1111/2049-632X.12118.

[296] E. S. Gloag, S. Fabbri, D. J. Wozniak, and P. Stoodley, "Biofilm mechanics: Implications in infection and survival," *Biofilm*, vol. 2, 2020. DOI: https://doi.org/10.1016/j.bioflm.2019.100017.

[297] P. A. Suci, M. Mittelman, F. P. Yu, and G. G. Geesey, "Investigation of ciprofloxacin penetration into Pseudomonas aeruginosa biofilms," *Antimicrobial agents and chemotherapy*, vol. 38, no. 9, 1994. DOI: https://doi.org/10.1128/aac.38.9.2125.

[298] R. M. Donlan, "Role of biofilms in antimicrobial resistance," *ASAIO journal*, vol. 46, no. 6, 2000. DOI: https://doi.org/10.1097/00002480-200011000-00037.

[299] M. Desai, T. Bühler, P. Weller, and M. Brown, "Increasing resistance of planktonic and biofilm cultures of Burkholderia cepacia to ciprofloxacin and ceftazidime during exponential growth," *The Journal of antimicrobial chemotherapy*, vol. 42, no. 2, 1998. DOI: https://doi.org/10.1093/jac/42.2.153.

[300] G. Anderson and G. O'toole, "Innate and induced resistance mechanisms of bacterial biofilms," in *Bacterial biofilms*, Springer, 2008, ch. 5.

[301] R. Patel, "Biofilms and antimicrobial resistance," *Clinical Orthopaedics and Related Research*, vol. 437, 2005. DOI: 10.1097/01.blo.0000175714.68624.74.

[302] WHO, *Antimicrobial resistance: global report on surveillance*. World Health Organization, 2014.

[303] S. L. Solomon and K. B. Oliver, "Antibiotic resistance threats in the United States: Stepping back from the brink," *American family physician*, vol. 89, no. 12, 2014.

[304] O. Paliy and T. S. Gunasekera, "Growth of E. coli BL21 in minimal media with different gluconeogenic carbon sources and salt contents," *Applied microbiology and biotechnology*, vol. 73, no. 5, 2007. DOI: 10.1007/s00253-006-0554-8.

[305] T. E. Shehata and A. G. Marr, "Effect of nutrient concentration on the growth of escherichia coli," *Journal of bacteriology*, vol. 107, no. 1, 1971. DOI: 10.1128/jb.107.1.210-216.1971.

[306] T. Bauchop and S. Elsden, "The growth of micro-organisms in relation to their energy supply," *Microbiology*, vol. 23, no. 3, 1960. DOI: 10.1099/00221287-23-3-457.

[307] H. Fujikawa and M. Matsushita, "Bacterial fractal growth in the concentration field of nutrient," *Journal of the Physical Society of Japan*, vol. 60, no. 1, 1991. DOI: 10.1143/JPSJ.60.88.

[308] M. Mimura, H. Sakaguchi, and M. Matsushita, "Reaction–diffusion modelling of bacterial colony patterns," *Physica A: Statistical Mechanics and its Applications*, vol. 282, no. 1-2, 2000. DOI: 10.1016/S0378-4371(00)00085-6.

[309] J. Wang, J. Wu, J. Li, R. Kong, X. Li, and X. Wang, "Simulation of various biofilm fractal morphologies by agent-based model," *Colloids and Surfaces B: Biointerfaces*, vol. 227, 2023. DOI: https://doi.org/10.1016/j.colsurfb.2023.113352.

[310] K. Sauer, M. Cullen, A. Rickard, L. Zeef, D. G. Davies, and P. Gilbert, "Characterization of nutrient-induced dispersion in Pseudomonas aeruginosa PAO1 biofilm," *Journal of bacteriology*, vol. 186, no. 21, 2004. DOI: https://doi.org/10.1128/jb.186.21.7312-7326.2004.

[311] D. Schleheck, N. Barraud, J. Klebensberger, *et al.*, "Pseudomonas aeruginosa PAO1 preferentially grows as aggregates in liquid batch cultures and disperses upon starvation," *PloS one*, vol. 4, no. 5, 2009. DOI: https://doi.org/10.1371/journal.pone.0005513.

[312] F. Díaz-Pascual, M. Lempp, K. Nosho, *et al.*, "Spatial alanine metabolism determines local growth dynamics of Escherichia coli colonies," *Elife*, vol. 10, 2021. DOI: 10.7554/eLife.70794.

[313] E. Wolfsberg, C. P. Long, and M. R. Antoniewicz, "Metabolism in dense microbial colonies: 13C metabolic flux analysis of E. coli grown on agar identifies two distinct cell populations with acetate cross-feeding," *Metabolic engineering*, vol. 49, 2018. DOI: 10.1016/j.ymben.2018.08.013.

[314] S. Benomar, D. Ranava, M. L. Cárdenas, *et al.*, "Nutritional stress induces exchange of cell material and energetic coupling between bacterial species," *Nature communications*, vol. 6, no. 1, 2015. DOI: 10.1038/ncomms7283.

[315] K. W. Kolewe, S. R. Peyton, and J. D. Schiffman, "Fewer bacteria adhere to softer hydrogels," *ACS applied materials & interfaces*, vol. 7, no. 35, 2015. DOI: 10.1021/acsami.5b04269.

[316] F. Song and D. Ren, "Stiffness of cross-linked poly (dimethylsiloxane) affects bacterial adhesion and antibiotic susceptibility of attached cells," *Langmuir*, vol. 30, no. 34, 2014. DOI: 10.1021/la502029f.

[317] N. Saha, C. Monge, V. Dulong, C. Picart, and K. Glinel, "Influence of polyelectrolyte film stiffness on bacterial growth," *Biomacromolecules*, vol. 14, no. 2, 2013. DOI: 10.1021/bm301774a.

[318] F. Song, M. E. Brasch, H. Wang, J. H. Henderson, K. Sauer, and D. Ren, "How bacteria respond to material stiffness during attachment: A role of Escherichia coli flagellar motility," *ACS applied materials & interfaces*, vol. 9, no. 27, 2017. DOI: 10.1021/acsami.7b04757.

[319] A. Cont, T. Rossy, Z. Al-Mayyah, and A. Persat, "Biofilms deform soft surfaces and disrupt epithelia," *Elife*, vol. 9, 2020. DOI: 10.7554/eLife.56533.

[320] E. Donnelly and F. Mothe, *Polar transformer*, https://imagej.nih.gov/ij/plugins/polar-transformer.html, 2007. (visited on 07/21/2021).

[321] K. Zuiderveld, "Contrast limited adaptive histogram equalization," in *Graphics Gems*. Academic Press, 1994, ch. VIII.

[322] B. Iglewicz and D. C. Hoaglin, *How to detect and handle outliers*. Asq Press, 1993, vol. 16.

[323] G. Chen and K. Strevett, "Impact of carbon and nitrogen conditions on E. coli surface thermodynamics," *Colloids and Surfaces B: Biointerfaces*, vol. 28, no. 2-3, 2003. DOI: 10.1016/S0927-7765(02)00143-1.

[324] M. R. Warren, H. Sun, Y. Yan, J. Cremer, B. Li, and T. Hwa, "Spatiotemporal establishment of dense bacterial colonies growing on hard agar," *Elife*, vol. 8, 2019. DOI: 10.7554/eLife.41093.

[325] J. W. Wimpenny, "The growth and form of bacterial colonies," *Microbiology*, vol. 114, no. 2, 1979. DOI: 10.1099/00221287-114-2-483.

[326] B. Qin, C. Fei, A. A. Bridges, *et al.*, "Cell position fates and collective fountain flow in bacterial biofilms revealed by light-sheet microscopy," *Science*, vol. 369, no. 6499, 2020. DOI: 10.1126/science.abb8501.

[327] D. O. Serra and R. Hengge, "Bacterial multicellularity: The biology of Escherichia coli building large-scale biofilm communities," *Annual review of microbiology*, vol. 75, 2021. DOI: 10.1146/annurev-micro-031921-055801.

[328] Z. Yao, R. M. Davis, R. Kishony, D. Kahne, and N. Ruiz, "Regulation of cell size in response to nutrient availability by fatty acid biosynthesis in Escherichia coli," *Proceedings of the National Academy of Sciences*, vol. 109, no. 38, 2012. DOI: 10.1073/pnas.1209742109.

[329] R. Waldrop, A. McLaren, F. Calara, and R. McLemore, "Biofilm growth has a threshold response to glucose in vitro," *Clinical Orthopaedics and Related Research®*, vol. 472, no. 11, 2014. DOI: 10.1007/s11999-014-3538-5.

[330] S. Pirt, "A kinetic study of the mode of growth of surface colonies of bacteria and fungi," *Microbiology*, vol. 47, no. 2, 1967. DOI: 10.1099/00221287-47-2-181.

[331] L. Chen, J. Noorbakhsh, R. M. Adams, *et al.*, "Two-dimensionality of yeast colony expansion accompanied by pattern formation," *PLoS computational biology*, vol. 10, no. 12, 2014. DOI: 10.1371/journal.pcbi.1003979.

[332] J. M. Chacón, W. Möbius, and W. R. Harcombe, "The spatial and metabolic basis of colony size variation," *The ISME journal*, vol. 12, no. 3, 2018. DOI: https://doi.org/10.1038/s41396-017-0038-0.

[333] A. Yang, W. S. Tang, T. Si, and J. X. Tang, "Influence of physical effects on the swarming motility of Pseudomonas aeruginosa," *Biophysical Journal*, vol. 112, no. 7, 2017. DOI: 10.1016/j.bpj.2017.02.019.

[334] G. Reshes, S. Vanounou, I. Fishov, and M. Feingold, "Timing the start of division in E. coli: A single-cell study," *Physical biology*, vol. 5, no. 4, 2008. DOI: 10.1088/1478-3975/5/4/046001.

[335] J.-U. Kreft, C. Picioreanu, J. W. Wimpenny, and M. C. van Loosdrecht, "Individual-based modelling of biofilms," *Microbiology*, vol. 147, no. 11, 2001. DOI: 10.1099/00221287-147-11-2897.

[336] E. Alpkvist, C. Picioreanu, M. C. van Loosdrecht, and A. Heyden, "Three-dimensional biofilm model with individual cells and continuum EPS matrix," *Biotechnology and bioengineering*, vol. 94, no. 5, 2006. DOI: 10.1002/bit.20917.

[337] L. A. Lardon, B. V. Merkey, S. Martins, *et al.*, "IDynoMiCS: Next-generation individual-based modelling of biofilms," *Environmental microbiology*, vol. 13, no. 9, 2011. DOI: 10.1111/j.1462-2920.2011.02414.x.

[338] J. B. Xavier, C. Picioreanu, and M. C. Van Loosdrecht, "A framework for multidimensional modelling of activity and structure of multispecies biofilms," *Environmental microbiology*, vol. 7, no. 8, 2005. DOI: 10.1111/j.1462-2920.2005.00787.x.

[339] B. Bottura, L. M. Rooney, M. Feeney, P. A. Hoskisson, and G. McConnell, "Fractal complexity of escherichia coli nutrient transport channels is influenced by cell shape and growth environment," *bioRxiv*, 2023.

[340] K. Falconer, *Fractal geometry: mathematical foundations and applications*. John Wiley & Sons, 2004.

[341] H. Koch, "Sur une courbe continue sans tangente, obtenue par une construction géométrique élémentaire," *Arkiv for Matematik, Astronomi och Fysik*, vol. 1, 1904.

[342] V. P. Dimri, *Application of fractals in earth sciences*. CRC Press, 2000.

[343] B. B. Mandelbrot, *The fractal geometry of Nature*. WH Freeman and Company New York, 1983, ch. 8.

[344] M. R. Schroeder, *Fractals, chaos, power laws : minutes from an infinite paradise*. W.H. Freeman, 1991.

[345] W. Klonowski, "Signal and image analysis using chaos theory and fractal geometry," *Machine Graphics and Vision*, vol. 9, no. 1/2, 2000.

[346] J. Gagnepain and C. Roques-Carmes, "Fractal approach to two-dimensional and three-dimensional surface roughness," *wear*, vol. 109, no. 1-4, 1986. DOI: https://doi.org/10.1016/0043-1648(86)90257-7.

[347] S. S. Cross, "The application of fractal geometric analysis to microscopic images," *Micron*, vol. 25, no. 1, 1994. DOI: https://doi.org/10.1016/0968-4328(94)90057-4.

[348] S. S. Chen, J. M. Keller, and R. M. Crownover, "On the calculation of fractal features from images," *IEEE Transactions on Pattern Analysis and Machine Intelligence*, vol. 15, no. 10, 1993. DOI: 10.1109/34.254066.

[349] C. Allain and M. Cloitre, "Characterizing the lacunarity of random and deterministic fractal sets," *Physical review A*, vol. 44, no. 6, p. 3552, 1991.

[350] B. B. Mandelbrot, "A fractal's lacunarity, and how it can be tuned and measured," in *Fractals in biology and medicine*, Springer, 1994.

[351] Y. Gefen, Y. Meir, B. B. Mandelbrot, and A. Aharony, "Geometric implementation of hypercubic lattices with noninteger dimensionality by use

of low lacunarity fractal lattices," *Physical Review Letters*, vol. 50, no. 3, 1983. DOI: 10.1103/PhysRevLett.50.145.

[352] R. E. Plotnick, R. H. Gardner, W. W. Hargrove, K. Prestegaard, and M. Perlmutter, "Lacunarity analysis: A general technique for the analysis of spatial patterns," *Physical review E*, vol. 53, no. 5, 1996. DOI: 10.1103/PhysRevE.53.5461.

[353] G. A. Losa, "The fractal geometry of life.," in *Biology Forum/Rivista di Biologia*, vol. 102, 2009.

[354] Z. Lewandowski, "Notes on biofilm porosity," *Water Research*, vol. 34, no. 9, 2000. DOI: https://doi.org/10.1016/S0043-1354(00)00186-X.

[355] X. Yang, H. Beyenal, G. Harkin, and Z. Lewandowski, "Quantifying biofilm structure using image analysis," *Journal of microbiological methods*, vol. 39, no. 2, 2000. DOI: https://doi.org/10.1016/S0167-7012(99)00097-4.

[356] B. Purevdorj, J. W. Costerton, and P. Stoodley, "Influence of hydrodynamics and cell signaling on the structure and behavior of Pseudomonas aeruginosa biofilms," *Applied and environmental microbiology*, vol. 68, no. 9, 2002. DOI: https://doi.org/10.1128/AEM.68.9.4457-4464.2002.

[357] J. Wang, X. Li, R. Kong, J. Wu, and X. Wang, "Fractal morphology facilitates Bacillus subtilis biofilm growth," *Environmental Science and Pollution Research*, vol. 29, no. 37, 2022. DOI: https://doi.org/10.1007/s11356-022-19817-4.

[358] A. Moreau, G. Lorite, C. Rodrigues, A. Souza, and M. Cotta, "Fractal analysis of Xylella fastidiosa biofilm formation," *Journal of Applied Physics*, vol. 106, no. 2, 2009. DOI: https://doi.org/10.1063/1.3173172.

[359] S. Dutta Sinha, S. Das, S. Tarafdar, and T. Dutta, "Monitoring of wild Pseudomonas biofilm strain conditions using statistical characterization of

scanning electron microscopy images," *Industrial & Engineering Chemistry Research*, vol. 56, no. 34, 2017. DOI: https://doi.org/10.1021/acs.iecr.7b01106.

[360] S. Peleg, J. Naor, R. Hartley, and D. Avnir, "Multiple resolution texture analysis and classification," *IEEE Transactions on Pattern Analysis and Machine Intelligence*, no. 4, 1984. DOI: 10.1109/TPAMI.1984.4767557.

[361] N. Sarkar and B. B. Chaudhuri, "An efficient approach to estimate fractal dimension of textural images," *Pattern recognition*, vol. 25, no. 9, 1992. DOI: https://doi.org/10.1016/0031-3203(92)90066-R.

[362] J. Li, Q. Du, and C. Sun, "An improved box-counting method for image fractal dimension estimation," *Pattern recognition*, vol. 42, no. 11, 2009. DOI: https://doi.org/10.1016/j.patcog.2009.03.001.

[363] C. Panigrahy *et al.*, "An approximated box height for differential-box-counting method to estimate fractal dimensions of gray-scale images," *Entropy*, vol. 19, no. 10, 2017. DOI: https://doi.org/10.3390/e19100534.

[364] C. Panigrahy, A. Seal, N. K. Mahato, and D. Bhattacharjee, "Differential box counting methods for estimating fractal dimension of gray-scale images: A survey," *Chaos, Solitons & Fractals*, vol. 126, 2019. DOI: https://doi.org/10.1016/j.chaos.2019.06.007.

[365] Y. Liu, L. Chen, H. Wang, *et al.*, "An improved differential box-counting method to estimate fractal dimensions of gray-level images," *Journal of visual communication and Image Representation*, vol. 25, no. 5, 2014. DOI: https://doi.org/10.1016/j.jvcir.2014.03.008.

[366] W.-S. Chen, S.-Y. Yuan, and C.-M. Hsieh, "Two algorithms to estimate fractal dimension of gray-level images," *Optical Engineering*, vol. 42, no. 8, 2003. DOI: https://doi.org/10.1117/1.1585061.

[367] X. Jin, S. Ong, *et al.*, "A practical method for estimating fractal dimension," *Pattern Recognition Letters*, vol. 16, no. 5, 1995. DOI: https://doi.org/10.1016/0167-8655(94)00119-N.

[368] P. Dong, "Test of a new lacunarity estimation method for image texture analysis," *International Journal of Remote Sensing*, vol. 21, no. 17, 2000. DOI: https://doi.org/10.1080/014311600750019985.

[369] D. Pendleton, A. Dathe, and P. Baveye, "Influence of image resolution and evaluation algorithm on estimates of the lacunarity of porous media," *Physical Review E*, vol. 72, no. 4, 2005. DOI: 10.1103/PhysRevE.72.041306.

[370] M. Obert, P. Pfeifer, and M. Sernetz, "Microbial growth patterns described by fractal geometry," *Journal of Bacteriology*, vol. 172, no. 3, 1990. DOI: https://doi.org/10.1128/jb.172.3.1180-1185.1990.

[371] S. Hermanowicz, U. Schindler, and P. Wilderer, "Fractal structure of biofilms: New tools for investigation of morphology," *Water Science and Technology*, vol. 32, no. 8, 1995. DOI: https://doi.org/10.1016/0273-1223(96)00013-3.

[372] H. Beyenal, C. Donovan, Z. Lewandowski, and G. Harkin, "Three-dimensional biofilm structure quantification," *Journal of microbiological methods*, vol. 59, no. 3, 2004. DOI: https://doi.org/10.1016/j.mimet.2004.08.003.

[373] T. Matsuyama and M. Matsushita, "Self-similar colony morphogenesis by gram-negative rods as the experimental model of fractal growth by a cell population," *Applied and environmental microbiology*, vol. 58, no. 4, 1992. DOI: https://doi.org/10.1128/aem.58.4.1227-1232.1992.

[374] D. Tomoiaga, J. Bubnell, L. Herndon, and P. Feinstein, "High rates of plasmid cotransformation in E. coli overturn the clonality myth and reveal

colony development," *Scientific Reports*, vol. 12, no. 1, 2022. DOI: https://doi.org/10.1038/s41598-022-14598-9.

[375] T. J. Rudge, F. Federici, P. J. Steiner, A. Kan, and J. Haseloff, "Cell polarity-driven instability generates self-organized, fractal patterning of cell layers," *ACS synthetic biology*, vol. 2, no. 12, 2013. DOI: https://doi.org/10.1021/sb400030p.

[376] M. Kimura, "Random genetic drift in multi-allelic locus," *Evolution*, 1955. DOI: https://doi.org/10.2307/2405476.

[377] J. Kayser, C. F. Schreck, Q. Yu, M. Gralka, and O. Hallatschek, "Emergence of evolutionary driving forces in pattern-forming microbial populations," *Philosophical Transactions of the Royal Society B: Biological Sciences*, vol. 373, no. 1747, 2018. DOI: https://doi.org/10.1098/rstb.2017.0106.

[378] M. Gralka, F. Stiewe, F. Farrell, W. Möbius, B. Waclaw, and O. Hallatschek, "Allele surfing promotes microbial adaptation from standing variation," *Ecology letters*, vol. 19, no. 8, 2016. DOI: https://doi.org/10.1111/ele.12625.

[379] B. Borer, D. Ciccarese, D. Johnson, and D. Or, "Spatial organization in microbial range expansion emerges from trophic dependencies and successful lineages," *Communications Biology*, vol. 3, no. 1, 2020. DOI: https://doi.org/10.1038/s42003-020-01409-y.

[380] H. Tronnolone, A. Tam, Z. Szenczi, *et al.*, "Diffusion-limited growth of microbial colonies," *Scientific Reports*, vol. 8, no. 1, pp. 1–11, 2018. DOI: https://doi.org/10.1038/s41598-018-23649-z.

[381] H. Fujikawa and M. Matsushita, "Fractal growth of Bacillus subtilis on agar plates," *Journal of the physical society of japan*, vol. 58, no. 11, 1989. DOI: https://doi.org/10.1143/JPSJ.58.3875.

[382] T. Matsuyama, M. Sogawa, and Y. Nakagawa, "Fractal spreading growth of Serratia marcescens which produces surface active exolipids," *FEMS microbiology letters*, vol. 61, no. 3, 1989. DOI: https://doi.org/10.1111/j.1574-6968.1989.tb03630.x.

[383] S. Matsuura, "Random growth of fungal colony model on diffusive and non-diffusive media," *Forma*, vol. 15, no. 3, 2000.

[384] E. Ben-Jacob, H. Shmueli, O. Shochet, and A. Tenenbaum, "Adaptive self-organization during growth of bacterial colonies," *Physica A: Statistical Mechanics and its Applications*, vol. 187, no. 3-4, 1992. DOI: https://doi.org/10.1016/0378-4371(92)90002-8.

[385] T. A. Witten Jr and L. M. Sander, "Diffusion-limited aggregation, a kinetic critical phenomenon," *Physical review letters*, vol. 47, no. 19, 1981. DOI: 10.1103/PhysRevLett.47.1400.

[386] N. Luo, S. Wang, J. Lu, X. Ouyang, and L. You, "Collective colony growth is optimized by branching pattern formation in Pseudomonas aeruginosa," *Molecular Systems Biology*, vol. 17, no. 4, 2021. DOI: https://doi.org/10.15252/msb.202010089.

[387] M. Matsushita and H. Fujikawa, "Diffusion-limited growth in bacterial colony formation," *Physica A: Statistical Mechanics and its Applications*, vol. 168, no. 1, 1990. DOI: 10.1016/0378-4371(90)90402-E.

[388] Y. Huang, I. Krumanocker, and M.-O. Coppens, "Fractal self-organization of bacteria-inspired agents," *Fractals*, vol. 20, no. 02, 2012. DOI: https://doi.org/10.1142/S0218348X12500168.

[389] K. D. Young, "The selective value of bacterial shape," *Microbiology and molecular biology reviews*, vol. 70, no. 3, 2006. DOI: https://doi.org/10.1128/mmbr.00001-06.

[390] H. Shi, B. P. Bratton, Z. Gitai, and K. C. Huang, "How to build a bacterial cell: MreB as the foreman of E. coli construction," *Cell*, vol. 172, no. 6, 2018. DOI: https://doi.org/10.1016/j.cell.2018.02.050.

[391] F. Van Den Ent, C. M. Johnson, L. Persons, P. De Boer, and J. Löwe, "Bacterial actin MreB assembles in complex with cell shape protein RodZ," *The EMBO journal*, vol. 29, no. 6, 2010. DOI: https://doi.org/10.1038/emboj.2010.9.

[392] G. Reshes, S. Vanounou, I. Fishov, and M. Feingold, "Cell shape dynamics in Escherichia coli," *Biophysical journal*, vol. 94, no. 1, 2008. DOI: 10.1529/biophysj.107.104398.

[393] K. J. Begg and W. D. Donachie, "Cell shape and division in Escherichia coli: Experiments with shape and division mutants," *Journal of bacteriology*, vol. 163, no. 2, 1985. DOI: https://doi.org/10.1128/jb.163.2.615-622.1985.

[394] E. Harry, L. Monahan, and L. Thompson, "Bacterial cell division: The mechanism and its precison," *International review of cytology*, vol. 253, 2006. DOI: https://doi.org/10.1016/S0074-7696(06)53002-5.

[395] M. Iwaya, C. W. Jones, J. Khorana, and J. Strominger, "Mapping of the mecillinam-resistant, round morphological mutants of Escherichia coli," *Journal of Bacteriology*, vol. 133, no. 1, 1978. DOI: https://doi.org/10.1128/jb.133.1.196-202.1978.

[396] S. Kumar, "Properties of adenyl cyclase and cyclic adenosine 3', 5'-monophosphate receptor protein-deficient mutants of Escherichia coli," *Journal*

of Bacteriology, vol. 125, no. 2, 1976. DOI: https://doi.org/10.1128/jb.125.2.545-555.1976.

[397] H. Matsuzawa, K. Hayakawa, T. Sato, and K. Imahori, "Characterization and genetic analysis of a mutant of Escherichia coli K-12 with rounded morphology," *Journal of Bacteriology*, vol. 115, no. 1, 1973. DOI: https://doi.org/10.1128/jb.115.1.436-442.1973.

[398] S. Normark, "Mutation in Escherichia coli K-12 mediating spherelike envelopes and changed tolerance to ultraviolet irradiation and some antibiotics," *Journal of Bacteriology*, vol. 98, no. 3, 1969. DOI: https://doi.org/10.1128/jb.98.3.1274-1277.1969.

[399] M. Wachi, M. Doi, S. Tamaki, *et al.*, "Mutant isolation and molecular cloning of mre genes, which determine cell shape, sensitivity to mecillinam, and amount of penicillin-binding proteins in Escherichia coli," *Journal of bacteriology*, vol. 169, no. 11, 1987. DOI: https://doi.org/10.1128/jb.169.11.4935-4940.1987.

[400] P. Carter, "Site-directed mutagenesis," *Biochemical Journal*, vol. 237, no. 1, 1986. DOI: 10.1042/bj2370001.

[401] T. Baba, T. Ara, M. Hasegawa, *et al.*, "Construction of Escherichia coli K-12 in-frame, single-gene knockout mutants: The Keio collection," *Molecular systems biology*, vol. 2, no. 1, 2006. DOI: https://doi.org/10.1038/msb4100050.

[402] K. A. Datsenko and B. L. Wanner, "One-step inactivation of chromosomal genes in Escherichia coli K-12 using PCR products," *Proceedings of the National Academy of Sciences*, vol. 97, no. 12, 2000. DOI: https://doi.org/10.1073/pnas.120163297.

[403] T. Ursell, T. K. Lee, D. Shiomi, *et al.*, "Rapid, precise quantification of bacterial cellular dimensions across a genomic-scale knockout library," *BMC biology*, vol. 15, no. 1, 2017. DOI: https://doi.org/10.1186/s12915-017-0348-8.

[404] M. Tong, S. French, S. S. El Zahed, W. k. Ong, P. D. Karp, and E. D. Brown, "Gene dispensability in Escherichia coli grown in thirty different carbon environments," *MBio*, vol. 11, no. 5, 2020. DOI: https://doi.org/10.1128/mbio.02259-20.

[405] M. Campos, S. K. Govers, I. Irnov, G. S. Dobihal, F. Cornet, and C. Jacobs-Wagner, "Genomewide phenotypic analysis of growth, cell morphogenesis, and cell cycle events in Escherichia coli," *Molecular systems biology*, vol. 14, no. 6, 2018. DOI: https://doi.org/10.15252/msb.20177573.

[406] J.-V. Höltje and E. I. Tuomanen, "The murein hydrolases of Escherichia coli: Properties, functions and impact on the course of infections in vivo," *Microbiology*, vol. 137, no. 3, 1991. DOI: https://doi.org/10.1099/00221287-137-3-441.

[407] L. Hedstrom, "IMP dehydrogenase: Structure, mechanism, and inhibition," *Chemical reviews*, vol. 109, no. 7, 2009. DOI: https://doi.org/10.1021/cr900021w.

[408] T. Mizuno and S. Mizushima, "Isolation and characterization of deletion mutants of ompR and envZ, regulatory genes for expression of the outer membrane proteins OmpC and OmpF in Escherichia coli," *The Journal of Biochemistry*, vol. 101, no. 2, 1987. DOI: https://doi.org/10.1093/oxfordjournals.jbchem.a121923.

[409] J. Weski and M. Ehrmann, "Genetic analysis of 15 protein folding factors and proteases of the Escherichia coli cell envelope," *Journal of bacteriology*, vol. 194, no. 12, 2012. DOI: https://doi.org/10.1128/jb.00221-12.

[410] A. J. Roe, S. W. Naylor, K. J. Spears, *et al.*, "Co-ordinate single-cell expression of LEE4-and LEE5-encoded proteins of Escherichia coli O157: H7," *Molecular microbiology*, vol. 54, no. 2, 2004. DOI: https://doi.org/10.1111/j.1365-2958.2004.04277.x.

[411] A. K. Camper, G. A. McFeters, W. G. Characklis, and W. L. Jones, "Growth kinetics of coliform bacteria under conditions relevant to drinking water distribution systems," *Applied and environmental microbiology*, vol. 57, no. 8, 1991. DOI: https://doi.org/10.1128/aem.57.8.2233-2239.1991.

[412] A. Cimdins and R. Simm, "Semiquantitative analysis of the red, dry, and rough colony morphology of Salmonella enterica serovar Typhimurium and Escherichia coli using Congo red," *c-di-GMP Signaling: Methods and Protocols*, 2017. DOI: https://doi.org/10.1007/978-1-4939-7240-1_18.

[413] E. Wershof, D. Park, D. J. Barry, *et al.*, "A FIJI macro for quantifying pattern in extracellular matrix," *Life science alliance*, vol. 4, no. 3, 2021. DOI: 10.26508/lsa.202000880.

[414] H. Ahammer, M. A. Reiss, M. Hackhofer, *et al.*, "ComsystanJ: A collection of Fiji/ImageJ2 plugins for nonlinear and complexity analysis in 1D, 2D and 3D," *Plos one*, vol. 18, no. 10, 2023. DOI: https://doi.org/10.1371/journal.pone.0292217.

[415] W. Wagner and M. Hiner, *Ridge detection*, https://imagej.net/plugins/ridge-detection, 2017. (visited on 04/11/2022).

[416] J. M. Blackledge, *Digital image processing: mathematical and computational methods*. Elsevier, 2005.

[417] *Koch curve in three dimensions ("delta" fractal).jpg - Wikipedia*, en, 2014. [Online]. Available: https://commons.wikimedia.org/wiki/File:Koch_Curve_in_Three_Dimensions_(%22Delta%22_fractal).jpg (visited on 11/16/2023).

[418] *Mandel zoom 00 mandelbrot set.jpg - Wikipedia*, en, 2013. [Online]. Available: https://commons.wikimedia.org/wiki/File:Mandel_zoom_00_mandelbrot_set.jpg (visited on 11/16/2023).

[419] *Benmiriello/fun-with-fractals - github repository*, en, 2020. [Online]. Available: https://github.com/BenMiriello/fun-with-fractals (visited on 11/16/2023).

[420] *Cubic starfish julia set.png - Wikipedia*, en, 2021. [Online]. Available: https://commons.wikimedia.org/wiki/File:Cubic_starfish_Julia_set.png (visited on 11/16/2023).

[421] *Xaos fractal 24.png - Wikipedia*, en, 2006. [Online]. Available: https://commons.wikimedia.org/wiki/File:Xaos_fractal_24.png (visited on 11/16/2023).

[422] P. E. McKight and J. Najab, "Kruskal-Wallis test," *The corsini encyclopedia of psychology*, 2010. DOI: https://doi.org/10.1002/9780470479216.corpsy0491.

[423] J. Van Gestel, H. Vlamakis, and R. Kolter, "From cell differentiation to cell collectives: Bacillus subtilis uses division of labor to migrate," *PLoS biology*, vol. 13, no. 4, 2015. DOI: https://doi.org/10.1371/journal.pbio.1002141.

[424] T. Ford, J. Graham, and D. Rickwood, "Iodixanol: A nonionic iso-osmotic centrifugation medium for the formation of self-generated gradients," *Analytical biochemistry*, vol. 220, no. 2, 1994. DOI: https://doi.org/10.1006/abio.1994.1350.

[425] P. R. Lambden and W. T. Drabble, "The gua operon of Escherichia coli K-12: Evidence for polarity from guaB to guaA," *Journal of bacteriology*, vol. 115, no. 3, 1973. DOI: https://doi.org/10.1128/jb.115.3.992-1002.1973.

[426] M. Kanehisa and S. Goto, "KEGG: Kyoto encyclopedia of genes and genomes," *Nucleic acids research*, vol. 28, no. 1, 2000. DOI: https://doi.org/10.1093/nar/28.1.27.

[427] B. Pang, J. L. McFaline, N. E. Burgis, *et al.*, "Defects in purine nucleotide metabolism lead to substantial incorporation of xanthine and hypoxanthine into DNA and RNA," *Proceedings of the National Academy of Sciences*, vol. 109, no. 7, 2012. DOI: https://doi.org/10.1073/pnas.1118455109.

[428] R. Simm, M. Morr, A. Kader, M. Nimtz, and U. Römling, "GGDEF and EAL domains inversely regulate cyclic di-GMP levels and transition from sessility to motility," *Molecular microbiology*, vol. 53, no. 4, 2004. DOI: https://doi.org/10.1111/j.1365-2958.2004.04206.x.

[429] U. Römling, "Cyclic di-GMP, an established secondary messenger still speeding up," *Environmental microbiology*, vol. 14, no. 8, 2012. DOI: https://doi.org/10.1111/j.1462-2920.2011.02617.x.

[430] S. Beyhan, A. D. Tischler, A. Camilli, and F. H. Yildiz, "Transcriptome and phenotypic responses of Vibrio cholerae to increased cyclic di-GMP

level," *Journal of bacteriology*, vol. 188, no. 10, 2006. DOI: https://doi.org/10.1128/jb.188.10.3600-3613.2006.

[431] Y. H. Foo, Y. Gao, H. Zhang, and L. J. Kenney, "Cytoplasmic sensing by the inner membrane histidine kinase EnvZ," *Progress in biophysics and molecular biology*, vol. 118, no. 3, 2015. DOI: https://doi.org/10.1016/j.pbiomolbio.2015.04.005.

[432] X. Liu and T. Ferenci, "Regulation of porin-mediated outer membrane permeability by nutrient limitation in Escherichia coli," *Journal of bacteriology*, vol. 180, no. 15, 1998. DOI: https://doi.org/10.1128/jb.180.15.3917-3922.1998.

[433] S. French, J.-P. Côté, J. M. Stokes, R. Truant, and E. D. Brown, "Bacteria getting into shape: Genetic determinants of E. coli morphology," *MBio*, vol. 8, no. 2, 2017. DOI: https://doi.org/10.1128/mbio.01977-16.

[434] A. Abay, G. Simionato, R. Chachanidze, *et al.*, "Glutaraldehyde–a subtle tool in the investigation of healthy and pathologic red blood cells," *Frontiers in physiology*, vol. 10, 2019. DOI: https://doi.org/10.3389/fphys.2019.00514.

[435] E. R. Oldewurtel, Y. Kitahara, and S. van Teeffelen, "Robust surface-to-mass coupling and turgor-dependent cell width determine bacterial dry-mass density," *Proceedings of the National Academy of Sciences*, vol. 118, no. 32, 2021. DOI: https://doi.org/10.1073/pnas.2021416118.

[436] L. Zhu, M. Rajendram, and K. C. Huang, "Effects of fixation on bacterial cellular dimensions and integrity," *Iscience*, vol. 24, no. 4, 2021. DOI: ttps://doi.org/10.1016/j.isci.2021.102348.

[437] D. K. Ranjit and K. D. Young, "The Rcs stress response and accessory envelope proteins are required for de novo generation of cell shape in Escherichia coli," *Journal of bacteriology*, vol. 195, no. 11, 2013. DOI: https://doi.org/10.1128/jb.00160-13.

[438] X. Wang, Y. Kong, H. Zhao, and X. Yan, "Dependence of the Bacillus subtilis biofilm expansion rate on phenotypes and the morphology under different growing conditions," *Development, growth & differentiation*, vol. 61, no. 7-8, 2019. DOI: 10.1111/dgd.12627.

[439] A. Liu, L. Tran, E. Becket, *et al.*, "Antibiotic sensitivity profiles determined with an Escherichia coli gene knockout collection: Generating an antibiotic bar code," *Antimicrobial agents and chemotherapy*, vol. 54, no. 4, 2010. DOI: https://doi.org/10.1128/aac.00906-09.

[440] S. Chakraborty and L. J. Kenney, "A new role of OmpR in acid and osmotic stress in Salmonella and E. coli," *Frontiers in microbiology*, vol. 9, 2018. DOI: https://doi.org/10.3389/fmicb.2018.02656.

[441] J. M. Wood, "Bacterial responses to osmotic challenges," *The Journal of General Physiology*, vol. 145, no. 5, 2015. DOI: 10.1085/jgp.201411296.

[442] X. Dai and M. Zhu, "High osmolarity modulates bacterial cell size through reducing initiation volume in Escherichia coli," *Msphere*, vol. 3, no. 5, 2018. DOI: https://doi.org/10.1128/msphere.00430-18.

[443] R. Buda, Y. Liu, J. Yang, *et al.*, "Dynamics of Escherichia coli's passive response to a sudden decrease in external osmolarity," *Proceedings of the National Academy of Sciences*, vol. 113, no. 40, 2016. DOI: https://doi.org/10.1073/pnas.1522185113.

[444] E. Rojas, J. A. Theriot, and K. C. Huang, "Response of Escherichia coli growth rate to osmotic shock," *Proceedings of the National Academy of*

Sciences, vol. 111, no. 21, 2014. DOI: https://doi.org/10.1073/pnas.1402591111.

[445] F. Li, X.-S. Xiong, Y.-Y. Yang, *et al.*, "Effects of NaCl concentrations on growth patterns, phenotypes associated with virulence, and energy metabolism in Escherichia coli BW25113," *Frontiers in microbiology*, vol. 12, 2021. DOI: https://doi.org/10.3389/fmicb.2021.705326.

[446] C. Beloin, J. Valle, P. Latour-Lambert, *et al.*, "Global impact of mature biofilm lifestyle on Escherichia coli K-12 gene expression," *Molecular microbiology*, vol. 51, no. 3, 2004. DOI: https://doi.org/10.1046/j.1365-2958.2003.03865.x.

[447] T. Kikuchi, Y. Mizunoe, A. Takade, S. Naito, and S.-i. Yoshida, "Curli fibers are required for development of biofilm architecture in Escherichia coli K-12 and enhance bacterial adherence to human uroepithelial cells," *Microbiology and immunology*, vol. 49, no. 9, 2005. DOI: https://doi.org/10.1111/j.1348-0421.2005.tb03678.x.

[448] F. Dong, S. Liu, D. Zhang, J. Zhang, and X. Wang, "Matrix-producing cells formed 'Van Gogh bundles' facilitate Bacillus subtilis biofilm self-healing," *Environmental Microbiology Reports*, vol. 14, no. 5, 2022. DOI: https://doi.org/10.1111/1758-2229.13099.

[449] Z. Ji, K. J. Card, and F. B. Dazzo, "CMEIAS JFrad: A digital computing tool to discriminate the fractal geometry of landscape architectures and spatial patterns of individual cells in microbial biofilms," *Microbial ecology*, vol. 69, 2015. DOI: https://doi.org/10.1007/s00248-014-0495-1.

[450] J. Kittler and J. Illingworth, "Minimum error thresholding," *Pattern recognition*, vol. 19, no. 1, 1986. DOI: https://doi.org/10.1016/0031-3203(86)90030-0.

[451] D. Bérubé and M. Jébrak, "High precision boundary fractal analysis for shape characterization," *Computers & Geosciences*, vol. 25, no. 9, 1999. DOI: https://doi.org/10.1016/S0098-3004(99)00067-9.

[452] R. K. Holmes and M. G. Jobling, "Genetics," in *Medical Microbiology*. Galveston (TX): University of Texas Medical Branch at Galveston, 1996, ch. 5.

[453] D. Summers, *The biology of plasmids*. John Wiley & Sons, 2009.

[454] C. I. Kado, "Origin and evolution of plasmids," *Antonie Van Leeuwenhoek*, vol. 73, 1998. DOI: https://doi.org/10.1023/A:1000652513822.

[455] A. Carattoli, "Plasmids and the spread of resistance," *International Journal of Medical Microbiology*, vol. 303, no. 6-7, 2013. DOI: https://doi.org/10.1016/j.ijmm.2013.02.001.

[456] J. A. Chemler and M. A. Koffas, "Metabolic engineering for plant natural product biosynthesis in microbes," *Current opinion in biotechnology*, vol. 19, no. 6, 2008. DOI: https://doi.org/10.1016/j.copbio.2008.10.011.

[457] C. Merlin, S. McAteer, and M. Masters, *Tools for characterization of Escherichia coli genes of unknown function*, 2002. DOI: https://doi.org/10.1128/jb.184.16.4573-4581.2002.

[458] B. Alberts, A. Johnson, J. Lewis, M. Raff, K. Roberts, and P. Walter, "Isolating, cloning, and sequencing DNA," in *Molecular Biology of the Cell. 4th edition*, Garland Science, 2002.

[459] K. C. Murphy, K. G. Campellone, and A. R. Poteete, "PCR-mediated gene replacement in Escherichia coli," *Gene*, vol. 246, no. 1-2, 2000. DOI: https://doi.org/10.1016/S0378-1119(00)00071-8.

[460] S. C. Kowalczykowski, D. A. Dixon, A. K. Eggleston, S. D. Lauder, and W. M. Rehrauer, "Biochemistry of homologous recombination in Escherichia coli," *Microbiological reviews*, vol. 58, no. 3, 1994. DOI: https://doi.org/10.1128/mr.58.3.401-465.1994.

[461] M. S. Dillingham and S. C. Kowalczykowski, "RecBCD enzyme and the repair of double-stranded DNA breaks," *Microbiology and Molecular Biology Reviews*, vol. 72, no. 4, 2008. DOI: https://doi.org/10.1128/mmbr.00020-08.

[462] S. D. Cosloy and M. Oishi, "Genetic transformation in Escherichia coli K12," *Proceedings of the National Academy of Sciences*, vol. 70, no. 1, 1973. DOI: https://doi.org/10.1073/pnas.70.1.84.

[463] K. C. Murphy, "Use of bacteriophage λ recombination functions to promote gene replacement in Escherichia coli," *Journal of bacteriology*, vol. 180, no. 8, 1998. DOI: https://doi.org/10.1128/jb.180.8.2063-2071.1998.

[464] D. Yu, H. M. Ellis, E.-C. Lee, N. A. Jenkins, N. G. Copeland, and D. L. Court, "An efficient recombination system for chromosome engineering in Escherichia coli," *Proceedings of the National Academy of Sciences*, vol. 97, no. 11, 2000. DOI: https://doi.org/10.1073/pnas.100127597.

[465] S. J. Aedo, H. R. Ma, and M. P. Brynildsen, "Checks and balances with use of the Keio collection for phenotype testing," in *Microbial Metabolic Engineering*, Springer, 2019. DOI: https://doi.org/10.1007/978-1-4939-9142-6_9.

[466] C. G. Miyada, L. Stoltzfus, and G. Wilcox, "Regulation of the araC gene of Escherichia coli: Catabolite repression, autoregulation, and effect on

araBAD expression," *Proceedings of the National Academy of Sciences*, vol. 81, no. 13, 1984. DOI: https://doi.org/10.1073/pnas.81.13.4120.

[467] C. Yanisch-Perron, J. Vieira, and J. Messing, "Improved M13 phage cloning vectors and host strains: Nucleotide sequences of the M13mpl8 and pUC19 vectors," *Gene*, vol. 33, no. 1, 1985. DOI: https://doi.org/10.1016/0378-1119(85)90120-9.

[468] Y. Bao, D. P. Lies, H. Fu, and G. P. Roberts, "An improved Tn7-based system for the single-copy insertion of cloned genes into chromosomes of gram-negative bacteria," *Gene*, vol. 109, no. 1, 1991. DOI: https://doi.org/10.1016/0378-1119(91)90604-A.

[469] M. Zatyka and C. M. Thomas, "Control of genes for conjugative transfer of plasmids and other mobile elements," *FEMS microbiology reviews*, vol. 21, no. 4, 1998. DOI: https://doi.org/10.1111/j.1574-6976.1998.tb00355.x.

[470] M. Lanzer and H. Bujard, "Promoters largely determine the efficiency of repressor action," *Proceedings of the National Academy of Sciences*, vol. 85, no. 23, 1988. DOI: https://doi.org/10.1073/pnas.85.23.8973.

[471] A. Saha, S. Haralalka, and R. K. Bhadra, "A naturally occurring point mutation in the 13-mer R repeat affects the oric function of the large chromosome of Vibrio cholerae O1 classical biotype," *Archives of microbiology*, vol. 182, 2004. DOI: https://doi.org/10.1007/s00203-004-0708-y.

[472] D. K. Summers, C. W. Beton, and H. L. Withers, "Multicopy plasmid instability: The dimer catastrophe hypothesis," *Molecular microbiology*, vol. 8, no. 6, 1993. DOI: https://doi.org/10.1111/j.1365-2958.1993.tb01648.x.

[473] J. Trevors, "Plasmid curing in bacteria," *FEMS microbiology reviews*, vol. 1, no. 3-4, 1986. DOI: https://doi.org/10.1111/j.1574-6968.1986.tb01189.x.

[474] W. N. Wood, K. D. Smith, J. A. Ream, and L. K. Lewis, "Enhancing yields of low and single copy number plasmid DNAs from Escherichia coli cells," *Journal of microbiological methods*, vol. 133, 2017. DOI: https://doi.org/10.1016/j.mimet.2016.12.016.

[475] J. Wang, R. Xu, and A. Liu, "IRDL cloning: A one-tube, zero-background, easy-to-use, directional cloning method improves throughput in recombinant DNA preparation," *PLoS One*, vol. 9, no. 9, 2014. DOI: https://doi.org/10.1371/journal.pone.0107907.

[476] L. C. Thomason, N. Costantino, and D. L. Court, "E. coli genome manipulation by P1 transduction," *Current protocols in molecular biology*, vol. 79, no. 1, 2007. DOI: https://doi.org/10.1002/0471142727.mb0117s79.

[477] M. J. Donath, M. A. Dominguez, and S. T. Withers III, "Development of an automated platform for high-throughput P1-phage transduction of Escherichia coli," *JALA: Journal of the Association for Laboratory Automation*, vol. 16, no. 2, 2011. DOI: https://doi.org/10.1016/j.jala.2010.08.005.

[478] M. Jinek, K. Chylinski, I. Fonfara, M. Hauer, J. A. Doudna, and E. Charpentier, "A programmable dual-RNA–guided DNA endonuclease in adaptive bacterial immunity," *science*, vol. 337, no. 6096, 2012. DOI: 10.1126/science.1225829.

[479] Y. Jiang, B. Chen, C. Duan, B. Sun, J. Yang, and S. Yang, "Multigene editing in the Escherichia coli genome via the CRISPR-Cas9 system," *Applied and environmental microbiology*, vol. 81, no. 7, 2015. DOI: https://doi.org/10.1128/AEM.04023-14.

[480] D. Zhao, S. Yuan, B. Xiong, *et al.*, "Development of a fast and easy method for Escherichia coli genome editing with CRISPR/Cas9," *Microbial cell factories*, vol. 15, 2016. DOI: https://doi.org/10.1186/s12934-016-0605-5.

[481] V. Ebrahimi and A. Hashemi, "Challenges of in vitro genome editing with CRISPR/Cas9 and possible solutions: A review," *Gene*, vol. 753, 2020. DOI: https://doi.org/10.1016/j.gene.2020.144813.

[482] F. Zhang, Y. Wen, and X. Guo, "CRISPR/Cas9 for genome editing: Progress, implications and challenges," *Human molecular genetics*, vol. 23, no. R1, 2014. DOI: https://doi.org/10.1093/hmg/ddu125.

[483] L. Beamish, R. Greenwood, K. Petty, and E. Preston, "Successful application of the λ-red recombinase system to inactivate lacI in Escherichia coli C29, BW25993 and MG1655," *J. Exp. Microbiol. Immunol*, vol. 12, 2004.

[484] J. Chen, Y. Li, K. Zhang, and H. Wang, "Whole-genome sequence of phage-resistant strain Escherichia coli DH5α," *Genome announcements*, vol. 6, no. 10, 2018. DOI: https://doi.org/10.1128/genomea.00097-18.

[485] R. E. Rose, "The nucleotide sequence of pACYC184," *Nucleic acids research*, vol. 16, no. 1, 1988. DOI: https://doi.org/10.1093/nar/16.1.355.

[486] N. E. Biolabs, *Neb tm calculator*, https://tmcalculator.neb.com/, 2022. (visited on 07/01/2022).

[487] E. Beck, G. Ludwig, E. Auerswald, B. Reiss, and H. Schaller, "Nucleotide sequence and exact localization of the neomycin phosphotransferase gene from transposon Tn5," *Gene*, vol. 19, no. 3, 1982. DOI: https://doi.org/10.1016/0378-1119(82)90023-3.